Geometrical, non-equilibrium and thermodynamic effects in topological systems

Published by

LOT
Trans 10
3512 JK Utrecht
The Netherlands

phone: +31 30 253 5775
e-mail: lot@uu.nl
http://www.lotschool.nl

Cover illustration: M.C. Escher, Band van Möbius II (Rode mieren), houtsnede in rood, zwart en grijsgroen, gedrukt van drie blokken, 1963.

ISBN: 978-94-028-0726-4
NUR: 925

Geometrical, non-equilibrium and thermodynamic effects in topological systems

Geometrische, niet-equilibrium en thermodynamische effecten in topologische systemen

(met een samenvatting in het Nederlands)

Proefschrift

ter verkrijging van de graad van doctor
aan de Universiteit Utrecht
op gezag van de rector magnificus, prof.dr. G.J. van der Zwaan,
ingevolge het besluit van het college voor promoties
in het openbaar te verdedigen op
vrijdag 5 september 2017
des ochtends te 10.30 uur

door

Anton Quelle

geboren 31 augustus 1988
te Amstelveen

Promotoren: Prof.dr. C. Morais Smith
Prof.dr. J-S. Caux

This thesis is dedicated to my parents,
who have raised me to see the lights
of curiosity, kindness and reason.

Contents

Publications xi

abbreviations xiii

1 Introduction **1**

2 Symmetry protected topological order **7**
2.1 Introduction 7
2.2 The relativistic quantum Hall effect 8
2.3 Time-reversal symmetry 10
2.3.1 Anomalous quantum Hall effect 10
2.3.2 Quantum spin Hall effect 11
2.4 Symmetry protected topological order 15
2.4.1 Bulk-boundary correspondence 15
2.5 Laughlin's charge-pumping argument 17
2.6 Conclusion 18

3 Topology in Floquet systems **21**
3.1 Introduction 21
3.2 Floquet theory 23
3.3 The shaken quantum chain 25
3.4 Topological phases of the Floquet Hamiltonian 26
3.4.1 Chirality of band gaps in Floquet systems 27
3.5 Dynamical competition between QHE and QSHE 29
3.5.1 The physical interpretation: a dynamical Haldane model 30
3.5.2 The band structure of irradiated honeycomb lattices . . 31

3.5.3 The interaction between ISO coupling and light 34
3.6 Topological resonances in Floquet systems 38
3.6.1 Numerical results 40
3.6.2 Low-energy effective theory 42
3.6.3 Experimental realisation 47
3.7 A Floquet topological phase without Chern number 49
3.7.1 The Model 50
3.7.2 Results 53
3.7.3 Experimental Realisation 58
3.8 Conclusion 63

4 Geometrical effects **65**
4.1 The Möbius band and its topological properties 67
4.1.1 Constraints on the lattice and Hamiltonian terms . . . 71
4.1.2 Topological phases on a Möbius system 75
4.2 The interplay between Möbius geometry and driving 84
4.2.1 Irradiated Möbius graphene without SO coupling . . . 85
4.2.2 Irradiated Möbius graphene with SO coupling 88
4.3 Topological superconductivity in non-planar systems 91
4.3.1 Introduction 92
4.3.2 Edge Modes on the cone 96
4.3.3 Edge Modes on the Möbius band 99
4.3.4 Fluxes and vortices in a p-wave Möbius band 103
4.4 Conclusion 105

5 Thermodynamic aspects **107**
5.1 Introduction 107
5.2 Global thermodynamics with a boundary 109
5.2.1 Hill Thermodynamics 110
5.3 Gibbs thermodynamics 112
5.4 Scaling of the grand canonical potential 113
5.5 Applications 117
5.5.1 Bernevig-Hughes-Zhang model 118
5.5.2 Kane and Mele model 123
5.5.3 Kitaev chain 126
5.5.4 Su-Schriefer-Heeger model 133
5.6 Conclusion 133

6 Concluding remarks **137**

A Trivialisability of Bloch Bundles **141**
A.1 The Bloch Bundle 141
A.2 The first Chern class of the Bloch bundle, and subbundles . . . 142
A.3 Systems with Time-Reversal Symmetry 143
A.4 A note on generalisations 145

B Induced vector potential in shaken lattices **147**

C Tight binding form of the 2D and 3D BHZ model **149**

Bibliography 151

Dankwoord **171**

Samenvatting **175**

Curriculum Vitae **179**

Publications

This thesis is based on the following publications:

1. Chapter 3.5 is based on the work in
   A. Quelle and C. Morais Smith. Dynamical competition between quantum hall and quantum spin hall effects.
   Phys. Rev. B, 90:195137, 2014.

2. Chapter 3.6 is based on the work in
   A. Quelle, M. O. Goerbig, and C. Morais Smith. Bandwidth-resonant Floquet states in honeycomb optical lattices.
   New Journal of Physics, 18(1):015006, 2016.

3. Chapter 3.7 is based on the work in
   A. Quelle, C. Weitenberg, K. Sengstock, and C. Morais Smith. Driving protocol for a Floquet topological phase without static counterpart.
   ArXiv:1704.00306

4. Chapter 4.1 is based on the work in
   W. Beugeling, A. Quelle, and C. Morais Smith. Nontrivial topological states on a Möbius band.
   Phys. Rev. B, 89(23):235112, 2014.

5. Chapter 4.2 is based on the work in
   A. Quelle, W. Beugeling, and C. Morais Smith. Topological Floquet states on a Möbius band irradiated by circularly polarised light.
   Solid State Communications, 215:27–33, 2015.

6. Chapter 4.3 is based on the work in
   A. Quelle, T. Kvorning, T. H. Hansson, and C. Morais Smith. Edge Majoranas on locally flat surfaces - the cone and the Möbius band.
   Phys. Rev. B 94, 125137 (2016), 2016.

7. Chapter 5 is based in part on
   A. Quelle, E. Cobanera, and C. M. Smith. Thermodynamic signatures of edge states in topological insulators.
   Phys. Rev. B, 94(7):075133, 2016.

8. Chapter 5 is also based on
   S. N. Kempkes, A. Quelle, and C. M. Smith. Universalities of thermodynamic signatures in topological phases.
   Scientific Reports, 6:38530, 2016.

In addition, I was involved in the following work, which does not appear in this thesis:

9. P. Cats, A. Quelle, S. Kempkes, and C. Morais Smith. Correlation functions for a 1D Weyl superconductor.
   In preparation.

10. J. van den Broeke, S. Kempkes, A. Quelle, and C. Morais Smith. Critical behavior of Kondo topological insulators.
    In preparation.

abbreviations

The following are the abbreviations appearing in this work, in order of appearance.

- QHE: Quantum Hall effect
- nD: n-dimensional
- TRS: Time-reversal symmetry
- QAHE: quantum anomalous Hall effect
- SPTO: Symmetry protected topological order
- QSHE: Quantum spin Hall effect
- SSH: Su-Schrieffer-Heeger
- TI: Topological insulator
- BZ: Brillouin zone
- UC: Unit cell
- NN: Nearest neighbour
- NNN: Next-nearest neighbour
- ISO: Intrinsic spin-orbit
- FTI: Floquet topological insulator

- GBZ: Generalised Brillouin zone
- ODC: Orientable double cover
- BHZ: Bernevig-Hughes-Zhang
- DOS: Density of states

CHAPTER 1

Introduction

The field of topological phases of matter dates back to the experimental discovery of the quantum Hall effect (QHE) by Von Klitzing in 1980 [1], although many of the conceptual implications were only clarified much later. This peculiar 2-dimensional (2D) state of matter has a vanishing longitudinal conductance in the bulk, but has a metallic edge, allowing for a quantised transverse conductivity. Shortly after its discovery, Thouless, Kohmoto, Nightingale and Den Nijs demonstrated a deep connection between this experimental fact and the notion of topology [2]. The quantised transverse conductivity is determined by a topological invariant of the system, the so-called Chern number, making it robust against perturbations to a high degree. The quantum Hall conductance is, in fact, so stable that it is used to define the Ohm [3] in terms of the fine-structure constant.

The first conceptual step towards a coherent picture of topological phases was made by Haldane, who realised that a magnetic field is not strictly necessary to manifest a quantised transverse conductance; the breaking of time-reversal symmetry (TRS) is enough [4]. Since there are no Landau levels in the absence of a magnetic field, one speaks of a quantum anomalous Hall effect (QAHE) instead. The quantisation of the transverse conductivity is only possible due to the presence of metallic modes at the edge of the material, a concept known as the bulk-boundary correpondence [5].

The converse of Haldane's observation is also true, there can be no QHE in

the presence of time-reversal symmetry. However, whether there was so-called symmetry protected topological order (SPTO) due to these symmetries was not clear until 2005. In that year, Kane and Mele theoretically predicted the quantum spin Hall effect (QSHE) in graphene, and showed that it is protected by a topological invariant, the spin Chern number [6, 7]. Unfortunately, the QSHE does not actually occur in this material, but it was soon predicted [8] and observed [9] in HgTe quantum wells. In the case of the QSHE, there is also a bulk-boundary correspondence, which dictates the presence of a time-reversal conjugate pair of edge states, in order to quantise the transverse spin conductivity. A material exhibiting a QSHE is usually called a topological insulator (TI) due to its vanishing electrical conductivity.

After these additional developments, it was not long until the connection with an older topological classification of the time-evolution operator was established [10], and all SPTOs were classified in terms of the ten-fold way by 2010 [11, 12]. The different topological phases in the ten-fold way all have their own version of the bulk-boundary correspondence, which can even be extended to more general defects in the lattice than boundaries [13].

The ten-fold way unifies in a topological framework the behaviour of not just the QHE and the QSHE, but many others. In 1 dimension (1D), this includes some prominent older models, such as the Su-Schrieffer-Heeger (SSH) model [14], the Kitaev chain [15] and the AKLT chain [16]. Of these examples, the Kitaev chain is especially interesting. It describes a 1D p-wave superconductor that hosts a topological phase with zero-energy Majorana states at the edge. Due to their topological protection, and their vanishing energy, these Majoranas are expected to be useful in the construction of q-bits for use in quantum computing.

A more ideal situation would be the realisation of a 2D topological superconductor, since the Majoranas trapped in the vortices of such a system are anyonic in nature. Although $\mathrm{SrRuO_4}$ is expected to be a p-wave superconductor, there is still experimental debate about the issue [17]. The other prominent 2D topological phases are those corresponding to the QHE and the QSHE.

Finally, in 3D, there also exists a TI phase, analogous to the 2D case, which has been predicted to exist in $\mathrm{Bi_{1-x}Sb_x}$ [18], and observed experimentally through ARPES [19]. The corresponding topological surface mode is somewhat unusual, since a single Dirac mode cannot exist in a purely 2D material, and the presence of TRS further enforces a spin-momentum locking that is not found when additional Dirac modes are present.

For a more pedagogical introduction to the theoretical concepts of topological states of matter, the reader is referred to Chap. 2, which can be omitted

by the reader already familiar with the field.

The ten-fold classification holds for *non-interacting* gapped fermionic systems in *equilibrium*, and all the above models are essentially free-particle models (including the superconductors, in the mean-field approximation). These caveats suggest some open questions, which remain to be resolved. One of these is the effect of interactions. For example, the different behaviour of the fractional QHE is reflected in the strongly interacting nature of the ground state, and the fractional QHE is said to be long-range entangled [20]. It should be noted that the integer QHE is also long-range entangled by the definition in Ref. [20], but because the corresponding topological field theory is invertible, so it is usually considered to obey SPTO also. Some interacting theories do not display fractionalisation, so that the corresponding topological field theory is invertible, and the system obeys SPTO. Possibilities include interacting systems that have a mean-field description, such as the p-wave superconductors already included in the ten-fold way, certain versions of the QAHE [21], or Kondo topological insulators [22,23]. Already in 2013, it was realised that the presence of interactions may change the topological classification [24], and their effects are currently an ongoing topic of active research [25].

For completeness, it is necessary to mention that there is also a recent interest in topological features in gapless phases, a behaviour which is also not described by the above topological classification. A prominent example of such a phase is the 3D Weyl Semimetal, which hosts pairs of Weyl cones at the Fermi energy. These systems have been theoretically predicted in 2011 [26], and they were recently observed experimentally [27]. Weyl semimetals exhibit interesting surface states due to their topological nature, and since each individual Weyl cone has a chiral anomaly, Weyl semimetals show the chiral magnetic effect, which has recently been observed [28].

One important question, which we will consider in Chap. 3 of this thesis, is what happens out of equilibrium, specifically in periodically driven, or Floquet systems. Floquet systems are prominent in optical lattices, where periodic driving has been used to induce a superfluid-insulator transition [29–31], or create frustrated magnetism through the use of artificial gauge fields [32]. Using these artificial gauge fields to create a QAHE is more difficult, but it has also been achieved [33,34]. There has been an independent development of Floquet topological phases of matter in the condensed matter community, where it was proposed that a Dirac cone opens a topological gap under circularly polarised irradiation [35–37], which was later verified experimentally [38]. Floquet topological phases with TRS have also been proposed [39]. Since it was realised that Floquet systems admit a richer phase behaviour [40], there has been activ-

ity to understand this in more detail [41–48]. In this thesis we present several works in this direction, dealing with Floquet honeycomb lattices. We discuss the interplay between spin-orbit coupling and a circularly polarised vector potential [44], how the appearance of a topological gap is associated with resonant behaviour [49], and how one can create a Floquet topological phase with vanishing Chern-number in optical lattices.

Another question, which we will consider in Chap. 4, is how topological behaviour depends on geometry. We mentioned that the bulk-boundary correspondence can be generalised to arbitrary lattice defects [13]. This already shows a relationship between topology and sample geometry. Here, it is important to note that the symmetries used in the ten-fold classification are not spatial in nature. Adding spatial symmetries, such as reflection symmetry [50], or the space groups of the unit cell [51, 52], will refine the classification further. For example, magnetic vortices in a 2D p-wave superconductor can host Majorana fermions, but whether they actually do so is measured by a separate topological invariant. The effects of geometry on topology are discussed in Chap. 4, where we consider the behaviour of topological phases on a Möbius band [53], how the results from Chap. 3 are modified on the Möbius band [54], as well as how Majorana fermions in a 2D topological superconductor interact with the curvature of a surface [55].

Finally, we will consider thermodynamic aspects of topological materials in Chap. 5. So far, the experimental detection of topological phases of matter has focussed on electronic transport, and spectroscopic measurements such as ARPES. The Majoranas in the 1D topological superconductor were detected using electronic tunneling experiments [56]. Similarly, in 2D, the QHE is a conduction phenomenon [1], and the QSHE was also experimentaly measured in terms of ballistic transport at the boundary [9]. On the other hand, the 3D QSHE was shown to exist through an ARPES measurement of the topological edge state [19]. Although there has been some recent interest in topological contributions to thermal conductivity [57,58], results on thermodynamic properties of topological materials have so far been lacking. This is a surprising situation, since thermodynamics is one of the oldest, and most well-established theories in physics, which has survived even the quantum revolution. Furthermore, as we show in Chap. 5, thermodynamics can be used to describe various interesting properties of topological materials. First we show how to set up a proper thermodynamic framework to describe topological phases [59]; this is necessary because the edge states cannot be described in the usual extensive formulation of thermodynamics. We then apply this framework to a variety of models [60], and show that the boundary contributions to the thermodynamic

potentials exhibit clear signatures of the topological edge states, such as in the specific heat and density of states. Additionally, a topological phase transition coincides with a thermodynamic one at $T = 0$, but the order of the phase transition in the bulk is one higher than at the boundary, implying universal behaviour. For 1D systems, we also analyse the topological phase transition at $T > 0$, and although there is no sharp phase transition there, we can use the thermodynamic data to reconstruct the phase diagram obtained using the Uhlmann phase [61].

In the following, we first present a more in-depth discussion of the theoretical framework of SPTO, which may benefit the reader not fully familiar with the field.

CHAPTER 2

Symmetry protected topological order

2.1 Introduction

In this chapter, we will provide the necessary background for an understanding of the original work appearing in subsequent chapters. The notion of topology is central to the exposition in this chapter. We will first give a historical account of the notion of SPTO. Hereby, we will explain how these notions emerged in the physics community, what is topological about SPTO and why it is protected by symmetry. It will also be explained how SPTO is currently understood in the community, which will provide some more depth to the introduction in the previous chapter.

As a mathematical field, topology could be described as the study of nearness. A topology is a mathematical structure that, roughly, endows a set with a concept of nearness, and topology is the study of topological spaces, i.e. sets with a topology. When one has a metric, or concept of distance associated to a set, this naturally endows the set with a topology, but topology is more general, just as nearness and farness are more vague than distance. This means that topology rears its head every time one takes a limit, uses an inner product or basically does anything a theoretical physicist likes to do. In mathematics also, topology is present almost everywhere, in part because it is useful in formally describing geometrical properties that only depend on topology, such as the number of holes in a space, or the winding number of a vector field.

In physics, perhaps the first appearance of topology is the circulation theorem in fluid dynamics, which was first proven by Lord Kelvin in 1869. It can be used to show the stability of certain topological features of the fluid velocity under time-evolution in the absence of friction. A notable example is a smoke ring. This in turn led to increased activity in the mathematical field of knot theory, which seeks to classify topologically distinct closed loops, called knots. The reason for this increased activity was the aim of classifying the possible topological behaviour that fluid velocity fields can have. Here, there is a link with the emergence of topology in modern physics, through the Chern-Simons theory. Witten showed that the expectation values of knots in the quantum Chern-Simons theory should yield knot invariants [62]. This is relevant because the Chern-Simons theory rears its head in the description of many topological phenomena in modern physics. An important example of this is the Callan-Harvey mechanism, which links it to the Chiral anomaly.

2.2 The relativistic quantum Hall effect

In condensed matter, this is related to the QHE [63], which was originally discovered by Von Klitzing in 1980 [1]. Here, a 2D material is subjected to a perpendicular magnetic field, and at low temperatures a quantised transverse conductivity is found. This observation was first made in systems where the kinetic energy of the electrons is quadratic, but here, the calculation will be presented for a linear kinetic energy, because this ties in better with the main topic of this thesis.

In this case, an electron in 2D is described by the Dirac Hamiltonian, which reads

$$H_{\boldsymbol{k}} = v_F \sum_{\sigma} \Psi^{\dagger}_{\boldsymbol{k},\sigma} (k_x \sigma_x + k_y \sigma_y) \Psi_{\boldsymbol{k},\sigma}, \tag{2.1}$$

where v_F is the characteristic velocity of the system (analogous to the speed of light in true relativity). According to the principle of minimal substitution [64], a magnetic field is incorporated in the Hamiltonian by making the replacement $\boldsymbol{p} \to \boldsymbol{\Pi} = \boldsymbol{p} + e\boldsymbol{A}$, where $\boldsymbol{A}$ is a vector potential for the magnetic field, so that $\boldsymbol{B} = \nabla \times \boldsymbol{A}$. Defining the magnetic length $l_B = \sqrt{\hbar/eB}$ yields the following commutation relations for the components of $\boldsymbol{\Pi}$:

$$[\Pi_x, \Pi_y] = -i\frac{\hbar^2}{l_B^2}.$$

From a mathematical point of view, the magnetic field turns the plane into a non-commutative space due to quantum effects. This implies that $a := l_B(\Pi_x -$

$i\Pi_y)/\sqrt{2}\hbar$ and its conjugate behave like annihilation and creation operators, respectively. In terms of a and $a^\dagger$, the Dirac Hamiltonian is written

$$H = \sqrt{2}\frac{\hbar v_F}{l_B}\begin{pmatrix} 0 & a \\ a^\dagger & 0 \end{pmatrix}. \tag{2.2}$$

From Eq. 2.2, it is easily deduced that the energy-spectrum is

$$E_n = \mathrm{sgn}(n)\frac{\hbar v_F}{l_B}\sqrt{2|n|}, \qquad n \in \mathbb{Z}. \tag{2.3}$$

It turns out that these energy levels, called Landau levels, are infinitely degenerate, a feature shared by the QHE for quadratic kinetic energy, which only has different energies corresponding to each level. The guiding centres of the cyclotron orbits can be used to define a second set of creation/annihilation operators that label the degeneracy. The details are omitted. It is important to note that the Landau levels for the QHE with linear kinetic energy are unbounded in energy both above and below, because the kinetic energy is, while the Landau levels of the QHE with quadratic kinetic energy are bounded from below. Finally, Eq. 2.3 predicts a zero-energy band, which does not appear in the non-relativistic QHE, where the lowest Landau level has a zero-point energy, similar to the Harmonic oscillator.

In Ref. [2], it is shown that up to linear response, the conductivity associated with each Landau level is given by

$$\sigma_H = \frac{ie^2}{2\pi h}\sum_i \int_{BZ}\int_{UC}\left(\frac{\partial u_i^*}{\partial k_x}\frac{\partial u_i}{\partial k_y} - \frac{\partial u_i^*}{\partial k_y}\frac{\partial u_i}{\partial k_x}\right) d\boldsymbol{r}d\boldsymbol{k}. \tag{2.4}$$

Here u_i is the normalised Bloch wave function on the unit cell for the i^{th} filled electron band, BZ for Brillouin zone and UC for the unit cell in the lattice. To make the link between the QHE and topological invariant theory explicit, note that the integrand in Eq. 2.4 reads

$$\frac{i}{2\pi}\sum_{i\in\text{bands}}\int_{BZ}\int_{UC}\left(\frac{\partial u_i^*}{\partial k_x}\frac{\partial u_i}{\partial k_y} - \frac{\partial u_i^*}{\partial k_y}\frac{\partial u_i}{\partial k_x}\right) d\boldsymbol{k} = \frac{i}{2\pi}\sum_{i\in\text{bands}}\int_{BZ} d\langle u_i, du_i\rangle.$$

As can be seen from appendix A, $\sum_{i\in\text{bands}}\langle u_i, du_i\rangle$ is the Berry connection (Eq. A.5) for the filled bands of the Bloch bundle. The Hall conductance in Eq. 2.4 is therefore given by e^2/h times the Chern number for these bands. Specifically σ_H is quantised in units of e^2/h, since the Chern number is an integer-valued topological invariant of the filled bands. The Hall conductance

is a statistical quantity, defining a phase of matter in the thermodynamic sense. It can only change by varying the topology of the filled energy bands, for which the gap at the Fermi level must close. Since the Hall conductance is a topological invariant, one speaks of a topological order parameter, defining a topological phase of matter. This phase is robust against perturbations, since a phase transition only occurs if the band gap at the Fermi level closes. It can even be shown, using the methods of non-commutative geometry [65], that the phase is robust against weak disorder. To do this, one writes the Chern number as the index of an elliptic operator that is still defined in the presence of weak disorder. It should be noted that this phase transition only occurs at $T = 0$, making it a quantum phase transition, which means that the phase transition is not caused by thermal effects, but by different structures of the ground-state wavefunction. The consequences of this, and the non-local nature of the order parameter are discussed in Chapter 5. We will discuss how the QHE is related to the Chern-Simons theory below, when the classification of SPTO is treated.

2.3 Time-reversal symmetry

2.3.1 Anomalous quantum Hall effect

The field of SPTO can be dated back to 2005, with the theoretical description of the QSHE [6, 7]. However, the notion that such a phenomenon might be possible dates from the eighties, and sprouted from a work by Haldane [4], that has now won the Nobel prize for its precociousness. Before this work, it was already realised that an energy band can only have non-vanishing Chern number in the absence of TRS [7]. This is because time-reversal changes the sign of the Chern-number; physically, the magnetic field changes sign under time-reversal, and therefore the Hall conductivity does so as well. A time-reversal symmetric system therefore has to have topologically trivial bands, which will be degenerate due to the existence of time-reversal conjugate pairs. If spin is a good quantum number, one spin will correspond to a Chern number c and the other to $-c$. By constructing an explicit example, Haldane showed that it is possible to have non-zero Chern number for an energy band without the application of a net magnetic field, and therefore without the appearance of Landau levels. All that was needed is the breaking of time-reversal symmetry (TRS). Because this state exhibits a QHE, even though the bulk bands are dispersive, one speaks of an quantum anomalous Hall effect (QAHE).

An obvious next question is, then, whether it is possible to have a different kind of topology in the presence of symmetries, if one demands the

topological equivalences to maintain this symmetry. This question can be considered purely mathematical in nature, and then the answer can be found in appendix A, but the answer was originally found from a physical perspective, by Kane and Mele.

2.3.2 Quantum spin Hall effect

In 2005, they wrote down a model hosting a non-trivial topological phase in the presence of TRS [6, 7]. Let us now discuss this model in more detail, to see the way in which the above reasoning is generalised. This will provide an appropriate basis from which to discuss SPTO in general. The Kane and Mele model describes graphene [66] in the presence of spin-orbit interactions, which turn out to generate a QSHE if spin is conserved; this gives an analogue of the QHE in the presence of TRS. Unfortunately, this effect cannot be observed in graphene, since the spin-orbit interactions are too weak. Nevertheless, the principle stands, and a QSHE was predicted in HgTe quantum wells the next year [8], where it was quickly observed experimentally [9].

Kane and Mele used the following Hamiltonian:

$$\begin{aligned} H :=& t_1 \sum_{\langle i,j \rangle} c_i^\dagger c_j + t_2 i \sum_{\langle\langle i,j \rangle\rangle} \nu_{ij} c_i^\dagger s^z c_j \\ &+ t_3 i \sum_{\langle i,j \rangle} c_i^\dagger (\boldsymbol{s} \times \boldsymbol{\delta}_{ij}) c_j + t_4 \sum_i \xi_i c_i^\dagger c_i. \end{aligned} \tag{2.5}$$

Here, $\boldsymbol{s}$ denotes the spin matrices, which act on a suppressed spin-index. Furthermore, δ_{ij} is the vector pointing from site j to site i, and the matrix ν_{ij} takes values ± 1 depending on whether the two NN hoppings from j to i take a left (for +) or right (for -) turn. The $\langle ... \rangle$ denotes a sum over nearest neighbour (NN) terms, while $\langle\langle ... \rangle\rangle$ denotes a sum over next-nearest neighbours (NNN). The first term in this Hamiltonian describes NN hopping on a honeycomb lattice, the second encodes the intrinsic spin-orbit (ISO) interaction, which will shortly be analysed further. The third term is called a Rashba term and describes a parity-breaking spin-orbit term that removes spin as a good quantum number. Finally the t_4 term describes a staggered sublattice potential: ξ_i is ± 1 depending on the sublattice.

If one puts t_3 and t_4 equal to zero, one obtains two copies of Haldane's model for the QAHE discussed above, with opposite sign for opposite spins. Together, these two copies generate the QSHE, both spins are associated with an QAHE of opposite parity, so while there is no electric Hall conductivity,

there is spin Hall conductivity. The only issue is that of robustness: the QSHE is only quantised if spin is a good quantum number, meaning that it is not topological in nature. Nevertheless, the presence of TRS allows one to define a topological invariant that is still defined even if spin is not conserved, showing that there is a topological phase. However, since the QSHE only exists if spin is conserved, this topological invariant is not connected to a physical observable in a simple manner. To show what happens, Figs. 2.1(a)-(d) depict the spectrum of the Kane and Mele Hamiltonian on a cylinder with zigzag edges for $t_4 = 0$, to show the behaviour of the spin-orbit interactions:

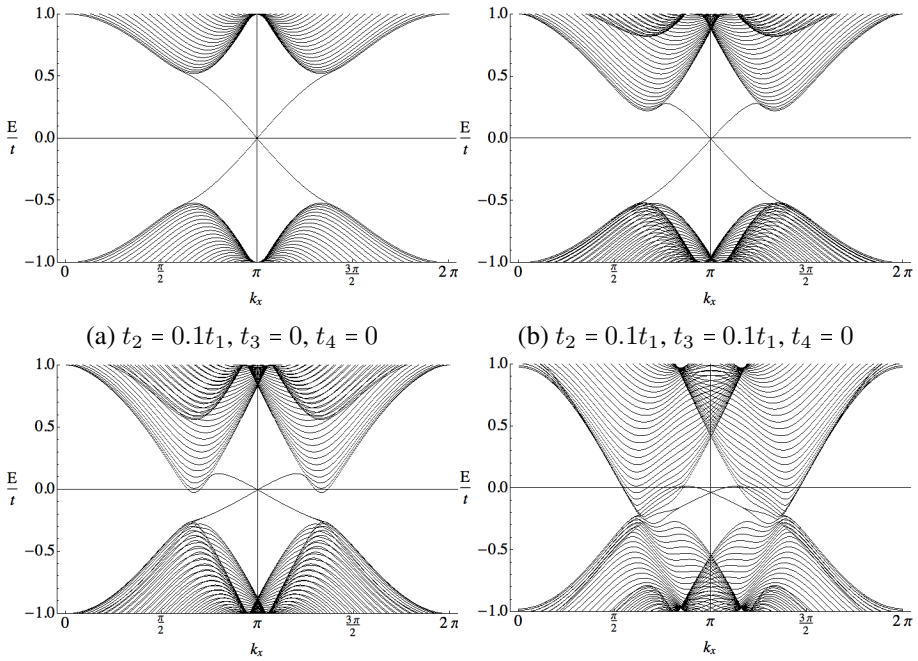

(a) $t_2 = 0.1t_1$, $t_3 = 0$, $t_4 = 0$

(b) $t_2 = 0.1t_1$, $t_3 = 0.1t_1$, $t_4 = 0$

(c) $t_2 = 0.05t_1$, $t_3 = 0.1t_1$, $t_4 = 0$

(d) $t_2 = 0.05t_1$, $t_3 = \frac{1}{5}\sqrt{3}t_1$, $t_4 = 0$

Figure 2.1: The spectrum of the Hamiltonian in Eq. (2.5) on a cylinder with zigzag edges as a function of the Bloch momentum k_x for several different parameter values. Energies are in units of t, the NN hopping constant.

From these figures, the conflicting effects of the ISO and Rashba terms can be read off. The ISO term has the effect of opening a gap between the valence and conduction bands. In doing so, it does not create a standard insulator, however, since the two bands are connected by gapless edge states. These edge states are also present in the QHE, and are indicative of the topological nature of the system. This happens through the bulk-boundary correspondence, which we will discuss in more detail below. Edge states are confined to the edges of the material, as can be seen by considering the model on the upper half-plane, and solving for exponentially decaying states. In the QHE, edge states on opposite edges have opposite dispersion. In the presence of TRS, the edge states always come in pairs at each edge, since time-reversal mirrors the dispersion by inverting the Bloch momentum $\boldsymbol{k} \mapsto -\boldsymbol{k}$. This is connected to the fact that every band in figure 2.1(a) is doubly degenerate since H is spin-diagonal without the Rashba term. As soon as the Rashba term is included, this degeneracy is lifted; this is most obvious in the bulk bands, but the edge states are also slightly separated. Another important effect of the Rashba term is that it closes the band-gap as it starts to dominate over the ISO term. The progression of this effect can be seen if one compares Figs. 2.1(a)-(d). The Rashba term closes the gap entirely for $t_3 > 3\sqrt{3}t_2$, as figure 2.1(d) demonstrates. In this case, the topological phase of the system is ill-defined, since there is no band gap.

The sublattice potential in Eq. (2.5) also opens up a gap, just like the ISO term, but in this case, a topologically trivial insulator appears. Especially its interplay with the ISO term is of interest, since the two terms compete. To

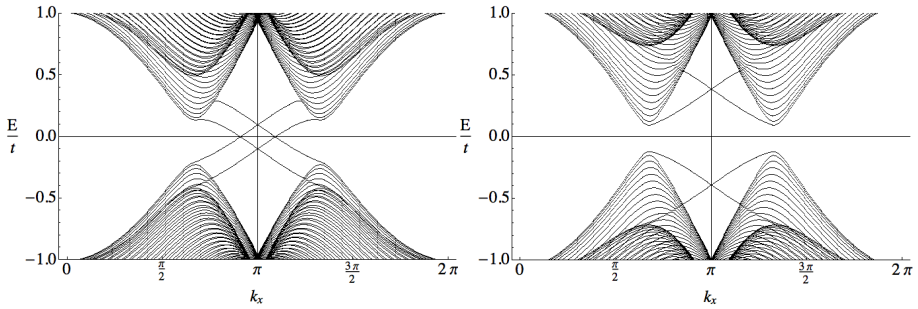

(a) $t_2 = 0.06t_1$, $t_3 = 0.05t_1$, $t_4 = 0.1t_1$ (b) $t_2 = 0.06t_1$, $t_3 = 0.05t_1$, $t_4 = 0.4t_1$

Figure 2.2: The spectrum of the Hamiltonian in Eq. (2.5) on a cylinder with zigzag edges as a function of the Bloch momentum k_x for several different parameter values. Energies are in units of t, the NN hopping constant.

show the effect of this competition, Fig. 2.2 shows the dispersion of Eq. (2.5)

on the cylinder for non-zero values of t_4. The total band-gap without Rashba term has size $|6\sqrt{3}t_2 - 2t_4|$. It follows that the band-gap closes, and then opens up again as t_4 increases. The sublattice term suppresses the edge states, as becomes clear from figure 2.2(b), where it dominates the ISO term.

Finally if the ISO term dominates, a beautiful interplay between the edge states and the sublattice term becomes visible. There are, in total, two pairs of edge states, one pair on each edge of the strip. The velocity of the electron in each edge state is coupled to its spin, with opposite spins moving in opposite directions. One of these edges consists of A-sublattice atoms, and the other of B-sublattice atoms. Consequently, the sublattice potential has an opposite effect on the different edges, and energy degeneracy between the two pairs is lifted, as is clearly seen in figure 2.2(a).

Accepting, for the moment, that edge states are indicative of topology, one can already argue about the topological nature of systems with TRS. By TRS, it is impossible for electrons in the same pair of edge states to scatter off each other and disappear into the bulk. The time-reversal operation exchanges the two modes in the pair, and a time-reversal symmetric Hamiltonian has no overlap between time-reversal conjugate states. However, it is possible to introduce an overlap between two different pairs of edge states, and hybridise them away from the edge. In general, interactions and lattice impurities will force such annihilations until either a single pair or no pairs survive. This suggests that the relevant topological invariant takes values in $\mathbb{Z}_2$, and counts the number of edge pairs mod 2. This is analogous to the Chern number, which counts the number of edge modes (with a sign for the slope of dispersion) in the QHE. In the QHE, each edge mode adds a single quantum to the Hall conductance, just as a pair adds a quantum to the spin Hall conductance in the presence of TRS.

Indeed, various equivalent formulations of a $\mathbb{Z}_2$ invariant are known [7,67], one of which is discussed in Appendix A. This invariant only changes value if the band gap at the Fermi energy closes, showing that there are topologically non-trivial states in the presence of TRS. This implies that the topological phase is robust under small perturbations in the Hamiltonian, as long as TRS is maintained. Whether this invariant exhaustively classifies all time-reversal symmetric band structures is unknown at the mathematical level of rigour, and the same is true for robustness of this invariant against disorder. Due to the consistent physical picture that can be formed, this is not particularly bothersome, however.

2.4 Symmetry protected topological order

The reason why it makes sense to consider topological states in the presence of TRS is that this symmetry can be considered robust. TRS breaking is usually considered roughly the same as magnetisation, although the Haldane model shows the caveats to this interpretation. Taking this interpretation at face value, however, shows that breaking TRS is usually not a spontaneous process: many materials do not spontaneously magnetise. Another way to put it is as follows: time-reversal is not a spatial symmetry. In general, there are two other symmetries that are not of a spatial nature, charge-conjugation and chiral symmetry. Charge-conjugation symmetry is usually associated to superconductivity, while, in 1D, chiral symmetry is associated to dimerisation effects, as in the Su-Schrieffer-Heeger (SSH) model. It should be noted that chiral symmetry is mathematically the product of time-reversal and charge-conjugation, so it is strictly more general than this.

In all these cases, this symmetry is considered robust due its non-spatial nature, and, consequently, it makes sense to perform a topological classification similar to the two cases already discussed, in the presence or absence of these symmetries. There are ten different possible combinations of the various symmetries [11, 12], causing the classification table to be called the ten-fold way. For example, in the absence of any symmetry, in 2D, there is a $\mathbb{Z}$ classification, corresponding to the QHE, and the Chern number gives the topological class. The QSHE corresponds to 2D with only TRS, which squares to -1. Indeed, the topological classification is $\mathbb{Z}_2$, as expected. The next question is then how to obtain this topological classification that holds for non-interacting systems. One way of doing so is purely mathematical in spirit, and is mentioned briefly in Appendix A. Another method is based on a classification of Anderson localisation in terms of non-linear σ-models [68]. It explains why topological materials are considered to be robust against disorder, and why they are associated with edge states.

2.4.1 Bulk-boundary correspondence

This method makes use of the bulk-boundary correspondence, a notion we have mentioned before, but that we will now treat in more detail. We have already seen that the topological invariant of a system can only change through a closing of the band gap. Assume for the moment that topological protection continues even when translational symmetry is broken, as can be proven for the QHE [65], and is an empirical observation for all other symmetry classes. If

AZ	Θ	Ξ	Π	1	2	3	4	5	6	7	8
A	0	0	0	0	$\mathbb{Z}$	0	$\mathbb{Z}$	0	$\mathbb{Z}$	0	$\mathbb{Z}$
AIII	0	0	1	$\mathbb{Z}$	0	$\mathbb{Z}$	0	$\mathbb{Z}$	0	$\mathbb{Z}$	0
AI	1	0	0	0	0	0	$\mathbb{Z}$	0	$\mathbb{Z}_2$	$\mathbb{Z}_2$	$\mathbb{Z}$
BD1	1	1	1	$\mathbb{Z}$	0	0	0	$\mathbb{Z}$	0	$\mathbb{Z}_2$	$\mathbb{Z}_2$
D	0	1	0	$\mathbb{Z}_2$	$\mathbb{Z}$	0	0	0	$\mathbb{Z}$	0	$\mathbb{Z}_2$
DIII	-1	1	1	$\mathbb{Z}_2$	$\mathbb{Z}_2$	$\mathbb{Z}$	0	0	0	$\mathbb{Z}$	0
AII	-1	0	0	0	$\mathbb{Z}_2$	$\mathbb{Z}_2$	$\mathbb{Z}$	0	0	0	$\mathbb{Z}$
CII	-1	-1	1	$\mathbb{Z}$	0	$\mathbb{Z}_2$	$\mathbb{Z}_2$	$\mathbb{Z}$	0	0	0
C	0	-1	0	0	$\mathbb{Z}$	0	$\mathbb{Z}_2$	$\mathbb{Z}_2$	$\mathbb{Z}$	0	0
CI	1	-1	1	0	0	$\mathbb{Z}$	0	$\mathbb{Z}_2$	$\mathbb{Z}_2$	$\mathbb{Z}$	0

Table 2.1: The ten-fold way [10–12], classifying the possible non-interacting topological band structures for the ten possible combinations of time-reversal, charge-conjugation and chiral symmetry. A 0 denotes the absence of the symmetry, while ± 1 denotes the symmetry is present and squares to ± 1. Here, Θ denotes time-reversal, Ξ denotes charge-conjugation and Π chiral symmetry. The horizontal numbering denotes the number of space dimensions. The $\mathbb{Z}$, $\mathbb{Z}_2$ and 0 denote the possible different topological phases. The possible topological phases are periodic in the dimension modulo 8, so the table is exhaustive.

this is the case, then at an interface between two materials in the same symmetry class, but with a different topological phase, the band gap has to close. The only way for this to happen is if gapless states get trapped at the edge. This argument can be made precise for the QHE [69], and it seems to be an empirical fact for the other symmetry classes in the ten-fold way, but there exist topological phases without protected edge modes that are protected by crystal symmetry [51, 52]. However, crystal symmetry is not a very robust symmetry, so the phases where topological protection is strongest seem to be characterised by the presence of edge states, as we have already explicitly demonstrated for the QSHE, and by extension for the QHE.

Now, if SPTO is robust against weak disorder, these gapless edge states have to remain intact even in the presence of translation-symmetry breaking perturbations. More specifically, they have to be protected against Anderson localisation, a phenomenon where the electron wavefunctions become localised in the presence of disorder. If they were not protected against this process, they

would be indistinguishable from other states outside the mobility gap, which generally do localise. It can be shown that the Anderson localisation transition can be described in terms of non-linear σ-models [68], where the precise model depends on whether there is time-reversal, charge-conjugation or chiral symmetry present in some combination. In some cases, there is the freedom to add topological terms to the σ-model action, which prevents the localisation transition from occurring. By classifying how many of these terms exist for each symmetry combination, the classification in Table 2.1 can be obtained.

This shows that the protection of edge states against Anderson localisation is also caused by a kind of topology. The fact that this topological structure is the same as that of the band structures describing the bulk physics only strengthens the picture of the bulk-boundary correspondence.

2.5 Laughlin's charge-pumping argument

As a final point, we will discuss how SPTO is related to the presence of anomalies in QFT [25, 57, 70]. For example, in the QHE the presence of a transverse Hall conductance breaks parity. In the continuum limit, a Chern-Simons term in the action makes this parity breaking explicit [71]. This verifies the claim in the introduction that the QHE is described by the Chern-Simons theory, and ties the topic of SPTO into the broader framework of topology in physics. This connection can be given a simple interpretation in terms of edge states through the use of Laughlin's charge-pumping argument [72].

Consider a 2D material of annular geometry that exhibits a QHE. From the previous results in this chapter, there must be chiral edge states on the two boundary components of the annulus. Consider adiabatically threading a flux through the center hole of the annulus. One can choose a gauge such that $\boldsymbol{A} = Ad\phi$, i.e. the vector potential points along the angular direction of the annulus. The flux through the hole can then be written as $\Phi(t) = 2\pi A(t)$, through a use of Stokes theorem. The changing magnetic flux creates an electric field $\boldsymbol{E} = -d\boldsymbol{A}/dt$ along the angular direction, which in turn creates a Hall current J_H along the radial direction

$$J_H = \sigma_H E = -\sigma_H dA/dt. \tag{2.6}$$

Integrating both sides of this equation with respect to time gives the pumped charge

$$\Delta Q = -\sigma_H \Delta\Phi \tag{2.7}$$

in terms of the flux difference $\Delta\Phi$. Since the current flows radially through the annulus, the charge can only have moved from one edge to the other. If one were to write down a low energy effective theory of one of the chiral boundary modes, it would appear that the current 4-vector is not conserved, which is precisely the chiral anomaly in (1+1)D. This strengthens the argument that for the QHE the Hall conductivity in the bulk and the chiral edge states are not independent. Indeed, the Hall conductivity is described by a Chern-Simons term in the effective action, and it is known that this is completely determined by the behaviour of the corresponding Wess-Zumino-Witten theory at the edge, which precisely describes the chiral edge states.

This connection between anomalies and topological phases of matter turns out to be more general, and an anomaly can be identified for most of the topological phases in the ten-fold way [57].

2.6 Conclusion

From the above discussion it becomes clear that topological states of matter are well understood in terms of the ten-fold classification. The topological classification can be performed via a variety of methods, the most physically intuitive one being, perhaps, the one in terms of Anderson localisation [68]. However, this topological classification really only works for non-interacting systems, which was well known by 2013, as the example of the fractional QHE shows [73, 74]. The fractional QHE is characterised by long-range correlations in the system, which prevent the system from being adiabatically connected to the trivial insulator state, and because of this, the system is said to exhibit long-range entanglement. Strictly speaking, the integer QH state also exhibits long-range entanglement, as shown by the non-vanishing Chern number, but the interacting nature of the fractional QH state makes it host excitations with fractional charge. Because of the absence of such fractional excitations in the integer QHE, the topological field theory describing the low energy degrees of freedom is invertible, and it is considered to exhibit SPTO.

In general, interactions could create a topological effect that is invertible like the integer QHE, and would therefore be classified as SPTO. Possibilities include interacting systems that have a mean-field description which is topological, such as the p-wave superconductors already included in the ten-fold way, certain versions of the QAHE [21], or Kondo topological insulators [22, 23]. Already in 2013, it was realised that the presence of interactions may change the topological classification [24]. The effect of interactions is

still an ongoing topic of research [25], and it is of fundamental importance to understand it.

However, we will not go into this topic here. Instead, we will focus on the three topics mentioned in the introduction, the first of which is the role of periodic driving.

CHAPTER 3

Topology in Floquet systems

3.1 Introduction

A closed system is necessarily described by a time-independent Hamiltonian; since there are no outside influences, the energetics is purely determined by the system constituents, which cannot be interchanged with an environment. The time-independence of the Hamiltonian implies that it is a constant of the motion, which is then the energy of the system [64], and this shapes much of our thinking about closed systems. In quantum theory, this is reflected in the fact that one, in principle, knows everything about a closed system if one diagonalises the Hamiltonian. For a time-independent Hamiltonian, the time-evolution operator U is simply its exponent, which is easily calculated if the Hamiltonian is diagonal. This is not to say that closed systems are necessarily easy to study. The structure of Hermitian operators, such as the Hamiltonian, can already be exceedingly complicated, as evidenced by the behaviour of quenched systems, or interacting ones, for example.

However, in driven systems, there is much more room for complexity; the Hamiltonian is necessarily time dependent, since the driving influences the energetics of the system, and a time ordering shows up in the expression for U. Usually, the eigenfunctions of $H(t)$ are not constant in time, and the time ordering complicates matters. Another point of view is that energy is no longer conserved, and the system has access to the full phase space under time evo-

lution, not just the subspace at the initial energy. The presence of symmetries constrains the possible behaviour of a system, and such a situation occurs in an important class of non-equilibrium systems: the periodically driven ones.

As we will see below, the periodicity of the Hamiltonian makes the time evolution of such systems much more mathematically tractable. There is, however, another reason for studying time periodic, or Floquet, systems; Floquet systems are experimentally quite common, especially in optical lattices. This prevalence occurs because driving allows access to a wider variety of phases.

In optical lattices, one studies the behaviour of particles in a lattice by placing atoms in a periodic potential created through the use of lasers. The valleys in the optical potential provide the lattice sites, and by manipulating the hyperfine structure of the atoms, fermionic or bosonic particles can be obtained. Although the particles in the optical lattice are electrically neutral, i.e. the role of charge density is mimicked by mass density in such systems, the analogy with electrons in an atomic lattice is clear. The hopping parameters determining the movement of particles through the lattice are determined by the depth of the valleys in the optical potential, with deeper valleys leading to lower hopping. Unfortunately, this bare hopping is not usually enough to create interesting behaviour, a notable exception is the realisation of p-band condensates [75, 76], so experimentalists generally work with periodically driven optical lattices [77, 78].

Periodic driving can be used to modulate the hopping parameters of an optical lattice in a variety of ways. Firstly, one can shake the lattice linearly, which simply renormalises the hopping parameters [29, 79, 80]. Through this method, it is possible to manipulate the Dirac cones in a honeycomb lattice [80, 81], or tune a superfluid-Mott insulator transition [29–31], amongst other things.

Shaking in a non-linear manner does not just change the amplitude of the hopping parameters, but also their phase, exactly as a gauge potential would. This technique was first used to simulate classical frustrated magnetism in a triangular optical lattice filled with bosons [32], but it is also a crucial instrument in the realisation of topological phases in optical lattices [33, 34, 82–86].

As will be discussed in more detail below, the topological behaviour of Floquet systems can be more complicated than in the undriven case, so one speaks of Floquet topological insulators (FTIs) in this case. These FTIs have garnered a great deal of attention in recent years, aimed at finding examples, and elucidating their topological behaviour [35–48, 87, 88]. Effectively, one can divide the different types of FTIs into three different regimes. Firstly the so-called quasi-equilibrium regime, where $J \ll \hbar\omega \ll \Delta$; here J is the hop-

ping parameter, which is roughly the bandwidth of the relevant set of bands, ω the driving frequency, and Δ the gap to possible other bands that one does not want to consider. In this case, the system constituents cannot follow the perturbation, and the system remains at quasi-equilibrium with simply renormalised lattice parameters. Then, the results from Chap. 2 hold, since the system can be effectively described as an undriven one. It is the regime that was studied first [29, 81, 89–91], due to its relative simplicity. Secondly, there is the regime where $J \ll \hbar\omega \sim \Delta$. This regime has attracted attention in optical lattices [92–94], but it has been unexplored in the context of condensed matter. Thirdly, there is the regime where $J \sim \hbar\omega \ll \Delta$, and where the special topological characteristics of Floquet topological phases are most readily apparent. Most of the theoretical work on FTIs has taken place in this regime [35–48, 87, 88], and this kind of system has even been simulated in twisted photonic waveguides [95], where the third spatial dimension takes the role of time.

There have been attempts to define Chern-type topological invariants valid for every frequency range [39, 40, 47, 48], and it is known that these invariants reduce to the equilibrium ones in the first regime. The transition between the first and third regime, which is characterised by the appearance of driving resonances in the system, has been investigated theoretically in Ref. [45] for graphene irradiated by circularly polarised light, and in Ref. [96] for the case of a periodically-driven dimer chain. Below, we will discuss two implementations of this regime in optical lattices. However, we shall first discuss the Floquet theory, which underpins the mathematical analysis of all that was just outlined above.

3.2 Floquet theory

Floquet theory is used to analyse periodically driven quantum systems. This means that the Hamiltonian is time dependent with period T:

$$H(t) = H(t+T).$$

The time evolution operator, defined by $U(t,t')\phi(t') = \phi(t)$, satisfies the initial condition $U(t',t') = 1$, and the Schrödinger equation

$$i\hbar\frac{\partial}{\partial t}U(t,t') = H(t)U(t,t'). \tag{3.1}$$

These two equations determine it uniquely, barring mathematical pathologies, and solving them gives full information about the system. However, using the

periodicity of the driving protocol, one can rewrite the Schrödinger equation as

$$i\hbar\frac{\partial}{\partial t}U(t+T,t'+T) = H(t+T)U(t+T,t'+T) = H(t)U(t+T,t'+T),$$

so $U(t+T,t'+T)$ and $U(t,t')$ satisfy the same differential equation with the same initial condition and are thus equal. From this it follows that

$$U(t,0) = U(t,nT)U(nT,(n-1)T)...U(T,0) = U(t,nT)U(T,0)^n. \quad (3.2)$$

By choosing n such that $0 \leq t - nT \leq T$, this demonstrates that the system is fully determined by $U(t,0)$ for $0 \leq t \leq T$. Furthermore, much of the large-time behaviour of the system is encoded in $U(T,0)$, which is called the Floquet operator. By the spectral theorem for unitary operators [97, 98] one gets a basis of (generalised) eigenfunctions for $U(T,0)$, if H is sufficiently well behaved. The properties of these eigenfunctions, such as normalisability, have important consequences for the stability of the system. The spectrum of a unitary operator lies in the unit circle, and therefore the eigenvalues are of the form $\exp(-i\epsilon T/\hbar)$, where the possible values of ϵ are called the quasi-energies of the system. The terminology rises from the fact that there exists a Floquet Hamiltonian:

$$H_F := \frac{i\hbar}{T}\ln(U(T,0)). \quad (3.3)$$

This expression is still ambivalent, since one needs to specify a branch cut of $\ln$ to get a single-valued operator. This H_F can be interpreted as a time-averaged version of H, and its eigenvalues are the quasi-energies chosen to lie in the BZ $(a, 2\pi + a]$, where a gives the position of the branch cut.

Related to the Floquet Hamiltonian is the Sambe Hamiltonian [99]. The Sambe Hamiltonian will be useful in discussing the high-ω limit, and the topological properties of Floquet systems. Let ψ_ϵ be an eigenstate of $U(T,0)$ with quasi-energy ϵ; here ϵ is not necessarily in the first BZ. Define $\phi_\epsilon(t)$ by $\phi_\epsilon(0) = \psi_\epsilon$ and

$$\left(H(t) - i\hbar\frac{\partial}{\partial t}\right)[\exp(-i\epsilon t)\phi_\epsilon(t)] = 0.$$

It is easy to see that $\phi_\epsilon(T) = \phi_\epsilon(0)$ and

$$\left(H(t) - i\hbar\frac{\partial}{\partial t}\right)\phi_\epsilon(t) = \epsilon\phi_\epsilon(t).$$

Furthermore, $\phi_{\epsilon+n\hbar\omega}$ determines the same physical state for all $n \in \mathbb{Z}$ and obeys $\phi_{\epsilon+n\hbar\omega} = \phi_\epsilon \exp(in\omega t)$. If $\mathcal{H}$ is the original Hilbert space on which $H(t)$ acted, then one can define the Sambe space

$$\mathcal{H}_F := \mathcal{H} \otimes L^2\left([0,T]/\{0,T\}, \frac{d\theta}{T}\right). \tag{3.4}$$

Here $L^2\left([0,T]/\{0,T\}, \frac{d\theta}{T}\right)$ is the Hilbert space of T-periodic functions with inner product

$$\langle f, g\rangle := \frac{1}{T}\int_{[0,T]} f^*(\theta)g(\theta)d\theta.$$

On the Sambe space, one can define the Sambe Hamiltonian

$$\mathfrak{H} := H(t) - i\hbar\frac{\partial}{\partial t}. \tag{3.5}$$

It is clear that the Sambe Hamiltonian has eigenstates ϕ_ϵ. Due to the ambiguity in ϵ, many different eigenstates of $\mathfrak{H}$ yield the same physical state, and the spectrum of $\mathfrak{H}$ is that of H_F, but periodically continued, with period $\hbar\omega$. The advantage of the Sambe Hamiltonian is that it acts on time-periodic wavefunctions, and is hence amenable to Fourier-transform methods.

3.3 The shaken quantum chain

To demonstrate the above theory, let us first consider the shaken quantum chain [100]. This is a simple tight-binding model, for which the propagator can be written down in closed form. Furthermore, the Floquet operator can be diagonalised explicitly, which serves well to introduce the Floquet theory.

The Hamiltonian for the shaken quantum chain can be written:

$$\begin{aligned} H &= H_0 + H_{\text{int}} \\ H_0 &= \frac{J}{2}\sum_n \left(c_{n+1}^\dagger c_n + c_n^\dagger c_{n+1}\right) \\ H_{\text{int}} &= V\cos(\omega t)\sum_n n c_n^\dagger c_n. \end{aligned} \tag{3.6}$$

The term H_0 in Eq. (3.6) is a simple NN-hopping term in one dimension. If one further shakes the chain along its length with sinusoidal amplitude and frequency ω, and then transforms to the reference frame of the chain, a pseudo-force is obtained which is given by H_{int}. If $|n\rangle$ denotes the Wannier state at site n, then $\chi_k := \sum_n \exp(ikan)|n\rangle$ is an eigenfunction of H_0 with energy

$E_k = -J\cos(ak)$, where a is the lattice constant. Since the χ_k are a complete set of eigenfunctions for H_0, the propagator of the system is determined by solving

$$\left(H - i\hbar\frac{\partial}{\partial t}\right)\phi_k(t) = 0,$$

subject to the initial condition $\phi_k(0) = \chi_k$ for all k in the Brillouin-zone. This solution is known to be

$$\begin{aligned}\phi_k(t) &= \sum_n \exp\left\{-ib_k(t)n + i\frac{J}{\hbar}\int_0^t \cos[b_k(\tau)]d\tau\right\}|n\rangle \\ b_k(t) &= ikan + i\frac{V}{\hbar\omega}\sin(\omega t)n.\end{aligned}$$

It follows immediately that $\phi_k(T) = \exp\left\{iJ/\hbar\int_0^T \cos[b_k(t)]dt\right\}\phi_k(0)$, from which one finds that the quasi-energy $\epsilon_k = -2J\cos(ak)J_0(V/\omega)$. Here, J_0 it the zeroth order Bessel function. The Floquet Hamiltonian H_F for this system is therefore equal to H_0 from Eq. (3.6), with a renormalised hopping $JJ_0(V/\omega)$. In the limit $\omega >> J$, i.e. when the shaking frequency is much larger than the unperturbed system energy, one expects the Floquet Hamiltonian H_F for the system to become a time-averaged version of the original Hamiltonian H. For this system, it can therefore be seen that the hopping parameter simply becomes renormalised in the quasi-static regime. In general, in the quasi static regime, periodic driving modifies any terms in the Hamiltonian that do not commute with the driving operator. Consequently, the modification of hopping parameters upon linear shaking of a lattice is not an uncommon feature [35, 81, 101–103]. As was discussed in the introduction to this chapter, this even allows one to impinge a phase on the hopping, which lies at the origin of many interesting phenomena in optical lattices. As a further example, one can induce topological phase transitions in the high-frequency Floquet Hamiltonian by tuning the parameters appropriately [35].

3.4 Topological phases of the Floquet Hamiltonian

It has already been mentioned that Floquet systems can exhibit more complex topological behaviour than their undriven counterparts. Indeed, several theoretical [39, 96, 104] and experimental [38] examples have been found that demonstrate this effect. Assuming that the Hamiltonian $H(t)$ has a lattice symmetry that is independent of t, one can perform a Bloch decomposition of the Hamiltonian. This yields Hamiltonians $H(\boldsymbol{k}, t)$, propagators $U(\boldsymbol{k}, t, t')$,

and corresponding Floquet Hamiltonians $H_F(\boldsymbol{k})$ via Eq. (3.3). The Bloch decomposed Floquet Hamiltonian $H_F(\boldsymbol{k})$ will usually have quasi-energy bands, by general considerations from spectral theory. If these quasi-energy bands are gapped, one can calculate their Chern invariant via Eq. (A.7), just as for the time-independent case. This Chern invariant gives rise to the same bulk-boundary correspondence as in the time-independent case, but the periodic nature of the spectrum of $\mathfrak{H}$ reveals a subtlety.

3.4.1 Chirality of band gaps in Floquet systems

To illustrate the problem, consider a system in the absence of symmetry, so that it would be classified by the Chern numbers of its energy bands in the absence of driving. In this case, the bulk-boundary correspondence tells us that, without driving, the number of protected edge modes in a given energy gap is equal to the Chern number of the bands below it (see Eq. (A.7)). From this, it follows that the Chern number C_i of a given band is equal to $W_i - W_{i-1}$, where W_i is the number of protected edge modes in the gap above band i. The reason why the Chern numbers C_i of the various bands classify the topology of the system completely is because there is a lowest band, and $W_0 = 0$. However, $\mathfrak{H}$ does not have a lowest energy band because the spectrum is periodic in ω. This means that every gap in the system can have the same number of protected edge modes, and all the Chern numbers will still vanish, as is shown in Fig. 3.1 for the case where each gap has a single edge mode. The immediate

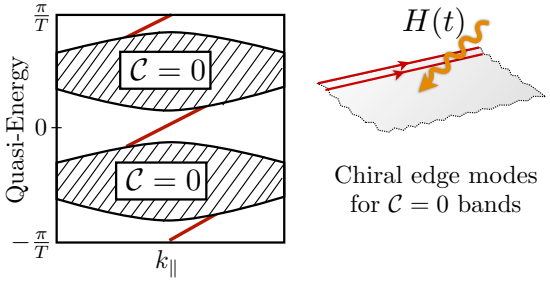

Figure 3.1: A Floquet system where $\mathfrak{H}$ has two bands within a period ω is depicted [40]. All the Chern numbers vanish, because each gap has a single protected edge mode: $W_i = 1$ for all i.

implication is that a more sensitive topological invariant is needed, which is able to calculate the W_i, rather than the C_i. Such an invariant has been found for the QH [40, 105], and QSH [47] classes of Floquet systems. Furthermore,

the topological classification for 2D Floquet systems with arbitray symmetry has been performed in terms of Weyl cones, by looking at the singularities of $U(\boldsymbol{k}, t)$ over the Brillouin zone and a single driving cycle [48]. It is also possible to perform a classification by considering the topological structure of the scattering matrix of the system [106]. In addition, the topological classification has also been written down in terms of the K-groups of the driving cycle [107], although the precise value of these K-groups has not been calculated in most cases.

To give an idea of the notions involved, we will present the invariant for the QH class in 2D as derived in Ref. [40], since this is the only invariant that will be used in the following. The crucial piece of insight is that the entire history over a single driving cycle is important for the topological classification. In 2D, the Fourier transformed time-evolution operator $U(\boldsymbol{k}, t)$ depends on three parameters that lie in a 3D generalised Brillouin zone (GBZ). The time evolution operator is periodic in $\boldsymbol{k}$, but not necessarily in t, since $U(T, 0) \neq 1$ in general. There is a way to build a time-periodic operator out of U though: define

$$V(\boldsymbol{k}, t) = \begin{cases} U\left(\boldsymbol{k}, \frac{t}{2}\right) & 0 \leq t \leq \frac{T}{2}, \\ \exp\left(-i(2T - 2t)H_F\right) & \frac{T}{2} \leq t \leq T. \end{cases} \tag{3.7}$$

The operator V is periodic over the GBZ, and there is a winding number that measures its topological class,

$$W = \frac{1}{8\pi^2} \int_{GBZ} dt dk_x dk_y \operatorname{Tr}\left(V^{-1}\partial_t V \left[V^{-1}\partial_{k_x} V, V^{-1}\partial_{k_y} V, \right]\right). \tag{3.8}$$

Because this integral is a topological winding number, it is quantised by integers if V is continuous as a function of $\boldsymbol{k}, t$. Now, if one looks back to Eq. (3.3), one sees that the definition of H_F depends on a choice of branch cut of the logarithm. This means that V is only a continuous function if the branch cut of the logarithm is chosen to lie in one of the energy gaps of $U(\boldsymbol{k}, T)$. For each choice of such a gap, Eq. (3.8) yields an integer, and it can be shown to equal W_i if the branch cut of the logarithm is chosen to lie in the gap Δ_i. The topological nature of a Floquet system is, in the absence of TRS, determined by an integer associated to each gap, meaning that there is an extra degree of freedom in the possible topological phases. The extra degree of freedom occurs because in H_F, the gap between the lowest energy band and the highest energy band is finite due to periodicity of the spectrum, and can host edge states. This leads to the presence of a topological phase, where all the Chern numbers vanish, which is protected by the driving cycle of the system. A similar

behaviour occurs for driven 2D systems with TRS [47]. However, for other symmetry classes, the topological classification is not necessarily as simple as associating an invariant to each gap [48].

3.5 Dynamical competition between QHE and QSHE

An interesting aspect of the QH and QSH classes in periodically driven systems is that their topological class can be easily classified by looking at the edge modes in each of the gaps, as long as the system is finite. Using this, one can investigate the interplay between these two classes by taking a topological system in the presence of time-reversal symmetry and breaking it through the driving term. One draws inspiration from the knowledge that perpendicularly irradiating a 2D lattice with circularly polarised light can create an FTI in the QH class [35, 37, 38, 87, 108]. Let us now describe a variation of this theme that was developed in Ref. [44]. The work in this publication was done by me, and Prof. Dr. Morais Smith supervised the project. The model describes a honeycomb lattice with an in-plane rotating vector potential.

There are two separate ways in which such an in-plane rotating vector potential can be realised. One option is to irradiate the lattice perpendicularly with circularly polarised light. The in-plane component of the vector potential then has constant magnitude and rotates in time. Another option is to shake the lattice is a circular manner. In the comoving reference frame, the resulting pseudoforces are also described by a rotating vector potential of constant magnitude, as is shown in Appendix B. The application using light is not possible in optical lattices, since the atoms loaded into the lattice have no net charge. On the other hand, shaking can be implemented in such systems straightforwardly.

The starting point is the graphene Hamiltonian, which reads [66]

$$H_0 = -J \sum_{\langle i,j \rangle} c_i^\dagger c_j. \tag{3.9}$$

Here, $J \geq 0$ is the NN hopping strength, and the brackets denote a sum over NN only, assuming a honeycomb geometry. It is well known that H_0 is still time-reversal symmetric. To break this time-reversal symmetry, we add a rotating vector potential

$$\boldsymbol{A}(t) = V\left(\cos(\omega t), \sin(\omega t)\right). \tag{3.10}$$

This is done through the Peierls substitution [109], which sends $J \mapsto J_{i,j}$, where

$$J_{i,j}(t) = J \exp\left[-i \int_i^j \boldsymbol{A}(t) \cdot d\boldsymbol{s}\right]. \tag{3.11}$$

Here, the path from site i to j is irrelevant, since the B-field lies in plane, and all higher order contributions in the substitution vanish. The magnitude V of the potential is equal to E/ω, where E is the radiation intensity, in the case of circularly polarised light, and it is equal to $r_0\omega$, where r_0 is the shaking radius, in the case of circular shaking. The final Hamiltonian for the model reads

$$H(t) = -\sum_{\langle i,j\rangle} J_{i,j}(t) c_i^\dagger c_j, \tag{3.12}$$

where $J_{i,j}$ is given by Eqs. (3.10) and (3.11). The new Hamiltonian H is no longer time-reversal symmetric because the circular polarisation changes sign under time reversal. Before continuing to a mathematical exploration of the model, let us discuss why circularly polarised radiation might be expected to generate a QHE. For this, it is useful to recall that, in the semi-classical picture, a QHE occurs because, under a perpendicular magnetic field, electrons start moving in cyclotron orbits. In the bulk, the motion of such a cyclotron orbit cancels against that of the neighbouring orbits, but at the edge an edge mode emerges, which is topologically protected by the magnetic field.

3.5.1 The physical interpretation: a dynamical Haldane model

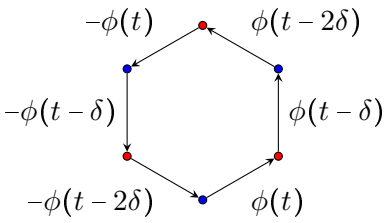

Figure 3.2: A plaquette of the honeycomb lattice is shown. Sites of the A (B) sub lattice are depicted as red (blue) dots. The arrows denote counter-clockwise hopping of an electron along the lattice bonds. Next to each arrow, the hopping phase ϕ is given. Important is that all the hoppings have the same functional form, but appear with a different phase due to the different orientation of the bonds [44].

This situation can be compared to that of irradiated graphene with the help of Fig. 3.2, where the hopping of an electron along a plaquette of the honeycomb lattice is shown. The electron picks up a complex phase with each

hopping due to the presence of the vector potential, as given in Eq. (3.11). All these phases have the same form $\phi(t)$, except that they appear out of phase due to the different values of $A(t) \cdot d\boldsymbol{s}$. At any given moment, the net flux through each unit cell vanishes, since the phases cancel in pairs.

Consider now an electron hopping between the sites depicted in Fig. 3.2. Assume the electron starts at the bottom site, at time t, and goes around in the direction of the arrows with velocity v. It takes the electron a finite time $\tau = a/v$ to move from one site to the next. As the electron moves around a lap, it will have obtained a total phase

$$\begin{aligned}\int_t^{t+\tau} [&\phi(t') + \phi(t' - \delta + \tau) + \phi(t' - 2\delta + 2\tau) \\ &+\phi(t' - 3\delta + 3\tau) + \phi(t' - 4\delta + 4\tau) \\ &+\phi(t' - 5\delta + 5\tau)]v dt'.\end{aligned}$$

Since $\phi(t - 3\delta) = -\phi(t)$, the total phase would be zero if the hopping were instantaneous, corresponding to the limit $v \to \infty$ in the integral. Instead, by assuming that the electron has a finite velocity v, a net total phase is picked up. Importantly, these phase differences appear because the vector potential rotates in time. From the electrons perspective, however, there is no distinction between this, and the phase differences appearing because the light field rotates in space: the electron sees a virtual $B = \nabla \times A$ field appear. This provides the link with the QHE, which is known to appear in graphene [110, 111], although it would be more accurate to compare this situation with the Haldane model [4]. In this model, the honeycomb lattice is subjected to staggered magnetic fluxes such that the electron picks up a phase while hopping between NNN, but the net total flux vanishes through each hexagonal cell. In this case, a QAHE effect is created; i.e. QH edge states are observed, but the usual splitting in Landau levels does not occur. In the case of circularly-polarized light, the electrons pick up a phase when hopping between NN, while there is no net flux through the hexagonal plaquettes. This causes the appearance of QH edge states, without leading to the occurrence of Landau levels [108]. In this way, circularly-polarized light creates a dynamical version of the Haldane model.

3.5.2 The band structure of irradiated honeycomb lattices

Through this analysis, it becomes intuitive that circularly-polarized light creates a QHE. In Figs. 3.3(a) and 3.3(b), the precise manner in which this happens is depicted. Here, the spectrum for the Sambe Hamiltonian defined in Eqs. (3.5) and (3.12) is shown for $V = J/\omega$, and two different values of the

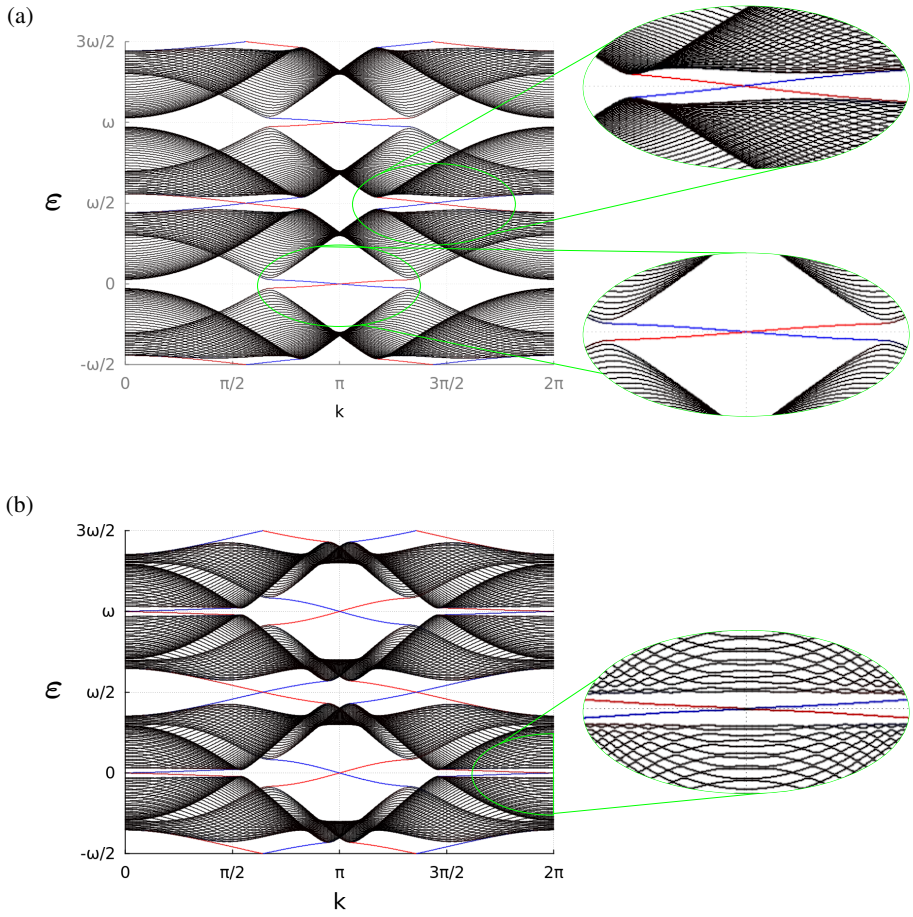

Figure 3.3: The spectrum of the Sambe Hamiltonian defined in Eqs. (3.5) and (3.12), for $V = J/\omega$; note that the entire spectrum is spin degenerate [44]. Plots were made for a ribbon geometry with zigzag edges, and k denotes the Bloch momentum along the length of the ribbon. Even though there are only two energy bands in graphene, the periodicity of the spectrum causes the existence of two inequivalent band gaps. The inlays show the gapless edge states with a magnification of two for greater clarity. Black bands are localised in the bulk, and red/blue bands are localised on the upper/lower edge of the system. Parameter values are (a) $\omega = 3J$ and (b) $\omega = 2.2J$. Since the band gaps open at multiples of $\omega/2$ for all values of ω, the quasi-energies ε are given in units of $\omega/2$, which takes a different value in (a) and (b).

light frequency: $\omega = 3J$ in Fig. 3.3(a) and $\omega = 2.2J$ in Fig. 3.3(b), for samples with a cylindrical geometry. In these figures, two inequivalent gaps are seen, each repeating with period ω: one at $\varepsilon = 0$ and one at $\varepsilon = \omega/2$. First, consider the spectrum in Fig. 3.3(a). Edge states at the top and bottom edge are depicted in red and blue, respectively, while bulk states are depicted in black. In the gap around $\varepsilon = 0$, a single spin degenerate edge mode is observed. It should be noted that the entire spectrum is spin degenerate due to the absence of Zeeman splitting in Eq. (3.12). The light opens a gap at the Dirac points, imparting an effective mass to the low-energy Floquet states. The opened gap is topological, hosting QH states, since the electrons feel an effective magnetic field. This behavior is characteristic of the QAHE, since no Landau levels are created. By inspection, this gap has $W = 1$ per spin, as defined in Eq. (3.8), so the total winding number is 2. Note that these winding numbers can be calculated per spin, since it is a good quantum number, and the propagator is diagonal in spin space. On the other hand, the gap around $\varepsilon = \omega/2$ has $W = 2$ per spin, for a total winding number of 4. The origin of these edge states is different, however. Because of the ω-periodicity of the Floquet spectrum, the conduction band above the $\varepsilon = 0$ gap overlaps with the valence band below the $\varepsilon = \omega$ gap, i.e. the valence band one period higher. The symmetry of the graphene spectrum in $E \mapsto -E$ imposes that this happens symmetrically around $\varepsilon = \omega/2$. At this point, the energy difference between valence and conduction band is precisely ω, allowing for photon resonances. These photon resonances cause hybridization of states in the valence and conduction bands, opening a gap. Because the electrons still feel an effective magnetic field, this gap is also topological, hosting QH states. These resonance-induced edge states can only occur in Floquet systems, due to the special nature of the gap at $\varepsilon = \omega/2$, as was mentioned before.

In Fig. 3.3(b), one may observe the same edge states as in Fig. 3.3(a), with the addition of an extra edge mode in the $\varepsilon = 0$ gap. The edge states in the $\varepsilon = \omega/2$ gap and those crossing at $k = \pi$ in the $\varepsilon = 0$ gap have the same origin as those in the case where $\omega = 3J$. The extra edge state crossing at $k = 0$ (or $k = 2\pi$) in the $\varepsilon = 0$ gap (see the inlay of Fig. 3.3(b)) is also caused by photon resonances. Because ω (and hence the periodicity) has decreased, the conduction band above the gap at $\varepsilon = -\omega$ has started to overlap with the valence band below the gap at $\varepsilon = \omega$. By symmetry, the overlap has to happen around $\varepsilon = 0$, and at this point the energy difference between valence and conduction band is 2ω. In this case, two photon absorption creates resonances between the valence and the conduction bands, once again opening a topological gap. Because the width of the valence and the conduction band in bare graphene

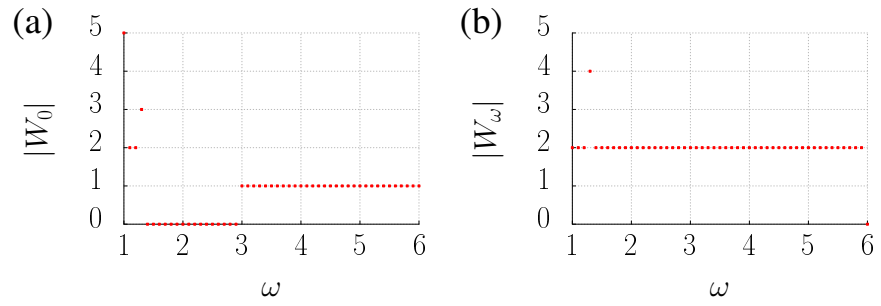

Figure 3.4: The Floquet spectrum for irradiated graphene has two inequivalent band gaps, one at $\varepsilon = 0$, and one at $\varepsilon = \omega/2$. The winding numbers W_i per spin of the two gaps are plotted against ω for $V = J/\omega$: (a) The magnitude $|W_0|$ of the gap at $\varepsilon = 0$. (b) The magnitude $|W_\omega|$ of the gap at $\varepsilon = \omega/2$ [44].

[given by Eq. (3.9)] is $3J$ (and hence, the total width is $6J$), resonances at ω and 2ω are possible for $\omega = 2.2J$. Although one would expect that for $\omega = 3J$ two photon resonances could still appear, in reality they do not because the light causes a slight flattening of the energy bands, thus decreasing the bandwidth. This is evident from Fig. 3.3(a), where the bands do not meet at $\varepsilon = 0,\ k = 0$.

For full generality, the two winding numbers W_0 and W_ω, corresponding to the gaps at $\varepsilon = 0$ and $\varepsilon = \omega/2$, respectively, have been plotted for $V = J/\omega$, the same intensity used in Fig. 3.3, for a wide range of ω. One can see that a change in winding corresponds to the onset of a new driving resonance. The systematics behind this behaviour will be discussed in the next section. The high winding numbers at low frequencies arise because the effects of subsequent resonances add, leading to potentially high numbers of edge states.

3.5.3 The interaction between ISO coupling and light

Although flat graphene surfaces have negligible ISO coupling [112], it has been demonstrated that in heavily curved graphene surfaces (for example carbon nanotubes) an appreciable intrinsic spin-orbit coupling (ISO) coupling is present [113]. It is well known [6, 7] that the ISO coupling opens a topological gap in graphene, hosting a time-reversal invariant pair of edge states. Mathematically, the two bands of graphene have a non-vanishing $\mathbb{Z}_2$ quantum number. In the QSHE, the propagation direction of the edge states is spin-polarized, whereas in the QHE it is not. This leads to a competition between

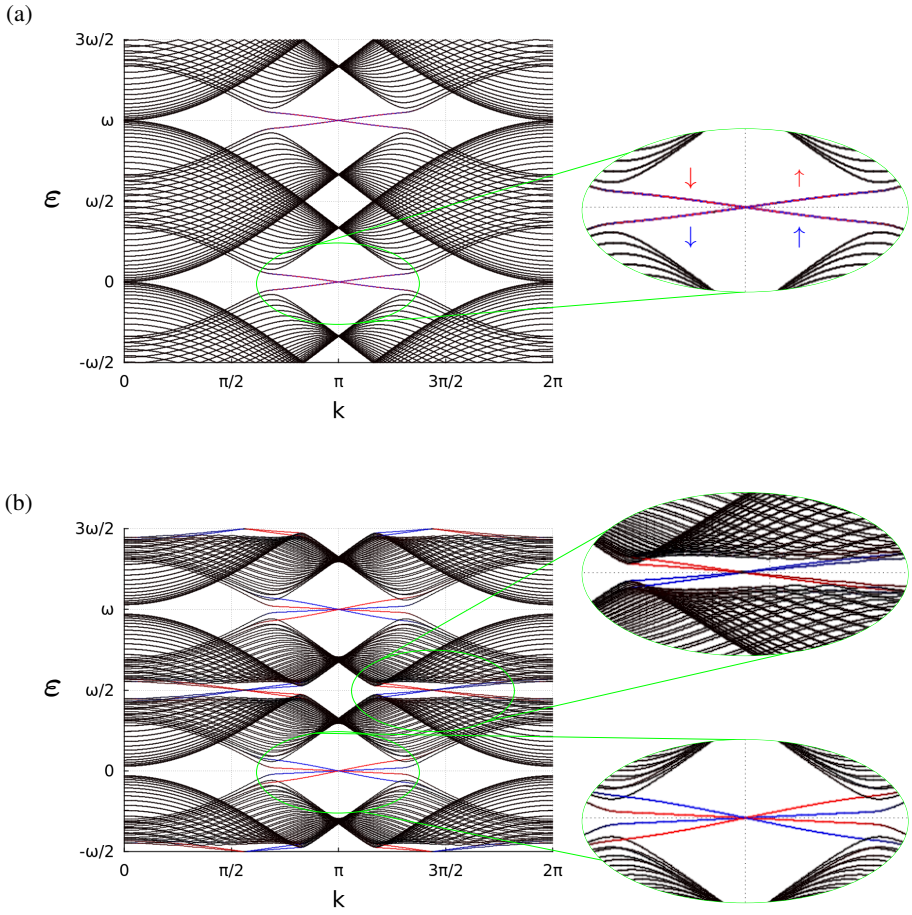

Figure 3.5: The spectrum of the Sambe Hamiltonian defined in Eqs. (3.5) and (3.13) for $\omega = 3J$ and $\lambda = 0.06J$ [44]. Plots were made for a ribbon geometry with zigzag edges, and k denotes the Bloch momentum along the length of the ribbon. The inlays show the gapless edge states with a magnification of two, for greater clarity. Black bands are localised in the bulk and red/blue bands are localised on the upper/lower edge of the system. (a) For $V = 0$, the known dispersion for the QSHE is observed, apart from a periodic continuation in ω, caused by artificially considering the Floquet spectrum despite a time independence. Since the spectrum is spin degenerate, The spin direction for each edge state is indicated in the inlay. (b) For $V = J/\omega$, in the presence of both ISO coupling and circularly-polarized light, the spin degeneracy in both edge and bulk states is lifted. In the gap at $\varepsilon = 0$, the QSHE still dominates.

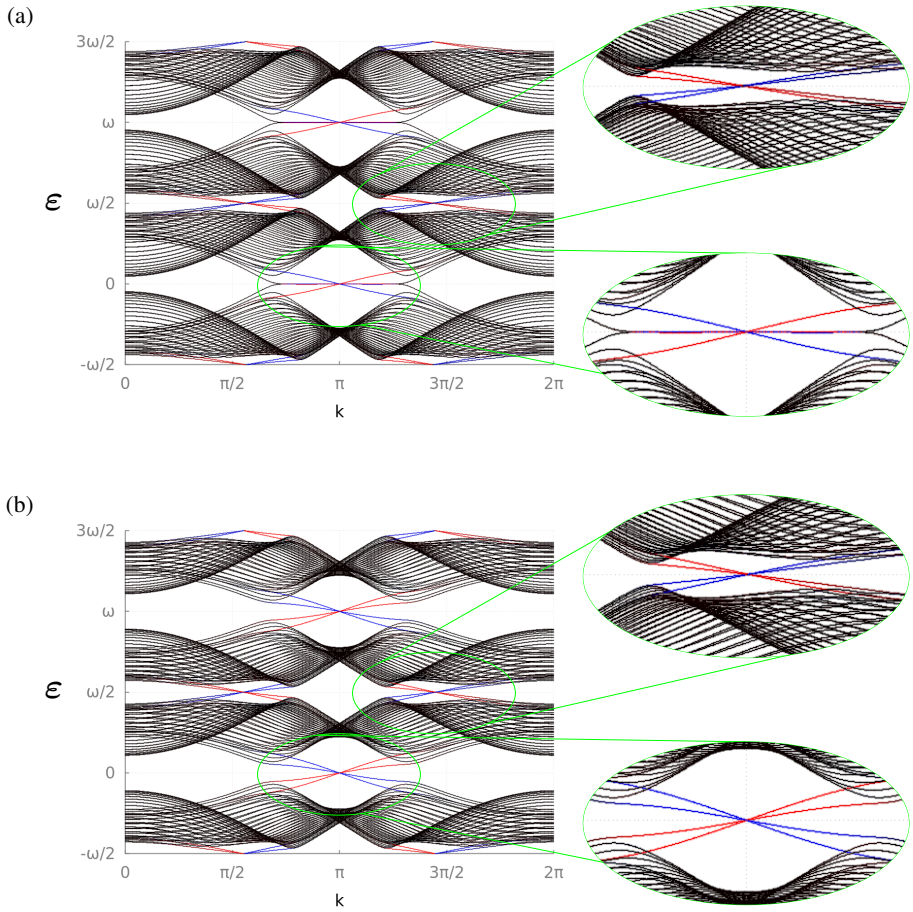

Figure 3.6: The spectrum of the Sambe Hamiltonian defined in Eqs. (3.5) and (3.13) for $\omega = 3J$ and $\lambda = 0.06J$ [44]. Plots were made for a ribbon geometry with zigzag edges, and k denotes the Bloch momentum along the length of the ribbon. The inlays show the gapless edge states with a magnification of two, for greater clarity. Black bands are localised in the bulk and red/blue bands are localised on the upper/lower edge of the system. (a) For $V = 1.3J/\omega$ and $\varepsilon = 0$, the QHE and QSHE effects annihilate each other for spin down, and enhance each other for spin up. This causes one of the states on each edge to become dispersionless. (d) For $V = 2J/\omega$, the irradiation dominates; aside from a lifting of the spin degeneracy, the graph resembles the one in Fig. 3.3(b), where QH states are generated.

the two effects, as the QHE becomes more pronounced and TR symmetry is increasingly violated, an effect that has been observed before in undriven systems [114–116]. This is the interplay alluded to in the beginning of this section. To model this competition, we add to the Hamiltonian in Eq. (3.12) an ISO term [6, 7]

$$H(t) = -\sum_{\langle i,j\rangle} J_{i,j}(t) c_i^\dagger c_j - i \sum_{\langle\langle i,j\rangle\rangle} \hat{s}_z \lambda_{i,j}(t) \nu_{i,j} c_i^\dagger c_j, \tag{3.13}$$

where double brackets denote a sum over NNN. Furthermore,

$$\lambda_{i,j}(t) = \lambda \exp\left[-ie \int_i^j \boldsymbol{A}(t) \cdot d\boldsymbol{s}\right], \tag{3.14}$$

with λ denoting the ISO coupling strength. Additionally, $\nu_{i,j} = \pm 1$, depending on whether the NNN hopping is clockwise or counter-clockwise, and $\hat{s}_z$ is the spin operator, yielding the sign change of the ISO interaction for the different spins. Note that $\hat{s}_z = \hat{\sigma}_z/2$, where σ is a Pauli matrix. This is similar to the ISO Hamiltonian from Kane & Mele [6, 7], except that in Eq. (2.5) there are the additional parameters t_3 and t_4. and importantly, the hopping is now modulated by the vector potential that incorporates the light field. This causes both the NN and the NNN hopping to have a real and an imaginary component. In the Kane & Mele model, the NN hopping is real, and the NNN hopping is purely imaginary. Apart from a difference in vector potential, this is the model considered by Beugeling et al. [116]. In Ref. [116], the authors consider a perpendicular magnetic field and $\nabla \times \boldsymbol{A} = \boldsymbol{B}$. Here, according to Eq. (3.10), $\nabla \times \boldsymbol{A} = 0$. The non-trivial topological phases in this case come from the time dependence of $\boldsymbol{A}$; it is this dynamical character that leads to the unexpected behavior.

The Sambe Hamiltonian corresponding to Eqs. (3.13) and (3.5) yields the dispersion relation which is shown in Figs. 3.5 and 3.6 for various values of the relevant parameters. In Fig. 3.5(a), the spectrum of the system is shown in the absence of light. In this case, the known dispersion is recovered, apart from a periodicity in ω, which is manually inserted to facilitate comparison with the time-dependent cases. In Fig. 3.5(b), all parameters are the same as for the dispersion in Fig. 3.3(a), apart from the addition of the ISO coupling. Here, the light field opens a gap at $\omega/2$, which hosts the same type of edge states as in the absence of ISO coupling. The ISO coupling cannot have an impact on the topological nature of this gap because it is caused by photon resonances between the conduction and valence bands; the ISO coupling cannot create such resonances. The same occurs for the two photon resonances at $\varepsilon = 0$ for $\omega = 2.2J$

(not shown): the degeneracy of the resulting edge states is lifted, but they will be QH states regardless of light intensity. In the gap at $\varepsilon = 0$, edge states of a QSH type are observed. Although the light breaks the TR symmetry of the system, and the QSH states are no longer protected, the perturbing effect of the light is not enough to break the QSH-like nature of the edge states. This leads to a so-called weak QSHE [114–116]. In both gaps, the degeneracy of the edge states is lifted, creating two states of different velocity on each edge. The slope of the state is related to the spin orientation, since the slope is increased for spin up, where the QH and QSHE enhance each other; on the other hand, for spin down they interfere destructively and the slope is decreased. Furthermore, the degeneracy of the bulk states is also lifted. The ISO coupling alone cannot do this, but applying a magnetic field [116], or circularly-polarized light will lift this degeneracy. It is also possible to lift the degeneracy by applying a Rashba spin-orbit coupling [117, 118], as was discussed in Chap. 2.3.2. In Fig. 3.6(a), the intensity of the light is further increased. As before, the nature of the edge states in the gap at $\varepsilon = \omega/2$ are unchanged, whereas the edge states in the gap at $\varepsilon = 0$ are affected by the increased competition between the QHE and QSHE. For the spin value where they enhance each other, the velocity of the edge state is increased, while for the other spin the two effects annihilate each other. The gap closes and the edge states become dispersionless. In Fig. 3.6(b), the light intensity has become so high that the QHE also dominates in the gap at $\varepsilon = 0$. The ISO coupling still causes a lifting of the spin degeneracy of the edge states, but all the gapless states are of a QH nature (see Fig. 3.3(a) for a comparison). Specifically, the gap closing at $\varepsilon = 0$ has led to a change in Chern number of two (since one of the spins changes propagation direction) for both bands, corresponding to the change in chirality of the gap. This clearly demonstrates the competition between the different topological properties of systems with or without TRS. The combination of ISO coupling and circularly-polarized light lifts the spin degeneracy of both the edge and the bulk states.

3.6 Topological resonances in Floquet systems

Apart from the competing nature of the QHE and the QSHE at $\varepsilon = 0$, the irradiation of graphene causes topological edge states to appear in the gap at $\varepsilon = \omega/2$, as discussed in the preceding section, and shown in Fig. 3.3(a). These states can only exist in Floquet systems, because they originate from driving resonances. It is important to have a more thorough understanding of how resonances in the driving lead to the appearance of these states. A detailed phase

diagram of the different topological phases in the irradiated graphene system has been obtained in Ref. [119], and there it can be seen that for low driving intensities, phase changes coincide well with the appearance of new resonances. For these low intensities, it is possible to obtain effective Hamiltonians describing the emergence of these resonances in perturbation theory [91]. Here, we present the details of a calculation, which was published in Ref. [49], to obtain these effective Hamiltonians, and relate them to topological systems in equilibrium. The work in this publication was done by me, while Prof. Dr. Goerbig and Prof. Dr. Morais Smith supervised it.

Let us reconsider the Hamiltonian in Eq. (3.12), which can be written in momentum space as

$$H(\boldsymbol{k},t) = J\sum_l \begin{pmatrix} 0 & \exp(i\tilde{\boldsymbol{k}}\cdot\boldsymbol{\delta}_l) \\ \exp(-i\tilde{\boldsymbol{k}}\cdot\boldsymbol{\delta}_l) & 0 \end{pmatrix}. \tag{3.15}$$

Here, $\tilde{k} \coloneqq k + eA$, and we use the convention $\boldsymbol{\delta}_0 = a(0,1)$, and $\boldsymbol{\delta}_{\pm 1} = -a\left(\pm\sqrt{3},1\right)/2$ for the NN hopping vectors $\boldsymbol{\delta}_l$, where a is the NN distance. Let us analyse this system in Sambe space, by using $\mathfrak{H}$ from Eq. (3.5). First, write the matrix elements of $\mathfrak{H}$ as

$$\begin{aligned}\langle n|\mathfrak{H}|m\rangle &= \frac{1}{T}\int dt \exp\left[i\omega(m-n)t\right](H + m\hbar\omega) \\ &= H_{m-n} + m\hbar\omega\delta_{m,n}.\end{aligned} \tag{3.16}$$

This gives H_n the interpretation of a frequency mode of $H(t)$. A direct computation gives

$$H_n = J\begin{pmatrix} 0 & \sum_l \kappa_{-n}\exp[i\left(\boldsymbol{k}\cdot\boldsymbol{\delta}_l + \alpha_{l,n}\right)] \\ \sum_l \kappa_n \exp[i\left(-k\cdot\boldsymbol{\delta}_l + \alpha_{l,n}\right)] & 0 \end{pmatrix}. \tag{3.17}$$

Here, $\kappa_n \coloneqq J_n\left(aV/\hbar\right)$, where J_n is the Bessel function of the n^{th} kind. Furthermore, $\alpha_{l,n} \coloneqq n\mathrm{Arg}[\boldsymbol{\delta}_l] + n\pi/2$, where Arg gives the angle of a vector with the x-axis. Using Eq. (3.17), $\mathfrak{H}$ can then be written as an infinite block matrix

$$\mathfrak{H} = \begin{pmatrix} \ddots & \vdots & \vdots & \vdots & \vdots \\ \cdots & H_0 + \hbar\omega & H_1 & H_2 & \cdots \\ \cdots & H_{-1} & H_0 & H_1 & \cdots \\ \cdots & H_{-2} & H_{-1} & H_0 - \hbar\omega & \cdots \\ \vdots & \vdots & \vdots & \vdots & \ddots \end{pmatrix}. \tag{3.18}$$

If the spectrum around an energy $n\hbar\omega$ is desired, it can be computed approximately by truncating the right-hand side of Eq. (3.18) around $H_0 + n\hbar\omega$. In the large-frequency limit, $\hbar\omega \gg J$, the spectrum of $\mathfrak{H}$ starts to resemble that of H_0, periodically repeated. In what follows, each such period will be referred to as a Floquet band. In this case, the gap between the different Floquet bands is effectively infinite (so the gap is certainly not topological), yielding the quasi-static regime discussed in the introduction to this chapter. As one lowers the frequency, these Floquet bands start to cross, indicating the appearance of resonances due to driving. These band crossings create additional, possibly topological gaps in the spectrum.

There are two resonances that will be focussed on in the rest of this section, the first resonance, which appears for $\hbar\omega \approx 5.8J$, at $\varepsilon = \omega/2$, and the second resonance, which appears for $\hbar\omega \approx 2.9J$ at $\varepsilon = 0$.

3.6.1 Numerical results

For $\hbar\omega \approx 6J$, the Floquet band n starts to overlap at the top with band $n + 1$ and at the bottom with band $n - 1$. This is the highest frequency at which such an overlap occurs because the width of a single band is almost $6J$, and this overlap is interpreted as coming from a resonance with a single quantum of the driving (i.e. a photon in the case of irradiation of a condensed matter system, or a phonon for the shaking of a honeycomb optical lattice). In Fig. 3.7, two Floquet bands of the spectrum of $\mathfrak{H}$ are shown for $\hbar\omega = 6J$. One can see the $n = 0$ Floquet band in the center, half of the $n = 1$ band between $\hbar\omega/2$ and $\hbar\omega$, and half of the $n = -1$ band between $-\hbar\omega$ and $-\hbar\omega/2$. The bands do not touch yet, and the band inversion is imminent. Lowering ω will cause the different Floquet bands to move towards each other, causing a band inversion. In Fig. 3.8, the spectrum is shown for $\hbar\omega = 5.6J$, where it can be seen that the bands have inverted. Because of the circularly polarised light, a gap is opened after the band inversion. The size of this gap is seen in Fig. 3.8(b), where a close up of the band inversion is shown. From this close up, it can also be seen that the gap is topological, hosting two pairs of protected edge states. The edge states are depicted in red and blue, while black states are located in the bulk.

At $\hbar\omega \approx 2.9J$, the second resonance appears. In Fig. 3.9, the spectrum of $\mathfrak{H}$ is plotted for $\hbar\omega = 3J$. In Fig. 3.9(a), the $n = 0$ Floquet band has been made translucent to draw attention to the impending band inversion. The bottom of the $n = 1$ valence band (on top) and the top of the $n = -1$ conduction band (below) are visible with a gap between them. In Fig. 3.9(b), the $n = 1$ and $n = -1$ Floquet bands have been made translucent to draw attention to the

$n = 0$ Floquet band, which hosts topological edge states at the Dirac points. It should be noted that the bottom half of Fig. 3.9(b) is identical to the top half of Fig. 3.9(a). This is because the spectrum is periodic in $\hbar\omega$, so the $n = 0$ valence band in Fig. 3.9(b) is identical to the $n = 1$ valence band in Fig. 3.9(a). The full spectrum can be obtained by superimposing Figs. 3.9(a) and (b), since the bands $n = \pm 1$ and $n = 0$ are the only ones visible in the first two periods of the spectrum. As ω is lowered, the valence band (on top in Fig. 3.9(a)) descends and the conduction band (at the bottom of Fig. 3.9(a)) ascends; a band inversion takes place at $\hbar\omega \approx 2.9J$, and due to the driving, the gap reopens after the bands invert (see Fig. 3.10(a)). An extra pair of edge states now crosses the gap where the band inversion took place, as is highlighted in Fig. 3.10(b), where a zoom in on a narrow energy window is shown. It should be noted that the edge states at the Dirac points (Fig. 3.9(b)) are still present after the band inversion, and the edge states at $k = 0$, which correspond to the two-phonon resonance, are counter-propagating with respect to them. (Remember that in Fig. 3.10, the edge states at the Dirac points have been made translucent at $\varepsilon = 0$. One can see the counter-propagating states in Fig. 3.3(b)) The appearance of new edge states at $k = 0$ removes the topological protection of the edge states in the $\varepsilon = 0$ gap. This can be seen by considering the winding number W from Eq. (3.8) for this gap. Because the two states counter-propagate, they contribute to this winding number with opposite sign, as can be checked by an explicit calculation. Furthermore, this lack of topological protection becomes evident when one considers the graphene ribbon with different edge structures. Two terminations that are commonly considered for the graphene ribbon are zigzag and armchair terminations. If one takes into account only NN hopping, the ribbon with zigzag edges hosts edge states, even though they are not topological, while the armchair ribbon does not. Similarly, we now find the counter-propagating edge modes for the zigzag geometry, even though they are not topologically protected. In contrast, for the armchair termination, the edge states corresponding to the zero-phonon and two-phonon resonances both occur at $k = 0$. Consequently, in this case they gap out because of hybridisation, which could not have occurred if the states were topologically protected. However, if only the edge state at the Dirac points is present, changing to the armchair termination does not gap it out due to the topological protection. These considerations show that the appearance of the two-phonon resonance indeed makes the $\varepsilon = 0$ gap trivial. The situation can be reversed by applying a staggered sublattice potential: this will destroy the zero-phonon resonance at the Dirac points, but leave the two-phonon resonance untouched. In this case, the appearance of the two-phonon resonance changes the gap at $\varepsilon = 0$ from

topologically trivial to non-trivial.

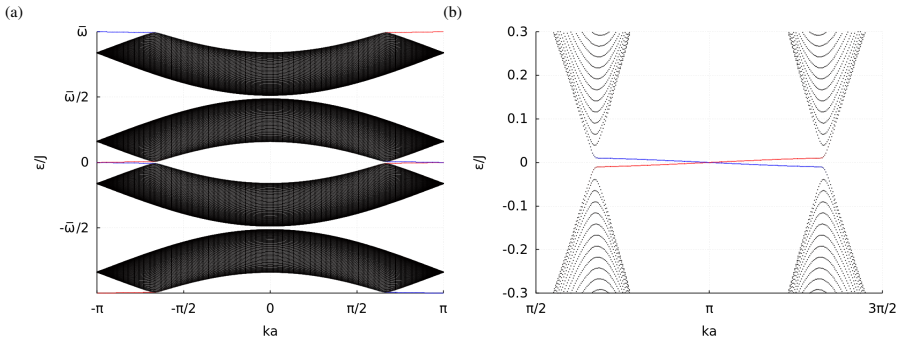

Figure 3.7: (a) Part of the spectrum of the Floquet Hamiltonian $\mathfrak{H}$ is shown. Plots were made for a ribbon geometry with zigzag edges, and k denotes the Bloch momentum along the length of the ribbon. Two periods of the spectrum of $\mathfrak{H}$ are shown for $Va = 2J/\omega$. (a) The frequency $\hbar\omega = 6J$, and the relevant feature is the impending gap closure at $\varepsilon = \hbar\omega/2$ and $k = 0$, when the Floquet bands $n = 1$ and $n = 0$ overlap. Red and blue represent different edges. The y-axis is labelled in terms of $\bar{\omega} := \hbar\omega/J$. (b) A zoom in on the Dirac points is shown, to make the gap size and the edge states more visible. Note that we plot a different region in momentum space than in (a), to improve the visualisation [49].

3.6.2 Low-energy effective theory

From the numerical results, it becomes clear that the appearance of driving resonances in the system is accompanied by band crossings in the Floquet spectrum. In undriven systems, the connection between band crossings and changes of topology is well understood. For example, one can calculate the change of Chern number of a pair of bands when they invert, and it depends only on the low energy spectrum [120]. For the time-reversal symmetric case, the situation seems to be similar [121], but a totally rigorous proof is missing. Heuristically, however, the situation seems to be clear, and it is natural to consider whether a similar situation holds for the Floquet case. To answer this question, an effective theory for the appearance of the resonance is needed, and a calculation to obtain it will be presented here. The first step is to extract the relevant energy bands from $\mathfrak{H}$, so we can perform a truncation. This is done by diagonalizing H_0, and for simplicity we only keep terms up to second order in $\boldsymbol{k}$. Define the

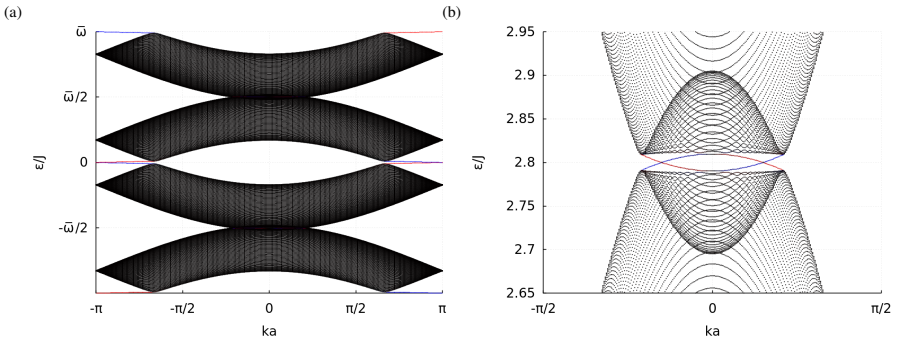

Figure 3.8: (a) The same spectrum as in Fig. 3.7 is shown, but for $\hbar\omega = 5.6J$. The band inversion has taken place, and 2 pairs of topological edge states are present in the topological gap that has opened after the band inversion. (b) A zoom in on the gap at $\bar{\omega}/2 = 2.8$ is shown, to make the size of the gap and the edge states more visible [49].

unitary transformation

$$U := \frac{1}{2}\sqrt{2}\begin{pmatrix} 1 & 1 \\ 1 & -1 \end{pmatrix} \tag{3.19}$$

and consider the transformed Hamiltonian

$$\bar{\mathfrak{H}} = \begin{pmatrix} \ddots & \vdots & \vdots & \vdots & \vdots \\ \cdots & \bar{H}_0 + \hbar\omega & \bar{H}_1 & \bar{H}_2 & \cdots \\ \cdots & \bar{H}_{-1} & \bar{H}_0 & \bar{H}_1 & \cdots \\ \cdots & \bar{H}_{-2} & \bar{H}_{-1} & \bar{H}_0 - \hbar\omega & \cdots \\ \vdots & \vdots & \vdots & \vdots & \ddots \end{pmatrix}, \tag{3.20}$$

where we define $\bar{H}_n := UH_nU$. From Eqs. (3.17) and (3.19), one finds the identity

$$\bar{H}_0 = J\kappa_0\left(3 - \frac{3}{4}k^2a^2\right)\sigma_z + \ldots$$

Now, we will treat the first resonance, which appears for $\hbar\omega \approx 6J$, in the gap at $\varepsilon = \omega/2$. The $(1,1)$ element of $\bar{H}_0$ and the $(2,2)$ element of $\bar{H}_0 + \hbar\omega$ are much closer to $\hbar\omega/2$ than all other energy scales in the problem. Since these two elements are next to each other on the diagonal of $\bar{H}_F$, H^1_{eff} is the 2×2 block matrix containing these two elements. This yields

$$H^1_{\text{eff}} = \begin{pmatrix} (\bar{H}_0 + \hbar\omega)^{2,2} & \bar{H}_1^{2,1} \\ \bar{H}_{-1}^{1,2} & (\bar{H}_0)^{1,1} \end{pmatrix}. \tag{3.21}$$

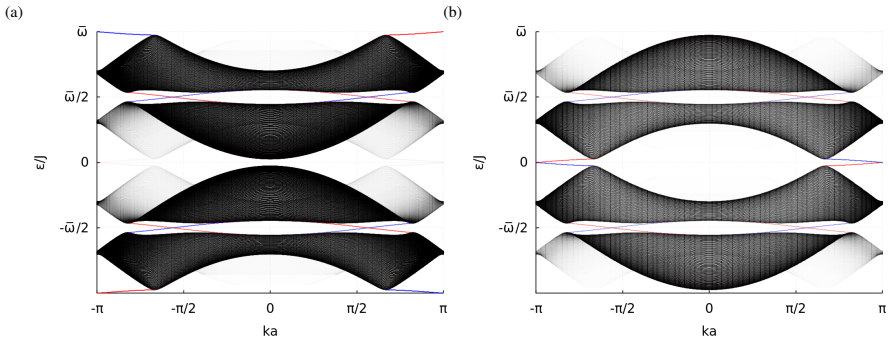

Figure 3.9: (a) The spectrum of the Floquet Hamiltonian $\mathfrak{H}$ is shown. Plots were made for a ribbon geometry with zigzag edges, and k denotes the Bloch momentum along the length of the ribbon. Two periods of the spectrum of $\mathfrak{H}$ are shown for $\hbar\omega = 3J$ and $Va = J/\omega$. The relevant feature is the impending gap closure at $\epsilon = 0$ and $k = 0$, when the Floquet bands $n = 1$ and $n = -1$ overlap. To highlight this, we have made all bands, except for $n = 1$ and $n = -1$, translucent. Red and blue represent different edges. The y-axis is labelled in terms of $\bar{\omega} := \hbar\omega/J$.(b) The same spectrum as in (a) is shown, but now all bands except for $n = 0$ have been made translucent. This draws attention to the edge states at the Dirac points in the $\varepsilon = 0$ gap. The one-phonon resonance at $\pm\bar{\omega}/2$ is also visible in this figure, because it is caused by an overlap between the $n = 0$ and $n = \pm 1$ bands [49].

where the superscripts denote a specific element of the corresponding matrix. Due to its periodic structure, the matrix in Eq. (3.20) has only two eigenvalues that repeat with periodicity $\hbar\omega$. These eigenvalues correspond to an effective 2×2 Hamiltonian that can be found through a series expansion detailed in Ref. [91]. This expansion is in orders of $1/\omega$ and the norm of the $\hat{H}_i$, which is V in this specific case. The lowest order term is precisely H^1_{eff}, and the first correction is $[\hat{H}_{-1}, \hat{H}_1]/\omega$. All higher-order corrections have similar expressions in terms of commutators containing the $\hat{H}_i$ and powers of $1/\omega$. Because the $\hat{H}_i$ contain progressively higher orders of V, this series expansion can be truncated when the matrix elements of H^1_{eff} are small compared to ω, and $V \ll 1$. For example, $[\hat{H}_{-1}, \hat{H}_1]$ is of the same order as H^1_{eff}, so $[\hat{H}_{-1}, \hat{H}_1]/\omega$ is suppressed by an extra factor of $1/\omega$ when the elements of H^1_{eff} are small. Around the first and second resonance, with the values of V used to generate the figures in this section, all higher-order terms can be dropped from the expansion, and H^1_{eff} is the desired effective Hamiltonian. For small ω and/or large vector poten-

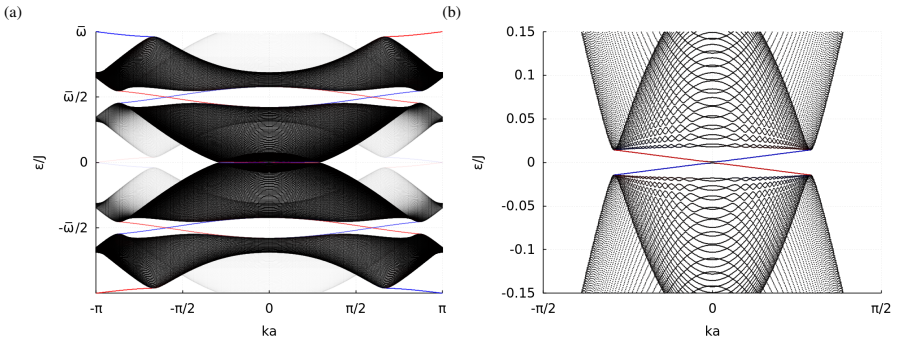

Figure 3.10: (a) Same as in Fig. 3.9, but for $\hbar\omega = 2.7J$. The relevant feature is the band inversion at $\epsilon = 0$ and $k = 0$, where the Floquet bands $n = 1$ and $n = -1$ overlap, creating a gap with topologically protected edge states. To highlight this, we have made all bands, except for $n = 1$ and $n = -1$, translucent. (b) A zoom in on the band crossing from (a) is provided to make the details of the gap visible [49].

tials V, the higher-order terms in the series do not decay, and they cannot be dropped from the expansion. The deviations caused by these extra terms have been investigated numerically in Ref. [119], where the full phase diagram of the system is calculated. They conclude that increasing V can lead to phase transitions without additional band inversions, as the off-diagonal blocks become sizeable. In irradiated graphene, this corresponds to an increase in the radiation intensity E, for a vector potential induced through circular shaking, as discussed in Appendix B, this corresponds to increasing the product $r_0\omega$, where r_0 is the shaking radius. For the first resonance, at the values of V used to generate the figures 3.7 and 3.8, it is enough to only consider the first-order terms as in Eq. 3.21. Filling in the expression for $\bar{H}_{\pm 1}$, one obtains

$$H_{\text{eff}} = \begin{pmatrix} \hbar\omega + \left(\frac{3}{4}k^2a^2 - 3\right) J\kappa_0 & \frac{3}{8}\left(k_x a - ik_y a\right)^2 J\kappa_1 \\ \frac{3}{8}\left(k_x a + ik_y a\right)^2 J\kappa_1 & \left(3 - \frac{3}{4}k^2a^2\right) J\kappa_0 \end{pmatrix}. \tag{3.22}$$

This expression is correct up to order $(Va/\hbar)^2$, and it describes a simple two-band model depicting a quadratic band inversion (as the gap closes, the energy goes as k^2 to lowest order). This means that the Chern number of the two bands changes by two for each spin. From Fig. 3.8(b), it is obvious that there are indeed two edge modes for each spin in the gap, showing that the band inversion picture is correct in this case. As an interesting aside, the effective model for the one-phonon resonance is similar to that of a gapped bilayer

graphene [66, 118], with the addition that the gap can be topological.

Now, let us consider the second photon resonance, which appears when $\hbar\omega \approx 3J$, at $\boldsymbol{k} \approx 0$ in the gap at $\varepsilon = 0$. Here, the $(2,2)$ element of the matrix $\bar{H}_0 + \hbar\omega$ and the $(1,1)$ element of $\bar{H}_0 - \hbar\omega$ are closer to 0 than all the other energy scales in the problem. They are the zeroth-order energies of the two bands near the band crossing shown in Figs. 3.9 and 3.10. To extract the effective theory, similar to the previous case, it is necessary to perform a unitary transformation that makes these two elements adjacent on the diagonal. To this effect, consider a transformation V with the matrix elements $\langle n|V|m\rangle = \sigma_+\delta_{m,n-1} + \sigma_-\delta_{m,n+1}$, that permutes the basis vectors in such a way that the $(1,1)$ elements of the 2×2 matrices along the diagonal of $\bar{\mathfrak{H}}$ are interchanged with the $(2,2)$ elements diagonally above. Here, $\sigma_\pm = (\sigma_x \pm i\sigma_y)/2$. With respect to this basis, the Sambe Hamiltonian $\hat{\mathfrak{H}} := V\bar{\mathfrak{H}}V$ reads

$$\hat{\mathfrak{H}} = \begin{pmatrix} \ddots & \vdots & \vdots & \vdots & \vdots \\ \cdots & H_{\text{eff}} + \hbar\omega & \hat{H}_1 & \hat{H}_2 & \cdots \\ \cdots & \hat{H}_{-1} & H_{\text{eff}} & \hat{H}_1 & \cdots \\ \cdots & \hat{H}_{-2} & \hat{H}_{-1} & H_{\text{eff}} - \hbar\omega & \cdots \\ \vdots & \vdots & \vdots & \vdots & \ddots \end{pmatrix}, \tag{3.23}$$

where the $\hat{H}_i$ are matrices obtained by interchanging elements of the $\bar{H}_j$, which do not need to be defined here. It follows that

$$H^2_{\text{eff}} = \begin{pmatrix} (\bar{H}_0 + \hbar\omega)^{2,2} & \bar{H}_2^{2,1} \\ \bar{H}_{-2}^{1,2} & (\bar{H}_0 - \hbar\omega)^{1,1} \end{pmatrix}. \tag{3.24}$$

Using the definition of $\bar{H}_2$, one obtains

$$\bar{H}_2^{2,1} = \frac{3}{2}J\kappa_2\,(ik_y - k_x) + \ldots,$$

and thus the BHZ Hamiltonian [8]

$$H_{\text{eff}} = \begin{pmatrix} M + Bk^2a^2 & A(k_x - ik_y)a \\ A(k_x + ik_y)a & -(M + Bk^2a^2) \end{pmatrix}, \tag{3.25}$$

where

$$M = \hbar\omega - 3\kappa_0 J, \qquad B = \frac{3}{4}\kappa_0 J, \qquad A = -\frac{3}{2}\kappa_2 J. \tag{3.26}$$

These expressions agree with the ones derived by Kundu et al. [45] upon replacing eE/ω by V. The BHZ Hamiltonian is the simplest model describing a

linear band crossing, which is associated with a change in the Chern number of unity. It is paradigmatic in undriven topological insulators for modelling band inversions, which are usually linear. The presence of the Bessel function of the second kind, J_2, through κ_2 in Eq. (3.26), shows that the opening of a gap at the band inversion is a second-order resonant process. It should be noted that for the NN-hopping $J < 0$, one finds that A in Eq. (3.26) acquires an additional minus sign, but the spectrum remains unaffected. Finally, honeycomb optical lattices with a slight deformation of the unit cell that breaks the three fold symmetry at each lattice site have recently been experimentally realised [80]. Such an anisotropy in the unit cell will change the effective Hamiltonian since the bond length a enters it through κ_i, causing A, B, M to become direction dependent. For small anisotropies, the results discussed above should still hold, except that the precise values of $\hbar\omega$ where the crossing occurs will depend on the renormalised A, B, M parameters, and the gap size will now become direction dependent.

From the effective Hamiltonian in Eq. (3.25), and following Ref. [122], one can derive an explicit solution for the edge state in the infinite half-plane. Using perturbation theory to linear order in k, the edge states then disperse as

$$E_k = \pm Ak = \mp\frac{3}{16}Jka\left(\frac{mr_0\omega a}{\hbar}\right)^2 + ...,$$

i.e. the edge states have a velocity quadratic in the frequency ω.

From H_{eff}, an expression for the gap size Δ can also be derived, and one obtains

$$\Delta = \frac{3}{4}J\sqrt{1-\frac{\hbar\omega}{3J}}\left(\frac{mr_0\omega a}{\hbar}\right)^2 + ... \tag{3.27}$$

By substituting the parameter values $\hbar\omega = 2.7J$ and $mr_0\omega^2 a = J$ into Eq. (3.27) yields a gap size $\Delta = 0.033J$, which is in good agreement with the numerical results shown in Fig. 3.10(b).

3.6.3 Experimental realisation

Considering that the Hamiltonian in Eq. (3.12) describes a honeycomb lattice irradiated with circularly polarised light, the question remains whether the discussed effects can be observed in condensed matter. In this case, the resonances are photon resonances, and one replaces V by eE/ω. A natural candidate would be graphene, but the relevant hopping parameter $J = 2.8$ eV and the

NN bond length $a = 1.4$ Å in graphene would require unphysically large frequencies beyond the THz regime, and a very high field strength of $E \approx 5.3{\cdot}10^{10}$ V/m. A more promising candidate is a self-assembled honeycomb lattice of CdSe nanocrystals [123, 124], which hosts an s-band exhibiting a dispersion similar to that of graphene. The hopping parameter in these artificial structures depends on the diameter and the contact area of the nanocrystals. A hopping parameter $J = 25$ meV, that is roughly two orders of magnitude smaller than that in graphene, has been theoretically predicted for nanocrystals with a diameter of 3.4 nm [123]. By using light with $E = 10^7$ V/m and $\hbar\omega = 65$ meV, a gap of 1.5 meV is obtained for these parameters, which is 6% of the hopping J. In Ref. [38], the Dirac states at the surface of a 3D topological insulator are irradiated by circularly polarised light, and the resulting photon resonance gaps are detected using ARPES. Although thermal excitation of the Dirac electrons is observed, it is possible to measure the Floquet spectrum before the states have been excited away from the bands. This, together with the predicted bandgap, implies that the two-photon resonance should be observable in the recently synthesised artificial superlattices of CdSe nanocrystals [123, 124], or in predicted similar structures [125].

It would be much more natural to attempt to realise the Hamiltonian in Eq. (3.25) through the use of optical lattices. Honeycomb lattices have been manufactured in the past [126], and they are more promising for two reasons. The first reason for this is the much larger lattice constant, compared to condensed matter systems: since the vector potential enters the Hamiltonian in the combination eAa, this allows for smaller vector potentials. The second reason is that the circular shaking described here creates a vector potential of the form $eA = mr_0\omega$, as opposed to eE/ω, so that increasing the frequency actually increases the vector potential, rather than suppressing it. In graphene, for example, the required frequencies suppress the vector potential too strongly, resulting in the necessity of unphysically large electric fields. In contrast, taking a honeycomb optical lattice with NN hopping J and recoil energy $E_r = \hbar^2k^2/2m$, one can rewrite

$$\frac{aeA}{\hbar} = \frac{ar_0\omega m}{\hbar} = \frac{1}{2}ar_0\frac{\omega\hbar}{E_r}k^2 = 2\pi^2\frac{r_0}{a}\frac{\hbar\omega}{E_r},$$

To obtain the bandgap derived in the previous section would require shaking by a frequency $\hbar\omega = 2.7J$, at a radius $r_0 = aE_r/(140J)$. For potassium atoms loaded in an optical lattice with wavelength $k = 1064$ nm, which corresponds to $E_r \approx 4410$ Hz, the shaking would be at several kHz, with a radius of several tens of nm, which means several percent of the lattice constant. Since possible

shaking amplitudes range from this regime [84] up to several times the optical wavelength [32], these parameters are easily achievable experimentally. This suggests that honeycomb optical lattices are a very promising candidate for realizing the topological states discussed here.

3.7 A Floquet topological phase without Chern number

It turns out, however, that honeycomb optical lattices provide the opportunity to realise an even more interesting state. The honeycomb lattice under circularly polarised vector potential that we discussed in the previous sections gives a good indication of the influence of driving resonances. Specifically, it shows how the novel topological behaviour of Floquet systems originates in their appearance/disappearance. However, there is one specific state that this system cannot realise, and that is the one schematically sketched in Fig. 3.1. This is a state where all Chern numbers vanish, which is yet topologically non-trivial [40, 105, 127, 128]. Because of the non-trivial topology, these systems host protected chiral edge modes, but there is no transverse conductivity in the bulk, due to the vanishing Chern number. As a consequence, the bulk is no longer robust against Anderson localisation, and it is possible to fully localise the bulk states while preserving the edge states [128]. Note that because of this, Laughlin's charge pumping argument, described in Chap. 2, does not hold for this state, and the edge state is not associated with a quantum anomaly. This behaviour is well understood from a theoretical viewpoint, and various models exhibiting these features have been studied [40, 105, 127, 128]. Additionally, there is experimental evidence for these states in quantum walks [129], microwave networks [130], plasmon structures [131] and photonic waveguides [132, 133]. However, this state has not yet been experimentally realised in optical lattices. Such a realisation would be desirable, because optical lattices allow for greater system sizes, as well as a greater tunability of the various parameters; the ability to tune the hopping amplitude is of special interest, because it is necessary for the full localisation of the bulk, but the possibility to include interactions is also interesting in light of possible future developments.

Here, we propose a simple shaking protocol for a honeycomb optical lattice loaded with fermions that allows for the realisation of this exotic topological state, which bears no analogue in equilibrium systems. The discussion is based on work published in Ref. [134]. The calculations in this work were done by me, while Dr. Weitenberg provided valuable experimental insight. Prof. Dr.

Sengstock and Prof. Dr. Morais Smith supervised the project. We construct the full topological phase diagram for the model, and determine which specific experimental parameters might be used to access the non-trivial phase with vanishing Chern number. Because the Hall conductivity vanishes, the topological nature of this system must be determined by measuring the edge states, or by directly measuring the winding number from Eq. (3.8), which requires full tomography of the driving cycle. We show that a 2D honeycomb optical lattice for fermions has favourable properties for the direct detection of the edge states.

3.7.1 The Model

It is known that a phase with $W_i = 1$ can be created through periodic modulation of NN hopping parameters either in a bipartite square [40, 127] or in a hexagonal lattice [105]. In optical lattices, the hopping amplitudes in the different directions can be simply tuned by varying the intensities of the lattice beams [135]. However, we propose here a different approach using lattice shaking [81], which has clear experimental advantages. First, the hopping amplitudes can be modulated more effectively, allowing for a full suppression of the undesired hopping amplitudes instead of just a finite anisotropy, which is useful for reasons discussed below. Second, the use of lattice shaking might allow for a cleaner implementation of the step-function-like switching of the hopping amplitudes that is at the origin of the perfectly flat bands we discuss later. Thirdly, lattice shaking couples differently to the higher bands than amplitude modulation of the lattice beams and therefore potentially leads to a smaller heating rate.

The driving protocol takes advantage of the fact that linear shaking of a lattice renormalises the hopping according to the projection of the shaking amplitude onto the bond [32, 81]. Specifically, let the lattice be subjected to a sinusoidal shaking

$$\boldsymbol{F}(t) = \sin(\omega t)\boldsymbol{f},$$

where ω is the shaking frequency, and $\boldsymbol{f}$ a vector determining the shaking direction and amplitude, as depicted in Fig. 3.11. Then, the NN hopping parameters γ in a tight-binding model become renormalised as

$$\gamma \mapsto \gamma_r = \gamma J_0\left(\frac{m\omega \boldsymbol{d}\cdot\boldsymbol{f}}{\hbar}\right). \tag{3.28}$$

Here, $\boldsymbol{d}$ is a vector in the bond direction with magnitude equal to the bond length, m is the particle mass, and J_0 is a Bessel function of the first kind. For

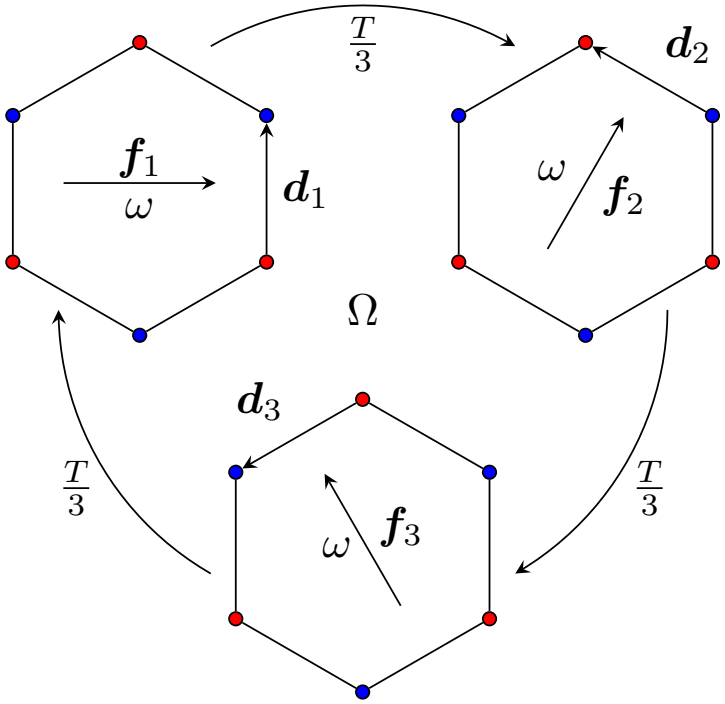

Figure 3.11: A scheme for the driving protocol is shown. The full driving cycle, with frequency Ω, consists of three separate subcycles, which each last for time $T/3$, a third of the full driving period T. In each of these subcycles, the lattice is shaken in the direction of the vector $\boldsymbol{f}_i$ at frequency ω. The shaking along $\boldsymbol{f}_i$ leaves the hopping parameter along the direction $\boldsymbol{d}_i$ unchanged, and may chosen such that it renormalises the hopping along the other two directions to zero. The bond vectors d_i are also indicated in the figure, and the net result of the driving is that an electron hops counter-clockwise along the plaquette [134].

future reference, let us now define x_0 to be the first zero of J_0. The expression in Eq. (3.28) is the first order in a perturbation expansion in terms of the number of exchanged phonons and their frequency [136]. Taking this into account, we start from the NN hopping Hamiltonian for a honeycomb lattice:

$$H(\boldsymbol{k}) = \gamma \sum_l \begin{pmatrix} 0 & \exp(i\boldsymbol{k}\cdot\boldsymbol{d}_l) \\ \exp(-i\boldsymbol{k}\cdot\boldsymbol{d}_l) & 0 \end{pmatrix}. \tag{3.29}$$

The convention $\boldsymbol{d}_1 = a(0,1)$, $\boldsymbol{d}_2 = a\left(-\sqrt{3},1\right)/2$, and $\boldsymbol{d}_3 = -a\left(\sqrt{3},1\right)/2$ is used for the NN hopping vectors $\boldsymbol{d}_l$, where a denotes the NN distance. By shaking in the 2D plane, perpendicularly to a particular bond, $\boldsymbol{d}\cdot\boldsymbol{f} = 0$ for that bond, and $af\cos(\pi/6)$ for the other two bonds. By choosing f and ω in Eq. (3.28) such that

$$mfa\omega\cos(\pi/6)/\hbar = x_0, \tag{3.30}$$

we can suppress two of the three hopping parameters through shaking, leaving the third one unaffected. In principle, it is also possible to aim for higher zeroes of the Bessel function than x_0, but since x_0 yields the smallest value of f for a given ω, convergence of the perturbation expansion is best when using x_0. This procedure yields the three renormalised Hamiltonians

$$H_l(\boldsymbol{k}) = \gamma \begin{pmatrix} 0 & \exp(i\boldsymbol{k}\cdot\boldsymbol{d}_l) \\ \exp(-i\boldsymbol{k}\cdot\boldsymbol{d}_l) & 0 \end{pmatrix}.$$

Finally, we consider the system with Floquet propagator

$$U(\boldsymbol{k}) = \prod_l \exp\left[-\frac{iT}{3\hbar}H_l(\boldsymbol{k})\right], \tag{3.31}$$

where the product is ordered with higher indices to the left. It should be noted that we apply the Floquet theory two consecutive times, first to construct the effective Hamiltonians H_l, and then to obtain Eq. (3.31). Note that we could also have applied Floquet theory only once to the full Hamiltonian with period T and frequency $\Omega := 2\pi/T$. However, by using the intermediate step with the effective Hamiltonians, we are able to derive exact results for the Floquet propagator, such as the phase diagram. We have checked through a numerical calculation of U that the errors induced by this perturbative treatment are negligible if one chooses ω large enough, where the precise meaning of large enough is discussed in Sec. 3.7.3. It is, therefore, the full driving frequency Ω that determines the presence of the driving resonances that will lead to the

Floquet topological phase. In contrast, ω must be large and obey Eq. (3.31) to realise the effective Hamiltonians, which are indeed non-topological. The consecutive application of Floquet theory is only possible if 3ω is a multiple of Ω, since the three individual shaking protocols then fit in the driving cycle in a commensurate way, as depicted in Fig. 3.11. The renormalised hopping in Eq. (3.28) imposes a constraint on $f\omega$, so by tuning the shaking amplitude f, one can achieve a commensurate ω at any desired value of γ_r.

3.7.2 Results

The Floquet propagator in Eq. (3.31) can be calculated in closed form as long as translational symmetry is present in the system. To do so, let us write

$$H_l(\boldsymbol{k}) = \gamma \left[\cos(\boldsymbol{k}\cdot\boldsymbol{d}_l)\sigma_x + \sin(\boldsymbol{k}\cdot\boldsymbol{d}_l)\sigma_y\right]. \tag{3.32}$$

We can define partial propagators

$$U_l(\boldsymbol{k}) \coloneqq \exp\left[-i\frac{T}{3\hbar}H_l\right] = \cos\left(\frac{\gamma T}{3\hbar}\right) - \frac{i}{\gamma}\sin\left(\frac{\gamma T}{3\hbar}\right)H_l(\boldsymbol{k}). \tag{3.33}$$

Here we have made use of the fact that all the eigenvalues of H_l are $\pm\gamma$, independent of $\boldsymbol{k}$, so that $H_l(\boldsymbol{k})/\gamma$ has unit norm on the Bloch sphere. It follows from the definition that $U = U_3U_2U_1$. To evaluate the various cross-terms in this product, we use

$$\frac{1}{\gamma^2}H_m(\boldsymbol{k})H_n(\boldsymbol{k}) = \cos\left[\boldsymbol{k}\cdot(\boldsymbol{d}_m-\boldsymbol{d}_n)\right] + i\sin\left[\boldsymbol{k}\cdot(\boldsymbol{d}_m-\boldsymbol{d}_n)\right]\sigma_z,$$

$$\frac{1}{\gamma^3}H_3(\boldsymbol{k})H_2(\boldsymbol{k})H_1(\boldsymbol{k}) = \sigma_x.$$

The last equality follows because in our convention $\boldsymbol{d}_1 + \boldsymbol{d}_3 = \boldsymbol{d}_2$, which simplifies the product. This allows us to write

$$\begin{aligned} U(\boldsymbol{k}) =& 1\Big[\cos^3(\tau) - \cos(\tau)\sin^2(\tau) \\ &\{\cos\left[\boldsymbol{k}\cdot(\boldsymbol{d}_1-\boldsymbol{d}_2)\right] + \cos\left[\boldsymbol{k}\cdot(\boldsymbol{d}_1-\boldsymbol{d}_3)\right] + \cos\left[\boldsymbol{k}\cdot(\boldsymbol{d}_2-\boldsymbol{d}_3)\right]\}\Big] \\ &+ i\sigma_x\Big\{\sin^3(\tau) \\ &- \cos^2(\tau)\sin(\tau)\left[\cos\left(\boldsymbol{k}\cdot\boldsymbol{d}_1\right) + \cos\left(\boldsymbol{k}\cdot\boldsymbol{d}_2\right) + \cos\left(\boldsymbol{k}\cdot\boldsymbol{d}_3\right)\right]\Big\} \\ &- i\sigma_y\cos^2(\tau)\sin(\tau)\left[\sin\left(\boldsymbol{k}\cdot\boldsymbol{d}_1\right) + \sin\left(\boldsymbol{k}\cdot\boldsymbol{d}_2\right) + \sin\left(\boldsymbol{k}\cdot\boldsymbol{d}_3\right)\right] \\ &- i\sigma_z\Big[\cos(\tau)\sin^2(\tau) \\ &\{\sin\left[\boldsymbol{k}\cdot(\boldsymbol{d}_1-\boldsymbol{d}_2)\right] + \sin\left[\boldsymbol{k}\cdot(\boldsymbol{d}_1-\boldsymbol{d}_3)\right] + \sin\left[\boldsymbol{k}\cdot(\boldsymbol{d}_2-\boldsymbol{d}_3)\right]\}\Big]. \end{aligned} \tag{3.34}$$

Here, $\tau = T\gamma/3\hbar$ is a dimensionless parameter characterising the driving frequency, which is equivalent to specifying Ω in units of γ. The full topological phase diagram can only be obtained by considering the driving cycle leading to this operator through Eq. (3.8). However, some information can already be gleaned from Eq. (3.34). For example, sending $\tau \mapsto \tau + \pi$ maps $U \mapsto -U$, and consequently $H_F \mapsto H_F + \omega/2$. This shows that the bands are exchanged under this transformation, and so are their Chern numbers. The method above can also be used to calculate $U(t, 0)$, from which one can determine W_0 and $W_{\Omega/2}$ to construct the phase diagram. Here, we have used that $U(t, 0)$ has two energy bands, and that the two corresponding gaps lie at $\epsilon = 0$ and $\epsilon = \Omega/2$ by the symmetry of the Hamiltonian in Eq. (5.11). Because of this, one can label the gaps as Δ_0 and $\Delta_{\Omega/2}$, and similarly for the corresponding winding numbers. This phase diagram is 2π periodic in τ, and the first period is depicted in Fig. 3.12. Three phases are visible, all of which are topological due to the presence of a gapless edge mode in at least one gap. In the following, we discuss these phases ϕ_i, $i = 1, 2, 3$.Representative dispersions from these phases are plotted in Figs. 3.13, 3.14 and 3.15, respectively, for a ribbon geometry with zigzag edges.

In Fig. 3.13, we have plotted the dispersion of $\mathfrak{H}$, as defined using Eq. (3.5), for the parameter value $\tau = 6\pi/25$. The spectrum is shown for two periods of the quasi-energy, to illustrate that $W_0 = 1$ (as evidenced by the chiral edge mode), while $W_{\Omega/2} = 0$. Consequently, this phase also has non-vanishing Chern number. By increasing the frequency, the gap around $\Omega/2$ increases in size (because the period of the spectrum increases, but the bandwidth does not), and one reaches a high-frequency regime in which the system is well described by a static Hamiltonian. The phase of this effective static Hamiltonian, with a single edge state between the two bands, is the topological phase of the Haldane model [4].

A situation that is only possible for Floquet systems occurs when one increases τ, i.e. if one lowers the frequency. When the frequency becomes low enough, the energy bands from different periods of the quasi-energy start to overlap, a situation that physically corresponds to the appearance of resonances due to the driving [49]. In this case, one enters the phase ϕ_2, where these driving resonances also cause topological edge states to appear in the gap around $\Omega/2$, as depicted in Fig. 3.14.

The distinguishing feature of phase ϕ_2 is that $W_0 = W_{\Omega/2} = 1$, meaning that the Chern numbers of both bulk bands vanish, while each gap hosts an edge mode. For the specific value of $\tau = \pi/2$ used in Fig. 3.14, the bulk bands of the system are also dispersionless, an interesting feature, since the flat bands

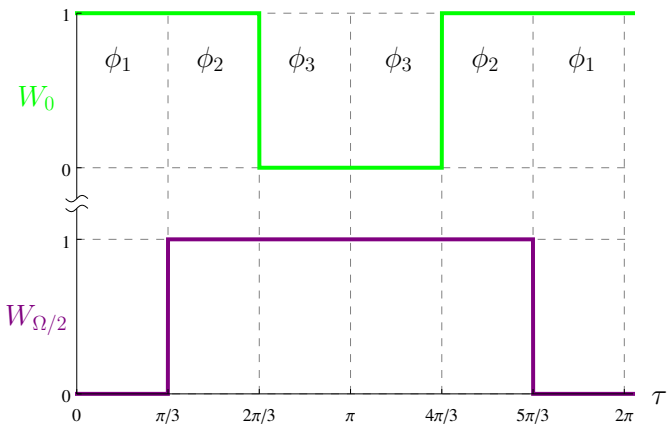

Figure 3.12: The winding numbers W_0 and $W_{\Omega/2}$ are plotted in green and purple, respectively. The different combinations of these two numbers yield three different phases, which are indicated by ϕ_i, for $i = 1, 2, 3$. It should be noted that the gap closes at $\tau = \pi$, so ϕ_3 is not well defined at this point; the gap closing does not change the topological phase, however. The Chern numbers of the bands are given by the difference of the two winding numbers, and therefore take the values 0 and ± 1 [134].

together with vanishing Chern number imply that a localised electron state remains localised under time evolution. Note that in this case, the localisation is not due to Anderson localisation, but due to the driving protocol, making it a different situation from that in Ref. [128]. The non-zero winding numbers associated to the gap are induced by the chiral nature of the driving protocol, and are thus topological. Consequently, this state can only occur in Floquet systems.

The final phase ϕ_3 is obtained by increasing τ further. The appearance of a two photon resonance in the system destroys the topological protection of the edge state in Δ_0, as can be seen in Fig. 3.12, which shows that $W_{\Omega/2} = 1$, while $W_0 = 0$. A respresentative dispersion relation is shown in Fig. 3.15. The winding numbers for ϕ_3 imply that the edge state in Δ_0 is not protected by topology, which is consistent with the fact that it is not chiral.

Being topological, these phases should be robust against various kinds of disorder. Due to our intended application in optical lattices, which are inherently defect free, we omit a detailed discussion of the influence of disorder.

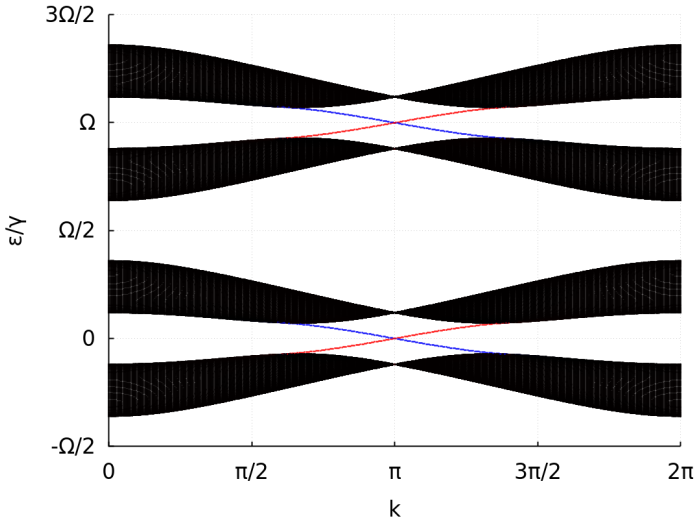

Figure 3.13: The dispersion of the propagator in Eq. (3.31) is shown for a ribbon geometry with zigzag edges for $\tau = 6\pi/25$, so the system is in phase ϕ_1. There are two energy bands indicated in black, separated by gaps Δ_0 and $\Delta_{\Omega/2}$. The blue and red states are localised on the top and bottom edge, respectively. For smaller τ, i.e. larger Ω, the dispersion looks similar, but the gap around $\Omega/2$ becomes larger, so the system behaves more like a static one [134].

It is expected that lattice disorder will not destroy the topological phase if the disorder is small enough compared to the gap size. Rather, in the case of ϕ_2, the disorder will serve to Anderson localise the bulk states, while leaving the edge states intact, demonstrating the special nature of this phase. Of greater interest is the robustness of the phase to the parameters that depend on the driving protocol: the Floquet propagator in Eq. (3.31) is built from effective Floquet Hamiltonians where only one of the NN hopping parameters in the honeycomb lattice is assumed to be non-zero. In general, this will not be precisely true, and one of the hopping parameters will merely be much larger than the others. There are two possibilities: the larger hopping parameter may have the same sign as the two smaller ones, or the opposite sign. In both cases, the qualitative behaviour is the same, as we describe in the following. Firstly, it should be noted that the driving frequencies at which the winding numbers W_i change will differ slightly from those depicted in Fig. 3.12. Nevertheless, the phase ϕ_2 from Fig. 3.14 persists even if the smaller hopping parameters be-

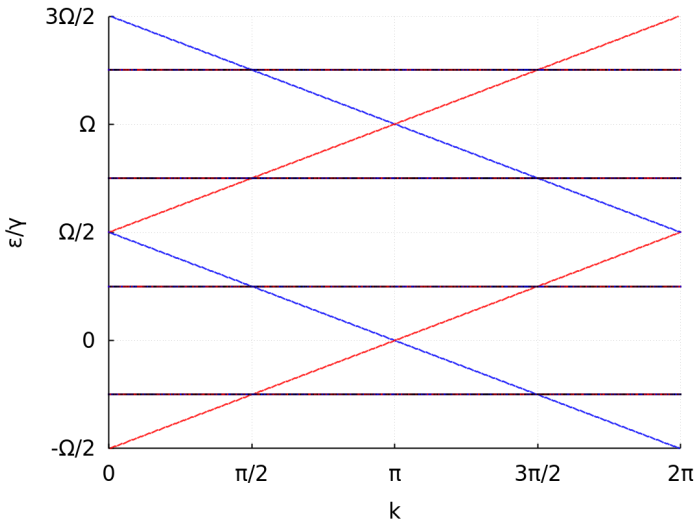

Figure 3.14: Same as in Fig. 3.13, except now the parameter $\tau = \pi/2$, so the system is in phase ϕ_2. By tuning the frequency away from this point, the bulk bands will no longer be flat, but the topological behaviour will be the same [134].

come as large as $\gamma/10$, if one is at the point $\tau = \pi/2$. The larger τ becomes, the larger are the deviations from the ideal case presented in Eq. (3.31), so the allowed uncertainty in the hopping parameters depends on the value of τ that one intends to work with.

A similar discussion can be held with respect to the presence of NNN hopping. Since NNN hopping naturally occurs in honeycomb optical lattices, a treatment of its effects is important to connect with experiments. In the honeycomb lattice, there are six NNN hopping vectors. These have length $\sqrt{3}a$, where a is the NN bond length, as defined previously. Two of these are perpendicular to $\boldsymbol{d}_1$, two to $\boldsymbol{d}_2$, and two to $\boldsymbol{d}_3$. When shaking according to the protocol discussed above, four of the NNN hopping parameters get renormalised to zero, and the two parallel to the shaking pick up a factor $J_0(2x_0) \approx -0.24$. Hence, the shaking protocol has the added benefit of strongly suppressing the NNN hopping contribution. Now, the phase ϕ_2 is accessible when the *renormalised* NNN hopping parameter is smaller than approximately $\gamma/4$. The *bare* NNN hopping strength is dependent on the lattice depth, and below we will consider a value of $4\gamma/100$ [137]. This is clearly within the required range, so

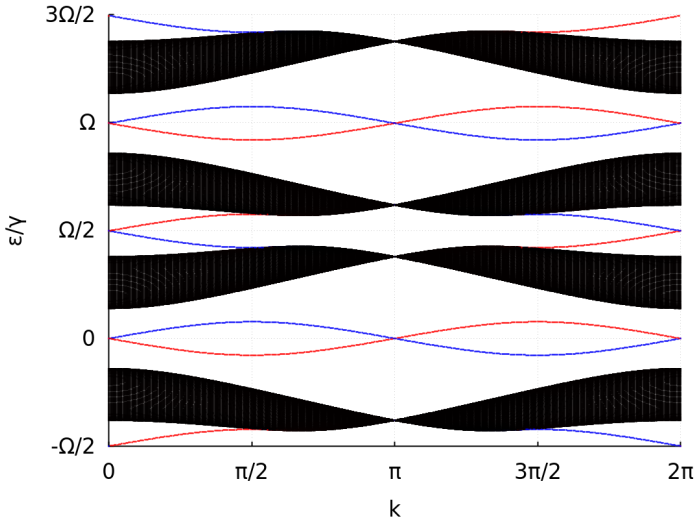

Figure 3.15: Same as in Fig. 3.13, except now the parameter $\tau = 19\pi/25$, so the system is in phase ϕ_3. The dispersion is like a flipped version of that in (a), where the two gaps have been interchanged. The only difference is the presence of trivial edge states in Δ_0 [134].

NNN hopping will not influence the experimental realisability of this phase. It must be noted that in the presence of NNN hopping, the bulk bands are no longer completely flat, but the topological characteristics of the phase remain unchanged.

3.7.3 Experimental Realisation

It should, therefore, be possible to tune the hopping parameters in such a way that the phase ϕ_2, which is characterised by a non-trivial topological structure but vanishing Chern numbers, can be reached. In light of this fact, we will now discuss some possible experimental parameters that might allow the experimental realisation of the phase ϕ_2 in optical lattices.

The condition that the renormalised hopping parameters in Eq. (3.28) vanish imposes a constraint on the shaking amplitude and frequency:

$$J_0\left(mfa\omega\cos(\pi/6)/\hbar\right) = 0.$$

Assuming that one uses the first solution to this equation, one can rewrite it in

terms of the recoil energy $\hbar\pi^2/2ma^2$ as

$$\frac{\omega}{\omega_{rec}} = \frac{4x_0}{\sqrt{3}\pi^2}\frac{a}{f}. \tag{3.35}$$

The recoil energy depends on the particle mass and on the lattice constant, and it is the only parameter in Eq. (3.35) that depends on the atomic species loaded into the lattice. For the realisation of the phase ϕ_2, taking $\tau = \pi/2\mathrm{mod}\pi$ is preferable. As shown in Fig. 3.14, the bands are flattest for this value, which is desirable for the reasons that we discuss below. The highest total frequency for which this holds is $\hbar\Omega = 4\gamma/3$. That Ω is constrained by a maximal value shows that it has to be small enough for resonances in the driving to appear, which is a necessity for the realisation of the phase ϕ_2. From now on, we will assume that $\hbar\Omega$ takes this maximal value, since it corresponds to the shortest time scale for the experiment. Since the two shaking frequencies have to be commensurate, $\omega = 3n\Omega$ for $n \in \mathbb{N}$, which corresponds to a shaking amplitude f given by Eq. (3.35). Because of Eq. (3.35), increasing n requires a lowering of f, but since both parameters can be tuned within a wide range, many possible values can be chosen. For concreteness, we will assume $n = 2$, which corresponds to $\hbar\omega = 8\gamma$. By numerically solving the Schrödinger equation for the full propagator, we have verified that the corresponding values of ω and f are such that the model discussed in Sec. 3.7.2 is accurate. In contrast, choosing $n = 1$ (corresponding to $\hbar\omega = 4\gamma$) would result in notable deviations from the effective model. This gives precise meaning to the claim that the effective model works well if ω is large enough. The NN hopping of fermions in an optical lattice is usually expressed in terms of ω_{rec}, since it naturally incorporates the effect of particle mass and the lattice constant. We consider a lattice depth of $7\omega_{rec}$, which corresponds to $\gamma = \hbar\omega_{rec}/10$, and a NNN hopping of $4\omega_{rec}/1000$ [137]. Using these values for the hopping parameters, and combining these with the chosen value of τ, we find the driving frequency of the system to be $\Omega \approx 4\omega_{rec}/30$, which is about $0.13\omega_{rec}$.

We can obtain specific numbers by choosing a particle mass and an optical wavelength, which allows us to specify a and ω_{rec}. Let us consider fermionic ^{40}K loaded in a honeycomb optical lattice with wavelength $\lambda = 1064\mathrm{nm}$, which amounts to a recoil frequency $\omega_{rec}/2\pi = 4.41\mathrm{kHz}$, and consequently, the minimal driving period $T = 1.7\mathrm{ms}$. The minimal commensurate shaking frequency ω is then $0.4\omega_{rec}/2\pi \approx 1.76\mathrm{kHz}$, which corresponds to a maximal shaking amplitude of $0.075a$. Since the lattice constant is $2\lambda/3$ for a honeycomb lattice, the maximum shaking amplitude $f \approx 53\mathrm{nm}$.

As mentioned earlier, the same phase can be obtained for a variety of parameters. For instance, the frequency ω can be chosen to be any multiple of $0.4\omega_{rec}$, as might be desired to minimise coupling to other bands in the lattice. The shaking amplitude will then be the corresponding fraction of $53\mathrm{nm}$. Furthermore, due to the periodicity of the phase diagram, the phase ϕ_2 can also be realised most generally if $(2n+1)\hbar\Omega = 4\gamma/3$. Choosing $n > 0$ allows one to use a lower Ω, and a correspondingly lower ω.

The distinguishing feature of the phase ϕ_2 is the presence of edge states, while there is neither time-reversal symmetry, nor a non-vanishing Chern number. The Chern number can be measured in terms of the Hall conductivity, which has been achieved in optical lattices [85], so one can experimentally prove that the Chern number vanishes in this topological phase. There are, nevertheless, edge modes present in the system, protected by the topological nature of the winding numbers associated to the quasi-energy gaps in the system.

The contribution to the transverse conductivity from a fully filled band is given by its Chern number. The fact that the phase ϕ_2 is dynamic in origin does not alter this conclusion. The total wavefunction corresponding to a single occupied energy band of the Floquet propagator is time dependent, returning to itself only after each period T, but this time evolution is unitary. The Chern number, because it is a topological invariant, is invariant under unitary transformations, so the Hall conductivity is constantly zero.

It is, therefore, necessary to detect the topological phase in a different way. One alternative would be to directly detect the edge states to prove the presence of a topological phase in the system. The principal difficulty in 2D systems is the presence of dispersive bulk bands, together with the fact that the edge mode is not present for all k. For this reason, an atom inserted at the edge of a system will have an overlap with the bulk modes, since a localised state has equal overlap with all momenta. If the bulk is dispersive, this overlap will cause the atomic wavefunction to partially leak away into the bulk, making a measurement of the edge state difficult at longer timescales. As can be seen in fig. 3.14, for certain parameter values the bulk is dispersionless, while the edge states exist for nearly all k-values. This makes the currently proposed system conducive to the direct measurement of topological edge states.

To make the behaviour of edge states in this system explicit, we have shown the time evolution of one such state in Fig. 3.16. To make a connection with experiments, we have taken the system discussed in Sec. 3.7.2, and included the NNN hopping of $\gamma/10$ that is present in an actual system. Because this term gives the dominant deviation from the phase in Fig. 3.14, we assume

that all other parameters have exactly the right values. To simulate a realistic edge, we have included a potential step of height 10γ, along the line $\mathrm{y} = 0$. This cuts the system into two domains separated by zigzag edges along the potential step. Such sharp steps have been realised in quantum gas microscopes [138], and provide a promising approach to generate a topological boundary mode experimentally. To show that this indeed leads to well-defined edge states, we have plotted the wavefunction at different times to show its localisation along the domain wall. The initial state has a constant non-vanishing amplitude for 3 unit cells along the wall at $\mathrm{y} = 1$ and $\mathrm{y} = 2$, as shown in the leftmost frame of Fig. 3.16. The time-evolution indicates that the part of the wavefunction located on the A sites of the edge (the tips of the zigzag, at $\mathrm{y} = 1$) stay localised there with a probability of approximately 90%, while the part of the wavefunction at $\mathrm{y} > 1$ slowly disperses into the bulk. It should be noted that this feature is only topologically protected in the limit of infinite step size, which splits the system into two. For such an infinite step, the system has a protected edge mode on either side of the step, and they counterpropagate (one is the top edge of one system, and the other the bottom edge of the other system). For a finite step size, there will be a small hybridisation between these two states, and the feature is not topologically protected anymore. This hybridisation causes some leaking of the wavefunction to the other side of the step, which causes the bidirectional movement that can be seen in Fig. 3.16. This bidirectional movement takes place on opposite sides of the potential step, and is suppressed with increasing step size. Nevertheless, if the system were not topological, one would not see the clear propagation along the potential step, but only the diffusive behaviour into the bulk. Note that the dispersion into the bulk is due to the NNN hopping, because at $\tau = \pi/2$ the bulk bands are completely flat in its absence, as shown in Fig. 3.14. Since the bulk is only weakly dispersive, the edge states have a higher group velocity, and the edge part of the wavefunction clearly separates from the bulk part. This shows that the combination of very flat bulk bands with edge states that exist for most k values ensures that the edge and bulk parts of a wavefunction can be clearly separated from the dynamics.

Instead of detecting the edge state directly, an alternative experimental approach would be to obtain the bulk winding number in Eq. (3.8), which dictates the presence of edge states. The newly developed state tomography [139] yields full access to the time-dependent bulk Bloch states. By reconstructing both the Chern number of the effective Floquet Hamiltonian obtained from the stroboscopic time steps and the winding number obtained from the full time-dependent state, one can experimentally disentangle the two topological indices.

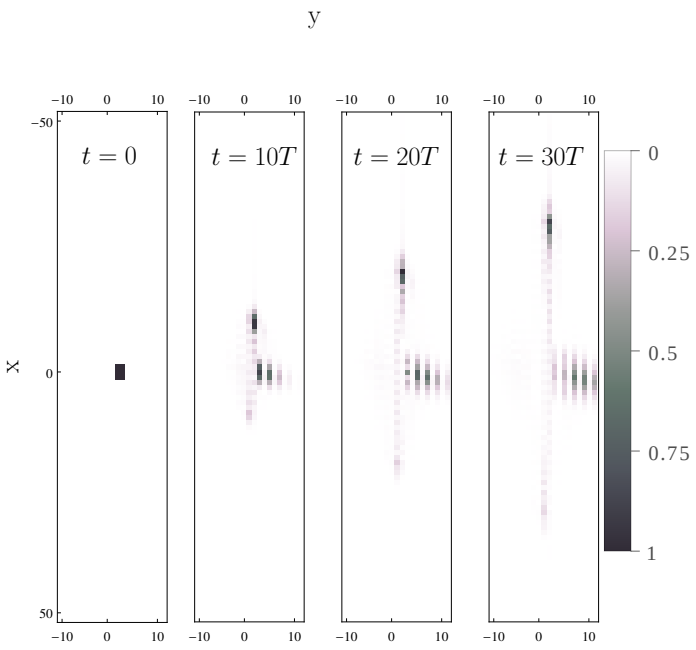

Figure 3.16: The probability density is depicted at 4 different times for a system with a sharp potential wall of height 10γ, for $\tau = \pi/2$ and a *bare* NNN hopping of $\gamma/10$, which corresponds to the parameter values discussed in the text. The coordinates x, y label sites of the lattice using the lattice vectors. The lattice vector associated with x lies parallel to the wall, meaning that x is periodic, while the vector associated to y points away from the wall. It should be noted that y is also used to label sublattice, so that $\mathrm{y} = \pm 1$ are the A-sites adjacent to the wall, $\mathrm{y} = \pm 2$ are the B-sites adjacent to the wall, etc. The parameter ranges are $\mathrm{x} \in (-200, 200]$ and $\mathrm{y} \in [-100, 100]$ (meaning 50 unit cells on either side), but due to the localisation of the wavefunction, only part of the system is shown.

Several models that exhibit such a Floquet topological phase have been proposed [40, 105, 127, 128], and an experimental realisation with cold atoms would be desirable. We propose a simple shaking protocol for a honeycomb optical lattice that allows for an experimental realisation of the model considered in Ref. [105], and we discuss possible experimental advantages of this approach. Because Chern numbers have been measured in 2D Floquet optical lattices [84, 85, 139], it is experimentally possible to show the vanishing of the Hall conductivity in this phase. The direct detection of topological edge states in optical lattices remains an experimental challenge: so far, edge states have only been experimentally observed in 1D systems [140], ladder systems [138, 141] or artificial dimensions [142, 143]. However, promising proposals for their detection in 2D systems exist using either Raman spectroscopy [144] or the different dynamics of the bulk and edge states after a removal of a barrier [145]. Detection methods involving sharp walls are especially promising for the system under discussion. By tuning the parameters, it is possible to make the bulk bands nearly flat, ensuring that the wavefunction of an electron injected at such a wall has minimal leakage into the bulk.

Beyond the scenario of edges induced by sharp walls, a promising direction are interfaces between regions of different topology induced by spatially varying lattice parameters [127, 146]. This scenario could apply to our proposal because the phase transitions are controlled by the shaking frequency relative to a resonance that depends on the spatially varying lattice depth.

Alternatively, recent advances in state tomography [139] could allow for a direct measurement of the winding number in Eq. (3.8). Since such a measurement has not been performed in photonic systems, this possibility allows for optical lattices to provide additional insight into the topological structure of matter. Together, these properties might make the present proposal a promising candidate for the experimental realisation and detection of a Floquet topological phase that has no static counterpart.

3.8 Conclusion

We have seen in this chapter what the Floquet theory is, and how it can be used to describe periodically driven systems. It has been explained how we currently look at the topological classification of Floquet systems. While much is still unknown, a comparison with Chap. 1 shows that there has been much improvement in the past few years. Specifically, an exhaustive classification of the topological structure in 2 + 1D is now possible.

The discovery of a great number of specific topological Floquet systems has helped to develop an intuition for what causes the different topological behaviour in out of equilibrium systems. This mostly holds true for systems without time-reversal symmetry, as the discussion in this chapter shows, but knowledge about other symmetry classes is growing [48, 106].

Without time-reversal symmetry, the possible Floquet topological phases are characterised by a winding number W_i associated to each gap Δ_i, allowing for an extra topological degree of freedom with respect to the undriven case, due to periodicity of the spectrum. If the driving amplitude is not too large, and the frequency not too low, the topological behaviour of these Floquet systems can be understood in terms of the appearance of driving resonances, leading to a band-inversion picture similar to the static case. Interestingly, Floquet systems allow for a curious topological phase, which is characterised by vanishing Chern numbers for all bands, but exhibits topologically protected edge states. Due to the vanishing Chern number, there is no Hall conductivity in the bulk, and the bulk electrons can localise. This has a surprising consequence for Laughlin's charge pumping argument [72]. Since there is no Hall conductivity present in the system, threading a flux through it, or briefly turning on an electric field, will not pump charge across the system. This can be seen from the spectrum in Fig. 3.14: the topological edge modes form a closed loop, which is only possible due to the branch cut. Threading a flux through the system merely moves electrons through the loop, but they never move into the bulk. This goes to show that the anomaly picture introduced in Chap. 2 does not fully describe the topology of periodically driven systems, and this road will probably not allow for a classification of interacting Floquet topological phases. Needless to say, despite the considerable progress over the past years, there is much that remains to be done.

CHAPTER 4

Geometrical effects

In Chap. 2, we gave a brief history of the notion of SPTO, and we discussed how one might go about classifying these different topological orders. Although we did discuss the breaking of translational symmetry through the addition of disorder, or by making a single dimension of the system finite (in order to see the appearance of edge modes), translational symmetry played a major role in the discussion. An implicit assumption underlying the entire discussion is that the geometry of the sample is in some sense trivial.

This sense of trivial geometry can be taken to mean at least two things. One can consider it to mean flat in the Riemannian sense, and one can take it to mean trivial in some topological sense, like orientability for example. We will also treat curved 2D p-wave superconductors in this Chapter, since they interact with curvature in interesting ways. However, my focus will be on the topological aspects of the system geometry. To see why this is the most promising aspect of geometry to look at, recall that SPTO is also a topological effect. Now, this is more than just a piece of semantics: by its very nature, SPTO is independent of the microscopic aspects of a system, as long as one does not close any band gaps. Specifically, changing details such as the curvature of a system might lead to interesting effects, and though they can be connected to the topological phase of the system, they cannot influence this phase. In contrast, changing the geometry of the system at the topological level might cause the topological nature of the system to also change.

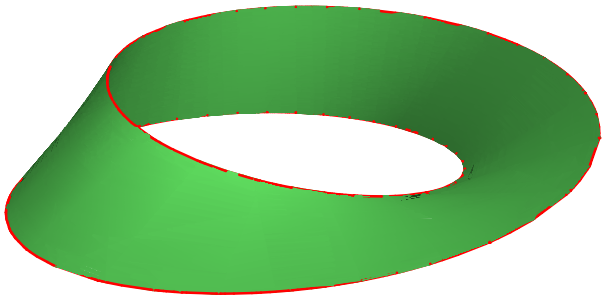

Figure 4.1: A picture of a Möbius band embedded in 3D space.

To illustrate this effect, we will mostly discuss the Möbius band (Fig. 4.1), since it is a convenient system for many reasons. For one, it is a non-orientable surface, meaning that it has only a single side. However, it still exhibits a translational symmetry, which makes it possible to define dispersion relations, allowing for a neat comparison with cylindrical systems. Additionally, the topological classification on the Möbius band can be exhaustively performed, allowing for a complete treatment of the system. Finally, the properties of condensed-matter systems with a Möbius geometry have attracted increasing interest in the past few years. This is because the Möbius band is not as simple as it might seem at first sight. For example, an embedding of the band in 3-space that minimises the deformation of the surface can only be found by numerically solving the relevant differential equations [147]. The problem can also be tackled at the quantum level through the use of density-functional theory calculations [148]. The twist induced by this spatial orientation has been shown to generate an effective gauge field in the system [149]. In the case of graphene, the electronic [148, 150–155], magnetic [156, 157], and thermal [158] properties of Möbius bands have been investigated theoretically. Similar studies have been performed for boron nitride ribbons [159]. Both graphene and boron nitride have hexagonal lattices, and investigation of these materials coincides with the recent popularity of carbon nanotubes. The experimental realisation of Möbius bands in the lab has proven difficult as of yet, but important progress has been made: Möbius bands made of $NbSe_3$ have been fabricated [160]. In addition, in the field of optical lattices, there is a re-

cent proposal for such a realisation through the use of synthetic dimensions, in which internal atomic degrees of freedom play the role of additional space dimensions [161]. By creating twisted boundary conditions in the internal degree of freedom, an artificial Möbius band could be constructed.

4.1 The Möbius band and its topological properties

In this section, we will discuss what the Möbius band is in detail, what constraints its geometry puts on the kind of lattices that one can define on it, and what its topological classification is. As an example, we will discuss the QHE and the QSHE in these systems. These results can mostly be found in Ref. [53]. Dr. Beugeling performed the calculations in this paper, but I have independently verified all the calculations appearing there, and the idea for the topological classification is mine. Prof. Dr. Morais Smith supervised the project.

A Möbius band, as depicted in Fig. 4.1, can be obtained from a rectangle by gluing together two of the opposite edges. In the language of point set topology, one puts an equivalence relation (identifying points on the space) on the rectangle [162]. Pictorially, what is happening can be seen in Fig. 4.2(a).

There, a rectangle is shown, and the left and right edges have arrows on them, indicating that one should identify the edges along the direction of the arrow. If both arrows had pointed the same way, one would have obtained a cylinder of length W and circumference L. In the case shown in Fig. 4.2(a), the arrows point the opposite way, indicating that one has to twist the rectangle before gluing in order to obtain the surface shown in Fig. 4.1. Because in the Möbius band edges are identified in opposite directions, it is not orientable. This can be easily seen in Fig. 4.2(a). An object that exits the rectangle on the right enters it on the left, but it will be reflected in the x-axis. The reflection changes the parity of space, and therefore such a parity cannot be chosen in a continuous manner at every point of the band (see Ref. [163] for additional details on orientability). If one considers the Möbius band as a surface in $\mathbb{R}^3$, such a continuous definition of parity is equivalent to a choice of continuous unit normal. That a continuous unit normal cannot be chosen may be promptly seen in Fig. 4.1. If one chooses such a unit normal at a single point, and transports it around the band in a continuous manner exactly once, it will point in the opposite direction in the end.

One can tackle a variety of problems most easily by considering the orientable double cover (ODC) of the Möbius band (a general definition can once again be found in Ref. [163]). Roughly speaking, the ODC is an orientable

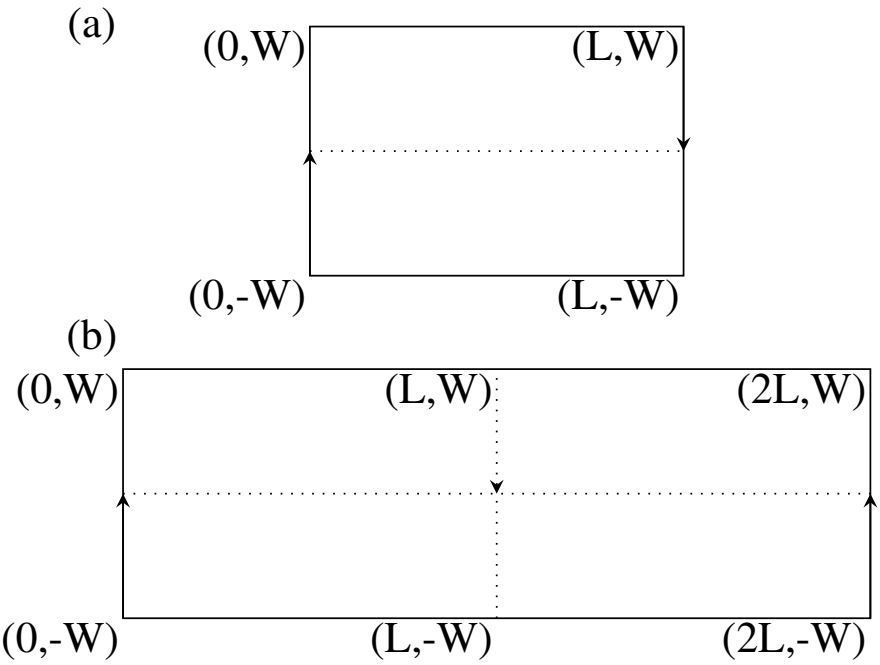

Figure 4.2: (a) The Möbius band of circumference L and width $2W$, shown as a rectangle of length L with vertical edges identified. The identification is such that the arrows point in the same direction, inducing the characteristic twist in the surface. The horizontal dotted line shows the center of the band, which is topologically a circle. (b) The double cover of the Möbius band, shown as a rectangle of length $2L$ and width $2W$. The two vertical edges should be identified in the direction of the arrows to obtain the cylinder. The vertical dotted line with arrow indicates where the two copies of the Möbius band lie inside the double cover. Applying a glide reflection $(x, y) \mapsto (x + L, -y)$ merges the two copies of the Möbius band.

surface that contains the original surface (in this case the Möbius band) twice. For the Möbius band, the ODC is just the cylinder. It is shown schematically as a gluing diagram in Fig. 4.2(b), together with the two Möbius bands lying inside it. The double cover is depicted as a surface embedded in $\mathbb{R}^3$ in Fig. 4.3.

Since the cylinder is a simple object, all calculations can be easily done in this case. What remains is to determine how to link the two. Looking at

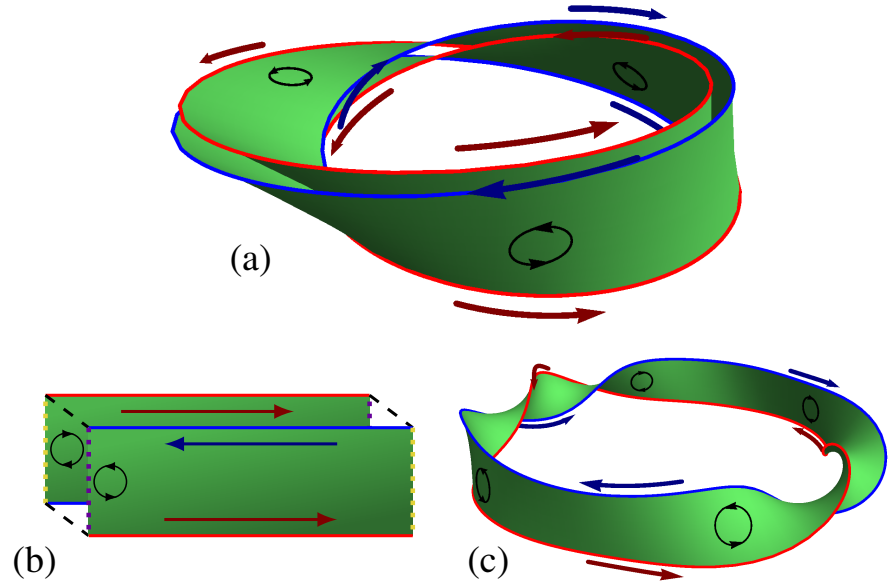

Figure 4.3: Various depictions of the ODC of the Möbius band are shown. The circling arrows indicate a particular choice of orientation for the ODC. The edges are coloured in red and blue, and the arrows indicate the induced orientation on the edge. (a) Here, it can be seen that the ODC contains the Möbius band twice, as evidenced by the double layer. The layers have opposite orientation, since the arrows at the edge point the opposite way, and so do the arrows in the bulk. This shows that gluing the two layers together into a single band destroys the orientability. (b) What happens when one makes a single transverse cut through the ODC from (a). The two sheets with opposite orientation are visible. (c) The double cover is homeomorphic to the cylinder with a 4π twist, and by unfolding the ODC from (a), this is the result. This version is most easily compared with Fig. 4.2(b), though the gluing diagram does not capture the twist [53].

Fig. 4.2(b), one can see that the Möbius band of length L can be obtained from the cylinder of length $2L$ (its ODC) by identifying points differing by a glide-reflection

$$R : (x, y) \mapsto (x + L, -y). \tag{4.1}$$

If one identifies points differing by an application of R in Fig. 4.2(b), or quotients out R in mathematical terms, the right half of the ODC collapses onto the left, and one identifies the dotted center line with the left edge along the arrows; this yields the Möbius band. Quotienting out R corresponds to collapsing the two layers of the ODC in Fig. 4.3(a).

The above discussion demonstrates that the Möbius band can be obtained from a cylinder through the glide reflection, and because the ODC is topologically unique, the reverse is also true. One can use this correspondence to map a quantum system on the Möbius band to a cylindrical system with R-symmetry and vice versa. Specifically, given a Hamiltonian H_M on the Möbius band, it can be uniquely extended to a Hamiltonian H_C on the cylinder by demanding that $[R, H_C] = 0$. The reverse operation consists of quotienting out the Hilbert space by R. It is this property that makes it possible to relate the eigenfunctions of H_M to those of H_C.

Let ϕ be an eigenfunction of H_C on the ODC. Using $R^2 = 1$ (The action of R on the spin part of a state is only determined up to a phase, but can be consistently put equal to 1 [164]), one obtains even and odd eigenfunctions of R:

$$\begin{aligned} \phi_+ &:= \frac{1}{\sqrt{2}}(\phi + R\phi) \\ \phi_- &:= \frac{1}{\sqrt{2}}(\phi - R\phi). \end{aligned} \tag{4.2}$$

Since $[R, H_C] = 0$ by hypothesis, the $\phi_\pm$ are still eigenfunctions of H_C, showing that the eigenspaces of H_C can be decomposed into even and odd pairs. The function ϕ_+, being invariant under R, correctly defines a function on the Möbius band by quotienting out R, and is an eigenfunction of H_M. Once again, the reverse also holds, showing that the Hilbert space of the Möbius band is the even part of the ODC Hilbert space. Furthermore, the spectrum of H_M is just that of H_C, but with the degrees of freedom halved. Note that in the case of electrons, R reverses spin, so that the ϕ_+ in Eq. 4.2 mixes the spin degree of freedom. This is to be expected because the Möbius band is non-orientable, the direction of spin-up cannot be defined continuously, and such spin-mixing is unavoidable.

4.1.1 Constraints on the lattice and Hamiltonian terms

The above way of constructing systems on a Möbius band from cylindrical ones with a certain symmetry turns out to be a useful method. In particular, it can be used to analyse the kind of 2D lattices that can be consistently shaped into a Möbius band without introducting lattice defects. Considering the spatial part of R, the constraint $[R, H_C] = 0$ implies that the lattice is symmetric under the glide reflection.

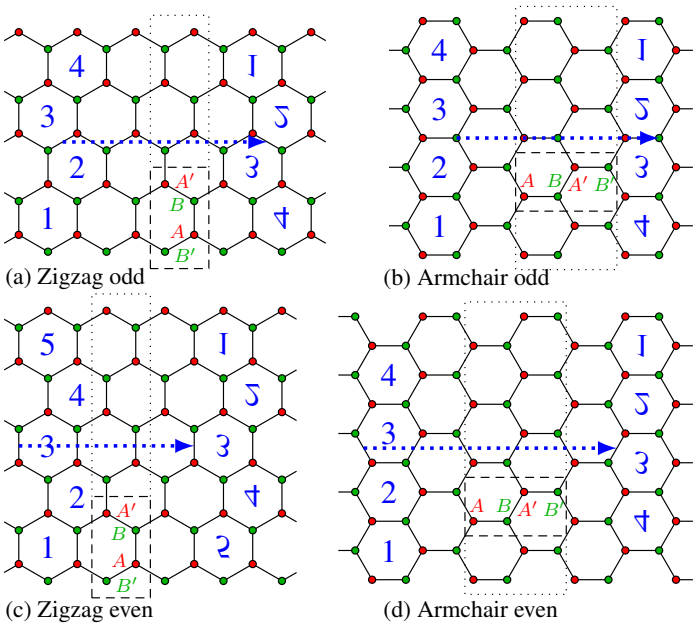

Figure 4.4: Construction of honeycomb Möbius bands using the glide reflection. The left and right edge are identified such that the blue numbers on the left- and right-hand sides coincide. This construction is possible due to the invariance under the glide reflection, with a translation indicated by the dotted arrow and the reflection perpendicular to this arrow. The dashed rectangle indicates a bulk unit cell with the four sublattice labels. The dotted rectangle is a ribbon unit cell. The four panels show zigzag and armchair, with even and odd widths [53].

We will discuss the honeycomb lattice as a first example. In Fig. 4.4, zigzag-edge and armchair-edge ribbons with different widths can be seen, together with glide reflection used to quotient the lattice into a Möbius band. The

reflection part of the glide reflection dictates that the elementary (bulk) unit cell is rectangular. The lattice vectors are parallel to the coordinate axes and hence perpendicular to each other. For both the zigzag and the armchair bands, it is therefore necessary to choose a unit cell with four sites. In comparison, for the cylindrical case, the lattice vectors need not be perpendicular, and can therefore be described with a two-site unit cell in the zigzag-edged case [116, 165]. It is interesting to note that both edge terminations support two inequivalent ways of quotienting the lattice, as is shown in Fig. 4.4. These two inequivalent lattices differ in whether they have an integer or half-integer number of unit cells along the transverse direction, and we will label them even and odd. These labels refer to the number of A and B sites in the transverse direction, being $2w$ and $2w - 1$ in the even and odd case, respectively, where w is an integer that denotes the width of the ribbon. (The total number of sites in the transverse direction is $4w$ and $4w - 2$ respectively.) Numbering the bulk unit cells $i = 1, \ldots, w$ from top to bottom (where there is only half a unit cell for $i = w$ in the odd case), the quotient operation induced by the glide reflection R can be characterized as

$$\begin{aligned}
&(A_i, B_i, A'_i, B'_i) \leftrightarrow (B_{\bar{i}}, A_{\bar{i}}, B'_{\bar{i}}, A'_{\bar{i}}) && \text{(zigzag, even)} \\
&(A_i, B_i, A'_i, B'_i) \leftrightarrow (B'_{\bar{i}}, A'_{\bar{i}-1}, B_{\bar{i}-1}, A_{\bar{i}}) && \text{(zigzag, odd)} \\
&(A_i, B_i, A'_i, B'_i) \leftrightarrow (A'_{\bar{i}}, B'_{\bar{i}}, A_{\bar{i}}, B_{\bar{i}}) && \text{(armchair, even)} \\
&(A_i, B_i, A'_i, B'_i) \leftrightarrow (A_{\bar{i}}, B_{\bar{i}}, A'_{\bar{i}-1}, B'_{\bar{i}-1}) && \text{(armchair, odd)}
\end{aligned} \tag{4.3}$$

where (A_i, B_i, A'_i, B'_i) denote the four sites of unit cell i, and $\bar{i}$ is shorthand for $w + 1 - i$. Note the differences in the invariance of the sublattice labeling. The four possible actions of the glide reflection are generated by the exchanges $(A, A') \leftrightarrow (B, B')$ and $(A, B) \leftrightarrow (A', B')$, forming a $\mathbb{Z}_2 \times \mathbb{Z}_2$ group structure. The transformation $(A, B) \leftrightarrow (A', B')$ preserves the color of the sites, where the pairs (A, A') and (B, B') each have a single color (see Fig. 4.4). The reflection is color preserving for the armchair and color inverting for the zigzag case.

This discussion also applies to other lattice structures known for showing topological effects, e.g. the dice [166], Lieb [167, 168], and kagome [169] lattices, see Fig. 4.5. These examples all have three atoms per unit cell in the bulk lattice. The dice lattice could be considered a honeycomb lattice with one extra site in each unit cell. For the Möbius band, a six-site unit cell must be taken, but the action of the glide reflection on the sublattice structure is analogous to that of the honeycomb lattice. The Lieb lattice has two inequivalent symmetry axes at a $45°$ angle. The Möbius band with a straight edge requires

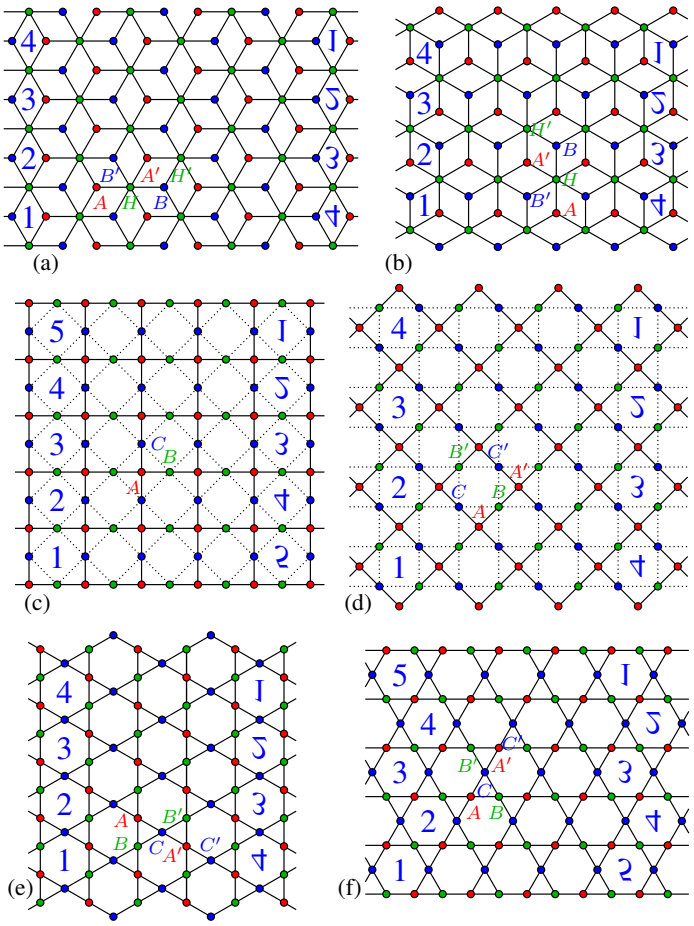

Figure 4.5: (a,b) The dice lattice. (c,d) The Lieb lattice. (e,f) The kagome lattice. The letter labels indicate a possible choice of the unit cell with sublattice labeling. The dotted lines indicate the NNN coupling. The numbers on the left and right of each lattice indicate how a strip with this lattice structure should be quotiented into a Möbius band: The quotient operation is such that the corresponding number symbols on the left and right edges coincide [53].

only three sites per unit cell, whereas the one with a zigzag edge requires six (see Figs. 4.5(c) and (d), respectively). The Kagome lattice has the peculiarity that there is no colour preserving glide reflection. In other words, the kagome lattice is chiral: The left-handed and right-handed version cannot be mapped onto each other by translation and rotation.

We will now discuss several terms that are commonly present in the Hamiltonians of fermionic systems. First, ordinary NN hopping in absence of a magnetic field is invariant under a glide reflection and can therefore appear in the tight-binding Hamiltonian for the Möbius band. If the hopping would be subject to a magnetic flux through the lattice, the Peierls substitution dictates that it would pick up complex phase factors $\mathrm{e}^{\mathrm{i}\theta_{jk}}$, as

$$H_{\mathrm{NN}} = -t \sum_{\langle j,k \rangle} \mathrm{e}^{\mathrm{i}\theta_{jk}} c_j^\dagger c_k, \tag{4.4}$$

where the sum is over nearest-neighbour sites j and k, t is the hopping amplitude, and c_i ($c_i^\dagger$) denotes the annihilation (creation) operator on site i. The glide reflection leaves θ_{jk} invariant. The reflection does invert rotational sense, i.e., it transforms clockwise to counterclockwise rotation and vice versa, so that the flux through a loop, given as the sum of the hopping phases in counterclockwise direction, flips its sign. Configurations where $B_z(-y) = -B_z(y)$ are possible by choosing $\theta_{j'k'} = \theta_{jk}$, where the reflection maps sites j and k onto j' and k', respectively.

The Zeeman term $H_{\mathrm{Z}} = -t_{\mathrm{Z}} \sum c_j^\dagger \sigma_z c_k$ anticommutes with R, since reflection flips spin, and is therefore not allowed on the Möbius band. Alternatively, one could argue that the Zeeman term requires a global, continuous definition of spin up and down, which does not exist due to lack of orientability. This problem vanishes if one considers spin to be defined in an ambient 3D space containing the Möbius band, so it does not couple to R.

A staggered sublattice potential, as used by Kane and Mele [7], can be applied only if it is compatible with the glide reflection properties, which happens precisely if R is colour preserving. For honeycomb ribbons, this property is satisfied only for the armchair configuration, as shown by Eq. (4.3).

The spin-orbit terms are characterized by a coupling between the spin degrees of freedom and the momentum of the charge carriers. The Rashba SO

term on a lattice can be written as

$$\begin{aligned} H_{\mathrm{R}} &= -\mathrm{i}t_{\mathrm{R}} \sum_{\langle j,k\rangle} c_j^\dagger (\sigma_x d_{jk}^y - \sigma_y d_{jk}^x) c_k \\ &= t_{\mathrm{R}} \sum_{\langle j,k\rangle} \left[c_{j,\uparrow}^\dagger (d_{jk}^x - \mathrm{i}d_{jk}^y) c_{k,\downarrow} + c_{j,\downarrow}^\dagger (d_{jk}^x + \mathrm{i}d_{jk}^y) c_{k,\uparrow} \right], \end{aligned} \tag{4.5}$$

where (d_{jk}^x, d_{jk}^y) denotes the vector from site j to k, and $c_k = (c_{k,\uparrow}, c_{k,\downarrow})$ is a spinor. The latter form of H_{R} in Eq. (4.5) shows the invariance under the combined glide reflection [which acts as $(d^x, d^y) \mapsto (d^x, -d^y)$] and spin flip. The ISO coupling acts as a NNN hopping term which we also used in Eq. (3.13),

$$\begin{aligned} H_{\mathrm{I}} &= -\mathrm{i}t_{\mathrm{I}} \sum_{\langle\langle j,k\rangle\rangle} \nu_{jk} c_j^\dagger \sigma_z c_k \\ &= -\mathrm{i}t_{\mathrm{I}} \sum_{\langle\langle j,k\rangle\rangle} \nu_{jk} (c_{j,\uparrow}^\dagger c_{k,\uparrow} - c_{j,\downarrow}^\dagger c_{k,\downarrow}), \end{aligned} \tag{4.6}$$

where ν_{jk} is the sign of $d_{jl}^x d_{lk}^y - d_{jl}^y d_{lk}^x$ with (d_{jl}^x, d_{jl}^y) and (d_{lk}^x, d_{lk}^y) the nearest-neighbor vectors that connect sites j and k via an intermediate site l. Furthermore, the $\langle\langle ... \rangle\rangle$ denote a sum over NNN. The invariance of this term follows from the fact that ν_{jk} changes sign under reflection, while spin flip also acts as a sign change. Consequently, both the Rashba and ISO coupling terms are allowed to appear in the tight-binding Hamiltonian on the Möbius band.

4.1.2 Topological phases on a Möbius system

Since the Hilbert space of states on a Möbius band simply consists of the R-equivariant states on its ODC, it is possible to classify the various topological phases it allows. In the case of a cylinder, the topological classification is simply given by the ten-fold way (see Chapter 2 and Appendix A). For the Möbius band, one performs this classification for the cylinder, but adds in each case the glide-reflection as a symmetry. In principle, planar lattices that have such a symmetry exist as well, leading to crystalline topological insulators [52, 170]. For these systems, edge modes protected by a crystal symmetry exist. However, crystal symmetry is not robust against lattice deformations; for the Möbius band, this symmetry is hard-coded in the topology of the Möbius band. In Ref. [50], this classification is performed using the method of minimal Dirac Hamiltonians. Chiu et al. consider the symmetries of the ten-fold way, and add a spatial symmetry R obeying $R^2 = 1$. For the various possible commutation relations R can have with the remaining symmetries, they classify

the possible equivariant Bloch bundles at the physical level of rigour. Clearly, the glide reflection considered here fits in this scheme.

We will continue by discussing the realisation of a QHE and a QSHE on the Möbius band, making the relevant symmetry classes those without symmetry and those with only time reversal. In the absence of symmetry all phases are trivial. It is easily checked that the glide reflection from Eq. 4.1 anti-commutes with time-reversal, yielding a $\mathbb{Z}_2$ classification in that case. This proves that no QHE is possible on a Möbius band, but an analogue of the QSHE does exist. A geometric reasoning to this effect follows.

As discussed in Chapter 2, the QHE typically arises in 2D electron gases subjected to a perpendicular magnetic field. Its hallmark is that the Hall conductance σ_{xy}, defined by the in-plane current response to a perpendicular (in-plane) voltage, is quantized in units of e^2/h. The integer prefactor is given by the Chern number. Both in experimental and theoretical analysis, the Hall measurement is generally performed on an orientable two-dimensional surface, such as a rectangle or a cylinder. These surfaces allow one to choose a single globally defined orientation. This choice fixes the sign of the Hall conductivity, which is therefore a well-defined quantity.

A nonorientable surface like the Möbius band does not admit a globally defined orientation. Orientations can be chosen locally, but it is not possible to connect them continuously on the whole surface. For any observable quantity to be well-defined on the Möbius band, it must be independent of the choice of orientation, i.e. invariant under a change of orientation. One tests this property by verifying its behaviour under R, since the glide reflection reverses orientation. Parity-odd quantities do not have an unambiguous definition: they change sign under a change of orientation, and thus they are orientation dependent.

The Hall conductance σ_{xy}, defined by $J_x = \sigma_{xy}E_y$ and $J_y = -\sigma_{xy}E_x$, where J and E are the current density and electric field, respectively, and the subscripts x and y label the components, is *not* invariant under a parity transformation of space: this transformation inverts the sign of σ_{xy}. Thus, the Hall conductance is ill-defined on the Möbius band. The Chern number, that is closely related to the Hall conductivity, shares this property. It is defined as the integral of the Berry curvature, which in turn is the curvature of the Berry connection. The definition of integration over differential forms requires a choice of orientation, so that the definition is ambiguous on a non-orientable surface.

A similar reasoning may be used for the perpendicular magnetic field that conventionally generates the QH effect. The magnetic field is a pseudovector, meaning that it changes sign under a parity transformation. As a consequence, one cannot apply a uniform perpendicular magnetic field to a Möbius band. It

remains possible to apply non-uniform magnetic fields, i.e., fields that depend on the spatial coordinates. Two such possibilities are shown in Fig. 4.6.

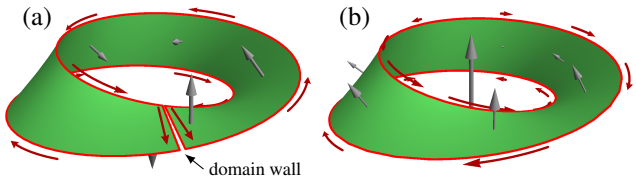

Figure 4.6: Two configurations of the Möbius band with magnetic fields (gray arrows) and edge currents (red arrows). (a) A Möbius band with a magnetic field perpendicular to the surface and of constant magnitude. At one transversal domain wall it changes sign. There are currents through the bulk at the domain wall. (b) A Möbius band subjected to a uniform magnetic field in the embedding space, indicated by the large arrow. The component perpendicular to the surface, indicated by the arrows on the surface, varies smoothly (cosine-like). The bulk currents are not indicated [53].

Here, two magnetic field configurations depending on the x (longitudinal) coordinate are depicted. In this case, there locally exist two counterpropagating edge modes. The currents propagate clockwise on half of the edge and counterclockwise on the other half. In Fig. 4.6, we show two examples of such configurations. In panel (a), the magnetic field is everywhere perpendicular to the surface and constant, except at the line defect spanning the band from one edge to the other. At this line, the direction of the magnetic field inverts, and it behaves like a domain wall. At the domain wall, currents flow through the bulk [171]. In Fig. 4.6(b), the magnitude of the perpendicular magnetic field is equal to the perpendicular component of a background magnetic field, i.e., a uniform magnetic field in the embedding space. In the coordinate system of the surface, the magnetic field dependence is cosine-like. However, the orientation of the magnetic field is discontinuous, since it changes sign. As a consequence, the Möbius band will be divided in patches with a QHE of opposite sign, and the system as a while will be topologically trivial.

It is also possible to discuss the QHE on a Möbius band from an anomaly perspective using Laughlin's argument, as in Chap. 2.5. A quantum Hall fluid defined on an annulus may be pierced through the central hole by a magnetic flux. As the flux is increased adiabatically by one flux quantum h/e, a circular current is generated inside the annulus, which in turn induces a Hall voltage. In this situation, the electric charge on the inner and outer boundary is $\pm\sigma_{xy}h/e$,

indicating the presence of a chiral anomaly in the low-energy edge theories. Thus, a charge of ne on the boundary indicates that the Hall conductivity is equal to (the integer) n times the conductivity quantum e^2/h. When one repeats this thought experiment for the Möbius band, with a solenoid flux tube through the central hole, the adiabatic flux change induces a circular current. However, as opposed to a separate inner and outer boundary of the annulus, here there is only one boundary. Conservation of the total boundary charge requires that the edge cannot have an anomaly, and that there can be no Hall conductivity.

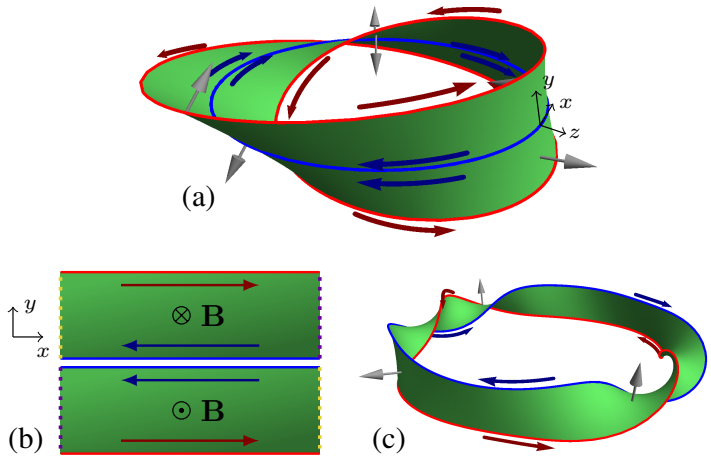

Figure 4.7: QH state on the Möbius band with a longitudinal cut. (a) The Möbius band is cut in two by the center line (blue). Magnetic fields (gray arrows) have opposite directions on both sides of the center line. (b) Cut-open model of (a). The pairs of yellow and purple edges should be identified in order to obtain the Möbius band shown in (a). The red and blue arrows along the edges indicate the propagation direction of the edge currents in the presence of the magnetic field $\mathbf{B}$. (c) The Möbius band cut at the center line yields a 4π twisted ribbon. The edge currents and magnetic fields are indicated as in (a) [53].

Secondly, one can consider a magnetic field that is uniform in the longitudinal direction, but dependent on the transversal coordinate y. For a cylindrical system, invariance under R requires that the perpendicular component B_z of the magnetic field satisfies $B_z(-y) = -B_z(y)$. In particular, on the center line $y = 0$ in Fig. 4.2 (i.e., halfway between two edges, seen locally), the field must vanish. One particularly interesting example is $B_z(y) = B_z \operatorname{sgn}(y)$, see

Figs. 4.7(a) and (b). In this configuration, Hall currents propagate on the edges in one direction, and on the center line in the opposite direction. Without affecting the topological transport properties, one can cut the Möbius band at the discontinuity on the center line. The resulting surface is homeomorphic (topologically equivalent) to a ribbon with a 4π twist, i.e. the ODC from Fig. 4.7(c). This manifold is orientable and has two separate (disconnected) edges. Thus, this configuration is equivalent to a cylinder with a uniform perpendicular magnetic field, with oppositely propagating edge currents on both edges. Note that one of the edges is the original edge of the Möbius band, the other is the center-line cut.

If one would perform a Hall measurement on half of the Möbius band, by probing the area between the edge and the center line, one would find a nonzero Hall conductivity. However, the sign of this conductivity changes through the center line, and the Möbius band as a whole does not exhibit a QHE [see the red arrows in Fig. 4.7]. The solenoid thought experiment described above has an interesting outcome in this configuration: By adiabatically increasing the flux in the solenoid through the central hole, one generates a circular current through the whole band. The current induces the charges $2ne$ on the center line and $-2ne$ on the edge, associated to the Hall conductivity of magnitude ne^2/h and opposite signs on opposite sides. This example shows that one should make a clear distinction between local (piecewise) Hall currents and the total Hall current. Thus, the statement that the Möbius band does not admit a total nonzero Hall current remains valid, even with a local field configuration.

Because a magnetic field configuration that depends only on y maintains translational invariance along the x-axis, it is possible to generate dispersion relations that demonstrate the issues discussed above. In Fig. 4.8(a) and (b), the dispersions for the Möbius band subjected to a magnetic flux $\phi = \phi_0/3$ per hexagon with a longitudinal domain wall are shown. Here ϕ_0 is the elementary flux quantum. In order to compute this dispersion, we have included the fluxes depicted in Fig. 4.8 through the Peierls substitution, and then considered the extended Hamiltonian on the cylinder, which has the same spectrum. The hexagons on the center line are not subjected to flux. The hopping strengths for the bonds crossing the center line are equal to t, i.e., equal to the magnitude of all other hopping amplitudes. This configuration of a longitudinal domain wall should be contrasted to that of a longitudinal cut, where the bonds across the central line are cut, i.e., the hopping across them line vanishes. The dispersion corresponding to such a longitudinal cut is shown in Fig. 4.8(c).

The resulting dispersions can also be interpreted by studying the edge modes in the bulk gap at $E/t = 1$. (The other bulk gaps show qualitatively

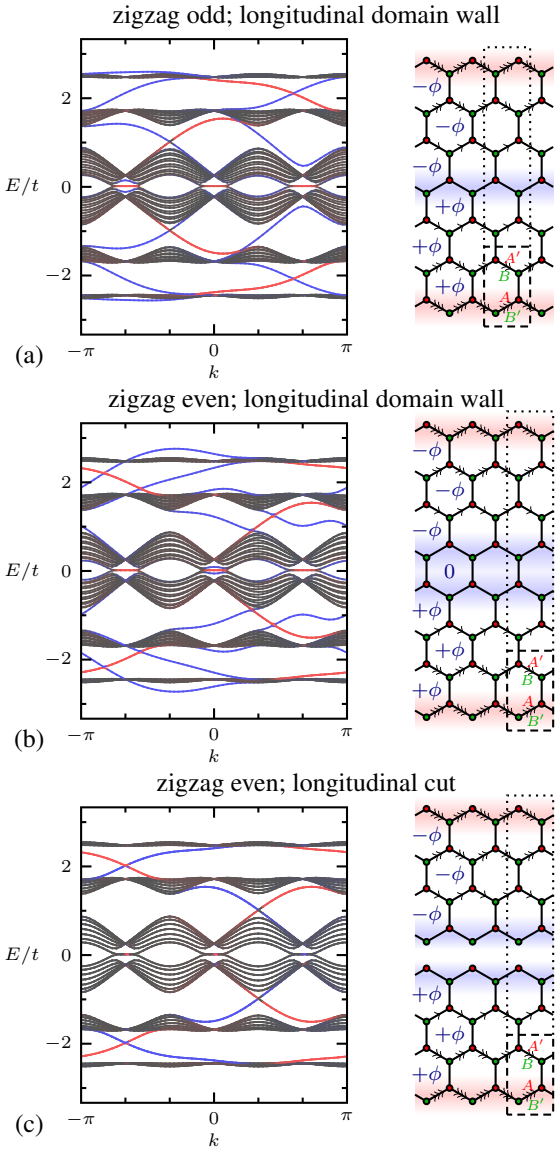

Figure 4.8: Dispersions of the Möbius band, subjected to a magnetic flux of $\phi = 1/3$ flux quantum per hexagon. On the right-hand side, the lattices are sketched, together with the sign of the flux, and the colour coding for the edge states. The dispersions and flux configurations are shown for (a) a longitudinal *domain wall* in an odd-sized zigzag ribbon, (b) a longitudinal *domain wall* in an even-sized ribbon, and (c) a longitudinal *cut* in an even-sized ribbon [53].

similar results.) In the domain-wall configuration [Figs. 4.8(a) and (b)], one sees edge modes on the edge of the Möbius band, shown in red. They are two-fold degenerate, because of the extra degrees of freedom included in order to describe the Möbius geometry. Alternatively, one could explain the number of two by recalling that at each x (longitudinal) coordinate of the Möbius band, there are two edges. The edge modes at the center line (colored blue) propagate in the opposite direction. This pair of edge modes is not degenerate, because they overlap and hybridize, which causes an energy splitting lifting the degeneracy. As a consequence, the spectrum has no vertical axis of reflection symmetry ($k \to -k$). The combination of the magnetic flux (being chiral) and the different natures of the edge and the longitudinal domain wall is the cause of this symmetry breaking.

This result can be contrasted to the configuration where the central line is cut [Fig. 4.8(c)]. In that case, the Möbius edge and the central line become equivalent because they have the same shape. No hybridization occurs between the two copies of the central-line edge modes, i.e., the blue dispersions remain degenerate as well. In fact, the complete dispersion is a two-fold degenerate copy of the honeycomb ribbon at $1/3$ flux [116], because at each longitudinal coordinate, there are two equal honeycomb ribbons under that same flux.

It is important to realize that the domain wall and the cut case share their topological properties. The hopping amplitude at the central line can be tuned adiabatically from t to 0, without closing any of the bulk gaps. Thus, no topological transition takes place: The number of edge modes inside each bulk gap remains the same. The same is true if one compares the domain-wall configuration for the even and odd case. The distinction between these two cases is merely due to the possibility of a cut; in odd-width zigzag ribbons, the cut cannot be made. The similarity of the topological properties is expected with the bulk-boundary correspondence in mind.

In a similar vein, one can consider a QSHE on a Möbius band. When spin is conserved, the QSHE can be understood as two opposite manifestations of the QHE, one for each spin. Although uniform magnetic fields and nonzero total Hall currents are forbidden on the Möbius band, QSH-like states do exist there [171], a fact that is corroborated by the topological classification of the Möbius band, which is $\mathbb{Z}_2$ in the presence of TRS.

Spin refers to two internal degrees of freedom at each point in space. Locally, there are two copies of the space, usually labeled with spin up and spin down, but one may consider more generally any two spins connected by time-reversal symmetry. In the description of the QSHE on a cylinder, the two copies are defined globally. There is a spin up and a spin down cylinder, and there is

no continuous spatial transformation that can turn a spin up into a spin down and vice versa. In the Möbius band, moving a spin around the band flips it. This behaviour is identical to that of local choices of orientation, showing that the two spin components can be conveniently analysed in terms of the ODC of the Möbius band. The two copies of the Möbius band fitted inside the ODC are interpreted as the two spin components. The two sheets of the Möbius band in Fig. 4.3(a) then correspond to the two spin components.

Consider subjecting the double cover (or equivalently, the 4π twisted ribbon) to a Haldane-like flux configuration on the honeycomb lattice, which is characterized by a vanishing total flux, but which still generates a QHE [4]. On the cylinder, the Haldane flux has a well-defined chirality, determined by the direction of the edge currents it induces. It is important to note that these notions are unambiguous on the ODC because it is orientable. Then, by virtue of the covering map, the two components at each point on the Möbius band are subjected to two Haldane fluxes of opposite chirality. This configuration essentially defines the ISO coupling term of Kane and Mele, [6, 7] that induces the QSHE: The two edge modes at each edge counterpropagate, and the edge modes of matching components at both sides of the ribbon counterpropagate as well, see Fig. 4.3. An important difference with the QSH state in the cylindrical case is that the spin labels cannot be assigned globally, because the double cover has only one connected component. Indeed, a translation once around the central hole in the Möbius band, i.e., such that the longitudinal coordinate is the same as before, maps spin up to spin down and vice versa. The spin flip connected to this single rotation has been observed in measurements of the time-resolved dynamics in RF circuits emulating the Möbius band [172].

By comparing Figs. 4.7(c) and 4.3(c), one sees that the QSHE on the Möbius band is topologically equivalent to the configuration with a longitudinal cut. In both cases, the total Hall conductivity vanishes. However, there is an important difference in the interpretation. In the spinful case, there are two edge modes, whereas in the spinless case there is only one: the other one is actually located at the domain wall. Only in the spin model can one speak of a spin Chern number and a nonzero QSH conductivity (the sign of which may be fixed from the mapping to the 4π ribbon).

This, in addition to the topological classification using Ref. [50], indicates that a QSHE can be present on the Möbius band. Since the ISO coupling term in the Hamiltonian is reflection symmetric [see Eq. (4.6)], its implementation is relatively straightforward: by including it in a cylindrical Hamiltonian it immediately quotients to the Möbius band. By analysing the cylindrical Hamiltonian one obtains the spectrum of the Möbius system as well. In Fig. 4.9, the

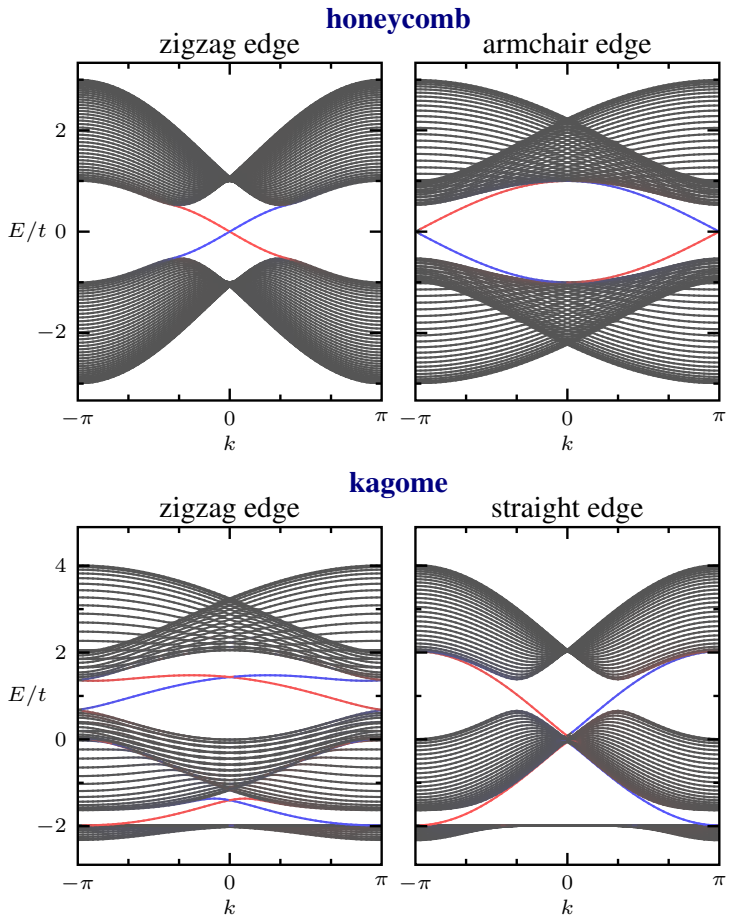

Figure 4.9: Dispersions of the Möbius band calculated for a honeycomb lattice with zigzag and armchair edges, and for a kagome lattice with zigzag and straight edges. The colors red and blue indicate the QSH-like edge modes, i.e., the two time-reversal conjugate edge modes propagating in opposite directions. The strength of the ISO term is set to $t_{\mathrm{I}} = t/10$ [53].

results are depicted for the honeycomb and kagome lattice structures; in both cases the two possible edge configurations are shown. The colors in Fig. 4.9 are determined from the product of the spin and location: The red curves indicate the two right-moving edge currents on the bottom edge of one and on the top edge of the other component of the double cover (which corresponds to the opposite spin). Similarly, the blue curves correspond, to the left-moving edge currents, cf. Fig. 4.3(a). After the R-odd states have been projected out, one observes only a single (i.e., nondegenerate) left-moving and a single right-moving edge current. Since there are no hybridization effects, this projection merely removes the two-fold degeneracy of the cylindrical spectrum. For this reason, the results for the honeycomb lattice are comparable to those found in Chapter 2, where the QSHE was discussed for planar honeycomb systems.

Rashba spin-orbit coupling [Eq. (4.5)] can be straightforwardly included in the Möbius band. As expected from the methods described above, it has a similar effect as in the cylindrical case: Rashba spin-orbit coupling by itself does not open a gap. In the presence of ISO coupling, the Rashba coupling decreases the size of the topological gap or opens a trivial one, depending on its strength [7]. The conservation of vertical spin is broken in this case, but this does not destroy the QSH-like state, similar to what is observed for the cylinder.

4.2 The interplay between Möbius geometry and driving

The discussion in the previous section focussed heavily on the QHE and the QSHE. An obvious question would be what happens for p-wave superconductors on a Möbius band, since they are also topological. We will tackle that question later in this chapter. First, we will spend some time to tie together two different topics that have been adressed. In Chapter 3, we discussed how irradiating honeycomb lattices with circularly polarised light, or shaking them in a circular manner, causes the appearance of quantum Hall states. In addition, this effect can be used to induce a competition between ISO coupling and irradiation, since both lead to a topological phase transition. We will now consider how these effects interplay with those covered in the previous section. The results are based on work published in Ref. [54]. I have performed the calculations in this work, while Dr. Beugeling and Prof. Dr. Morais Smith supervised the project.

4.2.1 Irradiated Möbius graphene without SO coupling

To analyse the system, it is necessary to construct the Hamiltonian H_M. We will do this by constructing a Hamiltonian H_C on the cylinder that commutes with R, and applying the tricks from the previous section. First, we will consider the system without ISO coupling, so that the effect of the Möbius geometry on the irradiated system can be analysed. For H_C, we use the Hamiltonian in Eq. (3.12), but with a modified vector potential $\boldsymbol{A}$ to ensure that it is symmetric under the glide reflection.

Under a change of orientation (i.e., of the direction of the unit normal to the surface), the Poynting vector of a coherent light wave changes sign. This shows that a Möbius band cannot be homogeneously irradiated with circularly polarised light. Alternatively, H_C does not commute with R, because $\boldsymbol{A}$ from Eq. (3.10) is not symmetric under reflection. However, by allowing a domain wall at the center of the strip (see the horizontal dotted line in Fig. 4.2(a)), the inclusion of a laser field in the Hamiltonian is possible. The fact that a domain wall is necessary is entirely analogous to the situation with a magnetic field, since they both induce a QHE, which cannot exist globally on the Möbius band.

To incorporate this domain wall, it is most convenient to define the vector potential on the ODC using the coordinate system defined in Fig. 4.2(b), so that

$$\boldsymbol{A} := \begin{cases} -V\big(\sin(\omega t), -\cos(\omega t)\big) & y < 0, \\ -V\big(\sin(\omega t), \cos(\omega t)\big) & y > 0. \end{cases} \tag{4.7}$$

Since we consider a vector potential induced by circularly polarised light, we can write $V = E/\omega$, where E is the magnitude of the applied electric field, a measure of the radiation intensity. Now the y-component of the vector potential changes sign along the domain wall, which corresponds to a sign change in the Poynting vector of the light field. It is easily checked that H_C given by Eqs. (3.12) and (4.7) commutes with the glide reflection R from Eq. (4.1), and therefore it descends to a Hamiltonian H_M on the Möbius strip.

The Hamiltonian H_M obtained from Eqs. (3.12) and (4.7) defines a Sambe Hamiltonian $\mathfrak{H}$ according to Eq. (3.5). In Figs. 4.10(a) and (b) the dispersion of $\mathfrak{H}$ is shown for different values of ω. These can be compared against Fig. 3.6, which depict the spectrum for a cylinder at the same parameter values.

Making this comparison, one sees that on the Möbius strip a QH-like state is created, similar to that on the cylinder. Because the light is circularly polarised, reflection symmetry in the x-direction is broken. Consequently, there is a preferred direction of propagation on the edge, and it is clear that the blue

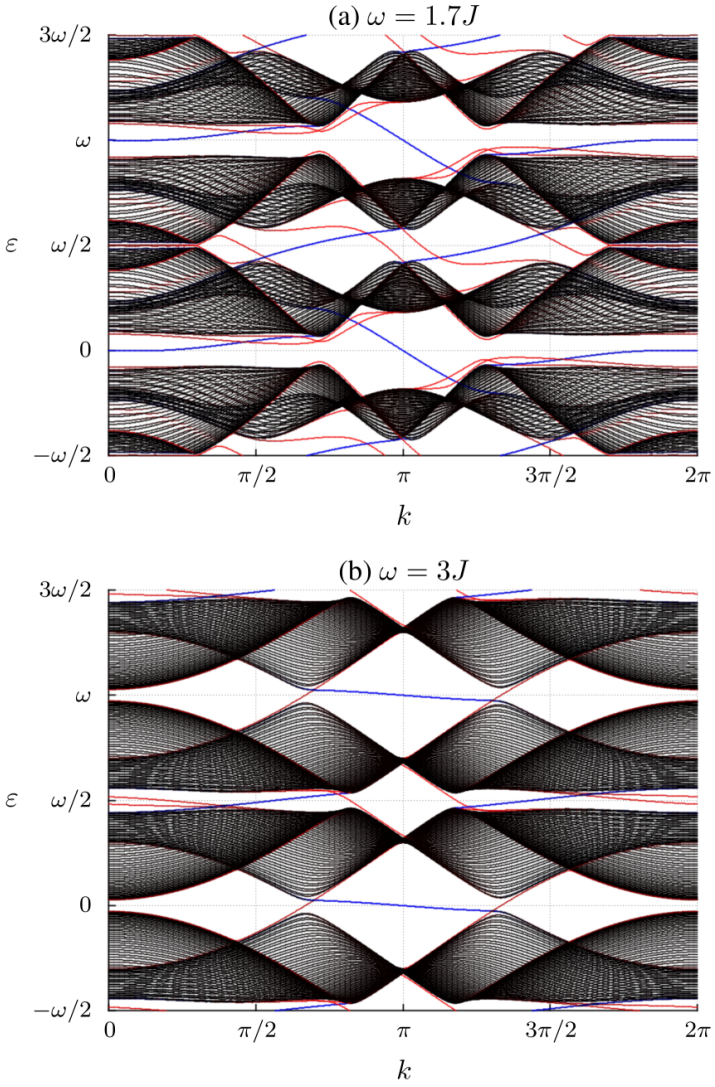

Figure 4.10: The dispersion of $\mathfrak{H}$, as defined by Eqs. (3.3), (3.12) and (4.7), for the Möbius geometry with zigzag edges and an even number of unit cells along the width of the band. The vector potential has magnitude $E = J/a$, where a is the lattice constant. (a) The radiation frequency is $\omega = 1.7J$. The edge modes are in blue, while the states localised at the domain wall are in red. Hybridisation of the domain wall states lifts their degeneracy. At $\varepsilon = 0$ the red states do not cross the gap; this is allowed because the chirality of this gap vanishes. (b) Same as (a), but for $\omega = 3J$ [54].

edge modes on the cylinder survive unaltered on the Möbius strip. Changing the polarisation causes the propagation direction to reverse. Furthermore, the dispersion of the edge modes (blue) is unaltered, because the edge modes are localised and do not notice the non-trivial geometry of the strip. The difference between the Möbius band and the cylinder can be seen in the states localised on the domain wall (the states in red). On the Möbius band, the domain wall starts functioning as a second edge, analogous to the edge on the cylinder for which the edge modes are coloured red in Figs. 4.10(a) and (b). However, the domain wall is not a hard boundary: hopping can occur across it. This causes the states localised on the domain wall to hybridise, splitting their degeneracy. Indeed, the red states are non-degenerate, while the blue states are doubly degenerate. The preservation of the degeneracy of the blue states can be understood from the lack of hybridisation between them, due to their spatial separation. In the interpretation of the two components of the double cover as two spin components, this degeneracy may be viewed as a spin degeneracy [53]. The glide reflection, which is used to obtain a Möbius band from a cylinder (see Fig. 4.2), involves a mapping of one component onto the other, which may be interpreted as a spin flip in this framework. The hopping across the domain wall can be seen as a hybridisation between the two (spin) components, which leads to a lifting of the degeneracy.

The equality of the number of states at the edge and at the domain wall is to be expected on physical grounds. A cylindrical system with a domain wall can be interpreted as two cylindrical systems interacting at their boundary. The hopping across this boundary causes hybridisation of the edge modes. Tuning the hopping strength across the domain wall shows that this is indeed the case; the hybridisation weakens as the hopping across the domain wall becomes smaller. If this hopping is put to zero, the dispersion for the cylinder is recovered just as discussed in the previous section.

It is reasonable to suppose that the hybridisation of the domain wall states cannot affect the total winding number of each gap. This implies that the chiral anomaly at the domain wall cancels that at the edge. Interestingly, the hybridisation does allow for a change in the number of crossing domain wall states, as long as the anomaly is preserved. This can be seen in the gap around $\varepsilon = 0$ in Fig. 4.10(a), where the two blue pairs of edge modes are counter-propagating, and the four red states do not cross. This occurs because there is no symmetry protecting the counter-propagating edge modes in the gap at $\varepsilon = 0$. Due to the lack of topological protection, the hybridisation at the domain wall can annihilate the gapless states.

4.2.2 Irradiated Möbius graphene with SO coupling

As mentioned in Chapter 3, flat graphene samples have a negligible ISO coupling [112], while in strongly bent graphene samples such as carbon nanotubes, the ISO coupling can take appreciable values [113]. A graphene Möbius band of small radius would fall into this category. For accuracy, the effect of ISO coupling has to be included in the Hamiltonian. We discussed in Chapter 3 what the interplay between these two effects in a cylindrical system is. We will now discuss the analogy of this effect in the Möbius band, where it works in tandem with the hybridisation effects at the domain wall visible in Fig. 4.10. Therefore, we will repeat the procedure above, but include the ISO coupling by using Eq. (3.13) instead of Eq. (3.12) to construct H_C.

In Fig. 4.11(a), the dispersion for a graphene Möbius band without any radiation is shown. This is completely analogous to the situation in Fig. 4.9. However, for ease of comparison with the irradiated case, the spectrum has been periodically continued in ε with period $\omega = 3J$. The gap at $\varepsilon = 0$ has opened up and a pair of counter-propagating edge modes has appeared on the single edge of the Möbius band, in agreement with previous studies that showed the occurrence of a QSH effect in Möbius graphene bands in the presence of ISO coupling [53, 171].

In Fig. 4.11(b), the dispersion is shown after the circularly polarised light has been turned on with $\omega = 3J$ and $V = J/\omega$. Even though the circularly polarised light breaks TRS (time reversal changes the rotational direction of the light, and hence the propagation direction of the QH states), a QSH-like state is still observed. This is similar to the weak QSHE observer in the cylinder [116]. The circularly polarised light also opens up a gap at $\varepsilon = \omega/2$, which is caused by photon resonances between the valence and conduction bands [44]. In this gap, QH-like states are observed, similar to those in Fig. 4.10(b). Tuning the strength of the SO coupling shows that in this gap only the QH-like states are possible. This is because the gap is opened by photon resonances, and the topological states are similarly created by these resonances. The SO coupling cannot create such resonances, and therefore cannot change the topological nature of this gap either.

In Fig. 4.12(a), the intensity of the light is further increased. Then, the edge state where QHE and QSHE oppose each other becomes increasingly dispersionless. At the light intensity $V \approx 1.7J/\omega$, the two effects annihilate each other and the gap at $\varepsilon = 0$ closes. The appearance of a state localised at the domain wall is also visible, but it is not topological, since the circularly polarised light does not yet dominate.

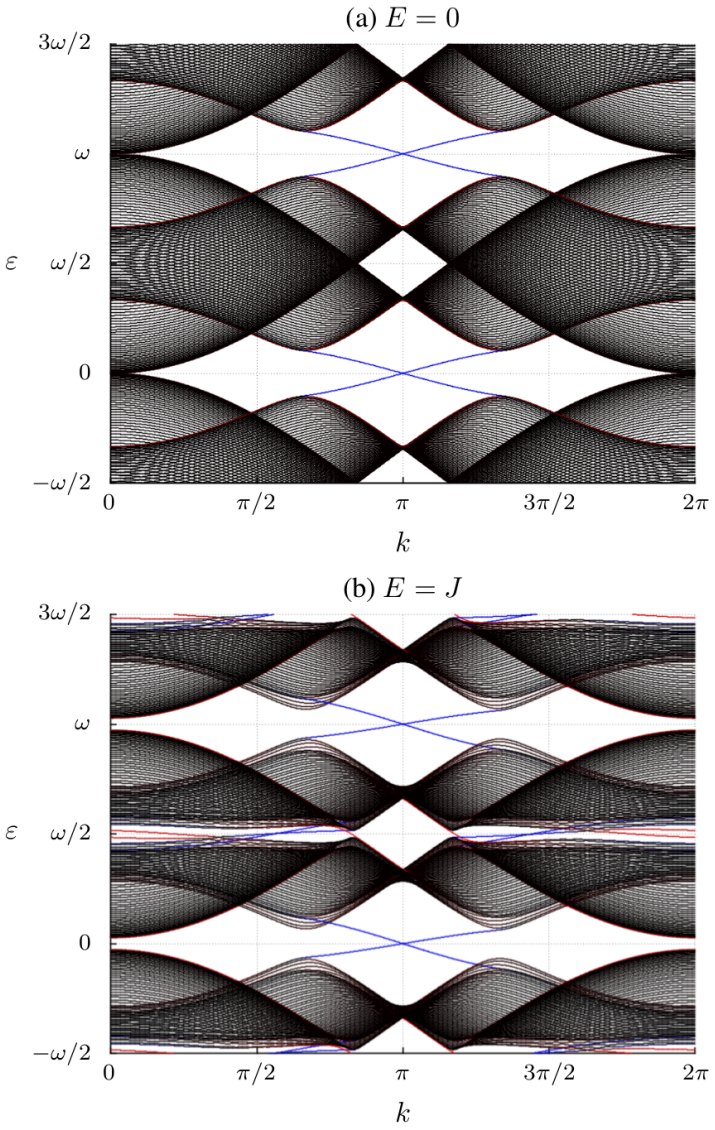

Figure 4.11: The dispersion of $\mathfrak{H}$, as defined through Eqs. (3.5), (3.13) and (4.7) for Möbius bands with zigzag edges and an even number of unit cells along the width of the band. We use $\omega = 3J$, while $\lambda = 0.06J$. (a) For $V = 0$, the ordinary QSH effect is observed. The spectrum has been periodically continued in ε for ease of comparison. (b) For $V = J/\omega$, a weak QSH effect is seen in the gap at $\varepsilon = 0$ since the SO coupling dominates. There, SO coupling also prevents the appearance of states at the domain wall. At the photon resonances, the QH-like states appear in the same manner as in the absence of SO coupling [54].

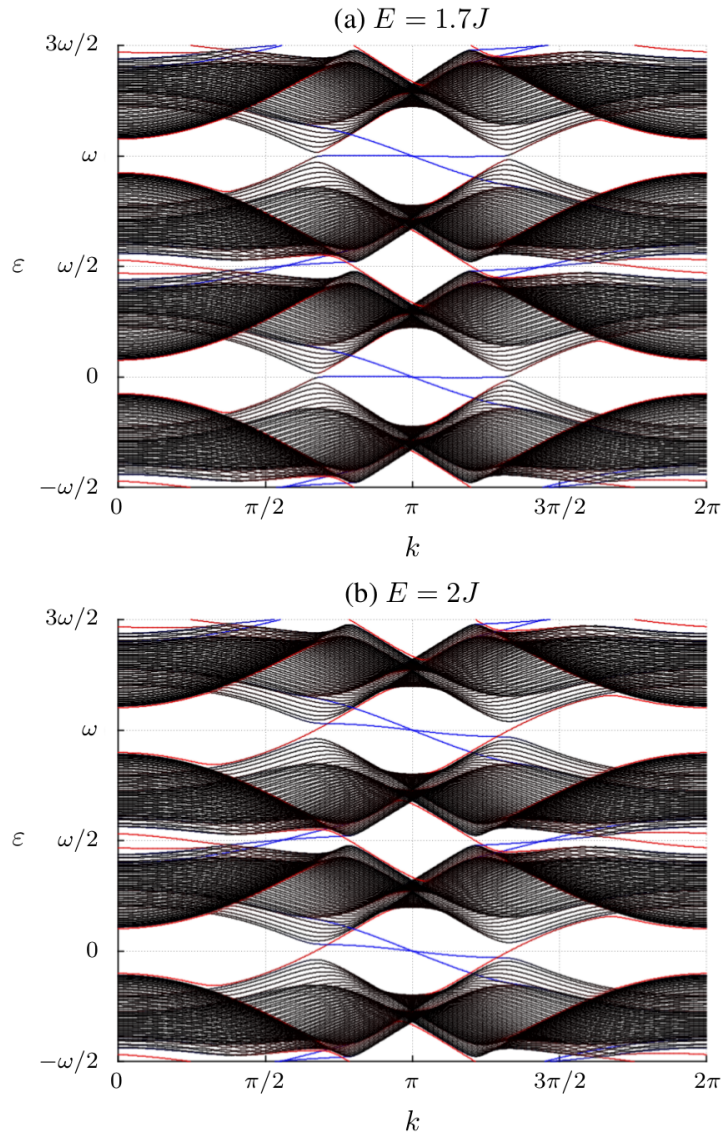

Figure 4.12: The same as in Fig. 4.11. (a) For $E = 1.7J/\omega$, the gap closes at $\varepsilon = 0$ since the SO coupling and the light annihilate each other. The phase transition occurs at this point. (b) For $E = 2J/\omega$, the light dominates the SO coupling; QH-like states now occur at $\varepsilon = 0$ as well as at $\varepsilon = \omega/2$. Apart from a lifting of the spin degeneracy of the edge modes, the dispersion looks similar to that in Fig. 4.10(d) [54].

In Fig. 4.12(b), the light intensity is increased yet again, and now the effect of the circularly polarised light is dominant. In the gap at $\varepsilon = 0$, the TRS is broken to such an extent that the QSHE has vanished, and a QH-like state has appeared. Two edge modes with fixed propagation direction appear together with two counter-propagating states at the domain wall, in accordance with Fig. 4.10(b). The ISO coupling lifts the degeneracy of the (blue) edge modes, but is not sufficiently strong to alter the QH nature of these edge modes. The (red) states at the domain wall already have their degeneracy lifted by the hybridisation, as discussed before.

This competition between the ISO coupling and the circularly polarised light is also seen for $\omega = 1.7J$ (not shown). Here, the gapless state at $k = 0$ in the $\varepsilon = 0$ gap causes a mentionable effect. For intensities where the light dominates, similar behaviour to that in Fig. 4.10(a) is observed. Specifically, there are counter-propagating edge modes, while no states cross at the domain wall. For frequencies where the ISO coupling dominates, the chirality of the gap is non-zero, and there are no domain wall states at the Dirac points around $k = \pi$. In this case, there is a gapless domain-wall state at $k = 0$; in the absence of ISO coupling, this gapless state annihilates against those at the Dirac points, as can be seen in Fig. 4.10(a).

These results show that much of the behaviour on the Möbius band is the same as on the cylinder. This situation can be understood by using the ODC to analyse the Möbius band. An intriguing difference is the necessity of including domain walls if one wants a QH like state, which leads to interesting hybridisation effects.

4.3 Topological superconductivity in non-planar systems

There is, however, another type of system that shows interesting additional effects on a Möbius band, or non-trivial geometries in general, and that is a 2D topological superconductor. These effects are all related to the vector nature of the p-wave superconducting order parameter. We will now discuss the details, which have also appeared in Ref. [55]. This project was performed in collaboration with T. Kvorning, while Prof. Dr. Hansson and Prof. Dr. Morais Smith supervised the project.

4.3.1 Introduction

Since this is the first place where we will talk about topological superconductors, and the anyonic excitations they host, we will first discuss some basic concepts. The existence of anyonic excitations in topological superconductors has been a major point of interest in these systems. In 1D and 2D, particles do not necessarily pick up a phase of 0 or π under interchange, like bosons and fermions, but they can be anyons. The name originates from the fact that the phase picked up on interchange can take any value. Even more generally, interchanging particles in a state can result in a different state than one started in, and then one speaks of non-Abelian anyons. These non-abelian anyons were first predicted to occur in quantum Hall systems at filling fraction $\nu = 5/2$ and $\nu = 7/2$ [173, 174], and later at other fractions in higher Landau levels [175]. In addition, they are expected to arise in 2D spinless $p_x + ip_y$ superconductors, where the vortices can be shown to obey non-Abelian Ising statistics [176–179]. The anyonic nature of the vortices in such a superconductor originates from the presence of zero-energy Majorana state in the vortex cores (in what follows, Majorana will always refer to a zero-energy Majorana state). Such Majorana states have not yet been observed in 2D systems, but there is experimental evidence pointing to their existence in 1D topological superconductors [180, 181]. An archetypal model for this 1D system is the Kitaev chain, which we discuss in Chap. 5.

In 2D superconductors, the presence of such Majorana states is determined by the amount of flux piercing the superconductor: an odd number of superconducting flux quanta (unit flux) in close proximity gives a Majorana, while an even number does not. Since Majorana states can only come in pairs, an odd total number of unit flux vortices requires the presence of a Majorana state at the boundary of the material. To understand this point, it is important to realize that a topological superconductor always has gapless edge modes in the thermodynamic limit, but there is not necessarily an edge state precisely at zero energy (an edge Majorana) for finite edge length [176]. To know the number of Majorana states in the presence of an arbitrary number of unit fluxes, one needs to know how many Majorana states are present in the absence of flux. For example, if the boundary consists of multiple edges, an even number of edge Majoranas might be present in the absence of flux.

To answer this question for a general geometry, one has to realise that the p-wave order parameter is not, as in the s-wave case, just a scalar field. Rather, it is a vector field, and, consequently, it couples to the geometry of the surface. At first, one would think that only the local curvature of the surface would matter,

so that, for example, a cylinder and an annulus would be indistinguishable because they are both locally flat and have the same topology. This is, however, not true, since it is known that in the absence of magnetic flux, the cylinder does support Majorana states, while the annulus does not [176].

We solve this puzzle by considering a cone, and letting the conical angle smoothly interpolate between the annulus and the cylinder. We show that there is a crossover between the ground state and the first-excited state at a critical opening angle of the cone, and that in general the ground state supports a current. These effects all depend on the internal geometry of the cone, but it is also interesting to study effects that depend on the topology. An interesting example is provided by a Möbius band.

Since the p-wave superconductor is chiral, one needs an orientable surface to define the chirality of the superconducting order parameter. The immediate consequence is that there are no topological superconductors on the Möbius band according to the topological classification from Chap. 4.1.2. However, it is possible to have a p-wave order parameter locally, if one allows for domain walls, like with the magnetic field or circularly polarised irradiation. Then it is possible to combine the issue of a Majorana mode with the presence of domain walls.

The Möbius band has only one boundary component. Therefore, the response to external fluxes, and the interplay between vortex excitations and edge Majoranas differ from that of an annulus or a cylinder. We will show that when the defect line is along the centre of the Möbius band, the Majorana at the defect cannot be removed by the addition of a unit flux. The existence of a Majorana at the line defect is only affected by half a unit of flux passing through the hole of the band. These effects can be understood by mapping the Möbius band to a corresponding cylinder. Although the existence of the Majorana is not affected by one unit of flux passing through the hole of the band, the profile of the Majorana wave function across the line defect will be modified.

We will start by reviewing the formalism for describing a spinless 2D $p_x + ip_y$ superconductor on a general curved surface, and by deriving the general form of the allowed boundary condition at the edges. This is the simplest model for a p-wave superconductor in 2D, which allows for a clear presentation of the relevant features.

Since the Pauli principle prevents a local interaction among spinless electrons, the dominating long wave-length part of any finite-range two-body interaction, which is only a function of the geodesic distance, can be written as $V(x, y) = \lambda\nabla^2\delta^2(x - y)$, where ∇^2 is the Laplacian. It should be noted that in any physical system, the Hamiltonian would also have terms that do not

depend on the intrinsic geometry, since the particles that mediate the interaction can generally move through the full 3D ambient space, but for simplicity we neglect such terms here. For the interaction to be well defined, the Fourier transform $V(q)$ of the potential $V(r)$, where r is the geodesic distance, has to vanish as $q \to \infty$. However, the precise behaviour at large momenta is not important for the long-wave-length physics.

The most convenient way to write this interaction in a coordinate-invariant form is to introduce an orthonormal frame: a pair of orthonormal unit vectors $\{e_a^\mu\}_{a=1,2}$ at every point. By construction, the metric can be expressed as $g^{\mu\nu} = e_a^\mu e^{a\nu}$, where $e_a^\mu = e^{a\mu}$ by definition.

Performing a partial integration and using that the square of any fermionic operator vanishes, the interaction can be expressed in second-quantized form as

$$\hat{V} = \lambda \int dS \left[\left(\psi^\dagger \partial_- \psi^\dagger\right) \left(\psi \partial_+ \psi\right) + \left(\psi^\dagger \partial_+ \psi^\dagger\right) \left(\psi \partial_- \psi\right) \right] ,$$

where $dS = d^2x\sqrt{\det g_{\mu\nu}}$, $\partial_\pm = e_1^\mu \partial_\mu \pm i e_2^\mu \partial_\mu$ and $\psi^\dagger$ and ψ are, respectively, the (spinless) electron creation and annihilation operators.

In a mean field approach, one approximates the pairing term by

$$\hat{V} = \frac{\lambda}{2} \int dS \left[\left(\psi^\dagger \partial_- \psi^\dagger\right) \phi_+ + \left(\psi^\dagger \partial_+ \psi^\dagger\right) \phi_- + h.c. \right] ,$$

where the values of $\phi_\pm = \langle \psi \partial_\pm \psi \rangle$ should, strictly speaking, be determined self-consistently. However, we shall take them as given background fields with the correct topological properties. For the ground state in the $p_x + ip_y$ case, we will use $\phi \equiv \phi_+ = const$ and $\phi_- = 0$.

Since ϕ is a vector field with charge $2e$, constant means covariantly constant. To this end, recall that, with respect to the normalized basis $\{e_a^\mu\}_{a=1,2}$, the covariant derivative of a general vector with components V^a is

$$D_\mu V^a = \left(\delta_b^a \partial_\mu + \omega_{\mu b}^{\ a}\right) V^b ,$$

where the connection form is defined by

$$\omega_{\mu b}^a = e_\nu^a \nabla_\mu e_b^\nu , \tag{4.8}$$

with ∇_μ the Levi-Civita connection. It can be shown that $\omega_{\mu b}^a$ is antisymmetric in a and b. Therefore, the covariant derivative of $V_\pm := V^1 \pm iV^2$ is $D_\mu V_\pm = \left(\partial_\mu \pm i\omega_\mu\right) V_\pm$, where $\omega_\mu \equiv \omega_{\mu 2}^{\ 1}$. In the presence of an electromagnetic vector potential, this generalises to

$$D_\mu \phi = \left(\partial_\mu + 2ieA_\mu + i\omega_\mu\right) \phi , \tag{4.9}$$

where A_μ is the electromagnetic gauge potential. Barring any geometric obstructions, this will vanish in the ground state to minimise the kinetic energy of the system.

The mean-field Hamiltonian reads

$$\hat{H} = \int dS \Psi^\dagger \begin{pmatrix} h_0 & \phi\partial_- \\ \phi^*\partial_+ & -h_0^* \end{pmatrix} \Psi \ , \tag{4.10}$$

where $\Psi \equiv \begin{pmatrix} \psi, & \psi^\dagger \end{pmatrix}^T$ and the non-interacting part of the Hamiltonian h_0 may in general contain any power of the Laplacian. However, for long-wavelength effects, only the lowest order in derivatives matters, so one can take h_0 to be a constant chemical potential $h_0 \equiv \mu$. Adding higher-order terms would also mean that the ansatz $\phi = const.$ is not a self-consistent solution close to vortices or edges.

The first-quantized Hamiltonian $\mathcal{H}$ is defined by how it acts on a general single quasi-particle state

$$|u, v\rangle = \int dS \left(\psi^\dagger, \psi\right) (u, v)^T |0\rangle,$$

where $|0\rangle$ is the ground state, the existence of which is assumed. Since the number of quasi-particles is conserved, the Schrödinger equation can be rewritten into a partial differential equation for the functions u, v:

$$i\hbar \frac{\partial}{\partial t} \begin{pmatrix} u \\ v \end{pmatrix} = \mathcal{H} \begin{pmatrix} u \\ v \end{pmatrix} \ .$$

Here, the first quantized Hamiltonian reads

$$\mathcal{H} = \begin{pmatrix} -\mu & \frac{1}{2\sqrt{g}}\{\sqrt{g}\phi, \partial_-\} \\ -\frac{1}{2\sqrt{g}}\{\sqrt{g}\phi^*, \partial_+\} & \mu \end{pmatrix} \ , \tag{4.11}$$

where $\{\cdot, \cdot\}$ denotes, as usual, the anti-commutator. The most general local boundary condition for which this Hamiltonian is self-adjoint reads

$$\hat{n}^\mu e_\mu^a \sigma_a \begin{pmatrix} \phi^* u \\ \phi v \end{pmatrix}\Big|_{\partial S} = s\Delta \begin{pmatrix} u \\ v \end{pmatrix}\Big|_{\partial S} \ , \tag{4.12}$$

where s is an arbitrary real number, $\hat{n}^\mu$ is the outward directed normal, $\Delta = |\phi|$ and ∂S is the edge of the surface S on which the system is defined.

The Bogoliubov-deGennes Hamiltonian satisfies

$$\sigma_x \mathcal{H}^* \sigma_x = \mathcal{H} \ , \tag{4.13}$$

which reflects that in first-quantized language, this Hamiltonian counts all the degrees of freedom twice. This property of the first quantized Hamiltonian is required for $\psi^\dagger$ to be the adjoint of ψ, and is thus not a symmetry, but a consequence of the original second-quantized structure. Therefore, only boundary conditions consistent with (4.13) are allowed, which further constrains $s = \pm 1$.

4.3.2 Edge Modes on the cone

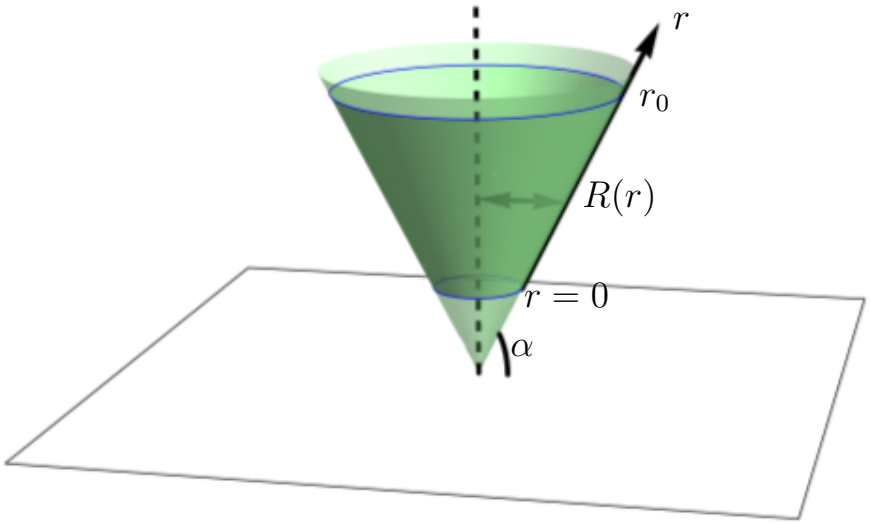

Figure 4.13: The embedding given by Eq. (4.14) [54].

We will now specialize to a conical surface, defined by the embedding

$$(r, \theta) \mapsto (R(r)\cos\theta, R(r)\sin\theta, r\sin\alpha)\,, \tag{4.14}$$

where $R(r) = R_i + r\cos\alpha$, $\theta \in [0, 2\pi]$, and $r \in [0, R_o]$ (see Fig. 4.13). For $\alpha = 0$, this is an annulus with inner radius R_i and outer radius $R_o = R(r_o)$, and for $\alpha = \pi/2$ it is a finite cylinder of radius R_i and length r_o. The parameter α is the angle that the conic surface makes with the xy-plane, and defines a smooth interpolation between the annulus and the cylinder. The metric in the (r, θ)-coordinates is inherited from the Euclidean one by the embedding (4.14):

$$g_{\mu\nu} = \begin{pmatrix} 1 & 0 \\ 0 & R(r)^2 \end{pmatrix}. \tag{4.15}$$

In this coordinate system, a natural choice of orthonormal frame is the set of normalised coordinate vectors,

$$e_1 = \hat{r} \equiv \partial_r \ , \qquad\qquad e_2 = \hat{\theta} \equiv \frac{1}{R(r)}\partial_\theta \ . \tag{4.16}$$

These are the normalised radial and angular vectors along the cone. In terms of the Cartesian-coordinate system on the ambient space in which the cone is embedded, one finds

$$\begin{aligned} \hat{r} &= \big(\cos\alpha\cos\theta, \cos\alpha\sin\theta, \sin\alpha\big) \\ \hat{\theta} &= \big(-\sin\theta, \cos\theta, 0\big) \ . \end{aligned}$$

We use the embedding in Eq. (4.14) to calculate the connection form, $\omega \equiv \omega_2^1$ in Eq. (4.8). It is equal to the Levi-Civita connection for the ambient space projected onto the cone. This gives

$$\omega = d\theta\, \hat{r}\cdot\partial_\theta\hat{\theta} + dr\, \hat{r}\cdot\partial_r\hat{\theta} = -\cos\alpha d\theta \ . \tag{4.17}$$

In terms of components, this reads $\omega_\mu = -R(r)\cos(\alpha)e^2_\mu$. Here, e^2_μ are the components of the 1-form dual to the frame field e_2. For a flat surface, the connection is fully determined by the holonomies $\int_C \omega$ around non-contractible curves.

For n units of flux through the hole in the cone, and no flux elsewhere, the electromagnetic vector potential reads $A_\mu = n(2e)^{-1}e^2_\mu$. Due to rotational symmetry, it is possible to take the superconducting order parameter to be

$$\phi = e^{-im\theta}\Delta \, , \tag{4.18}$$

where Δ is some non-negative real number, and m is an integer. This implies that

$$D_\mu\phi = i(n - m - \cos\alpha)e^2_\mu \ . \tag{4.19}$$

This expression can only vanish for the annulus ($\alpha = 0$), and for the cylinder ($\alpha = \pi/2$), which means that on a general cone, there is always a non-zero supercurrent present due to the presence of a geometric obstruction. For the annulus the current vanishes for $m = n - 1$, while for the cylinder this happens for $m = n$.

A direct calculation yields

$$\frac{1}{2\sqrt{g}}\{\sqrt{g}\phi, \partial_-\} = e^{-im\theta}\Delta\left(\partial_r + \frac{i}{R(r)}\partial_\theta + \frac{m+\cos\alpha}{2R(r)}\right) \ .$$

Substituting the ansatz

$$\begin{pmatrix} u \\ v \end{pmatrix} = e^{il\theta} \begin{pmatrix} e^{-im\theta/2} u_l(r) \\ e^{im\theta/2} v_l(r) \end{pmatrix} \tag{4.20}$$

into the Hamiltonian Eq. (4.11) for integer l and eliminating v_l gives

$$\left[\mu^2 - E^2 - \Delta^2 \left(\partial_r - \frac{l - \frac{1}{2}\cos\alpha}{R(r)} \right) \times \left(\partial_r + \frac{l + \frac{1}{2}\cos\alpha}{R(r)} \right) \right] u_l(r) = 0. \tag{4.21}$$

On the inner edge, the boundary condition (4.12) becomes,

$$v_l(0) = s u_l(0), \qquad\qquad s = \pm 1,$$

or, by using the equations of motion:

$$\left[s(\mu - E) + \Delta \left(\partial_r + \frac{l + \frac{1}{2}\cos\alpha}{R(r)} \right) \right] u_l(r) \Big|_{r=0} = 0\,. \tag{4.22}$$

For $|E| > \mu$, Eq. (4.21) has plane-wave solutions, so that μ is the size of the energy gap. From Eq. (4.21), one can also see that for $|E| < \mu$ there are two solutions, one which decays with increasing r, and one which increases. Which solution is allowed by the boundary condition Eq. (4.22) depends on the sign of μs. The decaying solution is only allowed for positive μs, and the increasing is only allowed for negative μs. Since the solutions have to be normalisable, this reflects that a change of the sign of μ corresponds to a phase-boundary between a topological and a non-topological phase, i.e. the phase $\mu s > 0$ supports edge modes, while the phase $\mu s < 0$ does not [176].

In this analysis, the absolute sign of μ is of no importance: only the sign relative to the boundary condition, represented by the product μs, matters. The boundary condition is, as always, fixed by the microscopic physics, *i.e.* by higher-derivative terms. Taking $h_0 = -\nabla^2/(2M) - \mu$, corresponding to a parabolic band, one will, in the $M \to \infty$ limit, re-obtain the Hamiltonian in Eq. (4.11), together with the boundary condition $s = 1$. Thus, for the usual kinetic term, the topological phase occurs for $\mu > 0$.

Because of Eq. (4.13), the spectrum is symmetric around $E = 0$. For $m = 0$, there is a single solution with $l = 0$, $E = 0$:

$$u_0 = v_0 \sim \frac{1}{\sqrt{R(r)}} e^{-s\mu r/\Delta}\,. \tag{4.23}$$

Note that this zero mode is present for any value of the angle α, as long as $m \in 2\mathbb{Z}$.

There is also a zero mode $\sim e^{-\mu(r_o-r)/\Delta}$ located at the other edge. Strictly speaking, these solutions are correct only for an infinitely extended cone, *i.e.* $r_o \to \infty$. However, they provide a very good approximation, as long as the distance between the edges is large compared to the size Δ/μ of the zero mode, since the overlap with the other edge will be exponentially small. In the limit $R_i \to \infty$, the expression for the full spectrum takes the simple form

$$u_l(r) \sim \exp\left[-\left(\frac{s\mu}{\Delta} + \frac{\cos\alpha}{2R_i}\right) r\right], \tag{4.24}$$

$$E_l = \frac{\Delta}{R_i} ls \ , \tag{4.25}$$

and this also shows that the system contains boundary modes if $\mu s > 0$. Furthermore, the Majorana boundary mode at zero energy occurs only if also $l = 0$, which can only happen when m is even.

It is now possible to answer one of the questions raised in the introduction – what happens when one starts from a cylinder, penetrated by an even number of flux quanta, and slowly squashes it into an annulus by changing the angle α? The zero mode from Eq. (4.23) remains as α is decreased towards zero, but the state will now carry current, as one can see from Eq. (4.19). By using the order parameter ϕ that minimises Eq. (4.19), one sees that for $\alpha < \pi/3$, the state with $n - m = 1$ carries the smallest current, while for $\alpha > \pi/3$ it is the $n - m = 0$ state. Assuming that the energy is a monotonic function of the current, the ground states of the cylinder and the annulus are *not* adiabatically connected. At $\alpha = \pi/2$, which coresponds to the cylinder, the zero-current ground state hosts Majorana states on the edges. Thus, if one makes an adiabatic change of α, the resulting state on the annulus will have a zero-energy mode, but it will not be the ground state. The ground state, on the other hand, will have odd m and thus support no Majorana. However, if one assumes that there is a magnetic field, and one then allows the system to relax to the ground state by a phase slip in ϕ, the resulting state on the annulus will enclose an extra flux and the zero-current state will then support a Majorana.

4.3.3 Edge Modes on the Möbius band

Through the example of a cone, we have shown how inducing a non-local geometric change to a surface can modify the properties of a p-wave superconductor. This occurs because the cone has a curvature defect in the hole,

which vanishes for the annulus, and reaches 2π for the cylinder. However, it is not necessary to introduce curvature defects to create surfaces with non-trivial geometric effects. The Möbius band is a good example of such a surface, and we have already discussed a variety of interesting effects related to its topology. Due to the importance of metric effects in the present discussion, it is pertinent to note that the lowest energy embeddings of a Möbius band in three dimensional space have a flat metric [147], since curvature has an elastic energy associated to it.

Since the Möbius band is not orientable, there is no globally defined orthonormal frame $\{e_a\}_{a=1,2}$. This occurs because the orientation of a basis is invariant under continuous deformations that preserve the linear independence of the basis vectors. Hence, it is impossible to have a uniform chiral superconductor on the Möbius band. However, for large enough systems, it is possible to induce such phases locally through the inclusion of defect lines, analogous to the QHE and the irradiation with circularly polarised light we discussed above. There are two topologically distinct choices for such a defect line, which are depicted in Fig. 4.14. These are minimal, in the sense that you can generate all other domain wall configurations by either deforming these lines, or by adding new lines surrounding contractible regions.

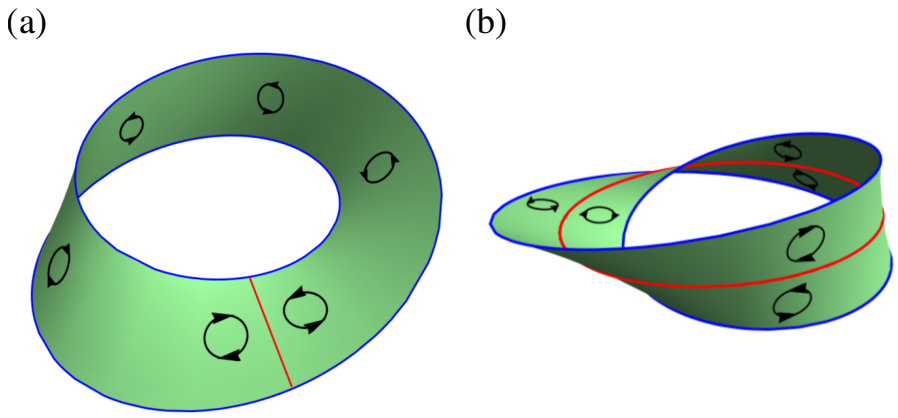

Figure 4.14: Illustration of the two different types of line defects on a Möbius band supporting a chiral superconductor. The edge of the strip is shown in blue, and the line defect is shown in red. The circular arrows indicate the chirality of a p-wave superconducting order parameter that is constant along the strip, except at the defect [54].

The configuration that first comes to mind is a defect along the red line in

Fig. 4.14(a), where one would glue a rectangle to make the Möbius band. In order to perform a microscopic calculation for this configuration, it is necessary to model the behaviour of the order parameter at the end points of the defect, where two normal edge modes of opposite chirality meet to form a double mode along the domain wall. We shall not construct such a model here.

It is more interesting to consider a longitudinal line defect, which lies along the centre line of the Möbius band, as shown in Fig. 4.14(b). By cutting the Möbius band along the defect line, one obtains a cylindrical geometry (the intrinsic geometry is insensitive to the 4π twist), as is depicted in Fig. 4.3(c). Using this, one can explain the presence of Majorana states in the Möbius band by considering the results for the cylinder in the previous section. Imagine that the line defect is not just a line, but is widened to form a thin gap, which is then further widened. Since the model used here only depends on the intrinsic geometry, there would now be no difference from the canonical cylindrical geometry. In this case, it is known when the edge Majorana states exist from the calculations in section 4.3.2. Since closing the gap will only affect the physics locally, at one edge of the cylinder, and since the Majorana states occur and disappear in pairs, the edge Majorana will not disappear when the cylinder is glued back into a Möbius band. With no flux, and for a large enough strip, there will thus be one zero-energy Majorana on the edge of the Möbius band and another at the domain wall.

To first order in the derivatives, the edge mode for the Möbius band will be given by the same solution as for a cylinder, but to better describe the Majorana state density profile at the line defect, it is necessary to take into account second-derivative terms in the Hamiltonian. For example, adding a quadratic derivative makes the Majorana wavefunction change under the addition of a superconducting flux-quantum through the hole, even though it does not change the existence of the mode. To be concrete, take

$$h_0 = -\frac{\nabla^2}{2M} - \mu$$

in Eq. (4.10), where M is the mass of a single Cooper pair. This choice will also explicitly demonstrate the statement made earlier, that higher-order terms select the boundary condition $s = 1$ in Eq. (4.12). Thus, the requirement for the existence of the Majorana state is, in fact, $\mu > 0$.

To construct a coordinate system adapted to the domain wall, let x denote the length along the domain wall, and y the distance perpendicular to it. This is the coordinate system used in Fig. 4.2(a). If the domain wall has length L, the twist in the Möbius band leads to the boundary condition $(L, y) \sim (0, -y)$. This

coordinate system is natural, in the sense that the domain wall is parametrised by the points $(x, 0)$. To find the edge states, we will take $y \in \mathbb{R}$, so that the Möbius band is infinitely wide, which is equivalent to ignoring the exponentially small splitting that will occur between the Majorana particles due to finite-size effects.

Upon crossing the line defect, the chirality of the superconductor should be flipped, as shown in Fig. 4.14(b). For example, if $\phi_+ \neq 0$ on one side of the line defect, then $\phi_- \neq 0$ on the other. This is equivalent to changing ∂_+ into ∂_- in Eq. (4.10) and vice versa, when one crosses the line defect. This procedure can be effected by replacing ∂_- with

$$\tilde{\partial}_- := e_1^\mu \partial_\mu - i\,\mathrm{sgn}(y) e_2^\mu \partial_\mu \ ,$$

and similarly for ∂_+. Because the metric is Euclidean, the connection form vanishes and it is convenient to make the gauge-choice $\phi = \Delta$. This yields the off-diagonal term (see Eq. (4.11))

$$\mathcal{H}_{12} = \frac{1}{2\sqrt{g}}\{\sqrt{g}\phi, \tilde{\partial}_-\} = \Delta\left[\partial_x + i\,\mathrm{sgn}(y)\partial_y + i\delta(y)\right]$$

in the first quantized Hamiltonian $\mathcal{H}$, which becomes

$$\mathcal{H} = \left(-\frac{\nabla^2}{2M} - \mu\right)\sigma^z + \Delta\left(\sigma^x\partial_x + \sigma^y\left(\mathrm{sgn}(y)\partial_y + \delta(y)\right)\right) \ .$$

Next, we make the ansatz $\mathcal{H}(u, v)^T = 0$ to find the solution of the Majorana equation

$$\begin{pmatrix} e^{-i\pi/4}u(y) \\ e^{i\pi/4}v(y) \end{pmatrix} = \begin{cases} \exp(-\alpha_1|y|)\chi & y > 0 \\ \exp(-\alpha_{-1}|y|)\chi & y < 0 \end{cases} \ , \tag{4.26}$$

where χ is a constant column vector and $\alpha_{\pm 1}$ are positive constants. After multiplying the Majorana equation on the left by $\mathrm{diag}(e^{-i\pi/4}, e^{i\pi/4})$ and σ_z, this results in two equations (one for $\xi = 1$ and one for $\xi = -1$),

$$0 = \left[-\frac{\alpha_\xi^2}{2M} + \frac{\alpha_1 + \alpha_{-1}}{2M}\delta(y) - \mu + \Delta(\alpha_\xi - \delta(y))\sigma_y\right]\chi \ .$$

Now, put $\chi = \chi_\epsilon$, where $\epsilon = \pm 1$ and $\sigma_y\chi_\epsilon = \epsilon\chi_\epsilon$. One then obtains

$$0 = -\frac{\alpha_\xi^2}{2M} - \mu + \epsilon\Delta\alpha_\xi \ , \tag{4.27a}$$

$$\epsilon\Delta = \frac{\alpha_1 + \alpha_{-1}}{2M} \ . \tag{4.27b}$$

From Eq. (4.27a), the four possible solutions (recall $\xi = \pm 1$),

$$\alpha_\xi^\pm = -M\left(-\epsilon\Delta \pm \sqrt{\Delta^2 - 2\frac{\mu}{M}}\right) \tag{4.28}$$

are found, which are positive if and only if $\epsilon = 1$ and $\mu > 0$. These solutions are two-fold degenerate since they do not depend on ξ. Then, Eq. (4.27b) is satisfied for the two pairs $\{\alpha_1^1, \alpha_{-1}^{-1}\}$ and $\{\alpha_{-1}^1, \alpha_1^{-1}\}$ in Eq. (4.26). The solution on the Möbius band needs to satisfy $u(y) = u(-y)$, since it must obey $u(x + L, y) = u(x, -y)$ because of the boundary condition. Therefore, there is a unique solution on the Möbius band without flux, which is the symmetric combination of the two solutions in Eq. (4.26),

$$u(y) = -v(y) \propto \left(\exp(-\alpha_1^1|y|) + \exp(-\alpha_1^{-1}|y|)\right) , \tag{4.29}$$

where we used $\chi_+ \propto \left(-e^{i\pi/4}, e^{-i\pi/4}\right)^T$.

It is now instructive to take the $M \to \infty$ limit to obtain the solution without the second order derivative. In this limit,

$$u(y) = -v(y) \propto \exp(-\mu|y|/\Delta) , \tag{4.30}$$

which is indeed the solution that one would obtain with boundary condition $s = 1$ in Eq. (4.12).

4.3.4 Fluxes and vortices in a p-wave Möbius band

We already depicted schematically in Fig. 4.2 how the Möbius band can be obtained by twisting and gluing a rectangle. Using this procedure, the configuration in Fig. 4.14(b), which has a local chirality, can be formed from an oriented system. It is known that cutting a Möbius band along the centre line will produce a cylinder with a 4π twist. Thus, by starting from a chiral state on such a twisted cylinder, and folding the cylinder into a band, as in Fig. 4.14(b), but with a gap instead of a domain wall. One can then close the gap in a limiting procedure, obtaining a Möbius band with chirality as depicted in Fig. 4.14(b).

We will now discuss what happens when a flux is threaded through the hole of the Möbius band. One can understand this configuration by viewing the Möbius band minus the line defect as an embedding of a cylinder, as depicted in Fig. 4.15(b). The winding number around the edge of a flux line passing through the hole in the Möbius strip is two rather than one, and the same holds for the winding number around the line defect. To better understand this statement for the line defect, consider that the latter consists, at each

point, of two edge points glued together, and that this doubling also doubles the winding number. Hence, whatever flux one threads through the Möbius band, it will correspond to twice that amount of flux through the cylinder, as shown in Fig. 4.15(b). Therefore, the magnetic flux through the hole of the Möbius band is not quantized in units of a flux quantum, but in units of half a flux quantum [182, 183]. Because of this behaviour, the Majoranas on the Möbius band can be created/destroyed by the addition of half a unit flux through the central hole.

In contrast, one can still only pierce a unit flux through the surface of the band, which will localize a Majorana at the vortex. This must, at the same time, add or remove a Majorana either on the edge or on the line defect. However, as illustrated in Fig. 4.16, no matter how the flux is pierced through, it will always, when the Möbius band is viewed as a cylinder, wind the edge corresponding to the line defect an even number of times, and thus cannot alter the existence of a Majorana state there.

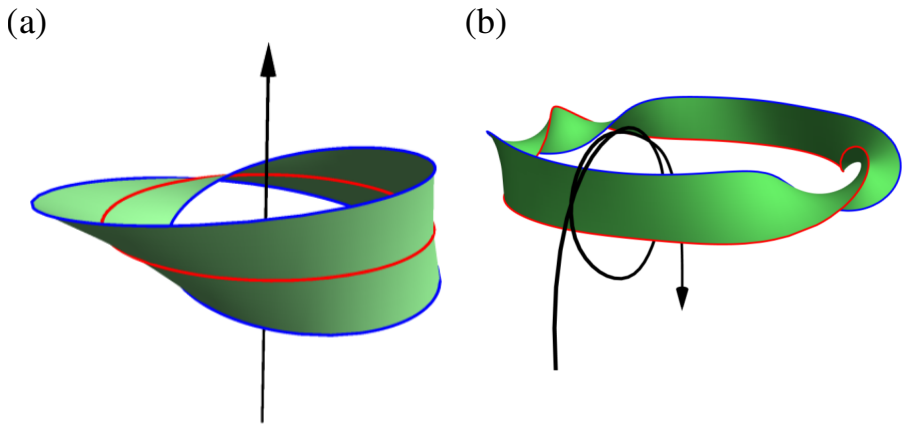

Figure 4.15: (a) The Möbius band with a domain wall configuration (in red), as in Fig. 4.14(b). The arrow depicts a flux quantum threaded through the hole. (b) The Möbius band from (a), but cut along the domain wall. After this cut, the band turns into a cylinder with a 4π twist, and the flux quantum winds around the band twice [54].

As we show now, even though piercing a flux through the Möbius surface cannot destroy the Majorana at the line defect, adding the quadratic derivative term to the Hamiltonian allows one to distinguish different density profiles for the Majorana state across the line defect. Adding a flux through the hole

of the Möbius band corresponds to adding a vector potential $A_x = \pi/(eL)$ in the (x, y) coordinate system constructed for the line defect. In the presence of this vector potential, p_x can only vanish for a solution of the form $\exp(-i\pi x/L)\phi(y)$. To fulfil the condition $u(x + L, y) = u(x, -y)$, one needs a solution antisymmetric in y, and one eventually obtains

$$u(x, y) = -v(x, y) \propto \exp(-i\pi x/L)\mathrm{sgn}(y)\left(\exp(-\alpha_1^1|y|) - \exp(-\alpha_1^{-1}|y|)\right),$$

which, in the $M \to \infty$ limit, becomes

$$u(x, y) = -v(x, y) \propto \exp(-i\pi x/L)\mathrm{sgn}(y)\exp(-\mu|y|/\Delta)\ .$$

Notice that for finite M the density profile $|u(y)|^2$ is different for the symmetric and the anti-symmetric solutions, while for $M \to \infty$ it is not.

4.4 Conclusion

We have shown in this chapter that geometrical effects can have an impact of the topological behaviour of a material. The Möbius band is a specifically interesting example because it is non-orientable, but geometrically simple enough that concrete results can be obtained. Specifically, it is possible to classify the Möbius band in terms of planar systems with reflection symmetry. This allows one to write down the topological classification, but also to analyse the possible lattices that are compatible with a Möbius geometry. One of the main results is that a chiral state cannot exist on the Möbius band due to a lack of orientability. Although a QSHE is possible, the QHE and also p-wave superconductivity cannot exist without domain walls.

In the case of topological superconductivity, geometry has a stronger impact because the p-wave order parameter is vectorial in nature. This implies that the superconducting pairing will couple to the curvature of the surface, an effect which is not topological. We have shown in detail how this works for the cone, where it has consequences for the Majorana zero-mode. Additionally, on the cone a supercurrent is present even in the ground state due to geometric frustration, an effect which we dub the geometric Josephson effect. This effect is expected to be present in any curved 2D p-wave superconductor. Finally an effect which is unique to p-wave superconductivity is that flux tubes trap Majorana particles. This has interesting features in the Möbius band, where the behaviour of such flux tubes is altered due to non-orientability.

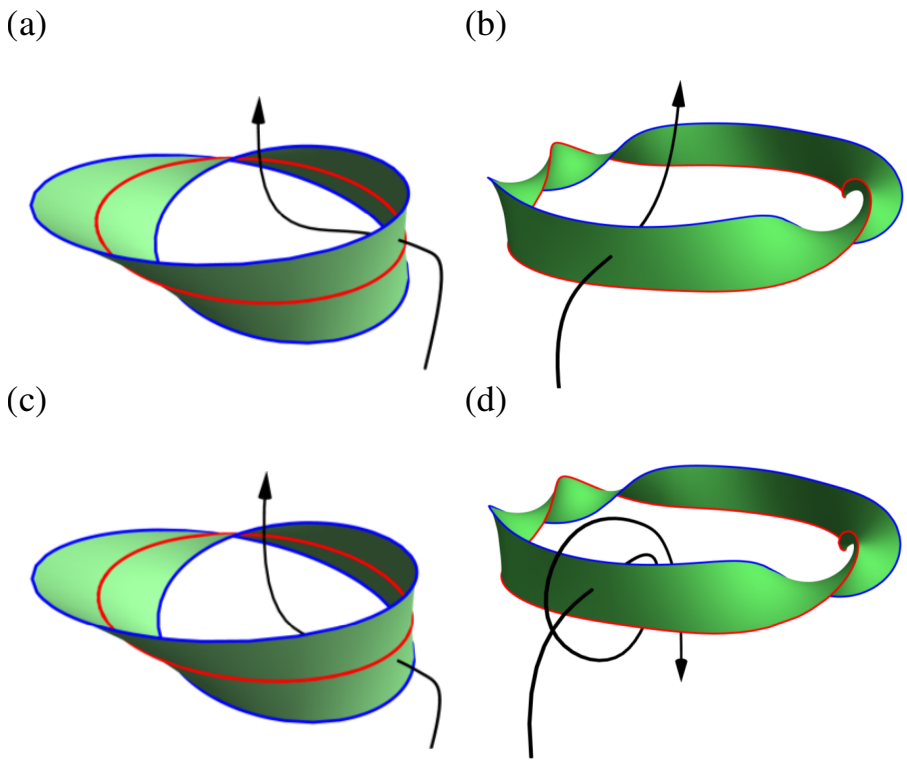

Figure 4.16: (a) One of two inequivalent ways to thread a flux through the surface of the Möbius band. The flux line only encircles the edge, and not the line defect. (b) The situation obtained by cutting the Möbius band from (a) along the line defect. It is explicitly visible that the flux line winds once around the edge, and not around the line defect. (c) One of two inequivalent ways to thread a flux through the surface of the Möbius band. The flux line encircles both the edge and the line defect. (d) The situation obtained by cutting the Möbius band from (c) along the line defect. It is now clear that the flux line winds once around the edge, and twice around the domain wall [54].

CHAPTER 5

Thermodynamic aspects

5.1 Introduction

The previous chapters all discuss aspects of topology by considering electronic structure. A topological phase transition is a so-called quantum phase transition. Here the word phase does not refer to a phase in the thermodynamic sense, but indicates that the ground-state of the quantum system has some fundamentally different structure. In the case of SPTO, this is evidenced by the topological invariants that act as order parameters for the topological phases. These order parameters are calculated for a specific quantum state, usually taken to be the ground state of the system, and characterise its topological properties. Changes in topological phase require a closing of the band gap, or a changing of the symmetry class, and are usually associated with a band inversion. If the gap closes, and the bands invert, the topological order parameter changes, as can be rigorously proven for the Chern number [120]. It is also the driving interpretation behind the $\mathbb{Z}_2$ invariant classifying TIs. The Chern number is odd under time-reversal, so it necessarily vanishes for these systems, but one can count the parity of the number of band inversions.

Experimentally, proving that a certain material is topological is usually also done by considering the electronic properties of a material. In 1D, the topological superconductor described by the Kitaev chain [15] has been realised experimentally, and the topological phase was identified through the

transport properties of the associated Majorana mode [56]. In 2D, for the QHE, the topological invariant directly describes the transverse conductivity of the material, and this can be measured. Similarly, the topological nature of TIs in 2D is usually verified by detecting the topologically protected edge states through transport measurements [9]. For Tis in 3D, one does not need to resort to transport measurements, but the boundary modes can be conveniently described spectroscopically using ARPES [184]. However, ARPES also deals with the electronic structure of a material.

Nevertheless, electronic measurements are not necessarily the only method of detecting topological phases. For example, recent results on the thermal Hall effect show [57, 58], edge modes also make a thermodynamic contribution to the material. This raises the question whether there are other interesting thermal effects associated with topological phases of matter. One can hope that this will lead to additional experimental probes of such systems, for example. Additionally, it is of fundamental interest to understand the thermodynamic aspects of topological phases of matter, not just those originating from the protected edge modes, but also those associated to the phase transition.

In this respect it is important to make a distinction between what we shall call local and global thermodynamics. Here, global thermodynamics refers to thermodynamic quantities describing a system as a whole; these are energy E, entropy S, volume V, particle number N, their conjugate variables, and any additional terms that one might add to the thermodynamic identity. In contrast, local thermodynamics assumes the whole thermodynamic system to consist of many interacting smaller subsystems. The quantities in the thermodynamic identity then become densities, and one considers them and their associated currents. It is common to construct thermodynamic theories from microscopic ones through the methods of statistical physics, but it is important to realise that the thermodynamic framework, and the thermodynamic identity specifically, gives the quantities computed using statistical physics their interpretation. Without the thermodynamic identity, the partition function would merely be a number.

This chapter will concentrate on global thermodynamic properties of topological materials, and how to separate bulk and boundary contributions using the thermodynamic identity only. The logic behind this approach is that topological phases are fundamentally non-local in nature: the associated order parameters are topological invariants depending on the quantum state everywhere. Consequently, detecting a topological phase requires a non-local measurement of some sort, and global thermodynamic quantities provide a natural example. Setting up a correct global thermodynamic theory for topological

materials requires some care, however. At the microscopic level, one usually considers infinite systems without boundaries to calculate topological invariants. The bulk-boundary correspondence then describes what will happen if the system acquires a boundary. However, there is no thermodynamic bulk-boundary correspondence. The thermodynamic potentials only depend on the spectrum of the Hamiltonian, while the topology of the bands depends on the eigenstates: two models can have the same spectrum in the bulk, but different topological characteristics. To describe the thermodynamic behaviour at the edge, one needs to consider a system with edges, so that the edge modes are explicitly present in the spectrum.

However, in that case, the thermodynamic potentials will pick up boundary terms due to the edge modes. In this chapter, we will discuss how to take this contribution into account properly, and what kind of results are obtained when one does so. The theoretical framework was constructed in Ref. [59], while the subsequent results have been published in Ref. [60]. The calculations in Ref. [59] were performed by me, while Dr. Cobanera and Prof. Dr. Morais Smith supervised. The calculations in Ref. [60] were performed by Mr. Kempkes, while I checked the calculations and helped with interpretation; Prof. Dr. Morais Smith supervised the project.

5.2 Global thermodynamics with a boundary

The main issue is to identify the extra degrees of freedom that enter into the thermodynamic framework due to the presence of possible boundary modes in the microscopic system. A very general method to take this into account was developed by Terrell Hill [185]. To reconstruct his reasoning, consider a finite system of size V, in contact with an environment at temperature T and electronic chemical potential μ. We take the extensive variable V to be the number of sites in the lattice associated to a tight-binding model of a topological material. Formally, V must be a fluctuating parameter, which can be achieved by considering a reservoir of ions capable of becoming attached to the lattice. Then, conjugate to V there is a variable ν characterizing the thermodynamic response of the band structure to an increase in the number of lattice sites. Formally, ν behaves like a pressure p, but since its physical interpretation is different, we reserve a separate symbol for it.

5.2.1 Hill Thermodynamics

The basic physical assumption in Hill thermodynamics is still the thermodynamic identity

$$dE = TdS - \nu dV + \mu dN. \tag{5.1}$$

Here S denotes the entropy of the system, and N the number of electrons in it. This is almost a necessity, since it can be considered to define the thermodynamic state variables that classify a system by specifying their impact on the energy. In order to integrate this equation, one usually assumes linearity in S, V, N. This amounts to ignoring anything other than the bulk contribution of a system. The reasoning behind this is that such effects usually become negligible if the system is large enough, in which case one speaks of the thermodynamic limit. If one relaxes extensiveness, Eq. (5.1) is no longer straightforwardly integrated. Although there is this practical concern, it should be noted that there is no fundamental reason to demand extensiveness in the thermodynamic framework. Hill realised that this problem may be overcome in a very astute manner: consider a macroscopic number $\mathcal{N}$ of independent copies of the system, and allow this number of copies to vary. The thermodynamic identity for the total system then reads

$$dE_t = TdS_t - \nu\mathcal{N}dV + \mu dN_t - \hat{\nu}Vd\mathcal{N}, \tag{5.2}$$

where the subscript t stands for the total system, V is the volume of an individual subsystem, and $-\hat{\nu}V$ is a formal thermodynamic response of the system to changes in $\mathcal{N}$. To describe a system with independent state variables T, V, μ, a Legendre transformation to the grand canonical potential Φ will be necessary. To facilitate this eventual step, consider the total system at fixed T, μ, V. Since E must be linear in $\mathcal{N}$, using Euler's theorem one can integrate Eq. (5.2) to get

$$E_t = TS_t - \hat{\nu}V\mathcal{N} + \mu N_t. \tag{5.3}$$

The energy of an individual system may be obtained by dividing Eq. (5.3) by $\mathcal{N}$. Using that $S = S_t/\mathcal{N}$ and $N = N_t/\mathcal{N}$, this gives

$$E = TS - \hat{\nu}V + \mu N. \tag{5.4}$$

This result holds for any V, T, μ system, and Eq. (5.4) is the properly integrated version of Eq. (5.1) for this case. The non-extensive behaviour is naturally incorporated, since $\hat{\nu}$ can depend on V. The energy of a stable thermodynamic system cannot grow faster than its volume, so νV has a leading term

linear in the volume, but $\hat{\nu}$ (and also ν) can now depend on volume to give sub-leading terms. The deviations of Hill's thermodynamics can be naturally separated from the conventional formalism by writing

$$E = TS - \nu V + \mu N + X. \tag{5.5}$$

Here, $X = (\nu - \hat{\nu})V$ defines Hill's subdivision potential; it is an extra degree of freedom that characterises the non-extensiveness of the system. Using this integrated version of Eq. (5.1), it is now possible to perform the Legendre transform to change variables. One still defines $\Phi = E - TS - \mu N$, which results in

$$\Phi = -\hat{\nu}V = -\nu V + X$$
$$d\Phi = -SdT - \nu dV - Nd\mu.$$

It follows that $\nu = -\partial\Phi/\partial V$, but this is only equal to $\hat{\nu}$ if Φ is linear in the volume. Since the thermodynamic identity is still the same as in ordinary thermodynamics, one can repeat the familiar reasoning [186] to recover the relationship from statistical mechanics

$$\Phi = -k_B T \ln \left\{ \mathrm{Tr} \exp \left[-(H - \mu N)/k_B T \right] \right\}. \tag{5.6}$$

In general, this quantity will not be linear in the system volume, and Hill's reasoning has identified the extra thermodynamic degree of freedom associated to this non-linearity. Furthermore, it has revealed a way to define these non-linear contributions purely in terms of an extra thermodynamic state variable.

As an interesting aside, Hill thermodynamics was originally developed for small systems, where highly non-linear thermodynamic potentials are computed by considering an independent ensemble of such systems [185]. The approach also works if the individual small systems are not independent, since it allows for a systematic computation of potentials from statistical mechanics [187–189]. Interestingly, Hill thermodynamics is just as necessary for systems as large as gravitationally bound systems [190], where conventional thermodynamics fails to apply because the gravitational force is long-ranged and universally attractive.

Topologically non-trivial states of electronic matter belong to neither one of these categories. What makes the subdivision potential important for TI's is the strong dependence of the spectrum on the boundary conditions, due to the bulk-boundary correspondence. Since the boundary is small compared to the bulk, systems with a strong behavioural dependence on boundary conditions are in a sense small themselves, and hence Hill's thermodynamics is the natural framework to describe them.

5.3 Gibbs thermodynamics

The generality of Hill thermodynamics makes it an attractive viewpoint from which to interpret the statistical physics of topological materials. Nevertheless, there is an alternative formalism that also serves. Specifically, Gibbs has developed a method to describe boundary effects in thermodynamics, which was originally used to describe classical fluids [191]. This method is less general than the one developed by Hill, but it also serves as a source of insight. Therefore, we discuss it now, and we will also use it later. In 1878, Gibbs described a thermodynamic approach to surface tension relying on the hypothesis that bulk and boundary could be treated as independent systems, in some approximate sense. In Gibbs' approach, the free energy of the fluid system acquires a term proportional to a suitable power (e.g. $2/3$) of the volume. The phenomenological success of Gibbs' approach is remarkable, since there is no sharp surface associated to any actual microscopic fluid system.

In Gibbs' approach, based on the conventional linear regime of thermodynamics, one retains linearity by absorbing the non-linear terms into the thermodynamic identity. We will show how the argument works if the only non-linear contribution scales with the system boundary. As a starting point, one treats the surface of the system as a separate thermodynamic system with its own energetics, independent from the bulk. Consider, for example, a bulk system B with a boundary b. The bulk system will have energy

$$U_B = S_B T_B - \nu V + N_B \mu_B,$$

and the boundary has its own energy

$$U_b = S_b T_b - \gamma A + N_b \mu_b,$$

where A is the area of the boundary, and γ the corresponding conjugate variable. Applying the equations of thermodynamic equilibrium, $T_B = T_b = T$ and $\mu_B = \mu_b = \mu$, the total energy U reads

$$U = T(S_B + S_b) - \nu V - \gamma A + \mu(N_B + N_b).$$

Considering the grand potential $\Phi_i = U_i - S_i T_i - \mu_i N_i$ for both subsystems, and defining the total grand potential $\Phi = \Phi_B + \Phi_b$, one obtains

$$\Phi = -\nu V - \gamma A. \tag{5.7}$$

Because the bulk and the boundary are separate systems, with their own grand potential, the thermodynamic identity reads

$$d\Phi = -S dT - N d\mu - \nu dV - \gamma dA. \tag{5.8}$$

This is different from the Hill approach: in the Gibbs approach, the extra degree of freedom is inserted into the thermodynamic identity, and then linearity is assumed. This enforces ν and γ to be independent of both V and A, which is the same as neglecting any terms scaling slower than the system boundary in Φ.

It is also possible to consider the bulk and boundary as a connected system in the Gibbs approach. In that case, one writes $A(V, \mu, T)$, so that

$$dA = \frac{\partial A}{\partial T} dT + \frac{\partial A}{\partial \mu} d\mu + \frac{\partial A}{\partial V} dV. \tag{5.9}$$

By using this identity, Eq. (5.8) becomes formally equivalent to Eq. (5.1). The net result of Eqs (5.8) and (5.9) is, therefore, the inclusion of the non-linear term in Eq. (5.7). In principle, one could extend the theory by any number of non-linear terms in this way. The advantage of Hill's reasoning is that it explicitly couples a thermodynamic state variable to these non-linear terms. However, for applications we can equally well use Gibbs' reasoning. The advantage of the Gibbs approach is that it formalises the notion that an area term should capture boundary physics.

Although the subdivision potential X, and hence the boundary behaviour, can be obtained from Φ by looking the scaling behaviour as a function of volume, there is no general way to separate topological from non-topological boundary behaviour. However, there is a natural way to define an effective boundary theory for non-trivial topological insulators: diagonalise the Hamiltonian, and single out boundary states based on the localisation of the eigenfunctions. This effective theory turns out to be a powerful tool in interpreting results when applicable. However, first it is necessary to find the regime where the only relevant contributions to the free energy are the bulk and the boundary terms. In the next section, we present an in-depth discussion of when this can be expected to hold.

5.4 Scaling of the grand canonical potential

We will do this by applying the developed formalism to the paradigmatic Bernevig-Hughes-Zhang (BHZ) model describing HgTe/CdTe quantum wells [8]. This model is important because the QSHE was first measured in such quantum wells, as described in Chap. 2.3.2. The Hamiltonian on the infinite plane will decompose as

$$H = \int_{BZ}^{\oplus} H_k, \tag{5.10}$$

and the Bloch Hamiltonian reads

$$\begin{aligned} H_k = &- A\sin(k_x)\sigma_x - Ai\sin(k_y)\sigma_y \\ &+ \{M + 2B[2 - \cos(k_x) - \cos(k_y)]\}\,\sigma_z \end{aligned} \tag{5.11}$$

Here, k_i denotes momentum in the i direction, σ_i are 2×2 Pauli matrices, with $i = x, y, z$, and A, B and M are parameters depending on the thickness of the quantum well. For $M < 0$, the system is in a topologically non-trivial phase, whereas for $M > 0$ the gap is trivial. It should be noted that this Hamiltonian can also be written in terms of a NN hopping model. We consider a ribbon with a finite width W and a length $L = 600 \approx \infty$ (so that $V = LW$), and impose the corresponding boundary conditions on the NN hopping form of Eq. (5.11), which is given in Appendix C. Then, we calculate the grand potential Φ/L numerically according to Eq. (5.6).

We will show, by analysing Φ/L using Hill thermodynamics, that there is a regime where there are only two relevant terms in Φ, so that one can write

$$\frac{\Phi(\mu, T, WL)}{L} = \Phi_0(\mu, T) + \Phi_c(\mu, T)W. \tag{5.12}$$

Here, $\Phi_0 = X/L$ is essentially the subdivision potential of the BHZ model. Gibbs thermodynamics then provides the interpretation of Φ_c as a bulk term, and Φ_0 as a boundary term. In what follows, we will take $A = B = 1$. In Fig. 5.1, we show the behaviour of the full grand potential per unit length Φ_W, as given by Eq. (5.6) for sample width W. In Fig. 5.1**a**, it can be seen that Φ_W is apparently linear. In Fig. 5.1**b**, we plot $\Phi_W - \Phi_c$, to show the deviations from linearity. Here, Φ_c was determined by fitting the ansatz Φ from Eq. (5.12) to Φ_W for the range $W \in [40, 100]$, to ensure that the fit is performed in the linear regime. It can be seen that for small W, there is a small deviation from linearity, as the system is so small that it cannot quite be seen as the sum of a bulk and a boundary. For large W, $\Phi_W - \Phi_c$ converges to a constant value, which is just Φ_0. This already indicates that Φ_W is approximated quite well by Eq. (5.12) for large W.

However, for additional rigour, we will analyse the size of the further subleading corrections in more detail. These subleading terms, as a function of W, depend on μ and T, and also on the gap size, which is determined by M. To analyse the deviations from Eq. (5.12), we will vary μ, T, and M, and study the relative error $(\Phi_W - \Phi)/\Phi$ by means of a fit, where Φ is the projection onto the leading terms in Eq. (5.12).

In Fig. 5.2, the relative error has been plotted for the trivial phase $M = 1$ at $T = 0$, with $W \leq 100$, although the fitting was done for $40 \leq W \leq 100$, where

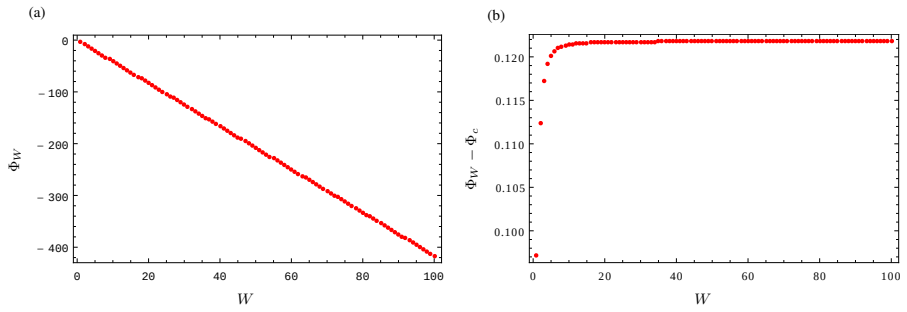

Figure 5.1: **a** The full grand potential Φ_W as defined by Eq. (5.6). The parameter values are $M = \mu = T = 0$. At first sight, Φ_W seems perfectly linear, but there is a constant offset, and for small W additional deviations can be seen. **b** These deviations, given by $\Phi_W - \Phi_c$, where Φ_c is determined by Eq. (5.12), are shown. It can be seen that Φ_W is not linear for small W, and that the error converges to a constant offset Φ_0.

the linear behaviour in W has set in. In this way, one observes the deviations from Eq. 5.12 at small W. The results are shown in Fig. 5.2**a** and **b** for $\mu = 0$, i.e. in the gap. Similarly, the results are shown in Fig. 5.2**c** and **d** for $\mu = -4/3$, i.e. in one of the bulk energy bands. One can see that for very small system width, there is a large deviation from the linear relation in Eq. (5.12), but the error quickly decreases. For μ in the gap, the error rapidly becomes negligible, while for μ in one of the energy bands, the error is much larger, and also shows a clear structure (notice the unequal scales 10^{-16} in Fig. 5.2**b** and 10^{-7} in Fig. 5.2**d**). A likely cause of this error is the discreteness of the spectrum, which causes Φ_W to deviate from Φ as the system width changes. This deviation occurs because varying the system width causes individual energies jump from above to below the chemical potential and vice versa. In the gap there are no states near the chemical potential, so this effect is absent, significantly reducing the error.

In Fig. 5.3, the relative error is plotted for $\mu = -4/3$ at $T = 0$ and $M = 1$ for a fit along $500 \leq W \leq 550$. The relative error has decreased by two orders of magnitude compared to Fig. 5.2**d**, which means that the absolute error has decreased by one order of magnitude. This implies that the energy spectrum becomes less dependent on W as W increases. Furthermore, the behaviour of the relative error is qualitatively similar if one takes $M = -1$, which puts the system in the topological phase, which shows that the presence of the edge states does not influence the qualitative behaviour of the bulk spectrum.

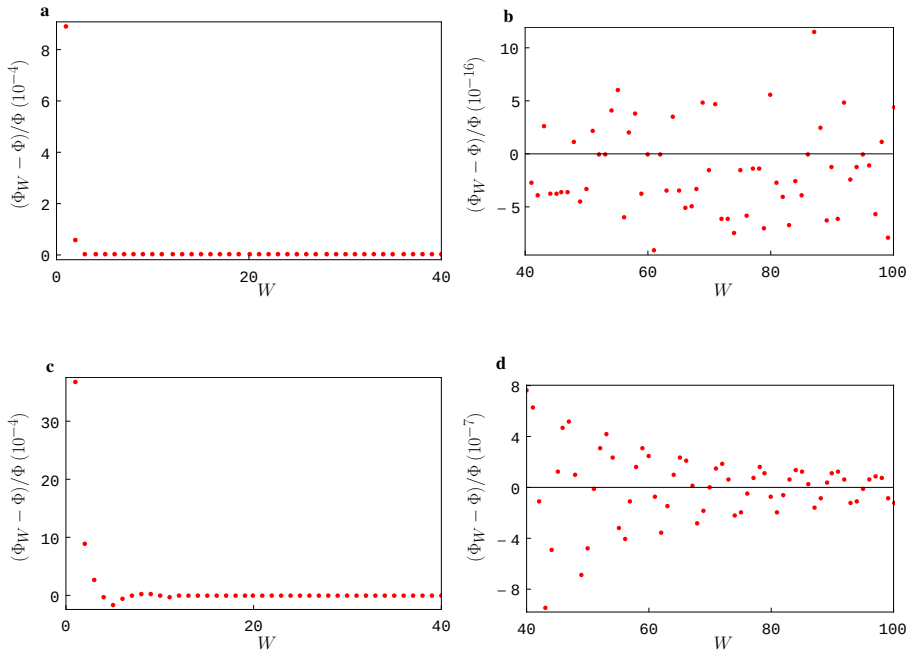

Figure 5.2: **a** The relative error between Φ_W and Φ, for $\mu = T = 0$ and $M = 1$. We have fitted along the interval $40 \leq W \leq 100$. **b** Same as in **a** but the range of W has been changed. **c** Same as in **a** but for $\mu = -4/3$. **d** Same as in **b** but for $\mu = -4/3$ [59].

When the gap becomes much smaller, the conclusions above still hold, but the width W above which the error becomes negligible is larger. In Fig. 5.4**a**, the relative error has been plotted for $\mu = T = 0$ at $M = 0$, for a fit along the values $90 \leq W \leq 100$. The errors show that the linear regime from Eq. (5.12) has not set in yet. In contrast, Fig. 5.4**b** shows a fit along $1000 \leq W \leq 1010$, for the same parameters, and here a linear scaling clearly holds.

Finally, in Fig. 5.5, the relative error is shown for $M = -1$, $\mu = -2$ for a fitting interval of $50 \leq W \leq 100$. In Fig. 5.5**a**, where $T = 1/100$, the relative error is of the same order of magnitude as in Fig. 5.2**d**, indicating that the temperature is not yet high enough to suppress the fluctuations. In Fig. 5.5**b**, where $T = 1/10$, the relative error has decreased by orders of magnitude, indicating that the smoothing of the Fermi-Dirac distribution at these temperatures suppresses the fluctuations in the energy spectrum.

These results indicate that Eq. (5.12) correctly describes the relevant fea-

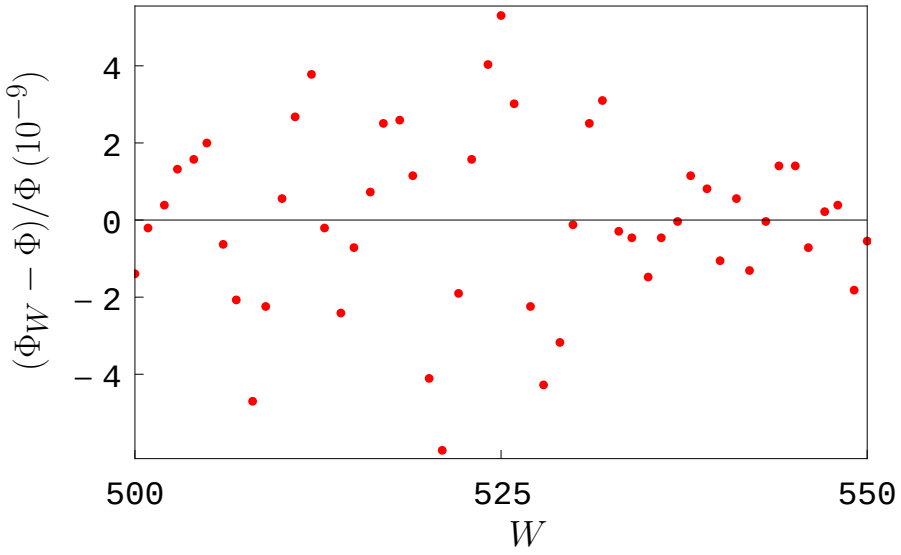

Figure 5.3: The relative error between Φ_W and Φ, for $T = 0$, $\mu = -4/3$, and $M = 1$. We have fitted along the interval $500 \leq W \leq 550$ [59].

tures of the model for large W. This occurs because the edge states merge into the bulk at the phase transition, and an effective theory can only be expected to hold if the system is larger than the decay length of the edge states. Alternatively, the low-energy theory becomes conformally invariant at the topological phase transition, so an ansatz of the form Eq. (5.12) cannot be correct. However, for systems larger than a floating cutoff width W_0 depending on the gap size, Eq. (5.12) holds as a generalised thermodynamic limit. Consequently, if one wants to correctly describe the phase transition, one needs to keep the system size above the floating cutoff. The generality of Hill thermodynamics provides a convenient way to show that such a floating cutoff exists, and what its value is. From Eq. (5.12), it is readily derived that $\nu = -\Phi_c$ and $\hat{\nu} = -\Phi_c - \Phi_0/W$, which indeed become equal as $W \to \infty$, as expected for large systems.

5.5 Applications

These results generalise to different dimensions in a straightforward manner. By considering a system with a finite width W in one direction, and a length

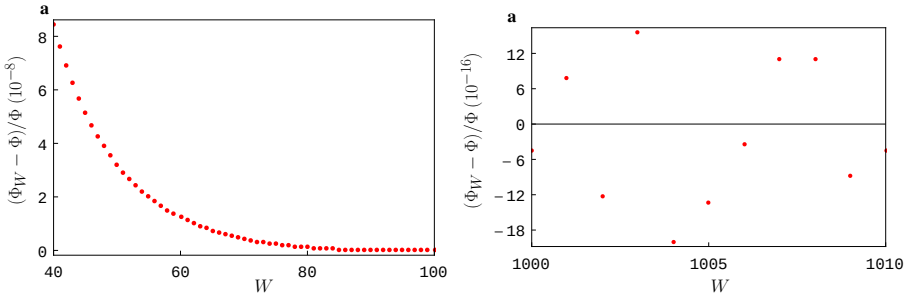

Figure 5.4: **a** The relative error between Φ_W and Φ, for $T = 0$, $\mu = 0$ and $M = 0$. We have fitted along the interval $90 \leq W \leq 100$. It can be seen that the linear regime has not set in for this system size. **b** The same as in **a**, but for $1000 \leq W \leq 1010$. The linear regime has set in, and the error is negligible [59].

$L = \infty$ in $d-1$ other directions, one gets

$$\frac{\Phi(\mu, T, WL^{d-1})}{L^{d-1}} = \Phi_0(\mu, T) + \Phi_c(\mu, T)W. \tag{5.13}$$

Using the thermodynamic identity, various thermodynamic responses can be calculated, and due to Eq. (5.13), these naturally split into a boundary and a bulk contribution.

5.5.1 Bernevig-Hughes-Zhang model

We first discuss the results of applying this procedure to the BHZ model from Eq. (5.11). In Fig. 5.6**a** and Fig. 5.6**c** (Fig. 5.6**b** and Fig. 5.6**d**), we plot the $T = 0$ ($\mu = 0$) density of states (heat capacity at constant volume) for the bulk (B) $D^B := -\partial^2\Phi_c/\partial\mu^2$ ($C_v^B := -T\partial^2\Phi_c/\partial T^2$) , and for the boundary (b) $D^b := -\partial^2\Phi_0/\partial\mu^2$ ($C_v^b := -T\partial^2\Phi_0/\partial T^2$) in red and in blue, respectively. In Fig. 5.6**a** (Fig. 5.6**b**), the system is in the trivial phase $M = 1$, whereas in Fig. 5.6**c** (Fig. 5.6**d**), the system is the topological phase $M = -1$.

The data show clearly that D^B vanishes in the energy gap $|\mu| < 1$ both in the topological and in the trivial phase (notice that the bulk curves have been vertically displaced from zero to increase visibility). However, due to the presence of edges, there is also a non-vanishing contribution D^b. To interpret this contribution, it is important to note that Φ_0 contains not just the topological edge states, but also other non-topological boundary effects, as evidenced by the finite value of Φ_0 even if $M > 0$. Outside the gap, these non-topological effects are dominated by the discreteness of the spectrum, and D^b is numerical

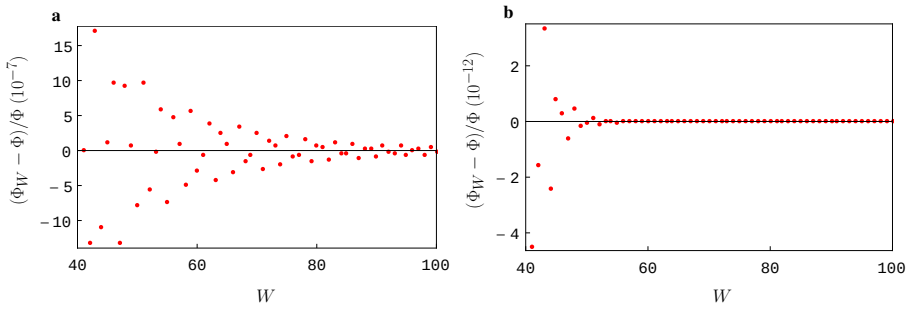

Figure 5.5: **a** The relative error between Φ_W and Φ, for $k_BT = 1/100$, $\mu = -2$ and $M = 1$. We have fitted along the interval $50 \leq W \leq 100$. The errors are of the same order as in Fig. 5.2**d**. **b** The same as in **a**, but for $k_BT = 1/10$. The errors are significantly smaller, since the temperature effectively smooths out the energy spectrum [59].

noise. This noise vanishes in the thermodynamic limit, where the discreteness of the spectrum vanishes, but this cannot be obtained numerically. The noise also becomes reduced in magnitude for non-zero temperatures, which smooths out the discreteness of the spectrum, or by fitting Eq. (5.12) to a larger range of W values. Nevertheless, despite the noise, a non-zero value of the boundary density of states can also be seen outside the gap, showing a charge redistribution on the edge due to non-topological effects. It should be noted that the boundary contribution is a correction to the bulk value, so a negative boundary density of states should be interpreted as a slight charge depletion away from the edge.

On the other hand, the energy spectrum of the edge states is much less dependent on the width W, and not subject to noise. Inside the gap, $D^B = 0$ and the scaling of the density of states with W vanishes, making D^b the only term for all system sizes. In this case, it can be interpreted as the density of topological edge states, since finite-size effects only show up in combination with bulk behaviour. Indeed, the Dirac states at the edge disperse with $E = Ak + \mathcal{O}(k^3)$ [192], yielding a density of states (DOS) $D = 1/(A\pi)$ at $\mu = 0$ from microscopic arguments; the line $1/\pi$ (obtained by putting $A = 1$) has been added in green in Fig. 5.6**c**.

To first order in T, the heat capacity behaves as

$$C_v = \frac{\pi k_B}{3A} T \tag{5.14}$$

since a Dirac fermion has conformal charge 1 [193]. Hence, to linear order the

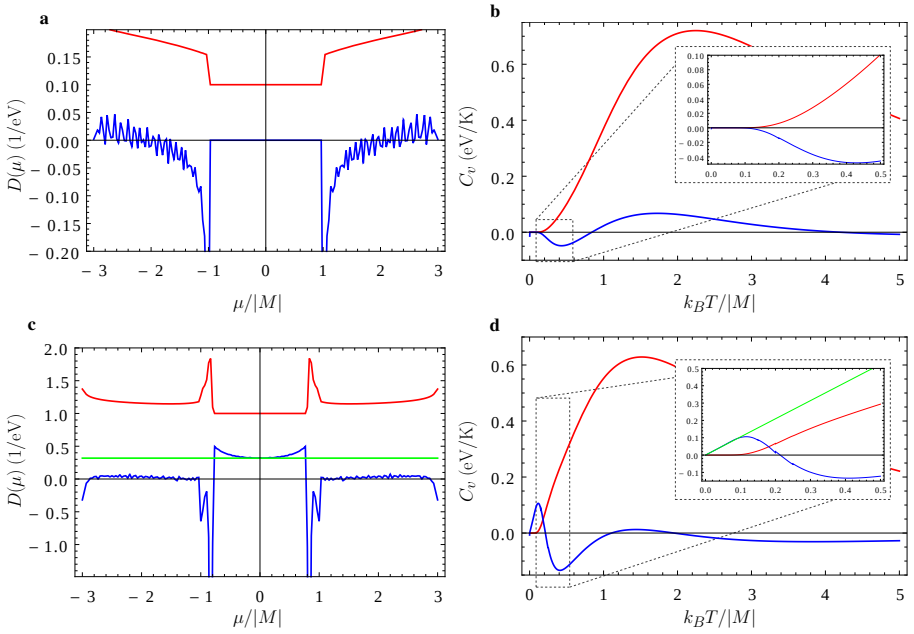

Figure 5.6: **a** In red, $D^B(\mu)/W$ is shown for $M = 1$; it has been shifted up by 0.1 for greater visibility. As expected, it vanishes in the energy gap. In blue, $D^b(\mu)$ for the same parameters, which is the DOS on the edge. Since the system is not in a topological phase, the DOS at the edge also vanishes in the gap. **b** In red, $C_v^B(T)/W$ is shown as a function of T for $M = 1, \mu = 0$. As expected, it vanishes to linear order as $T \to 0$. In blue, $C_v^b(T)$ for the same parameters. Since the system is not in a topological phase, C_v^b also vanishes to linear order as $T \to 0$. **c** The same as in **a**, except that the red curve has been shifted upwards by 1, and the system is in the topological phase $M = -1$. Furthermore, the line $1/\pi$ has been added in green to emphasise that the edge has a non-vanishing DOS in the gap. **d** The same as in **b**, but in the topological phase $M = -1$. One sees that C_v^b now is linear at the edge for low T. In the inset, the straight line with slope $\pi/3$ has been added to emphasise the linear scaling of C_v^b with temperature [59].

bulk C_v^B necessarily vanishes at low temperatures for $\mu = 0$. However, while one expects the boundary C_v^b to vanish at low temperatures in the trivial phase at $M = 1$ (Fig. 5.6**b**), for the topological phase with $M = -1$ the specific heat amounts to $C_v^b = \pi k_B T/3$, which can be obtained by simply substituting $A = 1$ into Eq. (5.14). Indeed, in Fig. 5.6**d**, one can observe a linear scaling of C_v^b at low temperatures. In the inset, the green line with slope $\pi/3$ has been added to confirm that the low temperature heat capacity derives from the edge states.

In both of these cases, the Φ_0 term in Eq. (5.12) could not be dropped because a derivative of Φ_c vanished, and hence the contribution from Φ_0 became dominant. This shows that for edge effects to become irrelevant, it is not only required that $\hat{\nu} \to \nu$, but that this also holds for all derivatives. There is another situation where the derivatives of $\hat{\nu}$ fail to converge, which is if a phase transition occurs at the boundary. In Fig. 5.7, we depict the behaviour of the thermodynamic potential in terms of the parameter M that controls the topological phase transitions in the BHZ model. In Fig. 5.7**a**, $\partial^2\Phi_c/\partial M^2$ is shown, which exhibits a slightly smoothed kink at $M = 0$. This smoothing is precisely as large as the sample spacing in M from which we interpolated to obtain the graph, indicating that it is a numerical artefact. The inlay shows $\partial^3\Phi_c/\partial M^3$, which is discontinuous at $M = 0$. Calculating the same graph for the system on an infinite plane yields the same behaviour, except that the kink is sharper. Therefore, the closing of the band gap is detected by the bulk free energy and characterised as a third-order phase transition. It is reminiscent of a lambda phase transition, and the divergence occurs in the non-topological regime. In contrast, Fig. 5.7**b** shows that $\partial\Phi_0/\partial M$ exhibits a kink. The inlay shows that the transition is again of lambda type, with the divergence occurring in the non-topological regime, but this time the order is different: the edge undergoes a second-order phase transition. All correlation lengths diverge at the gap closing; this also holds for the edge states, which merge into the bulk as the gap closes. This makes it difficult to distinguish topological and non-topological boundary effects. Nevertheless, it is possible to at least predict the order of the phase transition. The relevant model describes a Dirac mode on the edge with an energy cutoff equal to M. This model correctly describes a second-order phase transition, but it does not capture the divergence at the trivial side, since the grand canonical potential for this effective model vanishes there. This suggests a cause for the thermodynamic phase transition: the dominant contribution to the boundary effects changes from topological to non-topological, and due to their qualitatively different behaviour, a phase transition is observed.

This mixing between topological and non-topological boundary effects might cause doubt whether Φ_0 truly detects a thermodynamic phase transi-

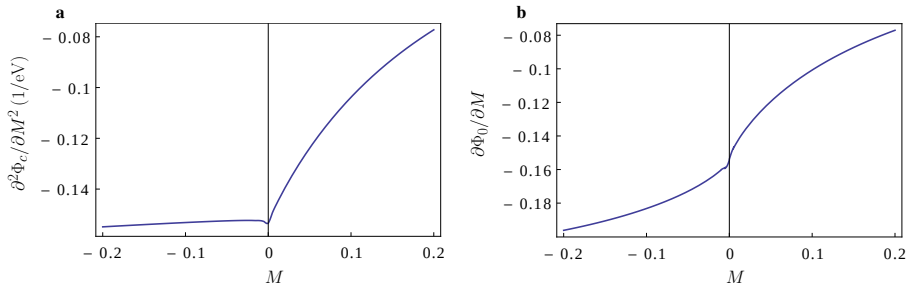

Figure 5.7: **a** The second derivative $\partial^2\Phi_c/\partial M^2$ is shown as a function of M. A kink is visible at $M = 0$, indicating that the bulk undergoes a third-order phase transition (see the inlay, where the discontinuity in the third derivative is depicted). **b** The first derivative $\partial\Phi_0/\partial M$ is shown as a function of M. A kink is visible at $M = 0$ indicating that the edge undergoes a second-order phase transition (the discontinuity in the second derivative is depicted in the inlay), which can be considered the order of the topological phase transition [59].

tion related to the appearance of topological edge states, rather than an echo of the bulk phase transition. This issue can be clarified by adding an on-site superconducting pairing to the BHZ-model. The same effect and results would be obtained from induced superconductivity on the edge [194]. The Bloch Hamiltonian for this system is

$$H_{\Delta,k} := \begin{pmatrix} H_k & \Delta \\ \Delta & -H_k^* \end{pmatrix}, \tag{5.15}$$

where H_k is the Hamiltonian from Eq. (5.11) and Δ is the superconducting pairing parameter. By adding superconductivity, one has added particle-hole symmetry to the system; the bulk stays gapped, but now the gapless edge states acquire a mass Δ [195]. Since the gap does not close, Φ_c is a smooth function of Δ, and no phase transition occurs in the bulk. However, the subdivision potential Φ_0 detects the opening of the mass gap for the Dirac electrons at the edge as a continuous boundary phase transition. This can be seen in Fig. 5.8, where $\partial^2\Phi_0/\partial\Delta^2$ is shown in blue. A clear divergence is present in $\partial^2\Phi_0/\partial\Delta^2$ at $\Delta = 0$, where the particle-hole symmetry is broken.

Because adding a Cooper pairing does not merge edge states into the bulk, but only gives them a mass, it is possible to describe a phase transition in Δ using an effective boundary theory, and thereby confirm our interpretation.

This theory reads

$$H_{e,k} := k\sigma_x + \Delta\sigma_z, \tag{5.16}$$

with a momentum cutoff $|k| < 1$ (since $A = B = -M = 1$, the edge states exist only for this range of k values). The free energy per unit length of $H_{e,k}$ is

$$\begin{aligned}\Phi_e &= \int_{-1}^{1} \sqrt{k^2 + \Delta^2}\, dk \\ &= \Delta^2 \ln\left(\frac{1 + \sqrt{1 + \Delta^2}}{\Delta}\right) + \sqrt{1 + \Delta^2}.\end{aligned} \tag{5.17}$$

The corresponding value of $\partial^2\Phi_e/\partial\Delta^2$ is shown in Fig. 5.8 in green. The divergence at $\Delta = 0$ indicates a continuous phase transition due to the appearance of gapless edge modes in Eq. (5.16). The behaviour of the subdivision potential Φ_0 is compatible with that of Φ_e, indicating that Φ_0 truly detects topological edge behaviour, since it gives the same qualitative results as an effective boundary theory.

5.5.2 Kane and Mele model

The above considerations can be repeated for another 2D model, which is the Kane and Mele model introduced in Eq. (2.5). For simplicity, we put $t_3 = t_4 = 0$. In Fig. 5.9**a-d**, we display the results for the conventional potential and its derivatives for $t_1 = 2$, and $t_2 = 0.2$ and different values of m. One observes a second-order phase transition at the edge (Fig. 5.9**c**) and a third-order one in the bulk (Fig. 5.9**d**). The order of the phase transitions is therefore identical to those in the BHZ model.

The behaviour of the DOS and the specific heat are also qualitatively similar. In Fig. 5.10**a**, the density of states $D_i = -\partial^2\Phi_i/\partial\mu^2$ has been shown for the chosen parameters. For $\mu < 0.52$, the Fermi energy is in the gap, and the topological edge states show up in the boundary DOS. In Fig. 5.10**b**, the heat capacity $C_{V,i} = -T\partial^2\Phi_i/\partial T^2$ is depicted. At the boundary, the heat capacity is linear in T at low temperatures, indicating an edge DOS. Both these results are analogous to those previously discussed for the BHZ model.

The 3D Bernevig-Hughes-Zhang model

There is also a topological phase of matter in 3D time-reversal invariant materials, such as Bi_xSb_{1-x} [196]. This phase belongs to the same symmetry class as the 2D QSHE, but in one dimension higher. The topological invariant is

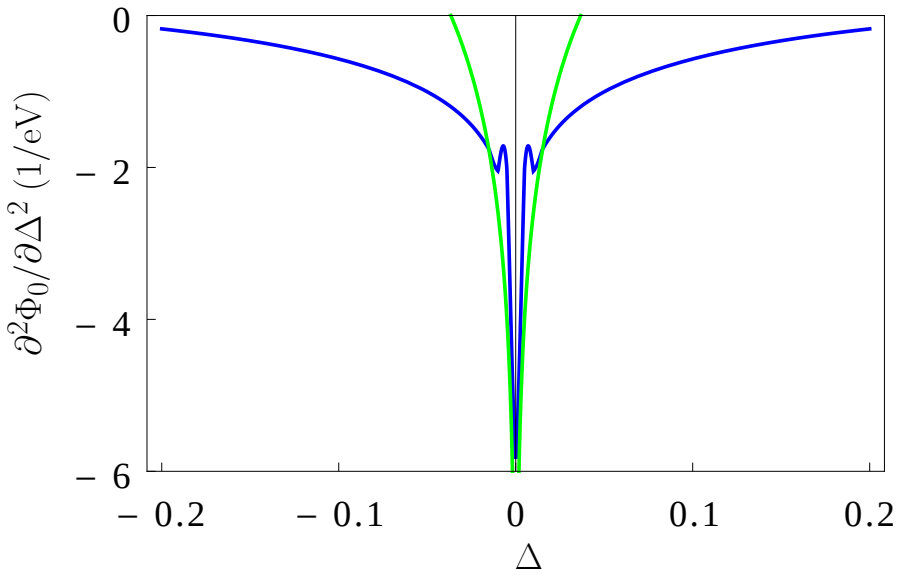

Figure 5.8: In blue, $\partial^2\Phi_0/\partial\Delta^2$ is shown as a function of Δ. The smoothing of an infinite peak is visible, which indicates the presence of a third-order phase transition at the boundary of the system. In green, $\partial^2\Phi_e/\partial\Delta^2 + 6$ is shown, using Eq. (5.17). The agreement between the two curves indicates that the phase transition at the edge of the model comes from the opening of a gap for the edge states [59].

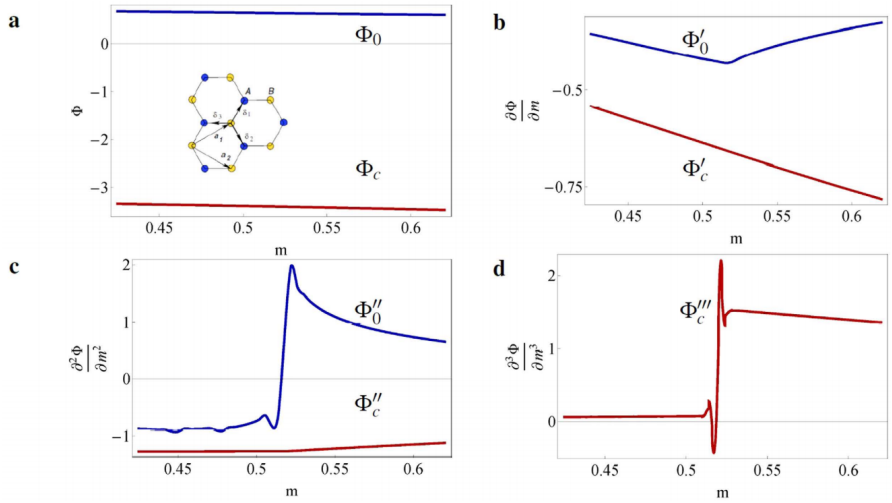

Figure 5.9: **a** The conventional potential Φ_c (red) and the subdivision potential Φ_0 (blue) and (**b, c, d**) their derivatives with respect to m for the Kane-Mele model with $t_1 = 2$, and $t_2 = 0.2$. The inset in **a** shows the honeycomb lattice of graphene, where the A and B sublattices are depicted in blue and yellow respectively. The phase change occurs at $m = 0.52$. The subdivision potential shows a discontinuity in the second derivative (**c**), whereas the conventional potential shows a discontinuity in the third derivative (**d**) [60].

also $\mathbb{Z}_2$ valued, and has roughly the same interpretation as its 2D cousin. The Hamiltonian to describe these 3D models is related to the BHZ model, and it looks as follows [196]

$$H_{\text{BHZ}}(\mathbf{k}) = \begin{pmatrix} M(\mathbf{k}) & A_2 k_+ & 0 & A_1 k_z \\ A_2 k_- & -M(\mathbf{k}) & A_1 k_z & 0 \\ 0 & A_1 k_z & M(\mathbf{k}) & -A_2 k_- \\ A_1 k_z & 0 & -A_2 k_+ & -M(\mathbf{k}) \end{pmatrix}, \tag{5.18}$$

where $M(\mathbf{k}) = M - B_1 k_z^2 - B_2(k_x^2 + k_y^2)$, M, A_1, A_2, B_1, and B_2 are constant parameters of the model, and $k_\pm = k_x \pm i k_y$. In the numerical calculations, we set these parameters to one and rewrite the matrix into a tight-binding description, the result of which is given in Appendix C. In Fig. 5.11**a-d**, we show the results for the thermodynamic potentials and their derivatives for the 3D BHZ model. The phase transition occurs for $M = 0$ and is third-order at the edge and fourth-order in the bulk. Note that both these phase transitions are one order

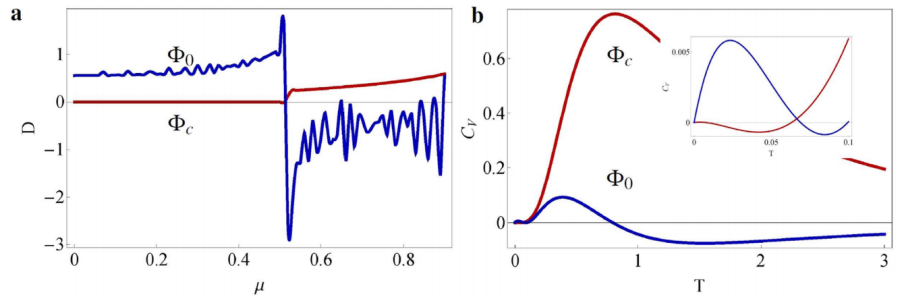

Figure 5.10: **a** At $T = 0$, the density of states scales with the velocity of the electrons and is zero in the bulk (red) for $\mu < 0.52$ (before the first conduction band), whereas at the boundary, the density of states should drop to zero after $\mu = 0.52$ (blue). The noise for the boundary is due to numerical errors. **b** The heat capacity for the bulk (red) and the boundary (blue) for $\mu = 0$. The inset shows the details of the low-T behavior. The negative value of the heat capacity should be interpreted as a lower total heat capacity for the whole system. The total heat capacity is always positive [60].

higher than those observed in 2D. In Figs. 5.11**b** and **c**, the features in Φ_0'' and Φ_c''' are kinks, and not discontinuities, although the precise feature is distorted by numerical errors. That this is so can be seen for the bulk by considering a generalisation of Eq. 5.17 to different dimensions. In this case, Δ has the interpretation of a mass-gap, and the free energy is that of a massive Dirac cone in d dimensions. This predicts a bulk phase transition of order $d + 1$, which is precisely what has been observed for the 2D BHZ model and the Kane & Mele model, and which implies a fourth order bulk phase transition here.

5.5.3 Kitaev chain

The Kitaev chain is a 1D topological superconductor, with a Z_2 topological invariant [15]. It is in the same symmetry class as the 2D p-wave superconductor we discussed in Chap. 4, but in one dimension lower. For the hopping parameter equal to Cooper pairing density, $t = \Delta$, it is dual to the Ising model [197], and it has long been known in this context. The interpretation of this model as describing a superconductor hosting a topological phase was proposed by Kitaev [15], however, and as a consequence, the model is named after him.

The Kitaev chain describes the recently realized superconducting phase in indium antimonide (InSb) quantum wires contacted with a normal (Au) and a

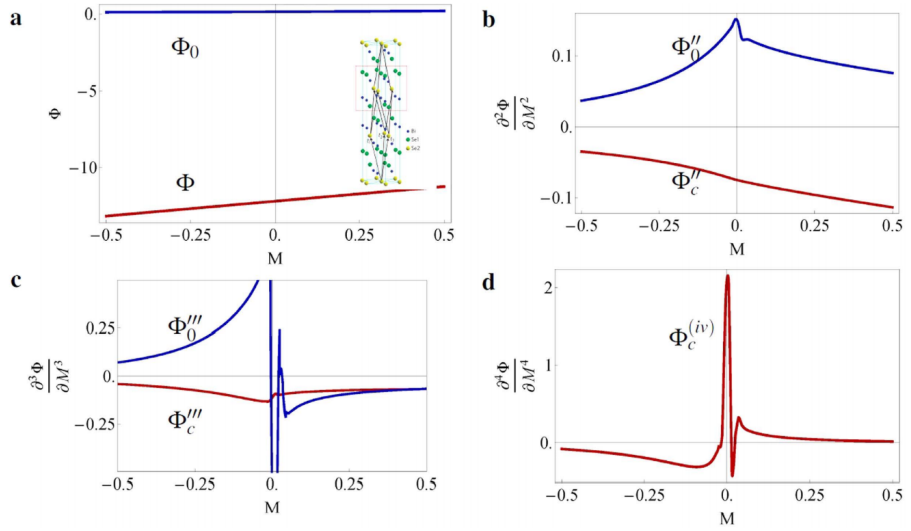

Figure 5.11: **a** The conventional potential Φ_c (red) and subdivision potential Φ_0 (blue) and (**b, c, d**) its derivatives with respect to M for the BHZ model with $A_1 = A_2 = B_1 = B_2 = C = D_1 = D_2 = 1$. The phase change occurs at $M = 0$. The subdivision potential shows a discontinuity in the third derivative, whereas the conventional potential shows a discontinuity in the fourth derivative. One should note that in **b** Φ_0'' does not show a discontinuity at $M = 0$ (the same holds for Φ_c''' in **c**), but a kink [60].

superconducting (NbTiN) electrode. The proximity to the conventional superconductor, allied to the topological features of InSb, allows for the realization of the long sought topological superconductor hosting Majorana bound states at the edge [56]. The Hamiltonian reads

$$H_{\text{Kitaev}} = -\mu \sum_{i=1}^{N} a_i^\dagger a_i - \sum_{i=1}^{N-1} \left[t a_i^\dagger a_{i+1} - \Delta a_i^\dagger a_{i+1}^\dagger + h.c. \right], \tag{5.19}$$

where μ denotes the chemical potential, $t \geq 0$ is the hopping parameter, $\Delta \geq 0$ is the superconducting gap (pairing energy in the mean-field approximation) and a_i ($a_i^\dagger$) are fermionic destruction (creation) operators at position i, satisfying the anti-commutation relation $\{a_i, a_j^\dagger\} = \delta_{i,j}$. The phase change occurs for $|\mu| = 2t$, and the system is in the topological (trivial) phase for $|\mu| < 2t$ ($|\mu| > 2t$).

The results are presented in Fig. 5.12**a**, for zero T and $t = \Delta = 0.25$ in natural units. At $\mu = 0.5$, the subdivision potential reveals a first-order phase

transition at the edge (Fig. 5.12**b**), whereas the conventional potential signals a second-order phase transition in the bulk (Fig. 5.12**c**). Furthermore, when considering periodic boundary conditions (the Kitaev ring) and taking the thermodynamic limit, the edge does not contribute anymore and indeed, the subdivision potential vanishes although the conventional potential remains the same (see dashed lines in Fig. 5.12**a-d**). Additionally, note that the same order of the phase transitions is obtained when changing phases in different ways, for example by varying the hopping parameter t instead of the chemical potential μ (not shown), as expected.

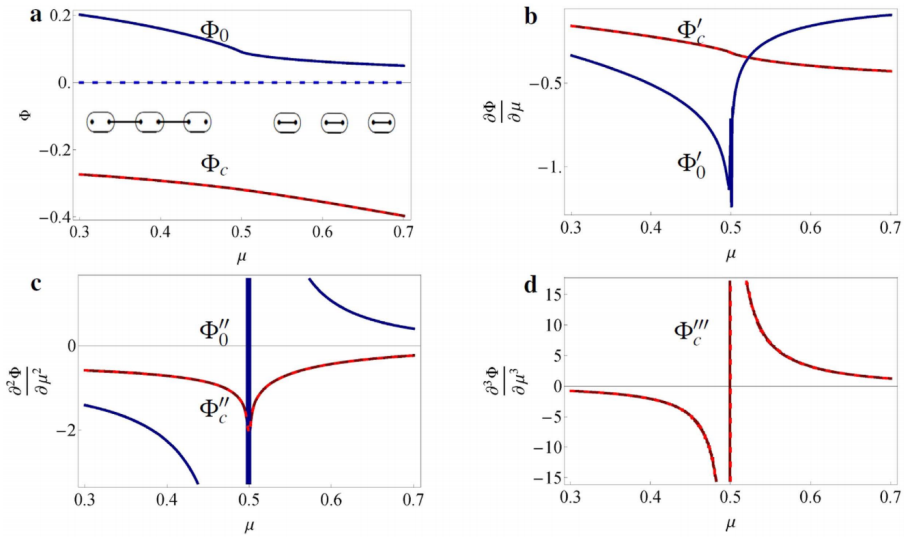

Figure 5.12: **a** The conventional potential Φ_c (red) and subdivision potential Φ_0 (blue) and (**b, c, d**) their derivatives with respect to μ for the Kitaev chain (solid lines) and the Kitaev ring (dashed lines), for $t = \Delta = 0.25$. In the thermodynamic limit, the subdivision potential of the Kitaev ring indeed vanishes, whereas the conventional potential does not change. The inset in **a** shows the topological (left) and trivial (right) phase of the Kitaev chain. The topological phase hosts Majorana zero modes at the edges. The phase change occurs at $\mu = 2t = 0.5$. **b** The subdivision potential shows a discontinuity in the first derivative, **c** whereas the conventional potential shows a discontinuity in the second derivative. **d** The third derivative is displayed to help the visualization of the discontinuity in the second derivative [60].

At the gap closing, the low-energy spectrum is well approximated by a conformal field theory (CFT), and we compare the thermal entropy and the heat capacity with the one obtained via CFT methods. We present the entropy $S_i = -\partial\Phi_i/\partial T$ in Fig. 5.13**a**, where Φ_i denotes either Φ_c (bulk, red solid line) or Φ_0 (edge, blue dashed line), for different values of μ. Especially the entropy at the edge shows an interesting behaviour near the phase transition, as it jumps from an initial value of $\log(2)$ value in the topological phase towards zero in the trivial phase (Fig. 5.13**a-b**). This value of $\log(2)$ comes from the Majorana zero mode, which makes the spectrum degenerate. Since this degeneracy does not scale with the system volume, it appears as a boundary contribution. At first glance, the negative entropy at the edge in the trivial phase seems peculiar, but it can be understood in the sense that it lowers the total entropy of the whole system. The total entropy is always positive for the considered lengths. At the phase transition, the entropy in the bulk is a linear function of T, as is expected for a CFT, but deviates from this linear behaviour further away from it. Furthermore, the heat capacity C_V of 1D quantum systems at low T is proportional to the central charge c: $C_V = \pi c k_\mathrm{B}^2 T L/(3\hbar v)$ [198], with v the velocity of the excitations, L the length of the system, k_B the Boltzmann constant and $\hbar$ the reduced Planck constant. At the phase transition $\mu = 2t$, the Kitaev chain is conformal, and has charge $c = 1/2$. By analysing the low-T behaviour of the Kitaev chain and choosing suitable parameters such that $k_\mathrm{B}/(\hbar v) = 1$, one indeed finds $C_v = \pi k_\mathrm{B} T/6$ per unit length, see Fig. 5.13**c**.

Now, we proceed by applying the method to finite T, which is most readily accomplished for 1D systems. Here we focus on the Kitaev chain, but a similar analysis can be done for other models like the Su-Schriefer-Heeger model below. In Fig. 5.13**d**, we display the discontinuous derivatives of the conventional potential ($\Phi_c{}''$, red) and of the subdivision potential ($\Phi_0{}'$, blue) for different T, using the same parameters as before. It becomes clear from Fig. 5.13**d** that the canonical potential becomes analytic at finite temperatures, reflecting the fact that the topological phase transition is a quantum phase transition. At high T, the discontinuity indicating a phase transition at $T = 0$ smooths out, and moves towards lower values of μ than at $T = 0$. Although no true phase transition remains at finite temperature, it is instructive to compare these thermodynamic results to previous work on topological materials at finite temperature.

There are two main approaches that have been used recently. The first approach has been suggested by Viyuela et al. [61], and makes use of the Uhlmann phase, which is defined as $\Phi_\mathrm{U}^\gamma = \arg \mathrm{Tr}\left[\rho(0) H_\mathrm{U}^\gamma\right]$, where $\rho(0)$ is an initial density matrix, γ is a loop through the Brillouin zone, and H_U^γ the

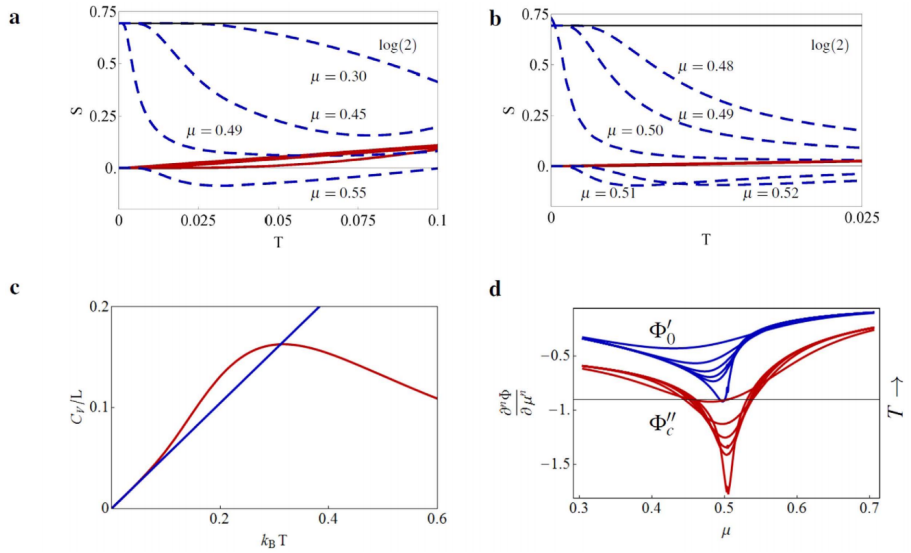

Figure 5.13: **a** Thermal entropy per lattice site in the bulk (red, solid) and at the edge (blue, dashed) for different values of $\mu = \{0.30, 0.45, 0.49, 0.55\}$. The other parameters are the same as before. Upon increasing μ, the entropy at the edge decreases at lower T from the zero-T Majorana $\log(2)$ value (black, solid), and suddenly jumps towards zero at the phase transition $\mu = 0.5$ (see also **b**). The entropy in the bulk overlaps for most of the values for μ and is only visibly different for $\mu = 0.30$ (lower red solid curve). **b** The same as **a**, but now for parameter values $\mu = \{0.48, 0.49, 0.50, 0.51, 0.52\}$. Near the phase transition, the Kitaev chain is conformal, and therefore the entropy in the bulk is a linear function of T. **c** Low-T heat capacity (in red) at the phase transition, for $t = \Delta = 0.25$ (in units where $k_B/\hbar v = 1$). For low T, we observe a linear T dependence (in blue) with a slope $C_V/Lk_BT = \pi/6$, which corresponds to a central charge $c = 1/2$. **d** Second derivative ($n = 2$ on y-axis) of the conventional potential Φ_c'' (red) and first derivative ($n = 1$ on y-axis) of the subdivision potential Φ_0' (blue), with respect to the chemical potential μ at different temperatures $T = \{1/300, 1/100, 1/80, 1/60, 1/40, 1/20\}$. For low T, the phase transition is sharp, but for high T it smooths out [60].

Holonomy along γ of the Uhlmann connection. The Uhlmann phase is analogous to the Abelian Berry phase $\Phi^\gamma = \arg\langle\psi(0)|\psi(T)\rangle$, where $|\psi\rangle\langle\psi|$ is a family of pure states, up to one crucial difference [199]: whereas the Berry phase is a U(1) holonomy and is additive in its group structure, which is essen-

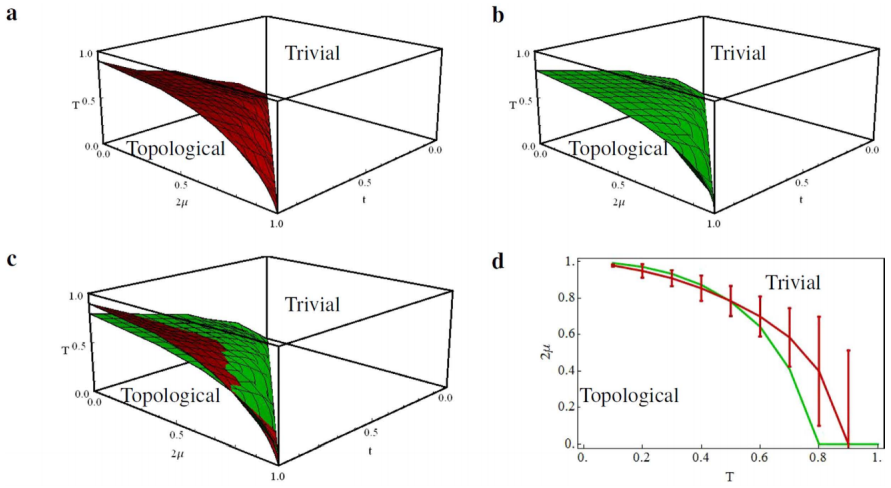

Figure 5.14: **a** The finite-T phase diagram obtained using Hill thermodynamics. Here, we use the same parameters as in Ref. [61]. **b** The finite-T diagram constructed from analytical calculation of the Uhlmann phase, as shown in Ref. [61]. **c** The comparison between the two previous phase diagrams using Hill thermodynamics (red) and the Uhlmann phase (green). The red curve is below the green curve for lower values of T, and hence not much visible in the figure. **d** A slice of the topological phase diagram for $t = 1.0$, depicting the minima of the second derivative of the conventional potential (red) and the Uhlmann phase (green). Note that in this figure, T is on the x-axis and 2μ is on the y-axis. The error bars indicate a margin of error of 0.25% around the value of Φ_c'' corresponding to the minimum [60].

tial for its interpretation as a topological invariant, as discussed in Appendix A, the Uhlmann phase is the trace of a holonomy. This is necessary because all the characteristic classes of the bundle of density matrices vanish, for the same reason that the Chern-numbers of all the energy bands sum to zero. The result is then a set of quantised numbers, which one can define in the 1D and 2D case relatively easily, since path ordering is unnecessary [200]. However, the Uhlmann phase is not a topological invariant in the traditional sense, since it is the trace of a holonomy, and does not obey the necessary composition laws as a result. This makes it unclear what the Uhlmann phase measures precisely. Nevertheless, as we will discuss now, it does contain some very interesting information that seems to be related to the thermodynamic behaviour of the

system.

Specifically, it can be used to extend the topological phase diagram at $T = 0$ to a phase diagram including finite temperatures, as depicted in Fig. 5.14**b**. One can compare this to the location of the minimum of Φ_c'' at a given value of T. It is natural to expect that the Uhlmann phase is a bulk quantity, since it is obtained by integration over the Brillouin zone. We already mentioned that the minimum of Φ_c'' shifts towards lower μ as T increases, as in Fig. 5.13**d**. The location of this minimum as a function of T is plotted in Fig. 5.14**a**. A comparison with Fig. 5.14**b** is shown in Fig. 5.14**c**, and the two are actually very similar (see also Fig. 5.14**d**, where the same results are shown only for a slice of the volume corresponding to $t = 1.0$). The deviations are due to the fact that, at finite T, the grand canonical potential is smooth and its exact minimum is subject to numerical errors. We have included an error bar to the bulk phase-transition points, which indicates an uncertainty of $\pm 0.25\%$ in the location of the minimum. The similarities in the results between these two fundamentally different approaches is extraordinary, and will hopefully trigger further investigations into their relation.

A second approach to dealing with finite-T topological phase transitions has been proposed in Ref. [199]. The observation here is that the topological structure of the bundle of density matrices is trivial, just as the topological structure of all energy bands together is trivial (this is reflected in the fact that the topological invariants of the energy bands always sum to zero.). However, a k-dependent set of density matrices is Hermitian and therefore has energy bands, just as the Hamiltonian does. One can associate topological invariants to these energy bands in the familliar manner. However, every density matrix can be written as $\rho = \exp(-\beta H)$, and this topological classification is then the same as that of H. Specifically, it is independent of temperature and contains no new information. Heuristically, one can remark that the inflection points of Φ_c''' always remain at $\mu = 0.5$, independently of T, see also Fig. 5.12**d**.

Although the thermodynamic approach does not give any results on the topological structure of the bundle of density matrices, it nevertheless sheds a new light on topological materials by linking various previous results to features of the free energy. From this perspective, it is interesting to observe that the Uhlmann phase and our numerical results capture the smoothing of the phase transition at finite T, following the expected finite-T behaviour of a quantum phase transition [197].

5.5.4 Su-Schriefer-Heeger model

The Su-Schriefer-Heeger (SSH) model describes another 1D system topological order. It was first used to study the dimerisation of polyacetylene [14]. It describes electrons hopping between two neighboring sites of a bipartite lattice, and has proven to be an adequate tight-binding model for capturing the behavior of conjugated polymer chains. The SSH Hamiltonian reads

$$H_{\text{SSH}} = \sum_n \left[t_1 c^\dagger_{A,n} c_{B,n} + t_2 c^\dagger_{A,n+1} c_{B,n} + h.c. \right], \tag{5.20}$$

where t_1 and t_2 denote unequal hopping amplitudes between the even and odd links for the even (odd) sites A (B). It is common to rewrite $t_1 = t(1+\Delta)$ and $t_2 = t(1-\Delta)$, which makes the Hamiltonian only dependent on the parameter Δ, and there is a phase change between the topological and trivial phases for $\Delta = 0$. In a periodic chain, there is no fundamental difference between the two phases, since the two are related by reflection, but on a finite chain there is. In the finite chain, a zero-energy state appears at an end of the chain if the final hopping parameter is weak, and this state is protected by topology. However, since the presence of an edge mode is determined by the number of lattice sites, the topological nature of this model is different from those discussed so far. In Fig. 5.15, we show the results for the SSH chain for $t = 3/2$ when both ends of the chain have either strong or weak hopping. When the strong and weak bonds are interchanged, one observes a first-order phase transition at the edge associated to the behaviour of the boundary states and a second-order phase transition in the bulk, which is precisely the same behaviour obtained for the Kitaev chain.

Upon increasing the temperature, the grand canonical potential becomes analytic at the topological phase transition point. In Fig. 5.16, we show the finite-T phase diagram [61], analogous to the one shown for the Kitaev chain in Fig. 5.14. Again, the comparison between the two results is clear.

5.6 Conclusion

As the discussion in this Chapter shows, topological phases of matter have clear signatures in global thermodynamic properties, despite the quantum nature of SPTO. Even though this only happens at zero temperature, a topological phase transition is associated with a thermodynamic phase transition, and this thermodynamic phase transition has an order associated to it in the sense of Ehrenfest [201]. Above, we have analysed this phase transition for 2 models in

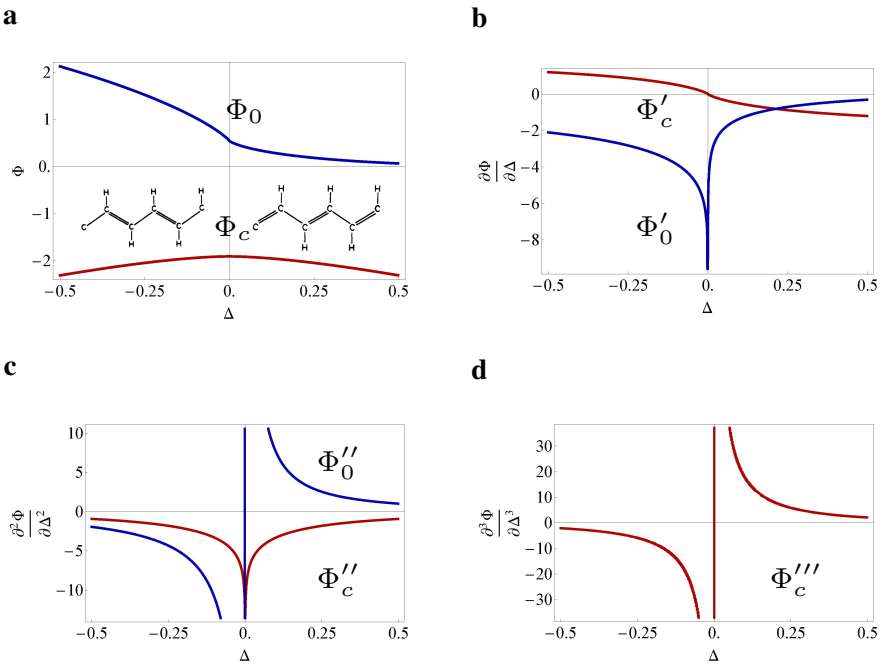

Figure 5.15: **a** The conventional potential Φ_c (red) and subdivision potential Φ_0 (blue) and (**b, c, d**) their derivatives with respect to Δ, for with $t = 3/2$. The figures show a similar behavior as the Kitaev chain, a first-order phase transition for the edge and a second-order phase transition in the bulk. The inset in **a** shows the topological (left) and trivial (right) phase of polyacetylene [60].

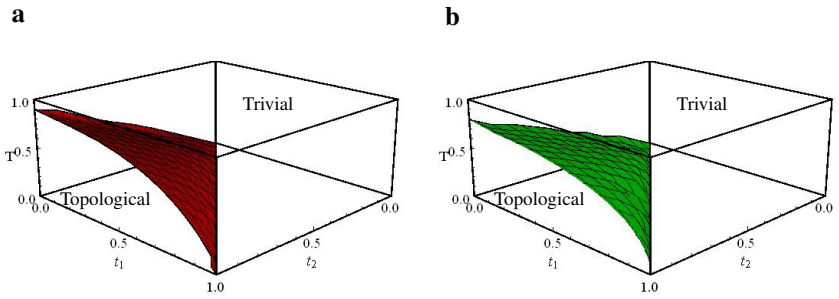

Figure 5.16: [60] The finite-T phase diagram for the SSH model obtained via **a** Hill thermodynamics (red) and **b** via the Uhlmann phase (green) [61] [60].

1D, the Kitaev Chain and the SSH model; for 2 models in 2D: the BHZ model and the Kane & Mele model; and for a single model in 3D, the BHZ model. In all these cases, one sees a phase transition in the bulk of order $d+1$, and a phase transition at the edge of order d, where d is the dimension of the model. This suggests a universal behaviour. The order of the bulk phase transition has a clear origin in the closing of the band gap, as can be seen by taking the system with periodic boundary conditions. The order of the boundary phase transition is correctly reproduced by a Dirac theory on the boundary with a momentum cutoff. This suggests that the boundary phase transition is driven by the disappearance of the topological edge mode, a conclusion which is supported by the behaviour of the 2D BHZ model with superconductivity. Nevertheless, the effective Dirac theory on the edge does not capture the quantitative behaviour correctly due to non-topological contributions to the boundary charge density.

The thermodynamic formalism can also be used to investigate the meaning of the Uhlmann phase, which has been introduced to study topological materials at finite temperature. As we discussed above, the Uhlmann phase is probably not topological in nature [199], but it does seem to measure some relevant quantity of a finite temperature topological system. The results above indicate that it might actually measure a feature of the grand canonical potential that can be used to define a topological phase transition at finite temperature. Although this is not a phase transition in the thermodynamic sense, one can hypothesise that it corresponds to the onset of critical behaviour, which usually indicates that a quantum phase transition is present at zero temperature [197].

CHAPTER 6

Concluding remarks

In Chap. 1, we provided an overview of the development of SPTO, set the open questions in the field at the time when this thesis was started, and described what would be done in this thesis. The subsequent Chapters, apart from Chap. 2, which served as a pedagogical introduction, each dealt with contributions to one of these open questions. In Chap. 3 we discussed topological materials in the presence of periodic driving, in Chap. 4 we discussed the effects of sample geometry, and in Chap. 5 we discussed how topological materials can be investigated from a thermodynamic point of view.

Of these chapters, Chap. 3 is composed of the most papers, because it describes the biggest area of research out of these topics. This activity is partially explained by the close connection between Floquet systems and optical lattices. We saw how, by 2013, periodic driving had been used to create QH like states in both optical lattices and condensed-matter systems [33, 34]. Furthermore, it had been shown what the topological invariant classifying Floquet systems of QH symmetry class was [40]: the winding number discussed in Chap. 3. Since then, there has been clear improvement in our undertanding of Floquet systems, both theoretically and experimentally. Theoretically, the topological behaviour of Floquet systems in (2+1)D is now understood for all symmetry classes, not just the QH class, and models with e.g. chiral or particle-hole symmetry are now known [48]. Experimentally, the realisation of symmetry classes other than the QH class has not been achieved. Never-

theless, there has been clear improvement. The topological phases realised in optical lattices by 2013 were Floquet approximations to undriven systems, and their topological behaviour could be understood in those terms [33, 34]. It is important to note that a Floquet topological phase had been realised at that point [95, 129–133], but in optical lattices it had not been achieved. As we have shown in Chap. 3, it should be possible to create a variety of such states in optical lattices, including one which is topological, yet has vanishing Chern number in all bands [40].

The effect of geometry on topological phases of matter has attracted less attention over the years, but because of this, the relative improvement has been greater. In the context of the Möbius band, this is especially pronounced. Although the material properties of a Möbius band has been the subject of research over the past years, before 2013 results on the topological properties of such systems were scarce [171, 202]. By now the topological classification of free fermions on a Möbius band has been performed, as well as a systematic analysis of what kind of lattices can be consistently folded into a Möbius shape. Progress in experiments might arise from synthetic optical lattices, in which internal degrees of freedom are coupled with a twist, as theoretically proposed in Ref. [161]. For the case of p-wave superconductors, our studies have lead to the discovery of the Geo-Josephson effect, the notion that the superconducting pairing can couple to the curvature of a topological material and which dictates whether or not a Majorana zero mode is present at the edge.

Finally, we have shown what kind of thermodynamic signatures topological materials have. As discussed in Chap. 2, the initial theoretical research focussed on the topological structure of the eigenstates of the Hamiltonian, and topological systems were not considered using traditional thermodynamic methods. This also extends to experiments, where the edge states characterising topological materials have been detected using transport measurements [1, 9, 56], or more directly using ARPES [19]. We have constructed a general thermodynamic framework that serves to describe finite topological systems, and allows for a separation of bulk from boundary effects. It is shown that the topological edge states manifest in thermodynamic quantities such as the specific heat and integrated density of states. Furthermore, the topological phase transition coincides with a thermodynamic phase transition, but it has a different order at the boundary and in the bulk. There seems to be a universality in the order of these phase transitions, as discussed in Chap. 5.

However, since this is a new area of inquiry, there is a lot of room for further research. In one ongoing project, we investigate how the thermodynamic properties can be described in terms of the correlation functions of the underly-

ing model [203]. This allows one to identify in detail what physical processes contribute to the thermodynamic behaviour. Furthermore, a topological material becomes quantum critical at the phase transition, and the order of the thermodynamic phase transition depends the manner in which the energy gap closes. The low energy spectrum determines the critical exponents characterising the critical point, and these determine the decay rate of the correlation functions, showing a further link between the two approaches. Another project involves the search for a topological phase transition that is truly thermodynamic in nature. In all examples so far, the thermodynamic phase transition only occurs at zero temperature, due to the quantum nature of the topological phase transition. However, Kondo topological insulators show a topological phase transition as a function of temperature, presenting the possibility to detect a truly thermodynamic phase transition that persists at finite temperature [204]. Apart from these current research projects, there are additional open questions, such as the role of disorder, and the influence of interactions.

All in all, in the four years since I started this thesis a lot of progress has been made in understanding SPTO. However, not all the original open questions on this topic have been answered, and new ones have been raised. Although the initial flurry of activity in research on SPTO has abated recently, and focus is shifting towards related topics such as Weyl semimetals, long-range entanglement, and interacting topological systems, topology will likely continue to be an exciting subject of research in the coming years.

APPENDIX A

Trivialisability of Bloch Bundles

A.1 The Bloch Bundle

The topological invariants used in the theory of topological insulators have a mathematical origin in the theory of vector bundles. Specifically, they are used to investigate the trivialisability of a certain vector bundle over the torus, called the Bloch bundle. In this appendix, the relevant notions are reviewed.

Let H be the Hamiltonian for a d-dimensional quantum system, that is

$$H : D(H) \to L^2(\mathbb{R}^d, d\boldsymbol{x})$$

is a Hermitian operator on the Hilbert space of states $\mathcal{H} := L^2(\mathbb{R}^d, d\boldsymbol{x})$; here $D(H)$ is the domain of H, which must be dense in the Hilbert space. Let us assume that there are d linearly independent vectors $\{\boldsymbol{a}_1, ..., \boldsymbol{a}_d\}$ such that H is invariant under translation along these vectors. It is always true that $\mathcal{H}$ decomposes into Hilbert spaces of quasi periodic functions c.f. Ref. [205]:

$$\mathcal{H} = \int_{\mathrm{BZ}}^{\oplus} \mathcal{H}_{\boldsymbol{k}} d\boldsymbol{k}. \tag{A.1}$$

Here, BZ is the Brillouin zone generated by $\{\boldsymbol{a}_1, ..., \boldsymbol{a}_d\}$, and

$$\mathcal{H}_{\boldsymbol{k}} := \{f \in \mathcal{H} | f(\boldsymbol{x} + \boldsymbol{a}_i) = \exp(i\boldsymbol{k} \cdot \boldsymbol{a}_i) f(\boldsymbol{x}),\ \forall i\}\,.$$

This is a Hilbert space if one uses the inner product

$$\langle f, g\rangle \coloneqq \int_{I^d} \bar{f}(x) g(x) d\boldsymbol{x}, \tag{A.2}$$

where I^d is the unit cell of the lattice. From the quasi-periodicity in space, one can see that $\boldsymbol{k}$ is just the Bloch momentum. If, however, the Hamiltonian H obeys $H(\boldsymbol{x} + \boldsymbol{a}_i) = H(\boldsymbol{x})$, then it also decomposes as

$$H = \int_{BZ}^{\oplus} H_{\boldsymbol{k}} d\boldsymbol{k}. \tag{A.3}$$

Here $H_{\boldsymbol{k}}$ is just the restriction of H to $\mathcal{H}_{\boldsymbol{k}}$, which is an alternative way of saying that $\boldsymbol{k}$ is a good quantum number.

The decompositions in Eqs. (A.1) and (A.3) give a trivial vector bundle (see Ref. [206] for a definition)

$$\pi : V \to \mathbb{T}^d \tag{A.4}$$

called the Bloch bundle. The base space $\mathbb{T}^d$ is the Brillouin zone, which is diffeomorphic to a d-dimensional torus; furthermore the fibre over a point $\boldsymbol{k}$ in the torus is $\mathcal{H}_{\boldsymbol{k}}$[1].

In most physical applications, the Hamiltonians $H_{\boldsymbol{k}}$ have compact resolvent, and are therefore diagonalisable; we will assume that the eigenvalues are bounded from below. In those situations, it is possible to define the subspaces $\mathcal{H}^m_{\boldsymbol{k}}$ of $\mathcal{H}_{\boldsymbol{k}}$ spanned by the m lowest energy eigenstates. This defines a sub-bundle, V^m of the Bloch bundle V by taking the fibre over $\boldsymbol{k}$ to be $\mathcal{H}^m_{\boldsymbol{k}}$. Contrary to the full Bloch bundle, V^m is not always trivialisable. It is this non-triviality that gives rise to topological phases of matter. Furthermore, the topological order parameters correspond to topological invariants of V_m. The main text deals with the physical reasoning behind this; here, a review of the mathematical background behind these topological invariants is presented.

A.2 The first Chern class of the Bloch bundle, and subbundles

Since each $\mathcal{H}^m_{\boldsymbol{k}}$ is an m-dimensional Hilbert space, one can equally well look at the corresponding principal bundle [207] of orthonormal frames (i.e. continuously varying bases). This is a principal bundle with structure group U_m,

[1] In practice, one usually uses approximation techniques to work with finite-dimensional subspaces of the $\mathcal{H}_{\boldsymbol{k}}$.

the group of unitary $m \times m$ matrices. In Ref. [208], it is proven that the isomorphism class of a U_m-bundle over $\mathbb{T}^d$ is uniquely determined by its first Chern-class [209] for $d = 1, 2, 3$. A representative of the first Chern class is given by $i\,\mathrm{Tr}(F_A)/2\pi$, where F_A is the curvature of an arbitrary connection A; a proof of this is found in Ref. [209].

A physically relevant choice of A is given by the Berry connection [210]. Let $u_i(k)$ be a local orthonormal frame for V^m, then the Berry connection is defined as

$$A_{ij} := \langle u_i, du_j \rangle . \tag{A.5}$$

One easily checks by a change of basis that this actually defines a connection. The corresponding first Chern-class (which is independent of the choice of frame) is then

$$c_1 = \frac{i}{2\pi} \sum_j d \langle u_j, du_j \rangle = \frac{i}{2\pi} \sum_{j,m,n} \left\langle \frac{\partial u_j}{\partial k^m}, \frac{\partial u_j}{\partial k^n} \right\rangle dk^m \wedge dk^n . \tag{A.6}$$

For $d = 1$, the class c_1 always vanishes; for $d = 2$, it is uniquely determined by its corresponding Chern number:

$$\int_{\mathbb{T}^2} c_1 = \frac{i}{2\pi} \sum_j \int_{\mathbb{T}^2} \left\langle \frac{\partial u_j}{\partial k_x}, \frac{\partial u_j}{\partial k_y} \right\rangle - \left\langle \frac{\partial u_j}{\partial k_y}, \frac{\partial u_j}{\partial k_x} \right\rangle dk_x dk_y . \tag{A.7}$$

Since the Chern classes are in the integer cohomology of the base space, the Chern number is always integer; this has important physical consequences. For $d > 2$, the first Chern class is more difficult to classify, since it depends on the Chern number of all possible surfaces. It is the first Chern class that protects the Weyl cones in 3D semimetals for example. This thesis is mostly about 2D systems, so we will restrict ourselves to this case, where the m-dimensional subbundles of the Bloch bundle are uniquely classified by the Chern number in Eq. (A.7).

A.3 Systems with Time-Reversal Symmetry

The situation is markedly different if TRS is involved in the system. In this case, there is an anti-unitary time-reversal operator Θ, obeying $\Theta^2 = \pm 1$, and the Hamiltonian obeys $\Theta H \Theta^\dagger = H$. The sign of Θ^2 depends on whether one considers fermions or bosons, and mathematically determines whether the Hilbert space is real or quaternionic. In terms of the Bloch decomposition, the

anti-unitarity of the time-reversal operator implies that it sends $\boldsymbol{k} \mapsto -\boldsymbol{k}$. TRS is thus equivalent to

$$\Theta H_{\boldsymbol{k}} \Theta^{\dagger} = H_{-\boldsymbol{k}}. \tag{A.8}$$

It follows immediately that Θ provides an (anti-)involution on the Bloch bundle that sends an eigenvector over $\boldsymbol{k}$ to an eigenvector with the same eigenvalue over $-\boldsymbol{k}$. This has two far-reaching consequenses: first, the energy bands of H are symmetric under inversion of $\boldsymbol{k}$, and second all energy bands are trivialisable subbundles of the Bloch bundle. This second property follows because the Berry connection is odd under time-reversal.

Although all energy bands of the Bloch bundle are trivialisable for a TRS system, these systems still show interesting topological behaviour. This happens because a stronger form of trivialisability can be demanded in TRS systems. One can ask whether an energy band can be trivialised by states $\{u_i\}$ such that $\Theta u_i = \pm u_j$ for some j depending on i. This is not always possible [211]. Topological obstructions arise because the phases of the u_i might not be well-defined at points in the Brillouin zone. We will discuss what this means in 2D, although the 3D case is very similar. In this case, the order parameter takes values in Z_2, and an explicit formula for its calculation will now be presented. This invariant was first introduced in Ref. [7], but here, it will be introduced in the form derived in Ref. [67], since this version is more generally applicable. In Ref. [211], an overview of the various equivalent formulations is presented, and Ref. [212] contains a rigorous mathematical treatment of the concepts involved, together with the link between TRS and twisted K-theory [213].

Consider an m-dimensional subbundle V^m of the Bloch bundle V, consisting of energy bands. By TRS, the Chern number vanishes and V^m is trivialisable by a trivialisation $\{u_i\}$. Since the obstruction to finding a TRS trivialisation of V^m comes from phase ambiguities, it is useful to study the phase of Θ. This is done by defining its matrix with respect to $\{u_i\}$:

$$w_{ij}(\boldsymbol{k}) := \langle u_i(-\boldsymbol{k}), \Theta(u_j(\boldsymbol{k})) \rangle \,. \tag{A.9}$$

The determinant of w has no winding along any curve in the Brillouin zone, and hence $\sqrt{\det(w)}$ can be globally defined. Furthermore, at the time-reversal invariant momenta in the Brillouin zone, where $\boldsymbol{k} = -\boldsymbol{k}$, the matrix w is antisymmetric, so its Pfaffian (Pf) is defined. The $\mathbb{Z}_2$ invariant ν is defined implicitly by the identity

$$(-1)^{\nu} = \prod_{\text{TRIM}} \frac{\mathrm{Pf}(w)}{\sqrt{\det(w)}}. \tag{A.10}$$

Since $\mathrm{Pf}(w)^2 = \det(w)$, ν measures the number of times the Pfaffian changes sign. A straightforward calculation indeed verifies that ν vanishes for a bundle that admits a TRS trivialisation, since in that case $\mathrm{Pf}(w)$ is everywhere real-valued and positive.

A.4 A note on generalisations

The above list of examples of topological phases is nowhere near exhaustive. A large number of dimensions has not been treated, and two symmetries that have not been discussed are particle-hole and chiral symmetry. Using K-Theory (amongst other methods [214]), it is possible to classify the equivalence classes of Bloch bundles with these two symmetries, as well as TRS in arbitrary dimensions. The result is known as the Ten-Fold way [192]. Other possibilities include the addition of various spatial symmetries of the lattice in the classification. This will be discussed in more detail in the main text for the case of reflection symmetry along an axis, owing to its importance in describing Möbius strips.

APPENDIX B

Induced vector potential in shaken lattices

In this appendix, it is shown how shaking a lattice induces a vector potential. The discussion is a more detailed version of an argument presented in Ref. [49]. Usually, this phenomenon in shown by taking a time-dependent Hamiltonian, quantising, and then performing a series of unitary transformations that yield a Hamiltonian of the required form. Alternatively, one can show that the Hamiltonian has the required form at the classical level in the comoving frame, and that the comoving variables are canonically conjugate. This means that the quantisation in the co-rotating frame is done in the usual manner, and provides a different derivation, that is of some interest in its own right.

To find the Hamiltonian in co-moving coordinates, consider the Poincaré-Cartan form

$$dS = \boldsymbol{p} \cdot d\boldsymbol{q} - H dt \tag{B.1}$$

along the trajectory of a system in phase space. This form generates the action principle in phase space: if one lifts a trajectory $q(t)$ to a trajectory $(p(t), q(t))$ in phase space, the integral of dS along this lifted trajectory is just the action. Hamilton's equations are obtained by considering the variation δS to $\delta \boldsymbol{q}$ and $\delta \boldsymbol{p}$ independently, with $\delta \boldsymbol{q} = 0$ at endpoints, but without constraint on $\delta \boldsymbol{p}$.

Now, consider a change of coordinates to $\tilde{\boldsymbol{p}}(\boldsymbol{q}, \boldsymbol{p}, t), \tilde{\boldsymbol{q}}(\boldsymbol{q}, \boldsymbol{p}, t)$ that is required to be such that it is possible to write

$$dS = \tilde{\boldsymbol{p}} \cdot d\tilde{\boldsymbol{q}} - \tilde{H} dt. \tag{B.2}$$

The action is still equal to the integral of dS, and the variation still yields the equations of motion (apart from a boundary term). Therefore, $\tilde{\boldsymbol{p}}$ and $\tilde{\boldsymbol{q}}$ must be a canonical pair at each t, and the equations of motion are given by Hamilton's equations for $\tilde{H}$ [215]. One can therefore quantise the system $\tilde{\boldsymbol{p}}, \tilde{\boldsymbol{q}}, \tilde{H}$ in the familiar manner, and get the quantum theory of the co-moving reference frame.

Now, we will apply this reasoning to a classical lattice that is shaken in time. The deviation of the lattice from its equilibrium position is denoted by $\boldsymbol{r}(t)$, and we assume this deviation is periodic $\boldsymbol{r}(t+T) = \boldsymbol{r}(t)$ for some period T. First, change to co-moving coordinates $\tilde{\boldsymbol{q}} = \boldsymbol{q} + \boldsymbol{r}(t)$, $\tilde{\boldsymbol{p}} = \boldsymbol{p}$, such that $d\tilde{\boldsymbol{p}} = d\boldsymbol{p}$ and $d\tilde{\boldsymbol{q}} = d\boldsymbol{q} + \dot{\boldsymbol{r}}(t)dt$, where $\dot{\boldsymbol{r}}(t)$ is the time derivative of $\boldsymbol{r}(t)$. The Poincaré-Cartan form can thus be rewritten as

$$\begin{aligned} dS &= \boldsymbol{p} \cdot d\boldsymbol{q} - H dt = \tilde{\boldsymbol{p}} \cdot \left[d\tilde{\boldsymbol{q}} - \dot{\boldsymbol{r}}(t) dt \right] - H dt \\ &= \tilde{\boldsymbol{p}} \cdot d\tilde{\boldsymbol{q}} - \left(H + \tilde{\boldsymbol{p}} \cdot \dot{\boldsymbol{r}}(t) \right) dt. \end{aligned} \tag{B.3}$$

This means that the general reasoning presented above applies, and one can immediately read off the Hamiltonian in co-moving coordinates: $\tilde{H} = H + \tilde{\boldsymbol{p}} \cdot \dot{\boldsymbol{r}}(t)$. The extra term encodes the pseudoforces arising because the co-moving frame is not inertial.

For a shaken optical lattice, the Hamiltonian reads

$$H = \frac{p^2}{2m} + V(\boldsymbol{q} + \boldsymbol{r}(t)), \tag{B.4}$$

where the potential determines the lattice.

In the co-moving frame $\tilde{\boldsymbol{q}}$ and $\tilde{\boldsymbol{p}}$, Eq. (B.4) becomes

$$\begin{aligned} \tilde{H} &= H(\tilde{\boldsymbol{p}}, \tilde{\boldsymbol{q}}) + \tilde{\boldsymbol{p}} \cdot \dot{\boldsymbol{r}}(t) = \frac{\tilde{p}^2}{2m} + V(\tilde{\boldsymbol{q}}) + \tilde{\boldsymbol{p}} \cdot \dot{\boldsymbol{r}}(t) \\ &= \frac{\|\tilde{\boldsymbol{p}} + m\dot{\boldsymbol{r}}(t)\|^2}{2m} + V(\tilde{\boldsymbol{q}}) - \frac{1}{2} m \|\dot{\boldsymbol{r}}(t)\|^2. \end{aligned} \tag{B.5}$$

The final term is a time-dependent constant, and does not affect the motion of the system. In the co-moving reference frame, the dynamics of the shaken system is, therefore, given by the original static Hamiltonian in the presence of a vector potential $e\boldsymbol{A} = m\dot{\boldsymbol{r}}$. For circular shaking at radius r_0, this gives a rotating vector potential $e\boldsymbol{A}$ of constant magnitude $eA = mr_0\omega$. This is equivalent to the Hamiltonian for a 2D system irradiated perpendicularly by circularly polarised light, where $eA = eE/\omega$ for an electric field E.

APPENDIX C

Tight binding form of the 2D and 3D BHZ model

In this appendix, we give the NN hopping forms of the 2D and 3D BHZ model, which are used in Chap. 5 to calculate the canonical potential for finite systems.

For the 2D BHZ model, the Bloch Hamiltonian presented in the text, is equivalent to the Hamiltonian

$$H_{2D} = \sum_{\boldsymbol{r},\boldsymbol{\delta}} \left(\Psi_{\boldsymbol{r}}^{\dagger} T_{\boldsymbol{\delta}} \Psi_{\boldsymbol{r}+\boldsymbol{\delta}} + \Psi_{\boldsymbol{r}}^{\dagger} \frac{\epsilon}{4} \Psi_{\boldsymbol{r}} + H.c. \right), \tag{C.1}$$

where $\Psi_{\boldsymbol{r}}^{\dagger} = \left(s_{\boldsymbol{r}}^{\dagger}, p_{\boldsymbol{r}}^{\dagger} \right)$, $\boldsymbol{\delta} \in (\hat{e}_x, \hat{e}_y)$, $\epsilon = (M - 4B)\sigma_z$, and

$$T_{\boldsymbol{\delta}} = \begin{pmatrix} B & \frac{t_{\boldsymbol{\delta}}}{2} \\ \frac{t'_{\boldsymbol{\delta}}}{2} & -B \end{pmatrix}. \tag{C.2}$$

Here, $t_x = t'_x = -iA$, and $t_y = -t'_y = -A$.

The Bloch Hamiltonian for the 3D BHZ model appearing in the main text is not periodic in $\boldsymbol{k}$. It is a low energy approximation of the following Hamiltonian

$$H_{2D} = \sum_{\boldsymbol{r},\boldsymbol{\delta}} \left(\Psi_{\boldsymbol{r}}^{\dagger} T_{\boldsymbol{\delta}} \Psi_{\boldsymbol{r}+\boldsymbol{\delta}} + \Psi_{\boldsymbol{r}}^{\dagger} \frac{\epsilon}{6} \Psi_{\boldsymbol{r}} + H.c. \right), \tag{C.3}$$

where $\Psi^{\dagger}_{\boldsymbol{r}} = \left(s^{\dagger}_{\boldsymbol{r},\uparrow}, p^{\dagger}_{\boldsymbol{r},\uparrow}, s^{\dagger}_{\boldsymbol{r},\downarrow}, p^{\dagger}_{\boldsymbol{r},\downarrow}\right)$, $\boldsymbol{\delta} \in (\hat{e}_x, \hat{e}_y, \hat{e}_z)$,

$$\epsilon = (M - B_1 - 2B_2) \begin{pmatrix} \sigma_z & 0 \\ 0 & -\sigma_z \end{pmatrix}, \tag{C.4}$$

and

$$T_x = \begin{pmatrix} B_2 & \frac{-iA_2}{2} & 0 & 0 \\ \frac{-iA_2}{2} & -B_2 & 0 & 0 \\ 0 & 0 & B_2 & \frac{-iA_2}{2} \\ 0 & 0 & \frac{-iA_2}{2} & -B_2 \end{pmatrix}, \tag{C.5}$$

$$T_y = \begin{pmatrix} B_2 & \frac{-A_2}{2} & 0 & 0 \\ \frac{A_2}{2} & -B_2 & 0 & 0 \\ 0 & 0 & B_2 & \frac{-A_2}{2} \\ 0 & 0 & \frac{A_2}{2} & -B_2 \end{pmatrix}, \tag{C.6}$$

$$T_z = \begin{pmatrix} B_1 & 0 & 0 & \frac{-iA_1}{2} \\ 0 & -B_1 & \frac{-iA_1}{2} & 0 \\ 0 & \frac{-iA_1}{2} & B_1 & 0 \\ \frac{-iA_1}{2} & 0 & 0 & -B_1 \end{pmatrix}. \tag{C.7}$$

Bibliography

[1] K. V. Klitzing, G. Dorda, and M. Pepper. New Method for High-Accuracy Determination of the Fine-Structure Constant Based on Quantized Hall Resistance. *Phys. Rev. Lett.*, 45:494–497, 1980.

[2] D.J. Thouless, M. Kohmoto, M.P. Nightingale, and M. den Nijs. Quantized Hall Conductance in a Two-Dimensional Periodic Potential. *Phys. Rev. Lett.*, 49(6):405–408, 1982.

[3] B Jeckelmann and B Jeanneret. The quantum Hall effect as an electrical resistance standard. *Reports on Progress in Physics*, 64(12):1603, 2001.

[4] F.D.M. Haldane. Model for a Quantum Hall Effect without Landau Levels: Condensed-Matter Realization of the "Parity Anomaly". *Phys. Rev. Lett.*, 61(18):2015–2018, 1988.

[5] Yasuhiro Hatsugai. Chern number and edge states in the integer quantum Hall effect. *Phys. Rev. Lett.*, 71:3697–3700, 1993.

[6] C.L. Kane and E.J. Mele. Quantum Spin Hall Effect in Graphene. *Phys. Rev. Lett.*, 95:226801, 2005.

[7] C.L. Kane and E.J. Mele. Z_2 Topological Order and the Quantum Spin Hall Effect. *Phys. Rev. Lett.*, 95:146802, 2005.

[8] B.A. Bernevig, T.L. Hughes, and S-C. Zhang. Quantum Spin Hall Effect and Topological Phase Transition in HgTe Quantum Wells. *Science*, 314(5806):1757–1761, 2006.

[9] M. König, S. Wiedmann, C. Brüne, A. Roth, H. Buhmann, L. W. Molenkamp, X.-L. Qi, and S.-C. Zhang. Quantum Spin Hall Insulator State in HgTe Quantum Wells. *Science*, 318:766–, 2007.

[10] Alexander Altland and Martin R. Zirnbauer. Nonstandard symmetry classes in mesoscopic normal-superconducting hybrid structures. *Phys. Rev. B*, 55:1142–1161, 1997.

[11] Andreas P. Schnyder, Shinsei Ryu, Akira Furusaki, and Andreas W. W. Ludwig. Classification of topological insulators and superconductors in three spatial dimensions. *Phys. Rev. B*, 78:195125, 2008.

[12] S. Ryu, A. P. Schnyder, A. Furusaki, and A. W. W. Ludwig. Topological insulators and superconductors: tenfold way and dimensional hierarchy. *New J. Phys.*, 12(6):065010, 2010.

[13] J. C. Y. Teo and C. L. Kane. Topological defects and gapless modes in insulators and superconductors. *Phys. Rev. B*, 82(11):115120, 2010.

[14] W. P. Su, J. R. Schrieffer, and A. J. Heeger. Solitons in Polyacetylene. *Phys. Rev. Lett.*, 42:1698–1701, 1979.

[15] A. Y. Kitaev. 6. QUANTUM COMPUTING: Unpaired Majorana fermions in quantum wires. *Physics Uspekhi*, 44:131, 2001.

[16] Ian Affleck, Tom Kennedy, Elliott H. Lieb, and Hal Tasaki. Rigorous results on valence-bond ground states in antiferromagnets. *Phys. Rev. Lett.*, 59:799–802, 1987.

[17] Andrew Peter Mackenzie and Yoshiteru Maeno. The superconductivity of $\mathrm{Sr_2RuO_4}$ and the physics of spin-triplet pairing. *Rev. Mod. Phys.*, 75:657–712, 2003.

[18] Liang Fu, C. L. Kane, and E. J. Mele. Topological Insulators in Three Dimensions. *Phys. Rev. Lett.*, 98:106803, 2007.

[19] D. Hsieh, D. Qian, L. Wray, Y. Xia, Y. S. Hor, R. J. Cava, and M. Z. Hasan. A topological Dirac insulator in a quantum spin Hall phase (experimental realization of a 3D Topological Insulator). *Nature*, 452:970–974, 2008.

[20] X. Chen, Z.-C. Gu, and X.-G. Wen. Local unitary transformation, long-range quantum entanglement, wave function renormalization, and topological order. *Phys. Rev. B*, 82(15):155138, October 2010.

[21] Rahul Nandkishore and Leonid Levitov. Quantum anomalous Hall state in bilayer graphene. *Phys. Rev. B*, 82:115124, 2010.

[22] Maxim Dzero, Kai Sun, Victor Galitski, and Piers Coleman. Topological Kondo Insulators. *Phys. Rev. Lett.*, 104:106408, 2010.

[23] M. Dzero, J. Xia, V. Galitski, and P. Coleman. Topological Kondo Insulators. *Annual Review of Condensed Matter Physics*, 7:249–280, 2016.

[24] S. Ryu and S.-C. Zhang. Interacting topological phases and modular invariance. *Phys. Rev. B*, 85(24):245132, 2012.

[25] Chang-Tse Hsieh, Gil Young Cho, and Shinsei Ryu. Global anomalies on the surface of fermionic symmetry-protected topological phases in (3+1) dimensions. *Phys. Rev. B*, 93:075135, 2016.

[26] Xiangang Wan, Ari M. Turner, Ashvin Vishwanath, and Sergey Y. Savrasov. Topological semimetal and Fermi-arc surface states in the electronic structure of pyrochlore iridates. *Phys. Rev. B*, 83:205101, 2011.

[27] Su-Yang Xu, Ilya Belopolski, Nasser Alidoust, Madhab Neupane, Guang Bian, Chenglong Zhang, Raman Sankar, Guoqing Chang, Zhujun Yuan, Chi-Cheng Lee, Shin-Ming Huang, Hao Zheng, Jie Ma, Daniel S. Sanchez, BaoKai Wang, Arun Bansil, Fangcheng Chou, Pavel P. Shibayev, Hsin Lin, Shuang Jia, and M. Zahid Hasan. Discovery of a Weyl Fermion semimetal and topological Fermi arcs. *Science*, 2015.

[28] Q. Li, D. E. Kharzeev, C. Zhang, Y. Huang, I. Pletikosić, A. V. Fedorov, R. D. Zhong, J. A. Schneeloch, G. D. Gu, and T. Valla. Chiral magnetic effect in $ZrTe_5$. *Nature Physics*, 12:550–554, 2016.

[29] André Eckardt, Christoph Weiss, and Martin Holthaus. Superfluid-Insulator Transition in a Periodically Driven Optical Lattice. *Phys. Rev. Lett.*, 95:260404, 2005.

[30] C. E. Creffield and T. S. Monteiro. Tuning the Mott Transition in a Bose-Einstein Condensate by Multiple Photon Absorption. *Phys. Rev. Lett.*, 96:210403, 2006.

[31] Alessandro Zenesini, Hans Lignier, Donatella Ciampini, Oliver Morsch, and Ennio Arimondo. Coherent Control of Dressed Matter Waves. *Phys. Rev. Lett.*, 102:100403, 2009.

[32] J. Struck, C. Ölschläger, R. Le Targat, P. Soltan-Panahi, A. Eckardt, M. Lewenstein, P. Windpassinger, and K. Sengstock. Quantum Simulation of Frustrated Classical Magnetism in Triangular Optical Lattices. *Science*, 333:996–999, 2011.

[33] M. Aidelsburger, M. Atala, M. Lohse, J. T. Barreiro, B. Paredes, and I. Bloch. Realization of the Hofstadter Hamiltonian with Ultracold Atoms in Optical Lattices. *Phys. Rev. Lett.*, 111:185301, 2013.

[34] Hirokazu Miyake, Georgios A. Siviloglou, Colin J. Kennedy, William Cody Burton, and Wolfgang Ketterle. Realizing the Harper Hamiltonian with Laser-Assisted Tunneling in Optical Lattices. *Phys. Rev. Lett.*, 111:185302, 2013.

[35] J-I. Inoue and A. Tanaka. Photoinduced Transition between Conventional and Topological Insulators in Two-Dimensional Electronic Systems. *Phys. Rev. Lett.*, 105:017401, 2010.

[36] Takuya Kitagawa, Takashi Oka, Arne Brataas, Liang Fu, and Eugene Demler. Transport properties of nonequilibrium systems under the application of light: Photoinduced quantum Hall insulators without Landau levels. *Phys. Rev. B*, 84:235108, 2011.

[37] Z. Gu, H.A. Fertig, D.P. Arovas, and A. Auerbach. Floquet Spectrum and Transport through an Irradiated Graphene Ribbon. *Phys. Rev. Lett.*, 107:216601, 2011.

[38] Y.H. Wang, H. Steinberg, P. Jarillo-Herrero, and N. Gedik. Observation of Floquet-Bloch States on the Surface of a Topological Insulator. *Science*, 342:453–457, 2013.

[39] N.H. Lindner, G. Refael, and V. Galitski. Floquet topological insulator in semiconductor quantum wells. *Nat. Phys.*, 7(1926):490–495, 2011.

[40] M.S. Rudner, N. H. Lindner, E. Berg, and M. Levin. Anomalous Edge States and the Bulk-Edge Correspondence for Periodically Driven Two-Dimensional Systems. *Phys. Rev. X*, 3:031005, 2013.

[41] B. M. Fregoso, J. P. Dahlhaus, and J. E. Moore. Dynamics of tunneling into nonequilibrium edge states. *Phys. Rev. B*, 90(15):155127, 2014.

[42] A. Gomez-Leon, P. Delplace, and G. Platero. Engineering anomalous quantum Hall plateaus and antichiral states with ac fields. *Phys. Rev. B*, 89:205408, 2014.

[43] P. M. Perez-Piskunow, Gonzalo Usaj, C. A. Balseiro, and L. E. F. Foa Torres. Floquet chiral edge states in graphene. *Phys. Rev. B*, 89:121401, 2014.

[44] A. Quelle and C. Morais Smith. Dynamical competition between quantum Hall and quantum spin Hall effects. *Phys. Rev. B*, 90:195137, 2014.

[45] Arijit Kundu, H.A. Fertig, and Babak Seradjeh. Effective Theory of Floquet Topological Transitions. *Phys. Rev. Lett.*, 113:236803, 2014.

[46] G. Usaj, P. M. Perez-Piskunow, L. E. F. Foa Torres, and C. A. Balseiro. Irradiated graphene as a tunable Floquet topological insulator. *Phys. Rev. B*, 90(11):115423, 2014.

[47] D. Carpentier, P. Delplace, M. Fruchart, and K. Gawedzki. Topological Index for Periodically Driven Time-Reversal Invariant 2D Systems. *Physical Review Letters*, 114(10):106806, 2015.

[48] Frederik Nathan and Mark S Rudner. Topological singularities and the general classification of FloquetBloch systems. *New Journal of Physics*, 17(12):125014, 2015.

[49] A. Quelle, M.O. Goerbig, and C. Morais Smith. Bandwidth-resonant Floquet states in honeycomb optical lattices. *New Journal of Physics*, 18(1):015006, 2016.

[50] C-K Chiu, H. Yao, and S. Ryu. Classification of topological insulators and superconductors in the presence of reflection symmetry. *Phys. Rev. B*, 88:075142, 2013.

[51] T. L. Hughes, E. Prodan, and B. A. Bernevig. Inversion-symmetric topological insulators. *Phys. Rev. B*, 83(24):245132, 2011.

[52] R.-J. Slager, A. Mesaros, V. Juričić, and J. Zaanen. The space group classification of topological band insulators. *Nature Phys.*, 9:98–102, 2013.

[53] W. Beugeling, A. Quelle, and C. Morais Smith. Nontrivial topological states on a Möbius band. *Phys. Rev. B*, 89(23):235112, 2014.

[54] A. Quelle, W. Beugeling, and C. Morais Smith. Topological Floquet states on a Möbius band irradiated by circularly polarised light. *Solid State Communications*, 215:27–33, 2015.

[55] A. Quelle, T. Kvorning, T. H. Hansson, and C. Morais Smith. Edge Majoranas on locally flat surfaces - the cone and the Möbius band. *Phys. Rev. B*, 94:125137, 2016.

[56] V. Mourik, K. Zuo, S. M. Frolov, S. R. Plissard, E. P. A. M. Bakkers, and L. P. Kouwenhoven. Signatures of Majorana Fermions in Hybrid Superconductor-Semiconductor Nanowire Devices. *Science*, 336:1003–, 2012.

[57] S. Ryu, J. E. Moore, and A. W. W. Ludwig. Electromagnetic and gravitational responses and anomalies in topological insulators and superconductors. *Phys. Rev. B*, 85(4):045104, 2012.

[58] R. Nakai, S. Ryu, and K. Nomura. Laughlin's argument for the quantized thermal Hall effect. *Phys. Rev. B*, 95(16):165405, 2017.

[59] A. Quelle, E. Cobanera, and C. Morais Smith. Thermodynamic signatures of edge states in topological insulators. *Phys. Rev. B*, 94(7):075133, 2016.

[60] S. N. Kempkes, A. Quelle, and C. Morais Smith. Universalities of thermodynamic signatures in topological phases. *Scientific Reports*, 6:38530, 2016.

[61] O. Viyuela, A. Rivas, and M. A. Martin-Delgado. Uhlmann Phase as a Topological Measure for One-Dimensional Fermion Systems. *Phys. Rev. Lett.*, 112(13):130401, 2014.

[62] Edward Witten. Quantum field theory and the Jones polynomial. *Comm. Math. Phys.*, 121(3):351–399, 1989.

[63] M. Stome. Edge Waves in the Quantum Hall effect. *Annals of Physics*, 207:38–52, 1991.

[64] Goldstein, Safko, and Poole. *Classical Mechanics*. Addison-Wesley, third edition, 2001.

[65] J. Bellissard, A. van Elst, and H. Schulz-Baldes. The noncommutative geometry of the quantum Hall effect. *Journal of Mathematical Physics*, 35:5373–5451, 1994.

[66] A.H. Castro Neto, F. Guinea, N.M.R. Peres, K.S. Novoselov, and A.K. Geim. The electronic properties of graphene. *Rev. Mod. Phys.*, 81:109, 2009.

[67] Liang Fu and C.L. Kane. Time Reversal Polarization and a Z_2 Adiabatic Spin Pump. *Phys. Rev. B*, 74(195312), 2006.

[68] Ferdinand Evers and Alexander D. Mirlin. Anderson transitions. *Rev. Mod. Phys.*, 80:1355–1417, 2008.

[69] R. S. K. Mong and V. Shivamoggi. Edge states and the bulk-boundary correspondence in Dirac Hamiltonians. *Phys. Rev. B*, 83(12):125109, 2011.

[70] E. Witten. Fermion path integrals and topological phases. *Rev. of Mod. Phys.*, 88(3):035001, 2016.

[71] A. Coste and M. Lüscher. Parity anomaly and fermion-boson transmutation in 3-dimensional lattice QED. *Nuclear Physics B*, 323:631–659, 1989.

[72] R. B. Laughlin. Quantized Hall conductivity in two dimensions. *Phys. Rev. B*, 23:5632–5633, 1981.

[73] D. C. Tsui, H. L. Stormer, and A. C. Gossard. Two-Dimensional Magnetotransport in the Extreme Quantum Limit. *Phys. Rev. Lett.*, 48:1559–1562, 1982.

[74] R. B. Laughlin. Anomalous Quantum Hall Effect: An Incompressible Quantum Fluid with Fractionally Charged Excitations. *Phys. Rev. Lett.*, 50:1395–1398, 1983.

[75] G. Wirth, M. Ölschläger, and A. Hemmerich. Evidence for orbital superfluidity in the P-band of a bipartite optical square lattice. *Nat. Phys.*, 7:147–153, 2011.

[76] M. Ölschläger, T. Kock, G. Wirth, A. Ewerbeck, C. Morais Smith, and A. Hemmerich. Interaction-induced chiral $p_x \pm ip_y$ superfluid order of bosons in an optical lattice. *New Journal of Physics*, 15(8):083041, 2013.

[77] M. Lewenstein, A. Sanpera, V. Ahufinger, B. Damski, A. Sen, and U. Sen. Ultracold atomic gases in optical lattices: mimicking condensed matter physics and beyond. *Advances in Physics*, 56:243–379, 2007.

[78] Immanuel Bloch, Jean Dalibard, and Wilhelm Zwerger. Many-body physics with ultracold gases. *Rev. Mod. Phys.*, 80:885–964, 2008.

[79] H. Lignier, C. Sias, D. Ciampini, Y. Singh, A. Zenesini, O. Morsch, and E. Arimondo. Dynamical Control of Matter-Wave Tunneling in Periodic Potentials. *Phys. Rev. Lett.*, 99:220403, 2007.

[80] L. Tarruell, D. Greif, T. Uehlinger, G. Jotzu, and T. Esslinger. Creating, moving and merging Dirac points with a Fermi gas in a tunable honeycomb lattice. *Nature*, 483:302–305, 2012.

[81] S. Koghee, Lih-King Lim, M.O. Goerbig, and C. Morais Smith. Merging and alignment of Dirac points in a shaken honeycomb optical lattice. *Phys. Rev. A*, 85:023637, 2012.

[82] A. Hemmerich and C. Morais Smith. Excitation of a d-Density Wave in an Optical Lattice with Driven Tunneling. *Phys. Rev. Lett.*, 99:113002, 2007.

[83] Q. Beaufils, G. Tackmann, X. Wang, B. Pelle, S. Pelisson, P. Wolf, and F. Pereira dos Santos. Laser Controlled Tunneling in a Vertical Optical Lattice. *Phys. Rev. Lett.*, 106:213002, 2011.

[84] G. Jotzu, M. Messer, R. Desbuquois, M. Lebrat, T. Uehlinger, D. Greif, and T. Esslinger. Experimental realization of the topological Haldane model with ultracold fermions. *Nature*, 515:237, 2014.

[85] M. Aidelsburger, M. Lohse, C. Schweizer, M. Atala, J.T. Barreiro, S. Nascimbѐne, N.R. Cooper, I. Bloch, and N. Goldman. Measuring the Chern number of Hofstadter bands with ultracold bosonic atoms. *Nat. Phys.*, 11:162, 2015.

[86] L. Chomaz, L. Corman, T. Bienaimé, R. Desbuquois, C. Weitenberg, S. Nascimbène, J. Beugnon, and J. Dalibard. Emergence of coherence via transverse condensation in a uniform quasi-two-dimensional Bose gas. *Nat. Commun.*, 6:6162, 2015.

[87] M. Ezawa. Photoinduced topological phase transitin and a single Dirac-cone state in Silicene. *Phys. Rev. Lett.*, 110:026603, 2013.

[88] Benjamin M. Fregoso, Y. H. Wang, N. Gedik, and Victor Galitski. Driven electronic states at the surface of a topological insulator. *Phys. Rev. B*, 88:155129, 2013.

[89] Alessandro Zenesini, Hans Lignier, Donatella Ciampini, Oliver Morsch, and Ennio Arimondo. Coherent Control of Dressed Matter Waves. *Phys. Rev. Lett.*, 102:100403, 2009.

[90] J. Struck, M. Weinberg, C. Ölschläger, P. Windpassinger, J. Simonet, K. Sengstock, R. Höppner, P. Hauke, A. Eckardt, M. Lewenstein, and L. Mathey. Engineering Ising-XY spin-models in a triangular lattice using tunable artificial gauge fields. *Nat. Phys.*, 9:738–743, 2013.

[91] N. Goldman and J. Dalibard. Periodically Driven Quantum Systems: Effective Hamiltonians and Engineered Gauge Fields. *Phys. Rev. X*, 4:031027, 2014.

[92] C. V. Parker, L.-C. Ha, and C. Chin. In situ observation of strongly interacting ferromagnetic domains in a shaken optical lattice. *Nat. Phys.*, 9:769, 2013.

[93] Wei Zheng, Boyang Liu, Jiao Miao, Cheng Chin, and Hui Zhai. Strong Interaction Effects and Criticality of Bosons in Shaken Optical Lattices. *Phys. Rev. Lett.*, 113:155303, 2014.

[94] W. Zheng and H. Zhai. Floquet topological states in shaking optical lattices. *Phys. Rev. A*, 89(6):061603, 2014.

[95] M.C. Rechtsman, J.M. Zeuner, Y. Plotnik, Y. Lumer, D. Podolsky, F. Dreisow, S. Nolte, M. Segev, and A. Szameit. Photonic Floquet topological insulators. *Nature*, 496:196–200, 2013.

[96] A. Gómez-León and G. Platero. Floquet-Bloch Theory and Topology in Periodically Driven Lattices. *Phys. Rev. Lett.*, 110:200403, 2013.

[97] W. Rudin. *Functional Analysis*. McGraw-Hill, 2nd edition, 1991.

[98] M. Reed. *Methods of Modern mathematical Physics*, volume 1. Academic press, 1st edition, 1981.

[99] H. Sambe. Steady States and Quasienergies of a Quantum-Mechanical System in an Oscillating Field. *Phys. Rev. A*, 7(6):2203–2213, 1973.

[100] M. Grifoni and P. Hänggi. Driven quantum tunneling. *Phys. Rep.*, 304:229–354, 1998.

[101] A. Hemmerich. Effective time-independent description of optical lattices with periodic driving. *Phys. Rev. A*, 81:063626, 2010.

[102] E. Arimondo, D. Ciampini, A. Eckardt, M. Holthaus, and O. Morsch. Kilohertz-Driven Bose-Einstein Condensates in Optical Lattices. *Advances in Atomic Molecular and Optical Physics*, 61:515–547, 2012.

[103] P. Delplace, A. Gomez-Leon, and G. Platero. Merging of Dirac points and Floquet topological transitions in AC driven graphene. *Phys. Rev. B*, 88:245422, 2014.

[104] Y.T. Katan and D. Podolsky. Modulated Floquet Topological Insulators. *Phys. Rev. Lett.*, 110:016802, 2013.

[105] T. Kitagawa, E. Berg, M. Rudner, and E. Demler. Topological characterization of periodically-driven quantum systems. *Phys. Rev. B*, 82:235114, 2010.

[106] I. C. Fulga and M. Maksymenko. Scattering matrix invariants of Floquet topological insulators. *Phys. Rev. B*, 93(7):075405, 2016.

[107] R. Roy and F. Harper. Periodic Table for Floquet Topological Insulators. *ArXiv e-prints*, 2016.

[108] A. Gomez-Leon, P. Delplace, and G. Platero. Engineering anomalous quantum Hall plateaus and antichiral states with ac fields. *Phys. Rev. B*, 89:205408, 2014.

[109] R. Peierls. On the theory of diamagnetism of conduction electrons. *Z. Phys. 80. World Scientific. pp. 763-791*, 80:763–791, 1933.

[110] Y. Zhang, Y-W. Tan, H.L. Stormer, and P. Kim. Experimental observation of the quantum Hall effect and Berry's phase in graphene. *Nature*, 438:201–204, 2005.

[111] M.O. Goerbig. Electronic Properties of Graphene in a Strong Magnetic Field. *Rev. Mod. Phys.*, 83:1193, 2011.

[112] H. Min, J. E. Hill, N. A. Sinitsyn, B. R. Sahu, L. Kleinman, and A. H. MacDonald. Intrinsic and Rashba spin-orbit interactions in graphene sheets. *Phys. Rev. B*, 74(16):165310, 2006.

[113] G.A. Steele, F. Pei, E.A. Laird, J.M. Jol, H.B. Meerwaldt, and L.P. Kouwenhoven. Large spin-orbit coupling in carbon nanotubes. *Nat. Comm.*, 4:1573, 2013.

[114] Y. Yang, Z. Xu, L. Sheng, B. Wang, D. Y. Xing, and D. N. Sheng. Time-Reversal-Symmetry-Broken Quantum Spin Hall Effect. *Phys. Rev. Lett.*, 107(6):066602, 2011.

[115] N. Goldman, W. Beugeling, and C. Morais Smith. Topological phase transitions between chiral and helical spin textures in a lattice with spin-orbit coupling and a magnetic field. *EPL*, 97:23003, 2012.

[116] W. Beugeling, N. Goldman, and C. Morais Smith. Topological phases in a two-dimensional lattice: Magnetic field versus spin-orbit coupling. *Phys. Rev. B*, 86:075118, 2012.

[117] Mahdi Zarea and Nancy Sandler. Rashba spin-orbit interaction in graphene and zigzag nanoribbons. *Phys. Rev. B*, 79:165442, 2009.

[118] R. van Gelderen and C. Morais Smith. Rashba and intrinsic spin-orbit interactions in biased bilayer graphene. *Phys. Rev. B*, 81(12):125435, 2010.

[119] P. M. Perez-Piskunow, L. E. F. Foa Torres, and G. Usaj. Hierarchy of Floquet gaps and edge states for driven honeycomb lattices. *Phys. Rev. A*, 91(4):043625, 2015.

[120] J. Bellissard. Change of the Chern number at band crossings. *eprint arXiv:cond-mat/9504030*, 1995.

[121] Liang Fu and C. L. Kane. Topological insulators with inversion symmetry. *Phys. Rev. B*, 76:045302, 2007.

[122] X.-L. Qi and S.-C. Zhang. The quantum spin Hall effect and topological insulators. *Phys. Today*, 63(1):33, 2010.

[123] E. Kalesaki, C. Delerue, C. Morais Smith, W. Beugeling, G. Allan, and D. Vanmaekelbergh. Dirac Cones, Topological Edge States, and Nontrivial Flat Bands in Two-Dimensional Semiconductors with a Honeycomb Nanogeometry. *Phys. Rev. X*, 4:011010, 2014.

[124] M. P. Boneschanscher, W. H. Evers, J. J. Geuchies, T. Altantzis, B. Goris, F. T. Rabouw, S. A. P. van Rossum, H. S. J. van der Zant,

L. D. A. Siebbeles, G. Van Tendeloo, I. Swart, J. Hilhorst, A. V. Petukhov, S. Bals, and D. Vanmaekelbergh. Long-range orientation and atomic attachment of nanocrystals in 2D honeycomb superlattices. *Science*, 344(6190):1377–1380, 2014.

[125] W. Beugeling, E. Kalesaki, C. Delerue, Y.-M. Niquet, D. Vanmaekelbergh, and C. Morais Smith. Topological states in multi-orbital HgTe honeycomb lattices. *Nat. Comm.*, 6:6316, 2015.

[126] P. Soltan-Panahi, J. Struck, P. Hauke, A. Bick, W. Plenkers, G. Meineke, C. Becker, P. Windpassinger, M. Lewenstein, and K. Sengstock. Multi-component quantum gases in spin-dependent hexagonal lattices. *Nat. Phys.*, 7:434–440, 2011.

[127] Matthew D. Reichl and Erich J. Mueller. Floquet edge states with ultracold atoms. *Phys. Rev. A*, 89:063628, 2014.

[128] P. Titum, E. Berg, M. S. Rudner, G. Refael, and N. H. Lindner. Anomalous Floquet-Anderson Insulator as a Nonadiabatic Quantized Charge Pump. *Phys. Rev. X*, 6(2):021013, 2016.

[129] T. Kitagawa, M.A. Broome, A. Fedrizzi, M.S. Rudner, E. Berg, I. Kassal, A. Aspuru-Guzik, E. Demler, and A.G. White. Observation of topologically protected bound states in photonic quantum walks. *Nat. Comm.*, 3:882, 2012.

[130] Wenchao Hu, Jason C. Pillay, Kan Wu, Michael Pasek, Perry Ping Shum, and Y. D. Chong. Measurement of a Topological Edge Invariant in a Microwave Network. *Phys. Rev. X*, 5:011012, 2015.

[131] F. Gao, Z. Gao, X. Shi, Z. Yang and. X lin, H. Xu, J.D. Joannopoulos, M. Soljacic, H. Chen, L. Lu, Y. Chong, and B. Zhang. Probing topological protection using a designer surface plasmon structure. *Nat. Comm.*, 7:11619, 2016.

[132] L.J. Maczewsky, J.M. Zeuner, S. Nolte, and A. Szameit. Observation of photonic anomalous Floquet topological insulators. *Nat. Comm.*, 8:13756, 2017.

[133] S. Mukherjee, A. Spracklen, M. Valiente, E. Andersson, P. Öhberg, N. Goldman, and R.R. Thomson. Experimental observation of anomalous topological edge modes in a slowly driven photonic lattice. *Nat. Comm.*, 8:13918, 2017.

[134] A. Quelle, C. Weitenberg, K. Sengstock, and C. Morais Smith. Driving protocol for a Floquet topological phase without static counterpart. *ArXiv e-prints*, 2017.

[135] Shi-Liang Zhu, Baigeng Wang, and L.-M. Duan. Simulation and Detection of Dirac Fermions with Cold Atoms in an Optical Lattice. *Phys. Rev. Lett.*, 98:260402, 2007.

[136] A. Eckardt. Colloquium: Atomic quantum gases in periodically driven optical lattices. *Rev. of Mod. Phys.*, 89(1):011004, 2017.

[137] Julen Ibañez Azpiroz, Asier Eiguren, Aitor Bergara, Giulio Pettini, and Michele Modugno. Tight-binding models for ultracold atoms in honeycomb optical lattices. *Phys. Rev. A*, 87:011602, 2013.

[138] M. E. Tai, A. Lukin, M. Rispoli, R. Schittko, T. Menke, D. Borgnia, P. M. Preiss, F. Grusdt, A. M. Kaufman, and M. Greiner. Microscopy of the interacting Harper-Hofstadter model in the few-body limit. *ArXiv e-prints*, 2016.

[139] N. Fläschner, B.S. Rem, M. Tarnowski, D. Vogel, D.-S. Lühmann, K. Sengstock, and C. Weitenberg. Experimental reconstruction of the Berry curvature in a Floquet Bloch band. *Science*, 352:1091–1094, 2016.

[140] M. Leder, C. Grossert, L. Sitta, M. Genske, A. Rosch, and M. Weitz. Real-space imaging of a topologically protected edge state with ultracold atoms in an amplitude-chirped optical lattice. *Nat. Comm.*, 7:13112, 2016.

[141] M. Atala, M. Aidelsburger, M. Lohse, J.T. Barreiro, B. Paredes, and I. Bloch. Observation of chiral currents with ultracold atoms in bosonic ladders. *Nat. Phys.*, 10:588–593, 2014.

[142] M. Mancini, G. Pagano, G. Cappellini, L. Livi, M. Rider, J. Catani, C. Sias, P. Zoller, M. Inguscio, M. Dalmonte, and L. Fallani. Observation of chiral edge states with neutral fermions in synthetic Hall ribbons. *Science*, 349:1510–1513, 2015.

[143] B.K. Stuhl, H.-I. Lu, L.M. Aycock, D. Genkina, and I.B. Spielman. Visualizing edge states with an atomic Bose gas in the quantum Hall regime. *Science*, 349:1514–1518, 2015.

[144] Nathan Goldman, Jérôme Beugnon, and Fabrice Gerbier. Detecting Chiral Edge States in the Hofstadter Optical Lattice. *Phys. Rev. Lett.*, 108:255303, 2012.

[145] N. Goldman, J. Dalibard, A. Dauphin, F. Gerbier, M. Lewenstein, P. Zoller, and I. B. Spielman. Direct imaging of topological edge states in cold-atom systems. *Proceedings of the National Academy of Science*, 110:6736–6741, 2013.

[146] N. Goldman, G. Jotzu, M. Messer, F. Görg, R. Desbuquois, and T. Esslinger. Creating topological interfaces and detecting chiral edge modes in a two-dimensional optical lattice. *Phys. Rev. A*, 94:043611, 2016.

[147] E. L. Starostin and G. H. M. van der Heijden. The shape of a Möbius strip. *Nat. Mater.*, 6(8):563–567, 2007.

[148] Xianlong Wang, Xiaohong Zheng, Meiyan Ni, Liangjian Zou, and Zhi Zeng. Theoretical investigation of Möbius strips formed from graphene. *Appl. Phys. Lett.*, 97(12):123103, 2010.

[149] Nan Zhao, H. Dong, Shuo Yang, and C. P. Sun. Observable topological effects in molecular devices with Möbius topology. *Phys. Rev. B*, 79:125440, 2009.

[150] Atsushi Yamashiro, Yukihiro Shimoi, Kikuo Harigaya, and Katsunori Wakabayashi. Novel electronic states in graphene ribbons—competing spin and charge orders. *Physica E*, 22(1–3):688–691, 2004.

[151] De-en Jiang and Sheng Dai. Spin States of Zigzag-Edged Mobius Graphene Nanoribbons from First Principles. *J. Phys. Chem. C*, 112(14):5348–5351, 2008.

[152] E. W. S. Caetano, V. N. Freire, S. G. dos Santos, E. L. Albuquerque, D. S. Galvão, and F. Sato. Defects in Graphene-Based Twisted Nanoribbons: Structural, Electronic, and Optical Properties. *Langmuir*, 25(8):4751–4759, 2009. PMID: 19239222.

[153] V. M. Fomin, S. Kiravittaya, and O. G. Schmidt. Electron localization in inhomogeneous Möbius rings. *Phys. Rev. B*, 86:195421, 2012.

[154] Zehao Li and L. R. Ram-Mohan. Quantum mechanics on a Möbius ring: Energy levels, symmetry, optical transitions, and level splitting in a magnetic field. *Phys. Rev. B*, 85:195438, 2012.

[155] Topi Korhonen and Pekka Koskinen. Electronic structure trends of Möbius graphene nanoribbons from minimal-cell simulations. *Comp. Mat. Sci.*, 81:264–268, 2014.

[156] Katsunori Wakabayashi and Kikuo Harigaya. Magnetic Structure of Nano-Graphite Möbius Ribbon. *J. Phys. Soc. Jpn*, 72(5):998–1001, 2003.

[157] E. W. S. Caetano, V. N. Freire, S. G. dos Santos, D. S. Galvão, and F. Sato. Möbius and twisted graphene nanoribbons: Stability, geometry, and electronic properties. *J. Chem. Phys*, 128(16):164719, 2008.

[158] Jin-Wu Jiang, Jian-Sheng Wang, and Baowen Li. Topological effect on thermal conductivity in graphene. *J. Appl. Phys.*, 108(6):064307, 2010.

[159] S. Azevedo, F. Moraes, and J.R. Kaschny. Structural and electronic properties of BN Möbius stripes. *Eur. Phys. J. B*, 85(5):1–4, 2012.

[160] Satoshi Tanda, Taku Tsuneta, Yoshitoshi Okajima, Katsuhiko Inagaki, Kazuhiko Yamaya, and Noriyuki Hatakenaka. Crystal topology: A Möbius strip of single crystals. *Nature*, 417(6887):397–398, 2002.

[161] O. Boada, A. Celi, J. Rodríguez-Laguna, J. I. Latorre, and M. Lewenstein. Quantum simulation of non-trivial topology. *New Journal of Physics*, 17(4):045007, 2015.

[162] F.H. Croom. *Principles of Topology*. Cengage Learning Asia, first edition, 2002.

[163] T. Frankel. *The Geometry of Physics*. Cambridge University Press, first edition, 2004.

[164] S. Weinberg. *The Quantum Theory of Fields, part 1*. Cambridge University Press, 1st edition, 1996.

[165] Yasuhiro Hatsugai, Takahiro Fukui, and Hideo Aoki. Topological analysis of the quantum Hall effect in graphene: Dirac-Fermi transition across van Hove singularities and edge versus bulk quantum numbers. *Phys. Rev. B*, 74:205414, 2006.

[166] D. Bercioux, N. Goldman, and D. F. Urban. Topology-induced phase transitions in quantum spin Hall lattices. *Phys. Rev. A*, 83:023609, 2011.

[167] C. Weeks and M. Franz. Topological insulators on the Lieb and perovskite lattices. *Phys. Rev. B*, 82:085310, 2010.

[168] N. Goldman, D. F. Urban, and D. Bercioux. Topological phases for fermionic cold atoms on the Lieb lattice. *Phys. Rev. A*, 83:063601, 2011.

[169] H.-M. Guo and M. Franz. Topological insulator on the kagome lattice. *Phys. Rev. B*, 80:113102, 2009.

[170] L. Fu. Topological Crystalline Insulators. *Phys. Rev. Lett.*, 106:106802, 2011.

[171] Lang-Tao Huang and Dung-Hai Lee. Topological insulators on a Mobius strip. *Phys. Rev. B*, 84:193106, 2011.

[172] N. Jia, C. Owens, A. Sommer, D. Schuster, and J. Simon. Time Reversal Invariant Topologically Insulating Circuits. *Phys. Rev. X*, 5:021031, 2013.

[173] Gregory Moore and Nicholas Read. Nonabelions in the fractional quantum hall effect. *Nuclear Physics B*, 360(2E23):362 – 396, 1991.

[174] N. Read and E. Rezayi. Quasiholes and fermionic zero modes of paired fractional quantum Hall states: The mechanism for non-Abelian statistics. *Phys. Rev. B*, 54:16864–16887, 1996.

[175] N. Read and E. Rezayi. Beyond paired quantum Hall states: Parafermions and incompressible states in the first excited Landau level. *Phys. Rev. B*, 59:8084–8092, 1999.

[176] N. Read and Dmitry Green. Paired states of fermions in two dimensions with breaking of parity and time-reversal symmetries and the fractional quantum Hall effect. *Phys. Rev. B*, 61:10267–10297, 2000.

[177] Martin Greiter, X.G. Wen, and Frank Wilczek. Paired Hall states. *Nuclear Physics B*, 374(3):567 – 614, 1992.

[178] D. A. Ivanov. Non-Abelian Statistics of Half-Quantum Vortices in p-Wave Superconductors. *Phys. Rev. Lett.*, 86:268–271, 2001.

[179] Ady Stern, Felix von Oppen, and Eros Mariani. Geometric phases and quantum entanglement as building blocks for non-Abelian quasiparticle statistics. *Phys. Rev. B*, 70:205338, 2004.

[180] V. Mourik, K. Zuo, S. M. Frolov, S. R. Plissard, E. P. A. M. Bakkers, and L. P. Kouwenhoven. Signatures of Majorana Fermions in Hybrid Superconductor-Semiconductor Nanowire Devices. *Science*, 336:1003, 2012.

[181] H. O. H. Churchill, V. Fatemi, K. Grove-Rasmussen, M. T. Deng, P. Caroff, H. Q. Xu, and C. M. Marcus. Superconductor-nanowire devices from tunneling to the multichannel regime: Zero-bias oscillations and magnetoconductance crossover. *Phys. Rev. B*, 87:241401, 2013.

[182] Masahiko Hayashi and Hiromichi Ebisawa. Little-Parks Oscillation of Superconducting Mbius Strip. *Journal of the Physical Society of Japan*, 70(12):3495–3498, 2001.

[183] Masahiko Hayashi, Hiromichi Ebisawa, and Kazuhiro Kuboki. Superconductivity on a Möbius strip: Numerical studies of order parameter and quasiparticles. *Phys. Rev. B*, 72:024505, 2005.

[184] C. Brüne, C. X. Liu, E. G. Novik, E. M. Hankiewicz, H. Buhmann, Y. L. Chen, X. L. Qi, Z. X. Shen, S. C. Zhang, and L. W. Molenkamp. Quantum Hall Effect from the Topological Surface States of Strained Bulk HgTe. *Phys. Rev. Lett.*, 106:126803, 2011.

[185] T.L. Hill. *Thermodynamics of small systems*. Courier Corporation, 1963.

[186] L. Landau and E. Lifshitz. *Statistical Physics, part 1*. London: Pergamon, 1938.

[187] R.V. Chamberlin. Mesoscopic mean-field theory for supercooled liquids and the glass transition. *Phys. Rev. Lett.*, 82(12):2520, 1999.

[188] R. V. Chamberlin. Mean-field cluster model for the critical behaviour of ferromagnets. *Nature*, 408(6810):337–339, 2000.

[189] R.V. Chamberlin. The Big World of Nanothermodynamics. *Entropy*, 17:52–73, 2014.

[190] Ivan Latella, Agustín Pérez-Madrid, Alessandro Campa, Lapo Casetti, and Stefano Ruffo. Thermodynamics of Nonadditive Systems. *Phys. Rev. Lett.*, 114:230601, 2015.

[191] Josiah Willard Gibbs. On the equilibrium of heterogeneous substances. *American Journal of Science*, (96):441–458, 1878.

[192] M. Z. Hasan and C. L. Kane. Colloquium. *Rev. Mod. Phys.*, 82:3045–3067, 2010.

[193] P. Di Francesco, P. Mathieu, and D. Senechal. *Conformal Field Theory*. Springer, New York, 1997.

[194] S. Hart, H. Ren, T. Wagner, P. Leubner, M. Mühlbauer, C. Brüne, H. Buhmann, L. Molenkamp, and A. Yacoby. Induced superconductivity in the quantum spin Hall edge. *Nat. Phys.*, 10:638–643, 2014.

[195] M. Ezawa, Y. Tanaka, and N. Nagaosa. Topological phase transition without gap closing. *Nat. Sci. Rep.*, 3:2790, 2013.

[196] Haijun Zhang, Chao-Xing Liu, Xiao-Liang Qi, Xi Dai, Zhong Fang, and Shou-Cheng Zhang. Topological insulators in Bi_2Se_3, Bi_2Te_3 and Sb_2Te_3 with a single Dirac cone on the surface. *Nat. Phys.*, 5(6):438–442, 2009.

[197] S. Sachdev. *Quantum Phase Transitions*. Cambridge University Press, 2011.

[198] Eduardo Fradkin. *Field theories of condensed matter physics*. Cambridge University Press, 2013.

[199] Jan Carl Budich and Sebastian Diehl. Topology of density matrices. *Phys. Rev. B*, 91:165140, 2015.

[200] O Viyuela, A Rivas, and MA Martin-Delgado. Symmetry-protected topological phases at finite temperature. *2D Materials*, 2(3):034006, 2015.

[201] J. Glimm and A. Jaffe. *Quantum Physics: A functional Integral Point of View*. Springer, second edition, 1987.

[202] Z.L. Guo, Z.R. Gong, H. Dong, and C.P. Sun. Möbius graphene strip as a topological insulator. *Phys. Rev. B*, 80(195310), 2009.

[203] P. Cats, A. Quelle, S. Kempkes, and C. Morais Smith. Correlation functions for a 1D Weyl superconductor. *In preparation*.

[204] J. van den Broeke, S. Kempkes, A. Quelle, and C. Morais Smith. Critical behavior of Kondo topological insulators. *In preparation*.

[205] M. Reed. *Methods of Modern mathematical Physics*, volume 4. Academic press, 1st edition, 1981.

[206] M. Spivak. *A Comprehensive Introduction to Differential Geometry*, volume 1. Publish or Perish, 3rd edition, 1999.

[207] M. Spivak. *A Comprehensive Introduction to Differential Geometry*, volume 2. Publish or Perish, 3rd edition, 1999.

[208] G. Panati. Triviality of Bloch and Bloch-Dirac bundles. *Ann. Henri Poincaré*, 8:995–1011, 2007.

[209] M. Spivak. *A Comprehensive Introduction to Differential Geometry*, volume 5. Publish or Perish, 3rd edition, 1999.

[210] F.R.S M.V. Berry. Quantal phase factors accompanying adiabatic changes. *Proc. R. Soc. Lond.*, 392:45–57, 1984.

[211] M. Fruchart and D. Carpentier. An Introduction to Topological Order in Insulators. 2013.

[212] D.S. Freed and G.W. Moore. Twisted equivariant matter. 2013.

[213] M. Karoubi. *K-Theory, An introduction*. Springer Verlag, 1st edition, 1978.

[214] A. Kitaev. Periodic table for topological insulators and superconductors. *ArXiv:0901.2686*, 2009.

[215] V.I. Arnold. *Mathematical methods of classical mechanics*. Springer-Verlag, second edition, 1989.

Dankwoord

Al met al is het doorlopen van een promotietraject een van de beste ervaringen van mijn leven geweest. Ik heb er als persoon een enorme groei door meegemaakt. Dan doel ik niet alleen op het verwerven van een wetenschappelijk denkkader. Ook heb ik tijdens mijn werk mensen uit veel verschillende culturen leren kennen, en dat heeft me in positieve zin gevormd. Toch zijn het niet deze exotische ervaringen en ontmoetingen die het belangrijkst zijn. Ze leveren je alleen wat op als je vanuit een goede basis opereert. Daarvoor zijn de mensen die je nabij staan erg belangrijk, en ik ben hen dankbaar dat zij de afgelopen vier jaar zo bijzonder hebben gemaakt.

Dat begint uiteraard bij mijn begeleider, Cristiane Morais Smith. Zij heeft uitstekend werk verricht, en me alles geboden wat ik nodig had om succesvol te zijn als promovendus. Ze heeft me niet alleen direct geholpen met het onderzoek wat ik heb verricht, maar me ook in contact gebracht met veel van de andere collega's die ik dank verschuldigd ben. Daar staat bovenaan haar voormalige postdoc Vladimir Juricic, met wie ik een tijd een kamer heb gedeeld. Hij heeft me geholpen de basis van het vakgebied te beheersen, en daarnaast heb ik vele andere dingen van hem geleerd. Om dezelfde reden ben ik Marco Di Liberto dankbaar, ook hij heeft me geholpen de begrippen te beheersen, en de literatuur te verkennen, die in veel van mijn werk terug komen. Daarbij komen ook Hans Hansson en Thomas Kvorning. Met hen heb ik een zeer productieve samenwerking gehad, die tot werk heeft geleid dat ik zonder hun technische kennis nooit had kunnen doen. Hun gastvrijheid in Stockholm zal ik ook nooit vergeten. Ook wil ik Jean-Sébastien Caux bedanken. Van de discussies met hem heb ik veel geleerd, en ideeën opgedaan die ik anders nooit gehad zou hebben. Hetzelfde geldt voor Carlo Beenakker, die ik dan ook erg dankbaar ben.

De meest leerzame periode tijdens mijn promotie was tijdens de school in Les Houches. Daarom wil ik Mark Goerbig bedanken voor mijn goede tijd daar. Niet alleen omdat hij die heeft helpen organiseren, maar ook vanwege de discussies die we samen hebben gehad, en het werk wat daaruit voortvloeide. Ook ben ik Lars Fritz, en zijn groepsleden Tycho Sikkenk en Andrew Mitchell, dankbaar. Met hen ben ik naar de March meeting geweest, en het gezelschap maakte dat een betere ervaring.

Ook wil ik Mucio Continentino bedanken, voor de wetenschappelijke discussies die we hebben gehad, maar ook voor zijn gastvrijheid in Rio de Janeiro. Daar heb ik niet alleen natuurkunde geleerd, maar ook mijn vriendin Marianne leren kennen.

Ik ben ook dank verschuldigd aan Christof Weitenberg en Klaus Sengstock, met wie ik zo vruchtbaar heb samengewerkt, en die me hebben geholpen nog een beetje in de experimentele werkelijkheid geaard te blijven. Om deze reden ben ik ook Laurens Molenkamp en Daniël Vanmaekelbergh dankbaar; hun experminentele kennis heeft een positieve invloed gehad op mijn werk.

Verder ben ik binnen onze vakgroep Giandomenico Palumbo nog dankbaar. We hebben vele nuttige discussies gehad, waar een paar vruchtbare ideeën uit zijn ontsproten. Daarnaast ben ik nog dankbaar Peter Cats, Sander Kempkes en Jette van den Broeke, die ik begeleid heb tijdens hun masterproject, waar we allemaal van zijn gegroeid. In verband met het project van Peter wil ik Dirk Schuricht nog bedanken voor de literatuur die hij ons heeft aangeraden. Binnen onze groep ben ik tenslotte Guido nog dankbaar, met wie ik vele critische discussies heb gevoerd, die dingen toch altijd weer helderder maakten in mijn hoofd.

Er zijn ook twee kantoorgenoten die ik nog wil bedanken. Ten eerste Luca Santoni, met wie ik veel interessante gesprekken heb gevoerd, en die altijd bereid is geweest mijn nieuwsgierigheid over zijn werk te voeden. Ten tweede Mariya Lizunova, die altijd gezelligheid met zich mee brengt.

Buiten de werkomgeving wil ik allereerst mijn familie noemen. Deel daarvan zijn uiteraard mijn ouders, Ger en Simone, die het zo natuurlijk hebben gemaakt dat mijn leven zijn huidige baan genomen heeft. Ook bedoel ik mijn zusje, Claudia, die nu in hetzelfde schuitje zit, en aan wie ik ook geestelijk zo verwant ben. Verder ben ik mijn neef Maarten en zijn moeder Evelien dankbaar, voor de gezelligheid die ik aan hen beiden heb gehad. Veel van die momenten komen bij mijn grootouders vandaan, die zich helaas niet meer bewust zijn van dit proefschrift. Marianne, die ik op de universiteit heb ontmoet, vind ik ook familie, en haar dagelijkse steun en aanmoediging lijken alles mogelijk te maken.

Mijn vriendenkring ben ik evenzeer dankbaar, voor de gezelligheid en steun die ik aan hen heb gehad. Dat betekend Daniel, die al jaren mijn beste vriend is, met wie ik heb samengewoond, gelachen en geruzied, met wie ik zoveel hobbies deel, en die ik recent heb zien trouwen met zijn geweldige vrouw, Nanda. Ook Bonita valt hieronder, die met ons traint en vuurspuwt en de moshpit induikt. Stefano en Pamela reken ik hierbij, want jullie verzorgen niet alleen uitstekende trainingen, jullie zijn zeker goede vrienden. Thomas, die het vuurgilde mogelijk maakt, en zijn vriendin Nikki, ben ik ook dankbaar voor de gezelligheid, het vermogen om met vuur te kloten en de mensen die ik daarbij verder heb leren kennen.

In het kader van sport wil ik dan tenslotte de familie Engelhardt bedanken voor de gastvrijheid bij Karatedo Yokoso, waar ik altijd de overpeinzingen van de dag van me af kon zetten door te trainen en te groeien als karateka. Veel van wie Daniel en ik geworden zijn, komt bij jullie vandaan.

Jullie allemaal hebben gezorgd dat mijn promotietraject geworden is wat het is, en dat zal ik nooit vergeten.

Samenvatting

In dit proefschrift behandel ik topologische fasen van de materie. Dat materie in verschillende fasen voorkomt is een verschijnsel waar iedereen ervaring mee heeft. Neem bijvoorbeeld een verzameling H_2O moleculen. Tussen de 0 en de $100°$ C, zullen deze moleculen water vormen. Onder de $0°$ C zal dit water bevriezen, en boven de $100°$ C zal het verdampen. Dit zijn drie voorbeelden van de verschillende fasen waarin H_2O moleculen zich kunnen bevinden. Belangrijk is, dat er veel meer fasen van de materie in de natuur voorkomen dan in het dagelijks leven duidelijk wordt. Zo zijn er minstens 17 verschillende soorten ijs, en daarmee kunnen H_2O moleculen zich in minstens 19 verschillende fasen bevinden.

Een ander voorbeeld, dat al abstracter is, maar wel relevanter voor dit werk, betreft de verschillende fasen waarin kristallen zich kunnen bevinden. Kristallen zijn vaste stoffen, zoals ijs, waarin de deeltjes die het kristal vormen in een regelmatig patroon vastzitten. Het merendeel van alle vaste stoffen in de natuur is een kristal. Kristallen kennen minstens twee verschillende fasen: stroom geleidend en niet stroom geleidend. Men spreekt dan van een metaal respectievelijk een isolator. Ik zeg minstens twee, omdat een gegeven kristal verschillende isolerende fasen kan kennen, net zoals H_2O moleculen verschillende soorten ijs kunnen vormen. Voor mijn werk is het belangrijkste voorbeeld een isolerende fase die het zogeheten kwantum-Hall-effect vertoont. Dit is in 1980 door Von Klitzing ontdekt [1], en ik zal het straks verder beschrijven. Sinds de ontdekking van het kwantum-spin-Hall-effect in 2005 [6,7] is bekend dat er meer van dit soort isolerende fasen zijn, en hoe ze systematisch zijn te onderscheiden [10–12].

Dit onderscheid maakt men met behulp van topologie. Topologie bestudeert of objecten op een continue manier in elkaar omgevormd kunnen worden.

Beschouw bijvoorbeeld een bol, zoals links afgebeeld in Fig. 1. Beeld u nu in dat dit boloppervlak wat rekbaar is, en daardoor vervormd kan worden. Met continu wordt bedoeld dat scheuren niet is toegestaan. In dit geval bestudeert de topologie eigenschappen die niet veranderen onder dit continue vervormen. Zo zal men er na enig experimenteren achter komen dat het boloppervlak niet continu te vervormen is tot de torus (midden in Fig. 1), of de twee-gatige torus (rechts in Fig. 1). Dit komt omdat het genus, het aantal gaten, van deze oppervlakken verschilt. Het genus van een oppervlak verandert niet onder continue vervorming, en wordt een topologische invariant genoemd. Twee oppervlakken zijn in elkaar om te vormen als en alleen als ze hetzelfde genus hebben. Dit betekent dat het genus als topologische invariant de topologie van oppervlakken volledig geclassificeerd.

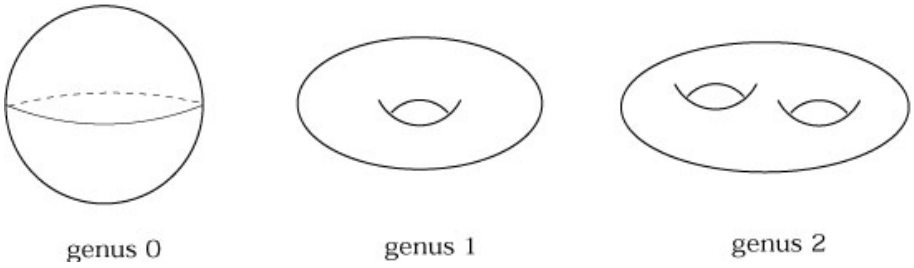

Figuur 1: In deze figuur zijn drie 2-dimensionale objecten weergegeven. Links het boloppervlak, in het midden de torus, en rechts de twee-gatige torus. Onder elk object is het genus, of aantal gaten in het object, gegeven. Het verschil in genus onderscheidt de topologie van deze objecten.

Het blijkt dat bepaalde verschillende isolerende fasen van een kristal zich ook door topologie laten onderscheiden. Om dit volledig netjes te doen is een stevige kennis van zowel de kwantummechanica als de topologie vereist, maar ik kan een redelijk intuitief plaatje schetsen voor 2-dimensionale kristallen.

De elektronen in een kristal gedragen zich ten gevolge van kwantummechanische effecten meer als golven dan als deeltjes. Concreet kan men een 2-dimensionaal kristal als een bak voorstellen, en de elektronen vormen een dunne vloeistoflaag in die bak. Als men een spanningsverschil (dat betekent een verschil in potentiele energie) over het kristal aanbrengt, bijvoorbeeld door het op een stopcontact aan te sluiten, is dit vergelijkbaar met het kantelen van de bak. Een kristal is een metaal als de elektronvloeistof makkelijk stroomt, en een isolator als de elektronvloeistof erg stroperig is. De kwantummechanica kan gebruikt worden om deze stroperigheid te bepalen. De elektronvloeistof

kan om verschillende redenen stroperig zijn, wat overeenkomt met verschillende isolerende fasen, en sommige van deze manieren zijn te onderscheiden met behulp van topologie. Neem bijvoorbeeld de isolerende fase die het kwantum-Hall-effect vertoont. In deze fase bevinden zich allemaal draaikolkjes in de elektronvloeistof, die dezelfde kant op draaien, maar is de elektronvloeistof wel erg stroperig omdat het een isolator betreft. De enige manier om deze draaikolkjes te doen verdwijnen is om de vloeistof minder stroperig te maken, zodat het materiaal een metaal wordt. Het aantal draaikolkjes verandert niet onder continue verstoringen van de isolator, waar continu betekent dat hij niet in een metaal mag veranderen. Het aantal draaikolkjes in de electronvloeistof is dus een topologische invariant van een isolator, net zoals het genus een topologische invariant van een oppervlak is. Verder zijn twee isolatoren alleen continu in elkaar om te vormen als ze hetzelfde aantal draaikolkjes hebben. Dus, net zoals het genus de topologie van een oppervlak uniek classifiseert, bepaalt het aantal draaikolkjes uniek de topologie van de isolator. Een isolerende fase die draaikolkjes vertoont wordt een topologische fase genoemd.

De draaikolkjes hebben ook een meetbaar effect. Als we de bak met vloeistof kantelen, door een voltageverschil over het kristal aan te leggen, dan gaat er geen stroom lopen in de kantelrichting, want de vloeistof is te stroperig. Er gaat echter wel een kleine stroom lopen loodrecht op de kantelrichting, doordat de wervelingen in de draaikolkjes de vloeistof een beetje opzij stuwen. Deze loodrechte geleiding gaat in stapjes, afhankelijk van hoeveel draaikolkjes er zijn, en deze kun je tellen. Net zoals we de topologie van een oppervlak kunnen bepalen door het genus, of het aantal gaten, te bepalen, zo kunnen we de topologie van een isolator bepalen door het aantal stapjes aan loodrechte geleiding in een lab te meten.

Sommige materialen zijn symmetrisch onder tijdsomkering. Dit heeft tot gevolg dat de draaikolkjes altijd in tegengesteld draaiende paren voorkomen, zodat ze netto naar nul optellen. De vraag is 25 jaar lang geweest of deze materialen toch topologisch kunnen zijn als je alleen continue verstoringen toestaat die de symmetrie onder tijdsomkering niet breken. Het heeft lang geduurt voordat deze vraag beantwoord was, omdat deze situatie wiskundig veel lastiger is; door de symmetrie kun je niet simpelweg de tegengesteld draaiende kolkjes tegen elkaar wegstrepen. In 2005 bleek het antwoord ja, en het kwantum-spin-Hall-effect laat dit zien. Toen dit eenmaal bekend was werd de systematiek achter dit soort topologische effecten snel ontdekt, en inmiddels is goed bekend wat de mogelijke topologische fasen zijn in de aanwezigheid van verschillende soorten symmetrie. De theorie hierachter herhaal ik in Hoofdstuk 2.

Ondanks dit succesverhaal is er nog veel over topologische fasen van de

materie wat we niet weten. Mijn eigen bijdrage aan dit voortgaande onderzoek wordt per onderwerp besproken in de verdere hoofdstukken. In hoofdstuk 3 beschrijf ik wat er met de topologie gebeurt als je een isolator volgens een periodiek patroon verstoort, bijvoorbeeld door er licht op te schijnen of hem te schudden. Dit verandert de mogelijke topologische fasen die een isolator kan hebben. Ik bespreek wat voor effect dit heeft in materialen met een honingraatrooster, zoals grafeen, en hoe enkele interessante effecten experimenteel waargenomen kunnen worden.

In hoofdstuk 4 bespreek ik welke invloed de vorm van de isolator zelf heeft op de topologie. Ik heb zoëven voor het 2-dimensionale geval besproken dat niet alle oppervlakken dezelfde topologie hebben, en hoe ze te onderscheiden zijn. De topologische eigenschappen van de isolator als ruimtelijk object hebben ook een invloed op de mogelijke topologische fasen waarin de isolator zich kan bevinden.

Ten slotte bespreek ik in hoofdstuk 5 welke invloed een topologische fase op de thermodynamische eigenschappen van een isolator heeft. De thermodynamica is een oude en zeer betrouwbare tak van de natuurkunde, en de thermodynamische eigenschappen van nieuwe systemen worden vaak uitvoerig bestudeerd vanuit theoretisch en experimenteel oogpunt. Een dergelijke analyse is voor topologische isolatoren nog nauwelijks uitgevoerd. De resultaten in hoofdstuk 5 laten echter zien dat er wel degelijk interessante resultaten te behalen zijn, en hopelijk leidt dit tot verdere aandacht.

Curriculum Vitae

Ik ben geboren te 31 augustus 1988 in mijn ouderlijk huis in Amstelveen, vlak buiten Amsterdam. Van 2000 tot 2006 heb ik aan het Hermann Wesselink College Atheneum gevolgd. Na mijn slagen heb ik eerst een jaar in China gewoond, waarna ik in 2007 natuur en sterrekunde ben gaan studeren aan de VU. In 2009 heb ik daar een studie wiskunde aan toegevoegd. Mijn bachelors heb ik beide cum laude gehaald in 2011 respectievelijk 2012. Hiervoor heb ik de scriptie *Precision Cosmology with the Einstein Telescope* geschreven, onder begeleiding van Walter del Pozzo. In 2011 ben ik begonnen met de Master Mathematische Fysica aan de universiteit van Amsterdam. Deze heb ik afgerond met de scriptie *Gauge theories with an application to Chern-Simons theory* onder begeleiding van Nicolai Reshetikhin. Na deze master ben ik aan de universiteit Utrecht begonnen aan mijn promotieonderzoek onder Cristiane Morais Smith, wat tot dit proefschrift geleid heeft.